

**A Thesis Submitted for the Degree of PhD at the University of Warwick**

**Permanent WRAP URL:**

<http://wrap.warwick.ac.uk/174590>

**Copyright and reuse:**

This thesis is made available online and is protected by original copyright.

Please scroll down to view the document itself.

Please refer to the repository record for this item for information to help you to cite it.

Our policy information is available from the repository home page.

For more information, please contact the WRAP Team at: [wrap@warwick.ac.uk](mailto:wrap@warwick.ac.uk)

# **Multiscale structuring and characterisation of polyvinylidene difluoride based nanodielectrics**

by

**Tom Pickford**

A thesis submitted in partial fulfilment of the requirements for  
the degree of

Doctor of Philosophy in Engineering

University of Warwick

Warwick Manufacturing Group

International Institute for Nanocomposites Manufacturing

**May 2022**

# Table of Contents

<b>Table of Contents .....</b>	<b>i</b>
<b>List of Figures.....</b>	<b>v</b>
<b>List of Tables .....</b>	<b>xi</b>
<b>List of Equations .....</b>	<b>xii</b>
<b>List of Abbreviations .....</b>	<b>xiii</b>
<b>Acknowledgements .....</b>	<b>xiv</b>
<b>Declaration of authorship.....</b>	<b>xv</b>
<b>Abstract.....</b>	<b>xvi</b>
<b>Chapter 1 Introduction.....</b>	<b>Error! Bookmark not defined.</b>
1.1. Background.....	<b>Error! Bookmark not defined.</b>
1.2. Fundamentals of dielectrics .....	<b>Error! Bookmark not defined.</b>
1.3. Performance metrics in dielectric materials.....	<b>Error! Bookmark not defined.</b>
1.4. Polyvinylidene difluoride (PVDF).....	<b>Error! Bookmark not defined.</b>
1.5. Research objectives and thesis structure .....	<b>Error! Bookmark not defined.</b>
1.6. References.....	<b>Error! Bookmark not defined.</b>
<b>Chapter 2 Literature review and theoretical background .....</b>	<b>Error! Bookmark not defined.</b>
2.1. Introduction.....	<b>Error! Bookmark not defined.</b>
2.2. Types of dielectric behaviour.....	<b>Error! Bookmark not defined.</b>
2.2.1. Linear dielectrics.....	<b>Error! Bookmark not defined.</b>
2.2.2. Paraelectric and ferroelectric materials.....	<b>Error! Bookmark not defined.</b>
2.3. Polarisation and conduction in dielectric polymers .....	<b>Error! Bookmark not defined.</b>
2.4. Polarisation mechanisms in polymeric systems.....	<b>Error! Bookmark not defined.</b>
2.4.1. Ionic Polarisation .....	<b>Error! Bookmark not defined.</b>
2.4.2. Orientational polarisation.....	<b>Error! Bookmark not defined.</b>
2.4.3. Interfacial Polarisation .....	<b>Error! Bookmark not defined.</b>
2.5. Electrical breakdown in polymers.....	<b>Error! Bookmark not defined.</b>

2.6.	Effects of processing methodologies on the properties of dielectric polymers.....	<b>Error!</b>
<b>Bookmark not defined.</b>		
2.6.1.	Linear polymers .....	<b>Error! Bookmark not defined.</b>
2.6.2.	Ferroelectric polymers .....	<b>Error! Bookmark not defined.</b>
2.6.3.	PVDF and it's copolymers.....	<b>Error! Bookmark not defined.</b>
2.7.	Polymer/inorganic nanoparticle composites .....	<b>Error! Bookmark not defined.</b>
2.8.	All-polymer dielectrics .....	<b>Error! Bookmark not defined.</b>
2.8.1.	PVDF blends.....	<b>Error! Bookmark not defined.</b>
2.8.2.	Multilayer polymer dielectrics .....	<b>Error! Bookmark not defined.</b>
2.9.	Conclusions.....	<b>Error! Bookmark not defined.</b>
2.10.	References.....	<b>Error! Bookmark not defined.</b>
<b>Chapter 3 Electrospinning of PVDF nanofibres .....</b>		<b>67</b>
3.1.	Introduction.....	67
3.2.	Experimental.....	68
3.2.1.	Materials and characterisation .....	68
3.2.2.	PVDF production methods.....	69
3.3.	Results and discussion .....	70
3.3.1.	Effects of an ionic liquid on the morphology of electrospun PVDF nanofibres.....	70
3.3.2.	Thermal analysis of PVDF and PVDF/AMIM composites .....	72
3.3.3.	Identification of PVDF crystal phases by FTIR.....	75
3.3.4.	Identification of PVDF crystal phases by 2D SAXS/WAXS .....	77
3.3.5.	Identification of PVDF crystal phases by 1D SAXS/WAXS .....	79
3.3.6.	Electrical properties of PVDF nanofibre membranes .....	83
3.3.7.	Optimisation of nanofibre production.....	84
3.4.	Conclusions.....	86
3.5.	References.....	87
<b>Chapter 4 Electrospun polymer nanocomposite dielectrics.....</b>		<b>90</b>
4.1.	Introduction.....	90
4.2.	Experimental.....	91

4.2.1.	Materials .....	91
4.2.2.	Electrospinning .....	91
4.2.3.	Synthesis of ZIF coated nanofibre membranes.....	92
4.2.4.	Processing of PAN/ZIF/PHA multilayer composites.....	92
4.2.5.	Characterisation .....	95
4.3.	Results and Discussion .....	95
4.3.1.	Electrospinning .....	95
4.3.2.	Morphology of PAN/ZIF .....	97
4.3.3.	Crystalline structure of PAN/ZIF nanofibres.....	99
4.3.4.	ZIF growth on PVDF-HFP/AMIM (PHA) nanofibres.....	100
4.3.5.	PAN/ZIF five-layer laminates.....	101
4.3.6.	PHA/ZIF three-layer laminates.....	107
4.4.	Conclusions.....	109
4.5.	References.....	110
<b>Chapter 5 Multilayer polymer dielectrics.....</b>		<b>113</b>
5.1.	Introduction.....	113
5.2.	Experimental.....	114
5.3.	Results and discussion .....	115
5.3.1.	Laminate structures by solution casting PMMA with PHA nanofibres.....	115
5.3.2.	Hot-pressed PMMA/PHA nanofibre layered laminates.....	119
5.3.3.	The effect of pressing temperature on PHA nanofibres.....	121
5.3.4.	The effect of pressing temperature on the morphology of laminates.....	130
5.3.5.	The effect of pressing temperature on nanofibre crystalline nanostructure .....	135
5.3.6.	The effect of pressing temperature on energy storage in laminates .....	137
5.3.7.	The energy storage performance of PHA nanofibres in multilayer laminates .....	139
5.3.8.	The effect of PMMA layers on energy storage performance of laminates .....	142
5.3.9.	The effect of the PHA:PMMA mass ratio on ferroelectric performance.....	144
5.3.10.	The effect of pre-pressing the PHA nanofibres on energy storage properties .....	147
5.3.11.	The effect of PMMA layer thickness on energy storage performance .....	150

5.3.12.	Optimised energy storage performance of 3-layer PMMA/PHA laminates .....	152
5.3.13.	Many layered PMMA/PHA nanofibre laminates.....	154
5.3.14.	Energy storage in many layered PMMA/PHA nanofibre laminates .....	158
5.4.	Conclusions.....	163
5.5.	References.....	165
<b>Chapter 6 Conclusions and prospects for future work.....</b>		<b>168</b>
6.1.	Conclusions.....	168
6.2.	Prospects for future work.....	170

## List of Figures

- Figure 1.1.** Ragone plot displaying how different energy storage technologies relate with respect to their energy and power densities, characterising their storage capacity and charge/discharge rates, respectively. Reprinted from ref. <sup>3</sup> with permission from Elsevier..... 1
- Figure 1.2.** Schematic of a generic polarisation-electric field loop, with key parameters and relevant relations labelled. A loop of this form is characteristic of a large domain ferroelectric material, in which there is a large loss due to remnant polarisation of domains after removal of the applied field.<sup>48</sup> Adapted with permission from ref. <sup>58</sup>, Copyright 2022 American Chemical Society..... 8
- Figure 1.3.** P-E loops describing (a) linear behaviour (b) paraelectric behaviour (c) ferroelectric behaviour (d) relaxor ferroelectric behaviour.<sup>62</sup> ..... 9
- Figure 2.1.** A generic response to an applied field in a polymer dielectric across the entire realistic range of applied field frequency. Probing the ultra-low frequency region is difficult and so tests are typically carried out in the  $10^0$ - $10^7$  Hz range. Polarisation  $P_{\text{int}}$  and  $P_{\text{ion}}$  in real materials may appear at higher frequencies than shown in this generalisation. Reprinted (adapted) with permission from Ref. <sup>22</sup>. Copyright 2012 American Chemical Society..... **Error! Bookmark not defined.**
- Figure 2.2.** Crystalline lamellae as a function of strain. Initially, tie molecules – amorphous phase polymer chains which hold adjacent crystalline lamellae together – elongate as the amorphous phase expands, leading to an increase in long period along the stretching direction (**a**=>**b**). Lamellae then begin to break up along the stretching direction (**b**=>**c**), where the polymer reaches its yield point. Then, the long period reaches a maximum (**c**=>**d**), and finally the lamellae are forced to orientate in the same direction as the long period decreases (**d**=>**e**). After this point, the amorphous phase is stretched to its maximum and voids and cavities will nucleate at higher strains. Reproduced from Ref. <sup>64</sup> with permission from the Royal Society of Chemistry. .... **Error! Bookmark not defined.**
- Figure 2.3.** Schematic of the development of electrical trees through the neat ferroelectric polymer, followed by composites containing ceramic nanofillers in various distributions, which significantly impacts how the trees propagate through the material structure. Left to right: no nanofillers, randomly distributed nanofillers, nanofillers distributed near the composite centre, nanofillers distributed near the composite edges. Reproduced from Ref. <sup>72</sup> with permission from the Royal Society of Chemistry. .... **Error! Bookmark not defined.**
- Figure 2.4.** Diagram of PVDF molecules in the 3 key crystalline phases, showing the polarity of the  $\beta$ -phase in particular.<sup>126</sup> ..... **Error! Bookmark not defined.**
- Figure 2.5.** Monomer molecular structures of commonly utilised ferroelectric copolymers of PVDF. Reproduced from Ref. <sup>43</sup> with permission from the Royal Society of Chemistry..... **Error! Bookmark not defined.**
- Figure 2.6.** Schematic of the electrospinning process..... **Error! Bookmark not defined.**

**Figure 2.7.** A schematic of the cross-sectional structure of a multilayer polymer composite, incorporating a polarisable nanofibre layer alongside an insulating, non-porous polymer layer. **Error! Bookmark not defined.**

**Figure 3.1.** SEM images of PVDF nanofibers: **(a)** PVDF 20 wt% in 7:3 DMF/acetone **(b-d)** PVDF in DMF with different concentrations of **(b)** 10 wt%; **(c)** 15 wt% and **(d)** 20 wt%. The fibres shown in **(d)** were formed at a flow rate of 3 ml hr<sup>-1</sup>, a voltage of 12.7 kV and a tip-collector distance of 15 cm.

..... 71

**Figure 3.2.** SEM micrographs of electrospun PVDF fibres containing **(a)** no additives, spun at a flow rate 3 ml hr<sup>-1</sup> and a voltage of 12.7 kV; **(b)** 1 wt% AMIM and **(c)** 3 wt% AMIM, both electrospun at a flow rate of 1.5 ml hr<sup>-1</sup> with a voltage of 7.4–8 kV..... 72

**Figure 3.3.** DSC heating thermograms of **(a)** neat PVDF and **(b)** PVDF/AMIM; and cooling thermograms of **(c)** neat PVDF and **(d)** PVDF/AMIM fabricated by various processing methods (note that the absolute value of the heat flow is arbitrary)..... 73

**Figure 3.4.** **(a)** FTIR of neat PVDF made with various processing methods; **(b)** expanded FTIR region between 740 and 880 cm<sup>-1</sup> **(c)** equivalent FTIR for PVDF/AMIM samples ..... 76

**Figure 3.5.** 2D SAXS/WAXS data of pure PVDF and PVDF/AMIM composites from the three different processing techniques (casting, hot-pressing and electrospinning). Major Bragg reflections are indexed on the 2D WAXS patterns for the  $\alpha$ ,  $\beta$  and  $\gamma$  crystal phases of PVDF. .... 78

**Figure 3.6.** 1D SAXS profiles of **(a)** pure PVDF and **(b)** PVDF–AMIM composites prepared by different processing conditions; **(c)** corresponding 1D correlation function of solution cast pure PVDF. .... 79

**Figure 3.7.** **(a, b)** Electrospun; **(c, d)** solution-cast and **(e, f)** melt-compressed 1D-WAXS spectra (note that the absolute value of the absorbance is arbitrary).is arbitrary). .... 81

**Figure 3.8.** **(a)** a.c. conductivity and **(b)** relative permittivity of the PVDF nanofibre membranes..... 83

**Figure 3.9.** FTIR of PVDF-HFP nanofibre membranes electrospun with various AMIM concentrations ..... **Error! Bookmark not defined.**

**Figure 3.10.** PVDF-HFP/AMIM nanofibres with AMIM loadings of **(a)** 0.02 wt%, **(b)** 0.1 wt% and **(c)** 0.5 wt%..... 85

**Figure 4.1.** **(a)** Schematic showing how the sandwich structured laminate ZIFLAM is formed. After the electrospinning process, the PAN fibres are coated with the BiZIF nanoparticles and pressed into the sandwich structure with the PVDF-HFP/AMIM (PVFHA) fibres and the solution cast PVDF films as shown. PANLAM was fabricated with an identical method without ZIF growth. **(b)** provides a schematic of the cross-section of the resulting laminate, with charge storage sites indicated..... 93

**Figure 4.2.** SEM images of as spun **(a)** PAN nanofibres and **(b)** PAN-2MI nanofibres. .... 96

**Figure 4.3.** SEM images showing the morphology of PAN/ZIF-8 nanofibres **(a, b)**, PAN/ZIF-67 nanofibres **(c, d)** and PAN/BiZIF nanofibres **(e, f)**, all grown for 3 hours. ZIF-8 showed good adherence of ZIF to the nanofibres, although in many regions ZIF agglomerates between fibres built



up, and in general zeolitic structure was not predominantly present. ZIF-67 crystals proved too large to coat the nanofibres once grown into fully zeolitic form, with sizes larger than individual nanofibres. BiZIF samples typically showed the best ZIF-fibre adherence across the whole sample, with less agglomeration and a more polyhedral structure than that seen in the PAN/ZIF-8 nanofibre composites.

..... 98

**Figure 4.4.** X-ray diffraction spectra and SEM images of BiZIF precipitates from samples grown without (a) and with (b) PAN nanofibres, along with SEM images of the resultant BiZIF precipitates with (c) and without (d) the nanofibre present. The peak shift from  $8.73^\circ$  to  $8.25^\circ$  shows a substantial shift in crystal structure due to the change in crystal structure with fibre addition. .... 99

**Figure 4.5.** XRD spectra of (a) a PAN nanofibre and (b) a PAN/BiZIF composite membrane ..... 100

**Figure 4.6.** SEM images of PVFHA nanofibres coated in (a, b) ZIF-8 and (c, d) BiZIF nanoparticles. .... 101

**Figure 4.7.** Fourier Transform Infrared Spectroscopy of the sandwich structured composites and their components. Peaks for the paraelectric  $\alpha$ -phase and polar  $\beta$ -phase, as well as the electroactive  $\gamma$ -phase are highlighted. Electrospun PVDF-HFP/AMIM show a clear  $\beta$ -phase signature, while the hot-pressed PVDF-HFP shows a clear  $\alpha$ -phase signature. Both composites show both  $\beta$ - and  $\alpha$ -phase signatures, implying the partial retention of the crystal structure of the fibres..... 102

**Figure 4.8.** SEM images of the (a) PANLAM and (b) ZIFLAM cross-sections, alongside higher resolution images of the inner layers of (c) PANLAM and (d) ZIFLAM ..... 103

**Figure 4.9.** (a) Permittivity (b) conductivity and (c) phase angle of the PANLAM and ZIFLAM sandwich structured hot-pressed composites, as well as data for a neat PVFHA nanofibre membrane for comparison, measured by broadband impedance spectroscopy. (d) Monopolar electric displacement-field loops measured with a ferroelectric analyser. .... 105

**Figure 4.10.** P-E loops of 3-layer PMMA:PVFHA laminates, containing ZIF-8, BiZIF or no ZIF. (a) Provides a comparison between the two laminates containing different forms of ZIF, whereas (b) provides a comparison between the BiZIF laminate and a laminate lacking ZIF nanofibre coatings. All composites utilised 300 mg PMMA layers alongside PVFHA nanofibre layers ranging from 60 mg (the ZIF absent case) to 90 mg in the BiZIF and ZIF-8 laminates. The ZIF absent laminate was also pressed at  $160^\circ\text{C}$ , whereas the other two samples were pressed at  $140^\circ\text{C}$ ..... 108

**Figure 5.1.** Schematic of the cross-section of the multilayer structure incorporating PVFHA nanofibre layers and PMMA layers, highlighting the orientational polarisation of PVDF polymer chains, the build-up of space charges at boundaries, and the impedance of breakdown events by the interfaces in the structure. Note that, for simplicity's sake, PVDF polymer chains have been shown here rather than PVDF-HFP, and the thickness of the PVFHA layers have been exaggerated. .... 113

**Figure 5.2.** SEM micrographs of the solution cast PMMA/PVDF-HFP laminates. (a) Shows a cross-section of the structure, with no clear layered structure visible; (b) shows a higher resolution image of the fibrous structure, which has been partially damaged by the solution casting process. .... 117

<b>Figure 5.3.</b> Schematic of nanofibre electrospinning and the chaotic form the nanofibre stream tends to exhibit. Setup identical to that <b>Figure 2.6</b> , but with a petri dish on the collector.....	117
<b>Figure 5.4.</b> SEM micrographs of the in-situ electrospun PMMA/PVDF-HFP laminate. <b>(a)</b> A section of the cross-section with a clear fibrous structure; <b>(b)</b> a higher resolution image of the fibrous structure, displaying it's foam like nature; <b>(c)</b> A separate part of the cross-section, showing an air pocket defect; <b>(d)</b> a second portion of the cross-section highlighting the inhomogeneity of the structure, with a lack of fibres and another large defect. <b>(e, f)</b> shows more detailed inhomogeneity in the cross-sections, where it is clear that the multilayer structure has been lost. ....	118
<b>Figure 5.5.</b> <b>(a, b)</b> the cross-section of the doctor bladed PMMA film cast from DMF, which is evidently foamy. <b>(c)</b> and <b>(d)</b> show images of the surface and cross-section of the toluene doctor bladed sample respectively, which provided no evidence of defects.....	121
<b>Figure 5.6.</b> FTIR spectra of PVFHA nanofibres pressed at various temperatures, with key signatures of the different phases indicated. EA here indicates the 'electroactive' peak, which receives contributions from both the $\beta$ and $\gamma$ -phases .....	<b>Error! Bookmark not defined.</b>
<b>Figure 5.7.</b> <i>In situ</i> FTIR measurements of a PVFHA nanofibre membrane, taken by utilising a heated plate built into the spectrometer, hence producing direct measurements of the PVDF-HFP crystal structure while it is in the melt phase.....	124
<b>Figure 5.8.</b> XRD plots of the pressed PVFHA nanofibre membranes, with key peaks indexed.....	125
<b>Figure 5.9.</b> <b>(a)</b> Peak position of the in-plane crystallite 20-21° peak and <b>(b)</b> a higher resolution image of this peak across samples .....	126
<b>Figure 5.10.</b> <b>(a)</b> WAXS diffraction patterns of PVDF-HFP nanofibres (PH nf) and PVFHA nanofibres (PVFHA nf), and PVFHA nanofibre membranes pressed at various temperatures and <b>(b)</b> associated WAXS intensity curves, showing more clearly the presence of orientation (or lack thereof) in the samples. The "as-spun sample" here is the 1D pattern for the "PVFHA nf" sample – no curve for "PH nf" is given. ....	127
<b>Figure 5.11.</b> PVFHA nanofibres pressed at <b>(a, b)</b> 130 <b>(c, d)</b> 140 <b>(e, f)</b> 145 and <b>(g, h)</b> 160 °C .....	129
<b>Figure 5.12.</b> SEM images of <b>(a, b)</b> neat PVFHA nanofibres and <b>(c, d)</b> 180 °C pressed PVFHA nanofibres.....	130
<b>Figure 5.13.</b> 3-layer 20:1 PMMA:PVFHA nanofibre laminates, pressed at <b>(a, b)</b> 135 °C <b>(c, d)</b> 150 °C <b>(e, f)</b> 160 °C .....	131
<b>Figure 5.14.</b> SEM cross-sections of laminates pressed at <b>(a-d)</b> 140 °C <b>(e, f)</b> 160 °C.....	132
<b>Figure 5.15.</b> EDS imaging of the cross-section of the 160°C pressed sample from <b>Figure 5.13.</b> <b>(a)</b> Provides a plain SEM image of the sample, while <b>(b)</b> provides the same image with the elemental maps of fluorine and oxygen superimposed. <b>(c)</b> and <b>(d)</b> provides the fluorine and oxygen maps on their own, highlighting the location of the PMMA and PVFHA layers. ....	133

<b>Figure 5.16. (a)</b> Cross-section of a 180 °C pressed laminate with <b>(b)</b> showing the total elemental map, <b>(c)</b> showing the oxygen content and <b>(d)</b> showing the fluorine content. No layer structure is discernible. ....	134
<b>Figure 5.17.</b> XRD data of laminates pressed at 140 °C and 160 °C, as well as neat PVFHA nanofibres for comparison. <b>(a)</b> provides the whole spectra while <b>(b)</b> shows only the in-plane crystallite peak. .	135
<b>Figure 5.18. (a)</b> WAXS intensity curves of laminates pressed at different temperatures, as well as an as-spun nanofibre membrane, also shown in the inset. <b>(b)</b> WAXS patterns of the same samples. ....	136
<b>Figure 5.19.</b> P-E curves for 3-layer PMMA/PVFHA laminates pressed at various temperatures, alongside a neat PMMA sample. ....	138
<b>Figure 5.20.</b> SEM images of a 3-layer laminate containing a hot-pressed PVDF-HFP central layer and two outer PMMA layers.....	140
<b>Figure 5.21.</b> P-E loops of 3-layer PMMA/PVDF-HFP laminates, containing electrospun and hot-pressed PVDF-HFP, at equal weight ratios of PMMA:PVDF-HFP, tested up to a field of 700 kV/cm, with a neat PMMA sample for control. While the biggest difference in performance comes in the form of adding PVDF-HFP to form a 3-layer laminate with either production method, the nanofibres still outperform their hot-pressed counterpart by over 20% in terms of discharged energy density, while producing a similar discharge efficiency. ....	140
<b>Figure 5.22. (a,b)</b> XRD spectra including labelled key peaks in samples of hot-pressed PVDF-HFP (PH HP), PVDF-HFP nanofibres (PH nf) and PVFHA nanofibres (PVFHA nf) and <b>(c)</b> SAXS diffraction patterns of the same samples. The $\alpha$ -phase clearly diminishes to give rise to the $\beta$ -phase both when moving from hot-pressing to electrospinning, and when adding AMIM to the electrospinning process. Additionally, a small $\gamma$ -phase (130) peak is seen at $\sim 33.2^\circ$ in the two samples lacking AMIM, particularly in the electrospun sample. <sup>26</sup> .....	141
<b>Figure 5.23.</b> Polarisation and current data for a PVFHA nanofibre membrane pressed at 140 °C, alongside data for a high PVDF-HFP content PMMA/PVFHA nanofibre laminate pressed at 160 °C. 400 kV/cm was the field selected here, as the nanofibre membrane underwent electrical breakdown at 420 kV/cm.....	143
<b>Figure 5.24.</b> Comparison of various multilayer laminates with differing PVDF-HFP/AMIM nanofibre loadings. The discharged energy density at 900 kV/cm almost doubles to over 600 mJ/cm <sup>3</sup> at a 2:1 PMMA:PVFHA ratio compared to neat PMMA. .... <b>Error! Bookmark not defined.</b>	
<b>Figure 5.25. (a)</b> Relationship of maximum polarisation against PVFHA nanofibre membrane mass content of laminates and <b>(b)</b> discharged energy density against the same mass variation .....	147
<b>Figure 5.26.</b> Comparison of ferroelectric performance of 3-layer laminates containing either of pre-pressed or neat (unpressed) PVFHA nanofibres, which seems to imply their performance is comparable.....	149

**Figure 5.27.** Comparison of polarisation-electric field loops of 3-layer PVFHA /PMMA laminates with 150 mg PVFHA fibre layers, but with different PMMA layer thicknesses of 300 and 600 mg. Both curves here are from tests at the 10 kV limit of our apparatus, reaching a field of 900 kV/cm. 150

**Figure 5.28.** Data from tests of our highest  $U_e$  laminate; a 160 °C pressed sample with 300 mg PMMA outer layers and 150 mg PVFHA nanofibre inner layers. **(a)** Displays the dependence of discharge efficiency on the applied field, while **(b)** gives the P-E curves for each of these tests. .... 153

**Figure 5.29.** Cross-sections of **(a, b)** 5-layer **(c, d)** 7-layer and **(e, f)** 9-layer 10:1 PMMA:PVFHA nanofibre laminates pressed at 160 °C. Individual layers can be seen, with thicknesses given in **(b)**, and typical laminate thickness provided in **(c)**. **(d)** Shows a rare fracturing incident in one of the layers, exposing retention of some fibrous microstructure. .... 155

**Figure 5.30.** Cross-sectional images of a standalone PMMA layer, with the thickness given in **(b)** 156

**Figure 5.31.** Cross-sections of 15-layer laminates containing **(a, b)** 100 mg PMMA and 4 mg PVFHA nanofibre layers and **(c, d)** 100 mg PMMA layers and 30 mg PVFHA nanofibre layers, pressed at 160 °C. .... 156

**Figure 5.32.** Cross-sectional image of a 10:1 PMMA:PVFHA 9-layer laminate pressed at 160 °C. **(a)** Provides an SEM micrograph of the cross-section, with **(b)** providing the elemental map superimposed on top. **(c)** provides a raw map of the oxygen content, indicating the presence of PMMA, while **(d)** provides a map of the fluorine content, indicating the presence of PVDF-HFP... 157

**Figure 5.33.** P-E loops for the multilayer laminates given in **Table 5.5**. The laminates clearly performed successively better with increasing the number of layers up to the 9-layer sample, when losses became more significant. This led to the lower observed discharge efficiency as well as a far lower maximum polarisation. .... 159

**Figure 5.34.** Maximum polarisation as a function of electric field for the samples given in **Table 5.5**. **(a)** Provides the data with polynomial fits applied to the data points. **(b)** Extrapolates the data points based on the fits produced to give an estimate of how the polarisation would increase if the voltage limit of the apparatus were higher. This extrapolation is an idealised estimate, as these samples may have undergone electrical breakdown before reaching these higher fields..... 160

**Figure 5.35.** P-E loops of PMMA/PVFHA nanofibre laminates **(a)** pressed at 160 °C, with differing layer number and PVFHA nanofibre membrane weight and **(b)** pressed at both 160 °C and 140 °C, with differing layer numbers, containing 300 mg PVFHA nanofibre membranes. .... 160

**Figure 5.36.** **(a, b)** XRD patterns for the 7-layer laminates pressed at 140 °C and 160 °C along with SAXS **(c)** intensity data and **(e, f)** diffraction patterns for these samples. **(d)** also provides SAXS intensity patterns of 3-layer samples for comparison, highlighting their far more substantial orientation. .... 162

## List of Tables

<b>Table 2.1.</b> A variety of polymers, linear and non-linear, listed with their key dielectric properties. Polymers in bold are linear dielectrics. * $U_e$ values calculated via <b>equation 2.1</b> using data extracted from the source paper. All data in this table was collected in experiments performed at room temperature. Permittivity measurements were typically taken at ~1 kHz.....	<b>Error! Bookmark not defined.</b>
<b>Table 3.1.</b> Melting point $T_m$ , crystallization point $T_c$ and total crystallinities $\chi_{dsc}$ determined by DSC. *Very broad melting peak seen due to presence of multiple phases. Value given is taken at the peak's maximum. ....	74
<b>Table 3.2.</b> Phase contents of electrospun PVDF samples containing AMIM. ....	77
<b>Table 3.3.</b> 1D SAXS correlation function results for PVDF and AMIM composites where the fits where reliable and lamellar parameters could be extracted .....	80
<b>Table 3.4.</b> Crystallographic planes identified for each phase from the 1D-WAXS data, for the $\alpha$ , $\beta$ and $\gamma$ phases of PVDF. Planes denoted in bold are observed as strong peaks in the WAXS data, whereas others are smaller, less distinct peaks. The (132) and (211) $\gamma$ -phase signatures are difficult to separate, and so are grouped. ....	80
<b>Table 4.1.</b> Measured $E_b$ of the composites and their components.....	106
<b>Table 5.1.</b> Percentage phase content of various PVFHA nanofibers pressed at different temperatures .....	125
<b>Table 5.2.</b> Ferroelectric performance metrics for the samples provided in <b>Figure 5.19</b> , along with the electric field at which these samples were tested. Notably, a clear drop off in energy storage capacity between 150 °C and 160°C is seen .....	139
Table 5.3. Values derived from Figure 5.24 .....	146
<b>Table 5.4.</b> Data taken in multiple areas of two samples with different PMMA loadings, with the two tests given in <b>Figure 5.27</b> taken from the areas listed as the first tests of each sample in the table. All rows display data for the highest fields reached in each sample area. *Sample underwent breakdown at this field – otherwise, electrical breakdown did not occur.....	152
<b>Table 5.5.</b> Ferroelectric properties of various many layered laminates constructed with 300 mg PMMA layers and 15 mg PVFHA nanofibre layers (i.e. a 20:1 ratio), pressed at 160 °C. The first four rows give data at 10 kV, the limit of the apparatus, with the applied field $E$ dependant on laminate thickness. There were no cases of electrical breakdown. The bottom 4 rows provide data at 400 kV/cm for comparison. ....	159
<b>Table 5.6.</b> Key ferroelectric performance metrics measured from the curves in <b>Figure 5.35(b)</b> , at an electric field of 400 kV/cm. ....	160

## List of Equations

<b>Equation 1.1</b>	Formula for capacitance of a dielectric .....	<b>Error! Bookmark not defined.</b>
<b>Equation 1.2</b>	Formula for conductivity in a dielectric .....	<b>Error! Bookmark not defined.</b>
<b>Equation 1.3</b>	Formula for permittivity of a dielectric .....	<b>Error! Bookmark not defined.</b>
<b>Equation 1.4</b>	Formula for dielectric impedance as a function of conductivity and capacitance.	<b>Error! Bookmark not defined.</b>
<b>Equation 1.5</b>	Formula for impedance of a dielectric as a function of permittivity.	<b>Error! Bookmark not defined.</b>
<b>Equation 1.6</b>	Formula for real and imaginary components of permittivity .....	<b>Error! Bookmark not defined.</b>
<b>Equation 1.7</b>	Formula for dielectric loss.....	<b>Error! Bookmark not defined.</b>
<b>Equation 1.8</b>	Formula for phase angle of the current in a dielectric..	<b>Error! Bookmark not defined.</b>
<b>Equation 1.9</b>	Relation between loss and phase angle in a dielectric..	<b>Error! Bookmark not defined.</b>
<b>Equation 1.10</b>	Formula for stored energy density in a capacitor .....	<b>Error! Bookmark not defined.</b>
<b>Equation 1.11</b>	Formula for discharged energy density in a capacitor .	<b>Error! Bookmark not defined.</b>
<b>Equation 1.12</b>	Formula for discharge efficiency in a capacitor .....	<b>Error! Bookmark not defined.</b>
<b>Equation 2.1</b>	Formula for discharged energy density in a linear dielectric .....	<b>Error! Bookmark not defined.</b>
<b>Equation 2.2</b>	Component of dielectric function arising from interfacial polarisation .....	<b>Error! Bookmark not defined.</b>
<b>Equation 2.3</b>	Relaxation time of interfacial polarisation in a dielectric .....	<b>Error! Bookmark not defined.</b>
<b>Equation 3.1</b>	Beer-Lambert law.....	68
<b>Equation 3.2</b>	1D SAXS correlation function .....	69
<b>Equation 3.3</b>	Formula for invariant quantity used in 1D SAXS correlation function .....	69
<b>Equation 3.4</b>	Formula for crystallinity of a sample as a function of melting enthalpy.....	72
<b>Equation 3.5</b>	Formula for crystallinity derived from the 1D SAXS correlation function .....	79

## List of Abbreviations

2MI	2-methylimidazole
AC/a.c.	Alternating current
AMIM	1-allyl-3-methylimidazolium chloride
BOPP	Biaxially oriented Polypropylene
CRR	Co-operative rearranging region
DC/d.c.	Direct current
DCM	Dichloromethane
DMF	Dimethyl formamide
DSC	Differential Scanning Calorimetry
FTIR	Fourier Transform Infrared Spectroscopy
EDS	Energy dispersive x-ray spectroscopy
IL	Ionic liquid
MOF	Metal-organic framework
P-E (loop/testing)	Polarisation-electric field (loop/testing)
PAN	Polyacrylonitrile
PC	Polycarbonate
PET	Polyethylene terephthalate
PHA (nanofibres)	Polyvinylidene difluoride-co-hexafluoropropylene / 1-allyl-3-methylimidazolium chloride (nanofibres)
PMMA	Polymethylmethacrylate
PVDF	Polyvinylidene difluoride
PVDF-HFP	Polyvinylidene difluoride-co-hexafluoropropylene
PVDF-CTFE	Polyvinylidene fluoride-co-chlorotrifluoroethylene
PVDF-TrFE	PVDF-trifluoroethylene
PVDF-TrFE-CTFE	PVDF-TrFE-1,1-chlorofluoroethylene
RFE	Relaxor ferroelectric
SAXS	Small-angle X-ray scattering
SEM	Scanning Electron Microscopy
WAXS	Wide-angle X-ray scattering
XRD	X-ray diffraction
ZIF	Zeolitic Imidazole framework

## Acknowledgements

I would firstly like to thank my parents for always believing in me in every step of my journey through education. This thesis is as much yours as it is mine, and it goes without saying that I could not have done any of this without your constant support.

I would of course like to thank my supervisor Chaoying for providing me the opportunity to do this project in the first place. Who would have thought an application for a short-term internship would have come this far? Without your support and guidance, I would not be where I am today.

I would like to thank my housemates Jono, Conor, Aly and Jamie, without whom my mental state would have surely collapsed. In particular I would like to thank Jono for making my world at Warwick feel so much bigger by bringing wonderful new people into my life, and for lending an ear when this PhD was at its hardest and I needed it the most. I would also like to thank Aly for being my rock throughout the writing process, I wouldn't have made it through without you!

I would like to give great thanks to Dr. Ellen Heeley, who's advice, support and friendship have been critical throughout my entire PhD. This project would have been several times more difficult without you, and I sincerely hope we get to work together again in the future.

Additionally, I would like to thank Martin Worrall, Alan Heeger, and my PhD colleagues Joe, Andy and Chris in particular for being both supportive and instructive throughout my project. I've learned so much from all of you and my work would have been far more painful without your guidance and advice! I would like to extend these thanks in this regard to Dr. Geoff West, Sabrina Yan, and everyone else who trained and assisted me in the WMG microscopy suite – it was always a pleasure to work with you. Similarly, I would like to thank Steve Huband for providing vital and rapid support for critical experiments in the Physics X-Ray suite at Warwick.

Finally, I would also like to thank my colleagues Andy, Syeda, Eimear, James, Esra, Alistair, Chris, Joe, Khoa, Azzurra, Lorena, David, Rose and Steve for the friendships we built during my time in the IINM. I wish you all the best of luck for the future!. I hope we all manage to stay in touch and I wish you all the very best with your futures, although I'm sure none of you will need it! I would like to thank Andy and Syeda in particular for the coffee breaks that kept me sane. Without your companionship I would have spent countless hours in the IINM labs with enormous weights on my shoulders, so thanks for being great friends and keeping me grounded.



## **Declaration of authorship**

This thesis is submitted to the University of Warwick in support of my application for the degree of Doctor of Philosophy in Engineering. It has been composed by myself and has not been submitted in any previous application for any degree to any other university or higher education institution or as any part of any other submission to the University of Warwick. It describes the work carried out from February 2018 to October 2021.

The work presented in this thesis (including data generated and data analysis) was carried out by the author, except with the support of Dr Ellen Heeley (School of Life Health and Chemical Sciences, Open University), who assisted in data gathering and analysis of small/wide-angle X-ray diffraction measurement and analysis of samples.

A portion of the experimental details chapter 3 of this thesis was published during the PhD period as:

T. Pickford, X. Gu, E. L. Heeley and C. Wan, Effects of an ionic liquid and processing conditions on the  $\beta$ -polymorph crystal formation in poly(vinylidene fluoride), *CrystEngComm*, 2019, 21, 5418–5428. Citations: 20

## Abstract

In the 21st century, the efficiency and sustainability of devices used for electrical energy storage presents a significant challenge for various technologies and industries. Despite many electrical devices and systems becoming more advanced, the components that power these systems are often based on technologies that have not substantially modernised over the past few decades. Dielectric polymers offer a new route for enhancing pulsed power delivery in electrical systems, offering a plethora of advantages over the industry standard ceramics that dominate the field, resolving both the sustainability and energy efficiency problems simultaneously.

This project explores the potential of electrospun polyvinylidene difluoride (PVDF) nanofibre membranes for use in pulsed power devices. PVDF is notable due to the ferroelectric behaviour of its crystalline  $\beta$ -phase, which leads impressive energy storage properties in the polymer, allowing it to compete with commercial capacitors. This has led to the development of a variety of approaches to producing PVDF with a high  $\beta$ -phase content in recent years, with many endeavours producing near 100%  $\beta$ -phase content. Hence attention is now being paid to the subtleties of the crystalline nanostructure of PVDF, such as crystallite size and the orientation of crystallites to further bolster its energy storage potential.

Here, the crystalline nanostructure of PVDF nanofibres is extensively explored under different processing conditions using materials characterisation techniques such as infrared spectroscopy, X-ray diffraction and scanning electron microscopy, while characterising the energy storage potential of these materials using . Correlations are drawn between processing conditions to crystalline nanostructure, and in turn nanostructure in relation to energy storage performance.

Notably in this work, PVDF is electrospun using an ionic liquid in the electrospinning solution, which seeks to maximise the  $\beta$ -phase crystallinity and optimise the crystalline nanostructure of the nanofibre membranes at minimal additional time or cost investment. The unique morphology of the nanofibres is utilised to construct nanocomposites by coating the nanofibres with nanoparticles – in particular, metal organic frameworks (MOFs) – to further increase the energy storage potential of the nanofibre membranes. Finally, multilayer all-polymer laminate materials are constructed to prevent the high energy losses and low-field electrical breakdown experienced by electrospun PVDF nanofibre membranes when used for capacitive energy storage in isolation, as well as alleviating the mechanical fragility of the membranes. This thesis presents a route to creating highly ferroelectric polymer-based materials with impressive energy storage properties that could shape the future of materials in pulsed power devices.

# Chapter 1

## Introduction

### 1.1. Background

Dielectric capacitive materials with ultrahigh energy storage densities are in high demand for important applications in mobile communication, biomedical devices, and self-powered electronics systems, as well as in renewable energy and power distribution. The appeal of microelectronic energy storage devices based on dielectric or ferroelectric capacitors comparative to electrochemical energy storage devices (such as batteries and fuel cells) lies in their higher power density due to their high charge and discharge rate.<sup>1</sup> However, their energy densities are generally lower than electrochemistry-based energy storage technologies.<sup>2</sup> A Ragone plot displaying the differences between various energy storage technologies is shown in **Figure 1.1**. The high-power density of capacitors - particularly electrostatic capacitors – provide their key advantage over alternative energy storage technologies, making them well suited for pulsed power systems.

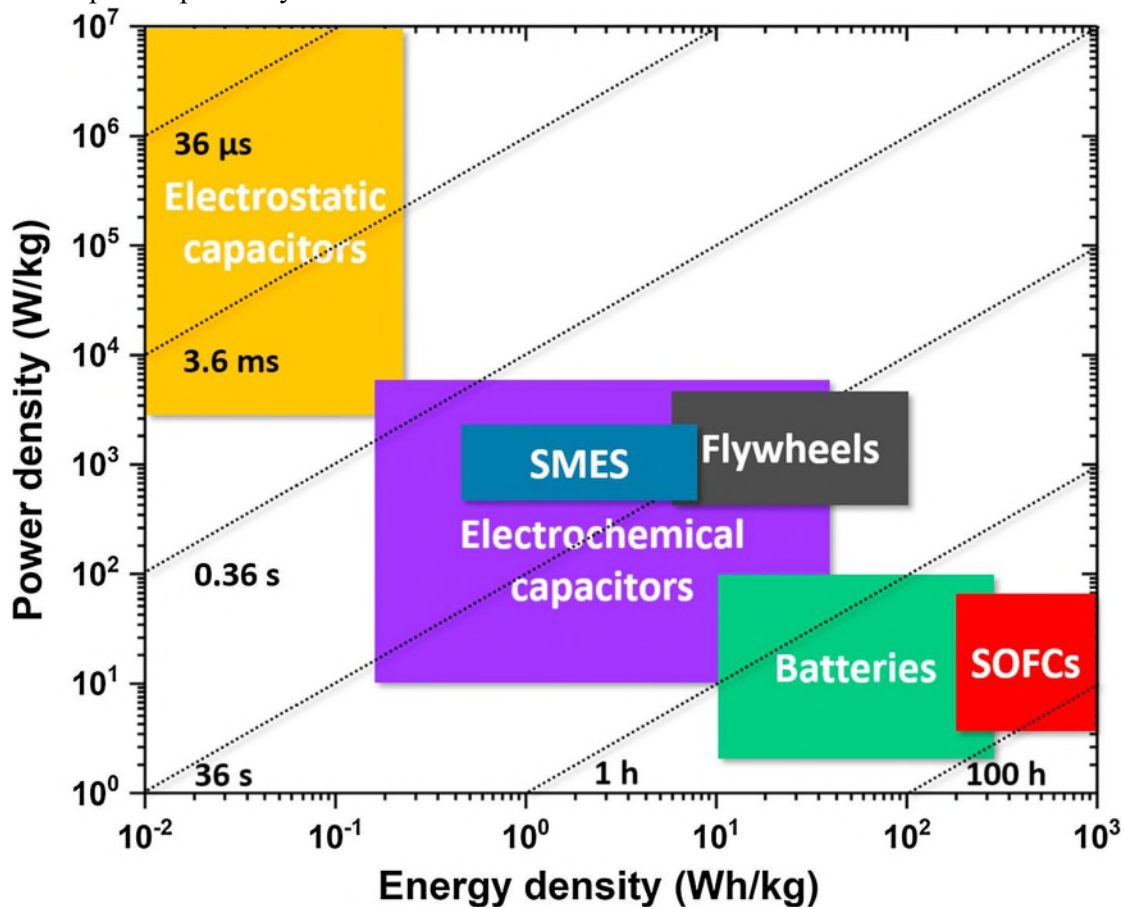


**Figure 1.1.** Ragone plot displaying how different energy storage technologies relate with respect to their energy and power densities, characterising their storage capacity and charge/discharge rates, respectively. Reprinted from ref. <sup>3</sup> with permission from Elsevier.

Waste energy harvesting in mechanical systems is also achievable with the employment of these capacitive devices. For example, hybrid electric vehicles, trains, and even construction equipment such as cranes may harvest waste energy by storing energy in supercapacitors. Supercapacitors in automotive regenerative braking systems may power the vehicle instead of the driving motor under certain conditions, improving its overall energy efficiency.<sup>2</sup> While in the past these systems have typically stored the braking energy in batteries and fuel cells, it has been shown that superior energy efficiency can be attained by utilising supercapacitors in their place due to their higher response speeds.<sup>4</sup> Similar to the case of regenerative braking, cranes also utilise DC/DC converters in tandem with supercapacitors in order to moderate the voltage supply to the capacitor device.<sup>5</sup> The result is that energy is stored while lowering a crate and is subsequently discharged to aid with the initial lift of the next crate.<sup>6</sup> In these applications, it is desirable that the device is small, lightweight, and cheap.<sup>7,8</sup> This reduces engineering constraints while maximising cost effectiveness and enhancing the energy efficiency of the system. There is now significant demand for capacitors fulfilling these requirements, which has led to increased interest in polymer dielectrics. For some time now the question has been whether polymer-based capacitors can attain the energy storage density of the commonplace ceramic materials more typically used today.<sup>9</sup>

Dielectrics may be split into three key categories for the purpose of capacitor applications – linear, paraelectric and ferroelectric.<sup>10</sup> Linear dielectrics have a straightforward reaction to an applied electric field in which they gradually polarise at a linear rate, as individual dipolar features of the material respond to the field independently. In this case, when the field is removed, the polarisation of the media returns to zero.<sup>11</sup> Paraelectric materials are similar but show a varying rate of polarisation with the applied field due to permanent polar structures in the material that respond to an applied field at different rates, rather than the constant rate seen in linear materials. Similarly, to linear dielectrics though, paraelectric materials do not retain their polarisation once the applied field is removed. Ferroelectric materials are far more complicated, however. In addition to polarising at a non-linear rate, ferroelectric materials retain a permanent polarisation even after the field has been removed. This polarisation can also be reversed by applying a field in the opposite direction, as is the case in electrical circuits driven by alternating currents. Ferroelectric materials typically attain this property by virtue of ordered microstructures in which dipoles are naturally aligned in domains, which may be co-oriented in response to an applied field.<sup>12</sup> Due to the large attainable energy storage capacities, ferroelectric capacitors are hence well suited to pulsed power systems requiring rapid energy delivery such as electric vehicle power inverters, portable electronics, electric guns, lasers defibrillators, and various other applications.<sup>13–20</sup>

Interest in polymer capacitors has indeed always been substantial due to some obvious behavioural disparities, which leads to some substantial differences in their performance. For

example, polymers may withstand ultrahigh electric fields without undergoing electrical breakdown. That is, the field at which the material's insulating properties fail, and the dielectric begins to conduct – a calamitous scenario for a capacitor, as it renders the device unable to hold electrical charge and therefore store energy. Ceramics by contrast will usually undergo breakdown at fields orders of magnitude below polymers.<sup>21</sup> But as the vast world of polymers has expanded and processing methodologies have been improved, interest in polymers for capacitive applications is now at an all-time high. In particular, ferroelectric polymer-based dielectric materials are now showing increasing potential to outperform their ceramic competitors. This has become apparent as a growing number of polymers and composites have exceeded the performance of the long-time benchmark dielectric polymer biaxially oriented polypropylene (BOPP). Despite being a linear dielectric, BOPP has energy storage properties competitive with ceramics due to its immense breakdown strength, often exceeding 700 kV/mm, and hence is routinely capable of attaining energy densities in the region of 1-2 J/cm.<sup>3</sup> As such, BOPP has been a widely used as a dielectric material for capacitive energy storage.<sup>22–25</sup> However, the need for higher energy and power densities than BOPP can provide has increased interest in ferroelectric polymers, whose non-linear dielectric behaviour can provide much higher energy densities at ultrahigh electric fields.<sup>26</sup>

With further advances in understanding the underlying physical mechanisms and processing methods in recent years, polymer-based thin film dielectrics have been developed significantly and a plethora of materials now have potential for applications in a variety of devices.<sup>27</sup> Dielectric polymers offer distinct advantages over their ceramic and inorganic counterparts. In particular, their typically higher electrochemical and mechanical stability makes them attractive to manufacturers by substantially improving the lifetime of the capacitor.<sup>28</sup> Similarly, since many ceramics capacitors are lead based, there has been demand for replacement of these materials with non-toxic substitutes, making polymers an obvious alternative.<sup>21</sup> In addition, dielectric polymers are flexible, lightweight, cheap, and most notably their easy processability leads to a large variety of device architectures being attainable with cost-effective production.<sup>29,30</sup> These properties mean they may be incorporated into a variety of device configurations into which ceramics could not be incorporated.<sup>9</sup> For example, smaller, more lightweight devices will reduce operating costs and improves product quality in the case of wearable and portable consumer devices.<sup>31</sup> Their employment will also relieve the strain on the scarce and expensive rare metal resources required for ceramic capacitors. These minerals are often produced via mining processes that can be damaging to the local environment – particularly when poorly regulated by the governments of countries which provide the vast majority of the global supply.<sup>32,33</sup> Considering many of these ceramics and rare earth metals are hazardous to humans and environmentally damaging in and of themselves, there are a multitude

of eco-friendly reasons to use polymers as an alternative.<sup>34,35</sup> However, the most distinct material advantages offered by polymers over ceramics are their processability and their flexibility.

Auxiliary points aside, polymers also offer some distinct technical advantages over their ceramic counterparts. Most notably, their high processability means that polymer heterosystems and polymer-based nanocomposites can be easily constructed with a range of tailored techniques. This contrasts with ceramics, which are often costly and difficult to process.<sup>10</sup> All organic devices containing two or more distinct polymers are often straightforward and cheap to produce and can act as impressive capacitors without the use of expensive inorganic materials to bolster their dielectric properties. For example, dual polymer systems often have distinct interphase regions and boundaries which may act as energy storage sites.<sup>36,37</sup> Nanofillers which may enhance dielectric properties may also occupy interphase sites such as these in a manner which single polymer nanocomposite structures cannot provide.<sup>38–40</sup> The insertion of nanoparticles and inorganic fillers into these systems can provide similar advantages in providing non-uniformities in the material structure, leading to performance enhancements.<sup>41,42</sup> This is in stark contrast to insulating polymers which have low dielectric constants. For example, the extremely insulating BOPP, which has an extremely uniform packing structure and does not provide any sites for charge accumulation, has a low polarisability but extremely high electrical breakdown strength.<sup>24</sup> BOPP instead relies on its ultra-low conductivity and high uniformity to reach ultra-high electric fields which also leads to extremely low energy losses of <0.02%.<sup>13</sup>

Herein lies the key trade-off between ceramic and polymeric dielectric materials. Specialised dielectric polymers are routinely able to withstand electric fields of several thousand kilovolts per centimetre, whereas ceramic materials break down at far lower fields.<sup>3</sup> Dielectric ceramics also possess high relative permittivity values of ~100 – 10000, in contrast to the low permittivity values of polymeric materials, which usually fall in the range of ~2 – 12.<sup>10,13,43</sup> While there is an array of dielectric polymers with vastly dissimilar properties due to their differing structures, their at least partially amorphous microstructure inhibits conduction by providing energy barriers, potential wells, and scattering sites, significantly increasing bulk resistivity and pushing their electrical breakdown to well above those seen in ceramics.<sup>23</sup> However, the dielectric permittivity may change substantially with polymer structure with the presence (or lack) of molecular dipoles. The low permittivity of BOPP originates from its complete lack of a molecular dipole, whereas the polar polymethyl methacrylate (PMMA) has a relative permittivity of ~4.5. Although a polar molecular structure does lead to a higher probability of electrical breakdown, as charge mobility will be enhanced at high electric fields.<sup>11</sup>

In contrast the highly crystalline structures typically seen in ceramic dielectrics possess a bulk electrical conductivity far higher than that seen in polymers due to their long-range structural order. Large crystalline domains in ceramic microstructures make it easy for free ions and electrons to displace along an external field, leading to a separation of charge between the crystal

lattice and free charges.<sup>44</sup> Hence when developing ceramic dielectrics, substantial effort must be made to reduce the conductivity, preventing electrical breakdown and minimising conduction losses.<sup>10,45</sup>

Of the polar polymers available that hold promise for capacitive energy storage, it is those with ferroelectric properties that offer the most potential due to their high polarisability which may increase at exponential rates with increasing electric fields.<sup>46–48</sup> This leads to a potentially extremely high energy storage capacity at ultrahigh fields, prompting research groups to attempt producing ferroelectric polymer materials that are highly insulating and highly polarisable, while also surviving at ultrahigh electric fields.<sup>11,49</sup> Polyvinylidene difluoride (PVDF) is a polymorphic crystalline polymer. It's polar, electroactive crystalline  $\beta$ -phase results in ferroelectric and piezoelectric behaviour in an external electric field.<sup>50</sup> The piezoelectricity and ferroelectricity of PVDF are hence directly dependent on the content of  $\beta$ -phase crystallites in the polymer matrix as well as their properties, such as their orientation and size. The crystalline structure of PVDF can be tuned through copolymerisation, blending or compositing, as well as processing conditions.<sup>51–54</sup> With this in mind, one must ask; what are the most important aspects to consider when designing and producing a polymer-based capacitive material, and how can their structures and properties be effectively characterised?

## 1.2. Fundamentals of dielectrics

To understand the energy storage mechanisms in complicated dielectric systems, it is imperative that the underlying physical mechanisms can be described by measurable quantities of the system. Firstly, it should be noted that the relative permittivity,  $\epsilon_r$ , is the crucial parameter when discussing the potential of various dielectric materials. A higher  $\epsilon_r$  implies a more polarisable medium and hence a medium with higher potential for electrical energy storage. However, this polarisability is only useful if the energy stored by it can be harvested. If the energy input to polarise the dielectric is largely lost as waste energy in the material, then the efficiency of the process will be too poor to be practical. These energy losses may be due to various processes, the most straightforward of which is conduction, which may be either due to direct currents and associated ohmic heating, or due to capacitive losses arising from an alternating applied field. Due to their insulating properties, applying d.c. voltages in dielectric materials will lead to excessive energy losses via this ohmic heating. Instead, dielectric energy storage relies on the application of a.c. electric fields, causing capacitive effects in the media.

In a conductive medium, an a.c. current will stay in phase with the applied a.c. voltage as charges in the system immediately respond and move along the applied electric field without much resistance. However due to their electrically insulating nature, dielectric media will take some time to respond to an applied a.c. voltage. This leads to a component of the current – the

*displacement current* – which is 90° out-of-phase with the applied voltage. This residual current contributes to a.c. losses in the dielectric, adding to the ohmic d.c. losses. Hence a complex formalism should be adopted to describe mathematically how dielectric systems behave, leading to the expressions:

$$\mathbf{C} = \frac{A}{d} \boldsymbol{\varepsilon} = \frac{A}{d} (\varepsilon' - i\varepsilon'') = C' + iC'' \quad (1.1)$$

$$\boldsymbol{\sigma} = \sigma' + i\sigma'' \quad (1.2)$$

$$\boldsymbol{\varepsilon} = \varepsilon' - i\varepsilon'' = (\varepsilon'_r - i\varepsilon''_r)\varepsilon_0 \quad (1.3)$$

Where  $\varepsilon'_r$  and  $\varepsilon''_r$  are the real and imaginary components of the *relative* permittivity,  $\varepsilon'$  and  $\varepsilon''$  are the real and imaginary components of the *absolute* permittivity  $\boldsymbol{\varepsilon}$ , (also commonly known as the dielectric constant),  $\sigma'$  and  $\sigma''$  are the real and imaginary components of the complex conductivity  $\boldsymbol{\sigma}$ ,  $C'$  and  $C''$  are the real and imaginary components of the complex capacitance  $\mathbf{C}$  and  $i$  is the imaginary unit. Additionally,  $A$  is the area of the capacitor's plates, while  $d$  is the separation between them. In these systems, dielectric losses are characterised by the imaginary component of the dielectric constant,  $\varepsilon''$ , as opposed to the real part  $\varepsilon'$ , which is associated with energy storage. To see why this is the case, it is helpful to understand that, fundamentally, energy losses arise from resistive properties of the medium. This may also be evaluated in a complex formalism in which the *impedance* of the system,  $\mathbf{Z}$ , is considered. This may be related to the conductivity and capacitance  $\mathbf{C}$  of the system by the relations:

$$\frac{1}{\mathbf{Z}} = \frac{A}{d} (\sigma' + i\sigma'') = i\omega\mathbf{C} \quad (1.4)$$

Where  $\omega$  is the (angular) frequency of the applied a.c. current, related to the ordinary frequency by  $\omega = 2\pi f$ .<sup>55</sup> As  $\omega$  tends towards 0, the case of a d.c. current is approached, whereas as  $\omega$  tends towards infinity, the a.c. limit is approached. In other words, in the low frequency limit, generally, the system behaves in a more resistive manor, whereas in the high frequency limit, the system behaves in a more capacitive manor. By substituting **equation 1.1** into **equation 1.4**, we produce the equation

$$\mathbf{Z} = \frac{A}{d} \omega (\varepsilon'' + i\varepsilon') \quad (1.5)$$

Hence, comparing **equations 1.4** and **1.5**, two key relations may be uncovered:

$$\varepsilon'' = \frac{\sigma'}{\omega}, \varepsilon' = \frac{\sigma''}{\omega} \quad (1.6)$$



From this, it can be understood that  $\sigma'$  is proportional to *power loss* (i.e., losses which are continuous in time) and hence  $\varepsilon'' = \sigma'/\omega$  is proportional to energy lost *per cycle* of the alternating current (i.e. due to the reversal of field direction).<sup>56</sup>  $\varepsilon_r''$  is also known as the loss factor and characterises the amount of energy lost during the charge-discharge process. Taking the ratio of the two relations in **equation 1.6**, we find

$$\frac{\varepsilon''}{\varepsilon'} = \frac{\varepsilon_r''}{\varepsilon_r'} = \frac{\sigma'}{\sigma''} = \tan \delta \quad (1.7)$$

Where  $\delta$ , the loss angle, is defined such that  $\delta = 0$  when the loss factor is also 0, i.e., an ideal capacitor. The loss tangent,  $\tan(\delta)$ , is a useful metric for analysing the proportion of energy stored and will vary from 0 for a lossless capacitor up to infinity for the theoretical case of 100% energy loss. The loss angle also represents the phase lag of the current, although this is better characterised by taking the reciprocal of **equation 1.8**

$$\frac{\varepsilon'}{\varepsilon''} = \frac{\varepsilon_r'}{\varepsilon_r''} = \frac{\sigma''}{\sigma'} = \tan \varphi \quad (1.8)$$

Where  $\varphi$  is the phase of the current in the material relative to the applied voltage.<sup>57</sup> When  $\varphi = 90^\circ$ ,  $\tan(\varphi)$  is infinite, and the displacement current leads the voltage by a quarter cycle – an ideal capacitor. At  $\varphi = 0^\circ$ ,  $\tan(\varphi)$  is also 0 as the current is in phase with the applied voltage – an ideal conductor.  $\delta$  and  $\varphi$  may be related directly by

$$\varphi = 90^\circ - \delta \quad (1.9)$$

i.e. the sum of the loss angle and phase must be  $90^\circ$ . Hence either of these metrics are useful for measuring capacitive behaviour and energy loss in a dielectric. Examining the variance of this behaviour with a.c. frequency is also very important to discern the capacitive mechanisms in the material and understand how the dielectric may store energy. In real dielectric systems, as the conductivity and permittivity of dielectric media always exhibit frequency dependence, the dielectric response will change substantially as different mechanisms in the material resonate with the applied field.<sup>55</sup> To clarify this, how polarisation in a polymer dielectric is probed must first be understood.

### 1.3. Performance metrics in dielectric materials

As mentioned previously and shown in **Figure 1.1**, the key parameter that must first be enhanced in capacitors is the specific energy, otherwise known as the energy storage density, which we will call  $U$ . This is the energy per unit volume held in the material upon application of an electric field. But to produce a truly effective capacitor, the charge storage process should be inspected more closely. It is helpful to deconstruct it into its two components: charge and discharge. A typical charge-discharge curve (also known as a P-E {polarisation-electric field} or D-E {electrical displacement-electric field} loop) of a high loss dielectric material labelled is

shown in **Figure 1.2** with key parameters labelled. The arrows on the curve indicate the direction of charge and discharge. Inspecting the P-E loop, the charge and discharge curves are evidently not identical, producing a hysteresis curve – behaviour which is observed in all real dielectrics. An ideal dielectric with 100% efficiency and no loss would see no hysteresis, behaviour which ultra-low energy loss linear dielectrics (such as BOPP) are close to attaining.<sup>13</sup> The form of hysteresis observed will depend on the dielectric nature of the material, and hence the relationship between material properties and energy storage will vary.<sup>49</sup> However, the capacitive properties of the material may be derived by integrating the relevant areas of a P-E loop. For example, the stored energy density,  $U_s$ , may be found via

$$U_s = \int_{P_0}^{P_{max}} E dP \quad (1.10)$$

Where  $E$  is the applied electric field and  $P$  is the net polarisation in the material during the charging phase,  $P_0$  is the polarisation at  $E = 0$  and  $P_{max}$  is the maximum polarisation.<sup>10</sup> As the

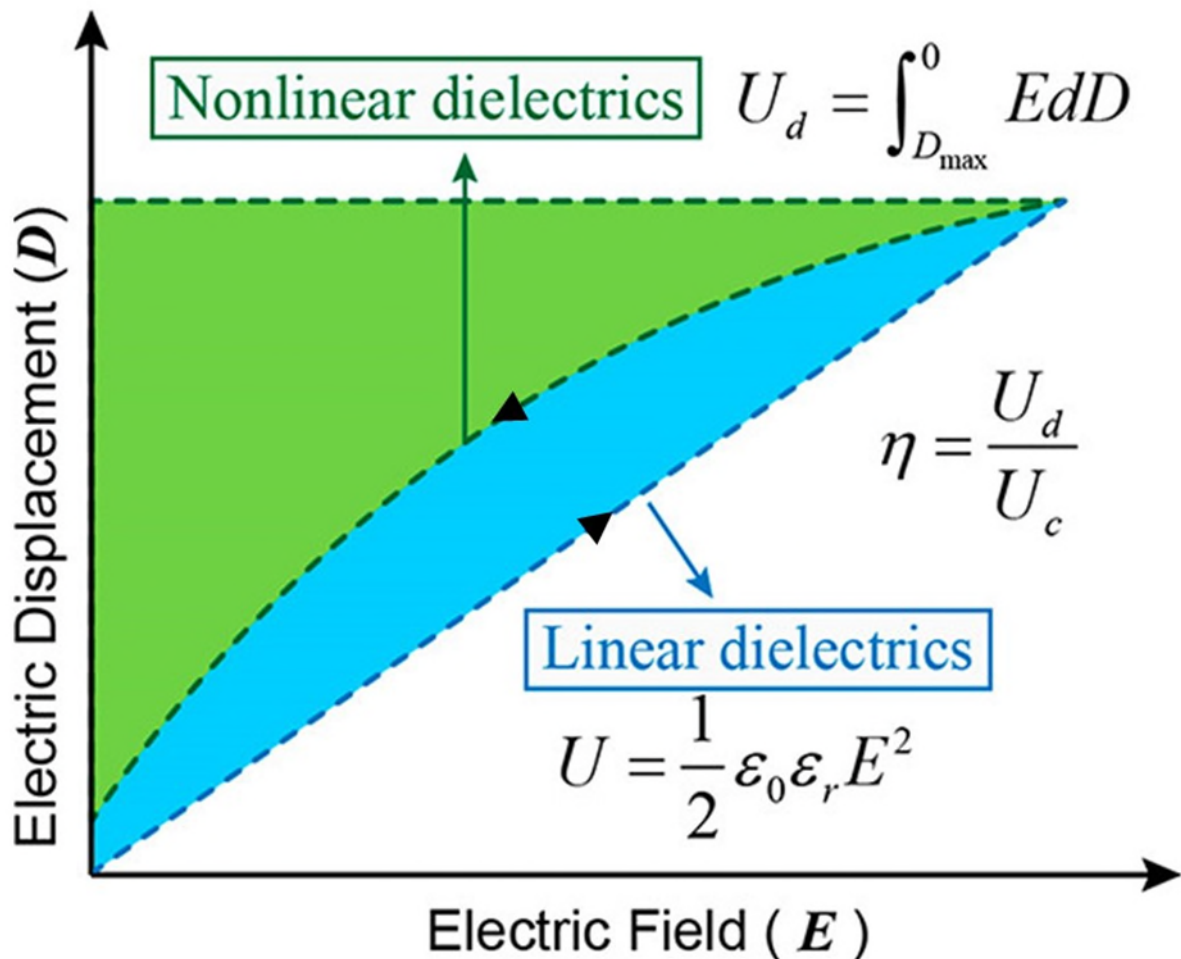


**Figure 1.2.** Schematic of a generic polarisation-electric field loop, with key parameters and relevant relations labelled. A loop of this form is characteristic of a large domain ferroelectric material, in which there is a large loss due to remnant polarisation of domains after removal of the applied field.<sup>48</sup> Adapted with permission from ref. <sup>58</sup>, Copyright 2022 American Chemical Society.

applied field is subsequently ramped down, the material depolarises from  $P_{max}$ . This allows for any stored charge to carry energy out of the dielectric. The rate of this discharge process will determine the efficiency of the capacitor as well as its power output, both of which are important to maximise to enhance performance in any application. A key metric to parameterise this is the remnant polarisation,  $P_r$ , which is the polarisation remaining in the material when the applied field has been reduced to 0. Knowing this and  $P_{max}$  allows us to calculate the most valuable performance metric; the discharged energy density,  $U_e$ , found by

$$U_e = \int_{P_r}^{P_{max}} E dP \quad (1.11)$$

Where  $P$  is the net polarisation within the dielectric during the discharging phase.<sup>10</sup> For a generalised dielectric, increasing  $U_e$  requires a high relative permittivity,  $\epsilon_r$ , and a high electrical breakdown strength,  $E_b$ . This poses an immediate problem as mechanisms that tend to increase  $\epsilon_r$  also tend to correlate with a more polarisable structure permissive to electrons, which can be detrimental to  $E_b$ . Hence, the trick is to create a structure capable of attaining high polarisation without providing conductive pathways which could cause electrical breakdown.<sup>59,60</sup> While maximising  $U_e$  is of utmost importance, the exact relationship of  $U_e$  with  $\epsilon_r$  and  $E_b$  depends on the kind of behaviour of the material exhibits under a high electric field.<sup>49</sup> Precisely how a polar material responds to an applied field depends heavily on its structure from the molecular scale to the mesoscale.<sup>61</sup> The ability of dipoles in polar materials to orientate along an applied field and to relax from this state determines the nature of both energy storage and energy discharge, in turn dictating the form of p-e loop observed in **Figure 1.2**. Several forms of P-E loop are shown in **Figure 1.3** to highlight the differing behaviour of various dielectric materials, some of which will be explored in more detail in the following chapter.<sup>62</sup> As is seen in **Figure 1.3(a)**, linear dielectrics are characterised by their low dielectric loss – the measure of undischarged energy lost in the charge-discharge process. This loss and its associated energy,  $U_L$ , may be characterised by the discharge efficiency  $\eta$ , given by

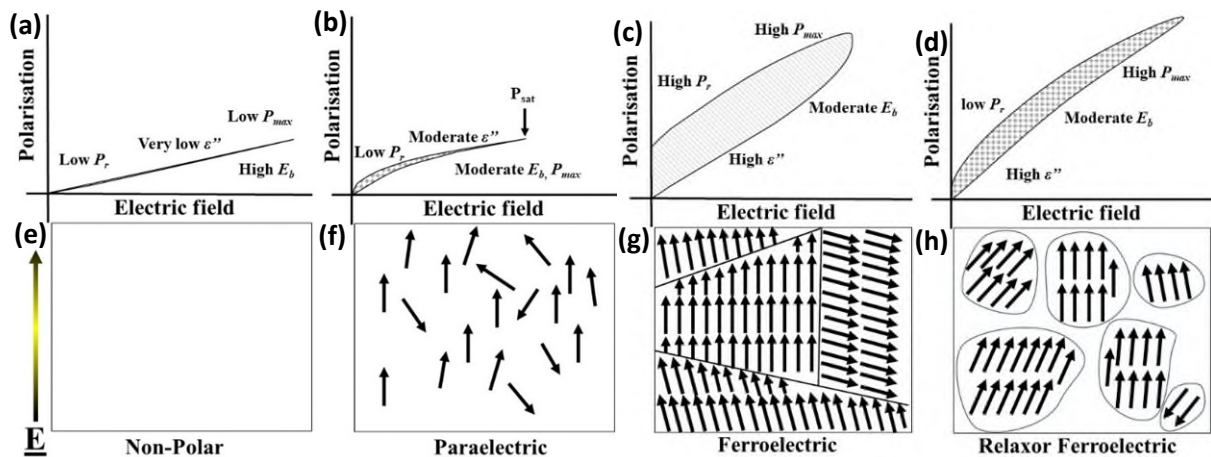


**Figure 1.3.** P-E loops describing (a) linear behaviour (b) paraelectric behaviour (c) ferroelectric behaviour (d) relaxor ferroelectric behaviour.<sup>62</sup>

$$\eta = \frac{U_e}{U_s} = \frac{U_e}{U_e + U_L} \quad (1.12)$$

The molecular configuration and crystallite structure of a dielectric material have large impacts on the response of the material to an applied field and will lead to vastly different signatures in the P-E loops when performing polarisation testing.<sup>10,39,63</sup>

#### 1.4. Polyvinylidene difluoride (PVDF)

In the pursuit of attaining sustainable, cost-effective materials with excellent electrical energy storage properties, polyvinylidene difluoride (PVDF) has attracted great interest in the field of energy harvesting as a flexible piezoelectric and ferroelectric material due to its dipolar, semicrystalline properties, which originate from the polar  $\beta$ -crystal conformation of its crystalline structure.<sup>64</sup> A high proportion of the  $\beta$ -phase in PVDF can increase the relative permittivity by over 10-fold.<sup>65</sup> Thus, various methods have been employed to enhance formation of the  $\beta$ -phase while suppressing the paraelectric  $\alpha$ -phase in PVDF. These include via tailoring the polymer chain structure, optimising processing parameters (temperature, pressure, cooling rate and by applying shearing forces), or by use of post-treatment techniques.<sup>53,66–74</sup> Furthermore, the addition of nanoparticles such as carbon nanotubes or ferrite particles can also significantly enhance the relative permittivity of PVDF and its copolymers.<sup>68,69,75,76</sup>

Solution-casting and hot-pressing are two typical polymer processing techniques for PVDF. Solution-casting using highly polar, low boiling point solutions or hot-pressing with high pressures, high temperatures and rapid cooling rates can all promote  $\beta$ -phase formation in the polymer.<sup>66,77–79</sup> In contrast, electrospun PVDF fibre membranes often exhibit very high piezoelectricity and ferroelectricity due to the electrical poling of the fibres induced by the electrostatic field used to form them during spinning, which can promote the formation of  $\beta$ -phase crystallites. This electrical poling causes alignment of the PVDF molecules into a dipolar configuration as the solvent dries eliminates the need for poling post-processing.<sup>80</sup> Also, rapid evaporation of the volatile solvents used during electrospinning assists in forming the  $\beta$ -phase; an affect also observed when solution-casting.<sup>72,77,81</sup> Finally, the high mechanical stress exerted on the nanofibres during electrospinning along with the poling effect greatly induces dipole formation.<sup>67,82</sup> Thus, electrospinning is advantageous in utilizing a combination of polar solvents, electrical poling and mechanical stretching to maximise the electroactive phase content in one single processing step. As such, electrospun PVDF has been used in the fields of medicine, environmental engineering, and energy.<sup>83–85</sup>

However, the finer details of crystallography induced by these processing paths and the effect of various aspects and subtleties of the method are not well understood. Most notably, precisely *why* differences in the ferroelectric properties and energy storage performance of PVDF are seen under different circumstances are largely unknown. By relating processing strategy – from the

broad to the fine details – to the multifaceted crystallography of the produced PVDF, and in turn relating these crystal structures to the ferroelectric properties could underpin the manufacturing of the next generation of polymeric materials for pulsed power devices. Further to this, the electrical energy storage potential of PVDF nanofibres used in nanocomposites – and when incorporated into dielectric materials with other polymers – have been seldom explored. On this note, nanofibres offer a unique morphological advantage over the macrostructures generated with hot-pressing and solution casting due to their porous structure and large surface area to weight ratio. This highlights the unexplored avenues of unique potential of composite structures utilising PVDF nanofibres for ferroelectric energy storage, such as coating nanoparticles onto nanofibres, or producing particularly lightweight multi-polymer dielectrics.

### 1.5. Research objectives and thesis structure

The core aim of this project is to explore processing methodologies and their effects on the crystalline nanostructure of polyvinylidene difluoride (PVDF), as well as the dielectric performance of the PVDF-based materials produced. The effects of additives, nanoparticles and processing conditions are discussed, with a focus on enhancing the discharged energy density,  $U_e$ , discharge efficiency,  $\eta$ , and electrical breakdown strength,  $E_B$  of the PVDF based dielectrics. This work has investigated the potential of a few approaches to PVDF processing, as well as outlining the rationale behind this research in the following chapters.

**Chapter 1 – Introduction**, introduced the fundamental concepts of dielectric and ferroelectric materials, most notably polymers. Capacitive energy storage mechanisms in polymers and some aspects of the theories behind them have been discussed. The primary polymer of interest – polyvinylidene difluoride (PVDF) has been discussed in particular, as well as the potential for enhancing its ferroelectric energy storage capacity from the perspective of the structural design and processing technologies.

**Chapter 2 – Literature review and theoretical background**, reviews the current status of dielectric polymers, notably the ferroelectrics which dominate the field at present. The underlying physics relating to the energy storage mechanisms in dielectric polymers are explored, along with a more detailed look at the effects of different processing methods on the crystalline nanostructure and dielectric properties of PVDF. PVDF copolymers, nanocomposites and multi-polymer dielectric materials are also reviewed.

**Chapter 3 – Electrospinning of PVDF nanofibres**, reports the investigation of utilising different processing methodologies for increasing electrically active crystal phases in PVDF, where an electrospinning procedure was selected and optimised. The addition of an ionic liquid to the electrospinning process was demonstrated to be effective at improving the stability of electrospinning and inducing a high proportion of polar crystal phases in PVDF nanofibers. The

relationship between the electrospinning parameters and the crystalline structure of PVDF nanofibers was characterised and discussed.

**Chapter 4 – Electrospun polymer nanofibre nanocomposite dielectrics**, explores the growth process of metal organic framework (MOF) nanoparticles on electrospun PVDF-HFP copolymer nanofibres, and subsequently investigates the creation of multilayer nanocomposite structures incorporating these nanofibres. The viability of various composite architectures were identified based on structural cohesiveness, and ferroelectric performance of these composites was then evaluated.

**Chapter 5 – Multi-layer polymer dielectrics**, investigates the advantages of a multi-layered architecture for electrical energy storage. The effect of processing parameters on the crystalline nanostructure of the PVDF is studied, with various approaches characterised with ferroelectric tests. In this case, the key trade-off during processing is between retaining the impressive crystalline nanostructure produced by the PVDF nanofibres manufactured in chapter 3 and creating a composition free of defects and voids in order to minimise ferroelectric losses and the risk of electrical breakdown.

Finally, **Chapter 6 – Conclusions**, summarises the main research outcomes of this project. The prospects for future work are discussed, focusing on the fabrication of all-polymer multi-layered dielectrics with high energy storage and low ferroelectric loss for capacitive applications.

## 1.6. References

1. Zhang, H. *et al.* Polymer Matrix Nanocomposites with 1D Ceramic Nanofillers for Energy Storage Capacitor Applications. *ACS Appl. Mater. Interfaces* **12**, 1–37 (2020).
2. Whittingham, M. S. Materials challenges facing electrical energy storage. *MRS Bull.* **33**, 411–419 (2008).
3. Yang, L. *et al.* Perovskite lead-free dielectrics for energy storage applications. *Prog. Mater. Sci.* **102**, 72–108 (2019).
4. Kim, B. H., Kwon, O. J., Song, J. S., Cheon, S. H. & Oh, B. S. The characteristics of regenerative energy for PEMFC hybrid system with additional generator. *Int. J. Hydrogen Energy* **39**, 10208–10215 (2014).
5. Li, Z. J., Wang, G. Q., Shen, K. Y., Zhao, T. F. & Ni, X. G. Research of the crane system based on technology of storing-energy with super-capacitor. *Proc. - Int. Conf. Electr. Control Eng. ICECE 2010* 4046–4049 (2010) doi:10.1109/iCECE.2010.984.
6. Miller, J. R. & Burke, A. F. Electrochemical capacitors: Challenges and opportunities for real-world applications. *Electrochem. Soc. Interface* **17**, 53–57 (2008).
7. Zhang, H., Tolbert, L. M. & Ozpineci, B. Impact of SiC devices on hybrid electric and plug-in

- hybrid electric vehicles. *IEEE Trans. Ind. Appl.* **47**, 912–921 (2011).
8. Wen, H., Xiao, W., Wen, X. & Armstrong, P. Analysis and evaluation of DC-link capacitors for high-power-density electric vehicle drive systems. *IEEE Trans. Veh. Technol.* **61**, 2950–2964 (2012).
9. Li, Q. *et al.* Flexible high-temperature dielectric materials from polymer nanocomposites. *Nature* **523**, 576–579 (2015).
10. Palneedi, H., Peddigari, M., Hwang, G. T., Jeong, D. Y. & Ryu, J. High-Performance Dielectric Ceramic Films for Energy Storage Capacitors: Progress and Outlook. *Adv. Funct. Mater.* **28**, 1–33 (2018).
11. Prateek, Thakur, V. K. & Gupta, R. K. Recent Progress on Ferroelectric Polymer-Based Nanocomposites for High Energy Density Capacitors: Synthesis, Dielectric Properties, and Future Aspects. *Chem. Rev.* **116**, 4260–4317 (2016).
12. Lovinger, A. J., Furukawa, T., Davis, G. T. & Broadhurst, M. G. Crystallographic changes characterizing the Curie transition in three ferroelectric copolymers of vinylidene fluoride and trifluoroethylene: 2. Oriented or poled samples. *Polymer (Guildf)*. **24**, 1233–1239 (1983).
13. Chen, Q., Shen, Y., Zhang, S. & Zhang, Q. M. Polymer-Based Dielectrics with High Energy Storage Density. *Annu. Rev. Mater. Res.* **45**, 433–458 (2015).
14. Kimura, T. *et al.* High-power-density inverter technology for hybrid and electric vehicle applications. *Hitachi Rev.* **63**, 96–102 (2014).
15. Ribeiro, P. F., Johnson, B. K., Crow, M. L., Arsoy, A. & Liu, Y. Energy storage systems for advanced power applications. *Proc. IEEE* **89**, 1744–1756 (2001).
16. Yu, G., Xie, X., Pan, L., Bao, Z. & Cui, Y. Hybrid nanostructured materials for high-performance electrochemical capacitors. *Nano Energy* **2**, 213–234 (2013).
17. Carpi, F. & De Rossi, D. Electroactive polymer-based devices for e-textiles in biomedicine. *IEEE Trans. Inf. Technol. Biomed.* **9**, 295–318 (2005).
18. Jow, T. R. *et al.* Pulsed power capacitor development and outlook. in *2015 IEEE Pulsed Power Conference (PPC)* vols 2015-Octob 1–7 (IEEE, 2015).
19. Beach, F. C. & McNab, I. R. Present and future naval applications for pulsed power. *Dig. Tech. Pap. Int. Pulsed Power Conf.* 1–7 (2007) doi:10.1109/PPC.2005.300462.
20. Guo, M., Hayakawa, T., Kakimoto, M. A. & Goodson, T. Organic macromolecular high dielectric constant materials: Synthesis, characterization, and applications. *J. Phys. Chem. B* **115**, 13419–13432 (2011).
21. Zhang, H. *et al.* A review on the development of lead-free ferroelectric energy-storage ceramics and multilayer capacitors. *J. Mater. Chem. C* **8**, 16648–16667 (2020).
22. Fillery, S. P. *et al.* Nanolaminates: Increasing dielectric breakdown strength of composites. *ACS Appl. Mater. Interfaces* **4**, 1388–1396 (2012).
23. Picci, G. & Rabuffi, M. Status quo and future prospects for metallized polypropylene energy

- storage capacitors. *PPPS 2001 - Pulsed Power Plasma Sci. 2001* **1**, 417–420 (2002).
24. Ritamaki, M., Rytoluoto, I. & Lahti, K. Performance metrics for a modern BOPP capacitor film. *IEEE Trans. Dielectr. Electr. Insul.* **26**, 1229–1237 (2019).
  25. Lu, J., Zhu, B., Zhang, X. & Wang, X. Dielectric Strength Structure-Activity Relationship of BOPP Film for High Energy Density Pulse Capacitor. *IEEE Trans. Plasma Sci.* **47**, 4342–4349 (2019).
  26. Zhang, X. *et al.* Achieving High Energy Density in PVDF-Based Polymer Blends: Suppression of Early Polarization Saturation and Enhancement of Breakdown Strength. *ACS Appl. Mater. Interfaces* **8**, 27236–27242 (2016).
  27. Fan, B., Zhou, M., Zhang, C., He, D. & Bai, J. Polymer-based materials for achieving high energy density film capacitors. *Prog. Polym. Sci.* **97**, 101143 (2019).
  28. Ho, J. S. & Greenbaum, S. G. Polymer Capacitor Dielectrics for High Temperature Applications. *ACS Appl. Mater. Interfaces* **10**, 29189–29218 (2018).
  29. März, M., Schletz, A., Eckardt, B., Egelkraut, S. & Rauh, H. Power electronics system integration for electric and hybrid vehicles. *2010 6th Int. Conf. Integr. Power Electron. Syst. CIPS 2010* (2011).
  30. Dang, Z. M., Yuan, J. K., Yao, S. H. & Liao, R. J. Flexible nanodielectric materials with high permittivity for power energy storage. *Adv. Mater.* **25**, 6334–6365 (2013).
  31. Zeng, W. *et al.* Fiber-based wearable electronics: A review of materials, fabrication, devices, and applications. *Adv. Mater.* **26**, 5310–5336 (2014).
  32. Alam, M. A., Zuga, L. & Pecht, M. G. Economics of rare earth elements in ceramic capacitors. *Ceram. Int.* **38**, 6091–6098 (2012).
  33. Binnemans, K., Jones, P. T., Müller, T. & Yurramendi, L. Rare Earths and the Balance Problem: How to Deal with Changing Markets? *J. Sustain. Metall.* **4**, 126–146 (2018).
  34. Ibn-Mohammed, T. *et al.* Life cycle assessment and environmental profile evaluation of lead-free piezoelectrics in comparison with lead zirconate titanate. *J. Eur. Ceram. Soc.* **38**, 4922–4938 (2018).
  35. Smith, L. Life Cycle Assessment and Environmental Profile Evaluations of High Volumetric Efficiency Capacitors. (2018).
  36. Zhou, Z. *et al.* Fracture phenomena in micro- and nano-layered polycarbonate/poly(vinylidene fluoride- co -hexafluoropropylene) films under electric field for high energy density capacitors. *J. Appl. Polym. Sci.* **131**, n/a-n/a (2014).
  37. Li, R. *et al.* Polyamide 11/Poly(vinylidene fluoride) Blends as Novel Flexible Materials for Capacitors. *Macromol. Rapid Commun.* **29**, 1449–1454 (2008).
  38. Zhang, X. *et al.* Hierarchical interfaces induce high dielectric permittivity in nanocomposites containing TiO<sub>2</sub>@BaTiO<sub>3</sub> nanofibers. *Nanoscale* **6**, 6701–6709 (2014).
  39. Jiang, J. *et al.* Ultrahigh discharge efficiency in multilayered polymer nanocomposites of high



- energy density. *Energy Storage Mater.* **18**, 213–221 (2019).
40. Feng, Y., Deng, Q., Peng, C. & Wu, Q. High dielectric and breakdown properties achieved in ternary BaTiO<sub>3</sub>/MXene/PVDF nanocomposites with low-concentration fillers from enhanced interface polarization. *Ceram. Int.* **45**, 7923–7930 (2019).
  41. Pourrahimi, A. M., Olsson, R. T. & Hedenqvist, M. S. The Role of Interfaces in Polyethylene/Metal-Oxide Nanocomposites for Ultrahigh-Voltage Insulating Materials. *Adv. Mater.* **30**, 1–25 (2018).
  42. Zhou, L. & Jiang, Y. Recent progress in dielectric nanocomposites. *Mater. Sci. Technol. (United Kingdom)* **36**, 1–16 (2020).
  43. Hall, D. A. & Stevenson, P. J. High field dielectric behaviour of ferroelectric ceramics. *Ferroelectrics* **228**, 139–158 (1999).
  44. Xia, W., Lu, J., Tan, S., Liu, J. & Zhang, Z. *Manipulating dielectric properties by modifying molecular structure of polymers. Dielectric Polymer Materials for High-Density Energy Storage* (Elsevier Inc., 2018). doi:10.1016/B978-0-12-813215-9.00004-X.
  45. Cain, M. G. Dielectric Breakdown in Dielectrics and Ferroelectric Ceramics. in *Physical Review* 243–266 (2014). doi:10.1007/978-1-4020-9311-1\_11.
  46. Setter, N. *et al.* Ferroelectric thin films: Review of materials, properties, and applications. *J. Appl. Phys.* **100**, 0–46 (2006).
  47. Qi, L., Petersson, L. & Liu, T. Review of Recent Activities on Dielectric Films for Capacitor Applications. *J. Int. Counc. Electr. Eng.* **4**, 1–6 (2014).
  48. Sun, W., Mao, J., Wang, S., Zhang, L. & Cheng, Y. Review of recent advances of polymer based dielectrics for high-energy storage in electronic power devices from the perspective of target applications. *Front. Chem. Sci. Eng.* **15**, 18–34 (2020).
  49. Zhu, L. & Wang, Q. Novel Ferroelectric Polymers for High Energy Density and Low Loss Dielectrics. *Macromolecules* **45**, 2937–2954 (2012).
  50. Ribeiro, C. *et al.* Electroactive poly(vinylidene fluoride)-based structures for advanced applications. *Nat. Protoc.* **13**, 681–704 (2018).
  51. Poulsen, M. & Ducharme, S. Why ferroelectric polyvinylidene fluoride is special. *IEEE Trans. Dielectr. Electr. Insul.* **17**, 1028–1035 (2010).
  52. Qiao, Y., Yin, X., Zhu, T., Li, H. & Tang, C. Dielectric polymers with novel chemistry, compositions and architectures. *Prog. Polym. Sci.* **80**, 153–162 (2018).
  53. Yee, W. A., Kotaki, M., Liu, Y. & Lu, X. Morphology, polymorphism behavior and molecular orientation of electrospun poly(vinylidene fluoride) fibers. *Polymer (Guildf)*. **48**, 512–521 (2007).
  54. Wang, Y. *et al.* Multilayered hierarchical polymer composites for high energydensity capacitors. *J. Mater. Chem. A* **7**, 2965–2980 (2019).
  55. Schönhals, A. & Kremer, F. *Broadband Dielectric Spectroscopy. Broadband Dielectric*

- Spectroscopy* (Springer Berlin Heidelberg, 2003). doi:10.1007/978-3-642-56120-7.
56. Grimnes, S. & Martinsen, Ø. G. Dielectrics. in *Bioimpedance and Bioelectricity Basics* vol. 17 37–75 (Elsevier, 2015).
  57. Opris, D. M. Polar Elastomers as Novel Materials for Electromechanical Actuator Applications. *Adv. Mater.* **30**, 1–23 (2018).
  58. Feng, Q.-K. *et al.* Recent Progress and Future Prospects on All-Organic Polymer Dielectrics for Energy Storage Capacitors. *Chem. Rev.* **122**, 3820–3878 (2022).
  59. Wang, Y., Hou, Y. & Deng, Y. Effects of interfaces between adjacent layers on breakdown strength and energy density in sandwich-structured polymer composites. *Compos. Sci. Technol.* **145**, 71–77 (2017).
  60. Liu, H. *et al.* Carbon nanotube array/polymer core/shell structured composites with high dielectric permittivity, low dielectric loss, and large energy density. *Adv. Mater.* **23**, 5104–5108 (2011).
  61. Pan, H., Kursumovic, A., Lin, Y. H., Nan, C. W. & MacManus-Driscoll, J. L. Dielectric films for high performance capacitive energy storage: Multiscale engineering. *Nanoscale* **12**, 19582–19591 (2020).
  62. Yang, L. *et al.* Novel polymer ferroelectric behavior via crystal isomorphism and the nanoconfinement effect. *Polymer (Guildf)*. **54**, 1709–1728 (2013).
  63. Wang, Y. *et al.* Ultrahigh electric displacement and energy density in gradient layer-structured BaTiO<sub>3</sub>/PVDF nanocomposites with an interfacial barrier effect. *J. Mater. Chem. A* **5**, 10849–10855 (2017).
  64. Ramadan, K. S., Sameoto, D. & Evoy, S. A review of piezoelectric polymers as functional materials for electromechanical transducers. *Smart Mater. Struct.* **23**, (2014).
  65. Martins, P. *et al.* Local variation of the dielectric properties of poly(vinylidene fluoride) during the  $\alpha$ - to  $\beta$ -phase transformation. *Phys. Lett. Sect. A Gen. At. Solid State Phys.* **373**, 177–180 (2009).
  66. Cui, Z., Hassankiadeh, N. T., Zhuang, Y., Drioli, E. & Lee, Y. M. Crystalline polymorphism in poly(vinylidene fluoride) membranes. *Prog. Polym. Sci.* **51**, 94–126 (2015).
  67. Wan, C. & Bowen, C. R. Multiscale-structuring of polyvinylidene fluoride for energy harvesting: the impact of molecular-, micro- and macro-structure. *J. Mater. Chem. A* **5**, 3091–3128 (2017).
  68. Aldas, M., Boiteux, G., Seytre, G. & Ghallabi, Z. Dielectric behaviour of BaTiO<sub>3</sub> / P (VDF-HFP) composite thin films prepared by solvent evaporation method. *Proc. 2010 IEEE Int. Conf. Solid Dielectr. ICSD 2010* (2010) doi:10.1109/ICSD.2010.5568042.
  69. Lallart, M., Cottinet, P. J., Lebrun, L., Guiffard, B. & Guyomar, D. Evaluation of energy harvesting performance of electrostrictive polymer and carbon-filled terpolymer composites. *J. Appl. Phys.* **108**, (2010).

70. Xu, H. Dielectric properties and ferroelectric behavior of poly(vinylidene fluoride-trifluoroethylene) 50/50 copolymer ultrathin films. *J. Appl. Polym. Sci.* **80**, 2259–2266 (2001).
71. Khomami, B. & Langton, C. A. h Fluoride/Trifluoroethylene Random Copolymers. **31**, (1991).
72. Ma, W., Zhang, J., Chen, S. & Wang, X. Crystalline phase formation of poly(vinylidene fluoride) from tetrahydrofuran/N,N-dimethylformamide mixed solutions. *J. Macromol. Sci. Part B Phys.* **47**, 434–449 (2008).
73. Mohammadi, B., Yousefi, A. A. & Bellah, S. M. Effect of tensile strain rate and elongation on crystalline structure and piezoelectric properties of PVDF thin films. *Polym. Test.* **26**, 42–50 (2007).
74. Lee, J. E. & Leung, S. N. Multi-stage crystallization mechanism of electroactive phase polyvinylidene fluoride induced by thermal and supercritical carbon dioxide processing. *CrystEngComm* **20**, 4080–4089 (2018).
75. Martins, P., Costa, C. M., Benelmekki, M., Botelho, G. & Lanceros-Mendez, S. On the origin of the electroactive poly(vinylidene fluoride)  $\beta$ -phase nucleation by ferrite nanoparticles via surface electrostatic interactions. *CrystEngComm* **14**, 2807–2811 (2012).
76. Yu, S. *et al.* Formation mechanism of  $\beta$ -phase in PVDF/CNT composite prepared by the sonication method. *Macromolecules* **42**, 8870–8874 (2009).
77. Chinaglia, D. L. *et al.* Influence of the solvent evaporation rate on the crystalline phases of solution-cast poly(vinylidene fluoride) films. *J. Appl. Polym. Sci.* **116**, 785–791 (2010).
78. Song, D., Yang, D. & Feng, Z. Formation of  $\beta$ -phase microcrystals from the melt of PVF2-PMMA blends induced by quenching. *J. Mater. Sci.* **25**, 57–64 (1990).
79. Tao, M. mi, Liu, F., Ma, B. rong & Xue, L. xin. Effect of solvent power on PVDF membrane polymorphism during phase inversion. *Desalination* **316**, 137–145 (2013).
80. Sencadas, V., Lanceros-Méndez, S., Sabater I Serra, R., Andrio Balado, A. & Gómez Ribelles, J. L. Relaxation dynamics of poly(vinylidene fluoride) studied by dynamical mechanical measurements and dielectric spectroscopy. *Eur. Phys. J. E* **35**, (2012).
81. Gregorio, R. & Borges, D. S. Effect of crystallization rate on the formation of the polymorphs of solution cast poly(vinylidene fluoride). *Polymer (Guildf)*. **49**, 4009–4016 (2008).
82. Zhong, G. *et al.* Understanding polymorphism formation in electrospun fibers of immiscible Poly(vinylidene fluoride) blends. *Polymer (Guildf)*. **52**, 2228–2237 (2011).
83. Qasaimeh, M. A., Sokhanvar, S., Dargahi, J. & Kahrizi, M. PVDF-based microfabricated tactile sensor for minimally invasive surgery. *J. Microelectromechanical Syst.* **18**, 195–207 (2009).
84. Kim, J. R., Choi, S. W., Jo, S. M., Lee, W. S. & Kim, B. C. Electrospun PVdF-based fibrous polymer electrolytes for lithium ion polymer batteries. *Electrochim. Acta* **50**, 69–75 (2004).
85. Balamurugan, R., Sundarrajan, S. & Ramakrishna, S. Recent trends in nanofibrous membranes and their suitability for air and water filtrations. *Membranes (Basel)*. **1**, 232–248 (2011)

## Chapter 2

### Literature review and theoretical background

#### 2.1. Introduction

In this chapter, the mechanisms of polarisation in dielectric polymers will be explored, as well as the impact these mechanisms have on the viability of various materials for energy storage. Firstly, we explore the internal effects that are occurring in a dielectric polymer when a given electric field is applied, and how these effects lead to polarisation. Secondly, the various polarisation mechanisms possible are explored in detail to understand what makes an effective ferroelectric polymer-based dielectric with excellent energy storage properties. The phenomena of electrical breakdown and how this may limit energy storage capabilities are also discussed. Finally, the selection of viable polymers for fabricating these polymer-based dielectric materials are reviewed, along with the relevant processing methodologies that may be employed to produce material architectures and polymer nanostructures that will maximise performance.

#### 2.2. Types of dielectric behaviour

##### 2.2.1. Linear dielectrics

The configuration of dipoles in the material microstructure of various forms of dielectrics is shown in **Figure 1.3**. Linear dielectrics are those which have a dielectric constant that bears no dependence on the magnitude of the applied field, and so obey the relation<sup>1</sup>

$$U_e = 0.5\epsilon_0\epsilon_r \cdot E^2 \quad (0.1)$$

This will be maximised for a given material just below  $E=E_b$ . The capacity of non-polar linear dielectric materials such as BOPP to store energy is typically quite limited due to their very low  $\epsilon_r$ . The lack of polar features leads to an absence of mechanisms for energy storage in the microstructure which must be compensated. BOPP for example stores energy primarily in the form of space charges – free charges in the material structure – in mobile amorphous domains of the material, and by impurities which may trap charge carriers in the amorphous phase or at amorphous-crystalline interfaces.<sup>2,3</sup> As linear polymers rely on possessing a high  $E_b$ , which enhances  $U_e$  quadratically as per **equation 2.1**. This allows BOPP to reach its benchmark  $U_e \sim 1-2 \text{ J/cm}^3$  at very high applied fields of several thousand kV/cm.<sup>1,4</sup> The P-E loops of linear dielectrics are also easily recognised by their low rate of polarisation under an applied electric field (due to their low  $\epsilon_r$ ) but often reach high electric fields, enhancing performance via  $U_e \propto E_b$ .<sup>2</sup> Their low loss leads to a typically high discharge efficiency, with BOPP often nearing 100%.

### 2.2.2. Paraelectric and ferroelectric materials

Like linear dielectrics, paraelectric and ferroelectric materials exhibit a polarisation after the application of an applied field. In these more complicated dielectric media, the electric field measured is often referred to as the *displacement field*, which describes the total field in a dielectric due to both the space charges and bound charges; those arising from dipoles in molecules and structures that compose the “skeleton” of the material.<sup>5</sup>

The real relationship between  $U_e$  and  $\epsilon_r$  or  $E_b$  does not manifest in such simple terms for materials containing dipoles. The relationship seen in **equation 2.1** only tends to apply at low fields in non-linear dielectrics, where it can be used to make estimates regarding energy storage properties. At high fields the relationship is more complex.<sup>6</sup> It is instead governed by a variety of mechanisms in polar materials – captured in the dependence  $\epsilon_r(\omega)$  – and as such is usually determined empirically.<sup>7–10</sup> Sophisticated models of field and energy density distributions in dielectrics are sometimes employed to investigate breakdown and energy storage mechanisms in a material, although the reliability of these simulations – particularly in multi-component composite systems – is unclear, so empirical data is collected to support these predictions regardless. Additionally, since higher permittivity dielectrics will polarise more quickly in response to an applied field, dielectrics with globally non-linear responses (i.e. where the dielectric constant changes with the applied field) will quickly diverge from this dependence even at low fields. In contrast  $\eta$  is likely to be far lower in polar materials and will change substantially with the magnitude and frequency of the applied a.c. voltage.<sup>11,12</sup> At high fields, the impedance of the material will increase significantly, leading to higher energy losses. Also, with short charging periods, the maximum achievable polarisation will not be reached as not all dipoles have time to orientate along the field before it reverses and will also fail to fully depolarise as the field ramps down, leading to a high remnant polarisation,  $P_r$ .<sup>13</sup> To this end,  $\eta$  is enhanced in polar materials when dipoles are mobile and capable of rapidly relaxing into an unpolarised state as the field reduces, correlating with a decreased  $P_r$ .

Two cases here must be distinguished: the paraelectric case shown in **Figure 1.3(b)**, and the ferroelectric case shown in **Figure 1.3(c)**. The key difference is that even in the absence of an applied electric field, the molecular dipoles in ferroelectrics form crystalline polar domains, which may respond to an applied field acting as one large dipolar crystal. Paraelectric materials conversely do not form these polar domains. Upon application of an applied field, polarisation occurs by individual molecular polarisation and via the separation of free charges.<sup>14,15</sup> Due to this, ferroelectrics may retain high polarisation after the applied field is removed as domains remain polarised, whereas paraelectric materials tend to return to near zero net polarisation as the molecular dipoles return to their resting state, as seen in **Figure 1.3(b)**. This may seem like a positive attribute in isolation, but in fact this leads to a low polarisability. At a local scale, dipoles will interact as and oppose each other’s orientation along the applied field, meaning

many will be oriented against the applied field, reducing net polarisation. In contrast, since ferroelectric domains will orientate as one large dipole, their polarisability is substantially higher. Although reorientation upon removal of the field is far more difficult, leading to a high remnant polarisation,  $P_r$ .

To overcome this issue, the ferroelectric domains must be able to relax more easily by overwhelming the inter-domain coupling which causes crystallites to remain frozen into states of net polarisation. One of the most straightforward ways of reducing this effect is simply by reducing the size of the domains. So-called nanodomains contain a small number of aligned dipoles and can exacerbate the behaviour seen in typical ferroelectric materials due to the reduced domain size making re-orientation less energy intensive.<sup>16–18</sup> This is known as ‘relaxor-ferroelectric’ (RFE) behaviour and is characterised by a narrow hysteresis loop as shown in **Figure 1.3(d)**. The nanostructure seen in **Figure 1.3(h)** means dipoles may relax as they do in the paraelectric case but will be able to reach net polarisations seen in ferroelectric materials due to the higher polarisability of domains comparative to individual dipoles. Losses due to remnant polarisation and dipole and domain interactions during reorientation are also reduced compared to bulk ferroelectric polymers due to their much smaller domain size. RFE behaviour is hence the most energy efficient mechanism for capacitive energy storage in dielectrics.<sup>19</sup> Creating a material nanostructure that contains a high density of polar nanodomains is the therefore the primary aim when designing a polymer-based capacitor with the highest  $U_e$  and  $\eta$  possible.

However, attaining RFE behaviour is not the only aspect of material structure that must be considered. Due to their multifaceted response to an applied field, the multiscale architecture of ferroelectric polymer-based capacitors should be optimised to maximise their energy output. For example, when designing a thin film device, the crystallite orientation in the material must not have a preferred direction along the applied field, such that the dipoles may rotate when a field is applied through the film.<sup>20,21</sup> X-ray scattering techniques and other nanostructure probes can provide direct insight into the nanocrystalline structure to investigate potential problems such as these, as it is hard to directly discern if these structures are present from ferroelectric testing.

In general, the domain structure of ferroelectric polymers, responsible for their high inherent polarisability, gives them a distinct advantage over linear dielectrics. Once the field required to rotate dipoles within a crystallite is reached – the coercive field,  $E_c$  – polarisation in the polymer will increase substantially.<sup>22</sup> At the nanoscale, the effective  $E_c$  will vary quite substantially between crystallites, so there is no step change in polarisation overall. But over a large range of fields, the rate of polarisation  $dP/dE$  should be significantly higher than in a linear material due to the continuous process of crystallites. Amorphous phase dipoles between crystallites will also gradually become polarised, although above the glass transition temperature of the polymer,  $T_g$ ,

as thermal fluctuations of dipoles will largely overwhelm these polarisations and prevent their permanency. As a crystallite attains a large net polarisation, an effective local ‘depolarisation field’ is induced in the surrounding microstructure, which opposes the local field induced by oriented dipoles in the crystallite.<sup>23</sup> In some ferroelectric materials, when the applied field is ramped down, the depolarisation field may end up exceeding the field induced by dipoles in the crystallite, as ferroelectric domain dipoles co-orientate back into a relaxed state, pulling each other as they rotate. This is known as *antiferroelectric* behaviour and leads to a very low remnant polarisation as the amorphous phase dipoles will generally orientate to compensate for each other. While it would be desirable behaviour due to the zero remnant polarisation,  $P_r$ , and thus low losses, this has not been truly observed in any polymer phase and is mainly observed in ceramics.<sup>24,25</sup> In contrast, ferroelectric polymer domains are more likely to be frozen-in to their polarised state than ceramics, and as such a remnant polarisation is consistently observed, unlike in the antiferroelectric case.

Similarly, an overabundance of paraelectric and amorphous domains can limit coherent co-axial polarisation by screening interactions between polar domains. Materials that exhibit this behaviour are known as dipolar glasses, although it is seldom seen in polymers.<sup>26</sup> Their polarisability is somewhat intermediate between ferroelectric and paraelectric behaviour, as no dipoles are independent, yet a domain structure is absent.<sup>27</sup> This means that dipoles do not interfere with each other when polarising as in the paraelectric case, but the lack of domains means they also do not easily co-align and produce high polarisations, as in the ferroelectric case. While this produces a low loss dielectric material, their low net polarisability means, as far as energy harvesting is concerned, they are not much more useful than paraelectric materials.

Since paraelectric and ferroelectric behaviour are a function of the polymer nanostructure, this necessitates a tailored design approach. In particular, the material structure at all scales must combat the inherent trade-off between polarisability and electrical breakdown, while aiming to avoid large dielectric losses. In recent years, focus has shifted to adopt mesoscale structuring approaches to achieve this. These methods have been well developed due to a rapidly increasing understanding of the mechanisms behind charge storage, electrical breakdown and conduction in polymers.<sup>8,10,28–30</sup> For example, it has become evident that interfaces between polymers may function to significantly increase  $E_b$ , while also providing sites for charge storage.<sup>31,32</sup> Furthermore, as the multifaceted effects of the crystalline nanostructure on charge storage and transport mechanisms in ferroelectric polymers have become clearer, the processes and causes of electrical breakdown in a variety of polymer-based systems are also now far better understood.<sup>9,33–36</sup> Hence these mechanisms should be broken down to better understand how to carry out a tailored design approach. First, the different forms of polarisation induced in the polymer matrix by an applied field should be clarified.

### 2.3. Polarisation and conduction in dielectric polymers

Several different possible forms of polarisation may exist in dielectric materials.<sup>27</sup> As polarisation is simply the separation of positive and negative charge, polarisations can manifest in polymers as a result of a separation of electrons or free ions, atomic vibration, molecular dipoles, or at interfaces at the microstructure scale and below.<sup>37</sup> Additionally, in the case of polar polymers, there may also be orientational polarisation – associated with the response of ferroelectric dipoles to the applied field. Each of these polarisation mechanisms will respond to the applied field in different ways which will depend on the form of polarisation *and* the environment surrounding the dipole. Similarly, these polarisations will dissipate with a characteristic relaxation time after the applied field is relieved.<sup>22</sup>

Since the permittivity of a dielectric can be interpreted as describing the polarisation mechanisms in the material via the function  $\epsilon_r(\omega)$ , the polarisation in a dielectric  $P = (\epsilon_r - 1)\epsilon_0 E$  is also dependent on  $\omega$ . This means that when inducing this polarisation with a sinusoidally alternating applied electric field, the polarisation will be a function of time  $P(t)$  as the various polarisation mechanisms respond to the constantly changing direction and magnitude of the applied field. For some dipoles in the material, the applied field may need to pass a threshold to become strong enough to polarise said dipole.

Take the example of subjecting a material containing ferroelectric domains of a variety of sizes to an applied field. In this case, as the field is ramped up, initially small domains (i.e. small dipoles) orientate along the field, as the relatively low field strength required to provide a force strong enough to exceed the restoring force exerted on them by the surrounding dipoles in the material structure is overcome. In such a case, this threshold field will need to be sustained for longer than the response time of the dipoles or domains to the field,  $\tau$ , to retain the polarisation and ‘freeze’ it in place, storing energy. Otherwise, the energy spent to rotate this domain will be dissipated. Applying a field with period  $T = 2\pi/\omega$  far lower than  $\tau$ , will lead to these dipoles being pulled back to their resting position by the restoring force of the surrounding unoriented dipoles. This touches on a critical point; the frequency  $\omega$  of the applied field will affect which dipoles are rotated and how strongly they respond. Since  $\epsilon$  is a function of the polarisability of the material, and in turn the polarisability is a function of  $\omega$ , the permittivity must vary with the applied field’s frequency. This is akin to viewing the electric field from the electrodynamic, wave-like perspective, and produces  $\epsilon(\omega)$ ; the dielectric function. This may be thought of as a dispersion relation for electromagnetic waves propagating through the material. In other words, the energy carried by the electric field will be attenuated by charges and dipoles within the material to different extents at different frequencies as work is done to polarise them. The dependence of the response as a function of frequency will depend on the specific material properties, although a general form is consistent across polymer dielectrics.<sup>38–40</sup> Recalling that  $\epsilon'$  correlates with energy stored via polarisation and  $\epsilon''$  correlates with energy dissipated (i.e.



losses), the dielectric response of a generalised polymeric material as a function of frequency of the applied field is shown in **Figure 2.1**, with the different forms of polarisation which arise labelled.

In the low frequency regime, i.e. converging towards the d.c. case,  $\epsilon'$  reaches a maximum as all of the polarisation mechanisms in the system are able to respond before the direction of the applied field changes. However, operating in the d.c. regime also leads to far higher dissipative dielectric losses, causing peaks in the loss spectrum  $\epsilon''(\omega)$ . Additionally, conductive losses will vastly increase in this regime, rendering it largely unviable for storing energy polymer dielectrics. Conversely, in the high frequency regime, material dipoles and domains are not capable of responding quickly enough to this applied field, i.e.  $\tau \gg T$ , meaning work done to rotate the dipoles and domains is dissipated, not stored as energy. Hence, when polarising a ferroelectric material with an a.c. field, the field should be applied at a frequency where  $\epsilon'(\omega)$

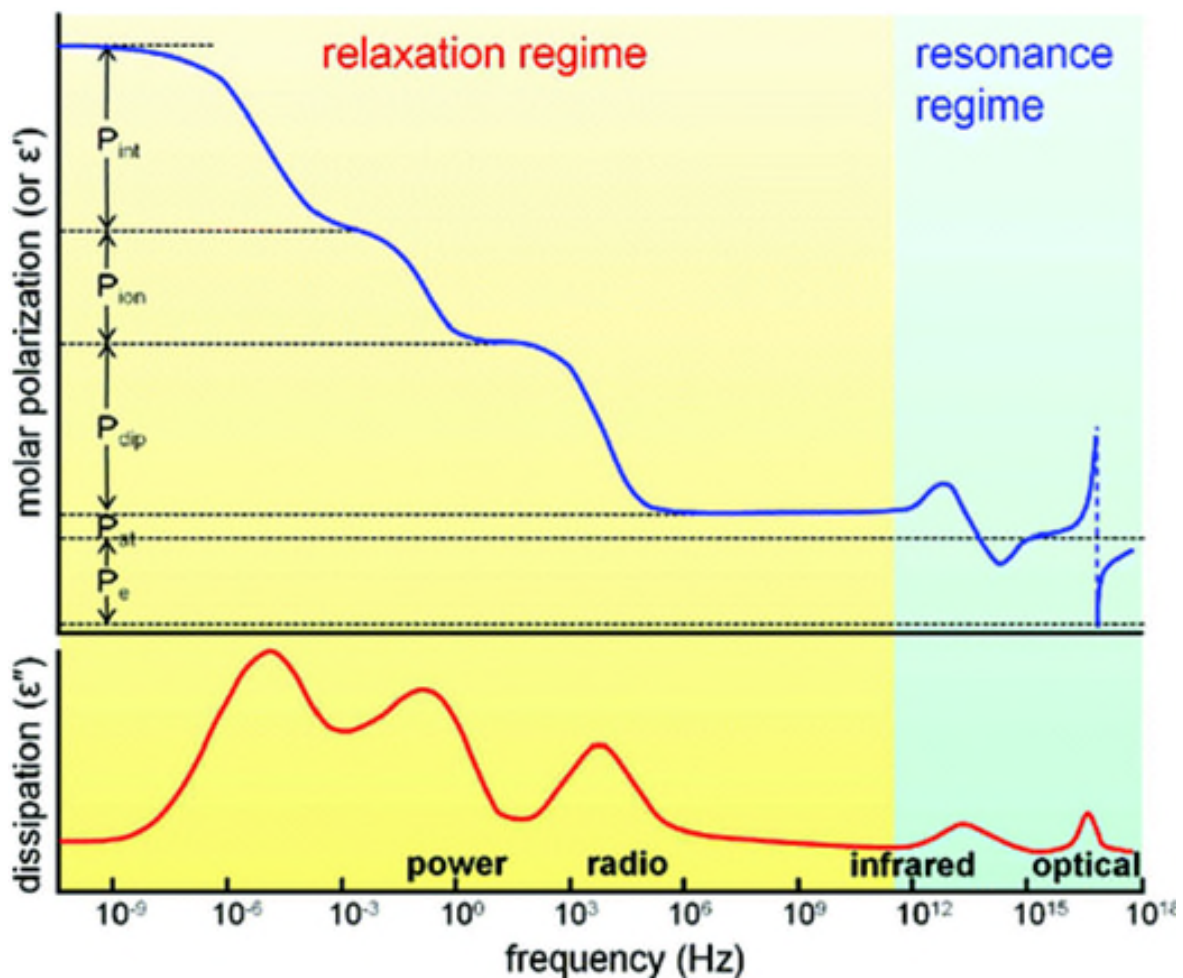


**Figure 0.1.** A generic response to an applied field in a polymer dielectric across the entire realistic range of applied field frequency. Probing the ultra-low frequency region is difficult and so tests are typically carried out in the  $10^0$ - $10^7$  Hz range. Polarisation  $P_{\text{int}}$  and  $P_{\text{ion}}$  in real materials may appear at higher frequencies than shown in this generalisation. Reprinted (adapted) with permission from Ref. <sup>22</sup>. Copyright 2012 American Chemical Society.

is high, and  $\varepsilon''(\omega)$  is low. Hence the applied frequency should be away from the resonance frequency of polarisation mechanisms.

The exact form of the curve  $\varepsilon'(\omega)$  given in **Figure 2.1** is dependent on the specific material structure and properties and may be determined empirically. Nonetheless a variety of models are often employed to describe these dependencies considering the behaviour of different material archetypes and polarisation mechanisms.<sup>40</sup> However, these models are usually quite straightforward and typically assume only one polarisation mechanism and hence one relaxation peak. In a real polymeric dielectric system, there will be a superposition of several polarisation responses across the frequency spectrum, with different relaxations and resonances originating from various sources including molecular dipoles, functional groups, space charges and interfacial charges at barriers between phases and crystallites. Additionally, real physical systems do not produce the symmetric relaxation peaks which these models often produce, making their applicability in polymer-based polymorphic dielectrics somewhat limited. A distribution of polarisation signatures like those seen in **Figure 2.1** is therefore closer to reality, so these models will not be explored in detail here.

## 2.4. Polarisation mechanisms in polymeric systems

As has now been shown, there are a variety of different forms of polarisation that may be found in a polymer system. Dielectric impedance spectroscopy may be used to produce this frequency spectrum and identify relaxation peaks, which may then be associated with polarisation processes. There are 5 key forms of polarisability that are most important to consider in polymer dielectrics, which will be discussed in detail in this section. First, it should be noted there are 3 polarisations which are intrinsic to the material of choice, arising from the *electronic*, *atomic*, and *molecular* effects. Electronic and atomic polarisations have extremely fast response times to an electric field, and so their ‘relaxation peaks’ are seen far above frequencies utilised in standard electronics, in the  $\sim 10^{12}$  Hz range and above in **Figure 2.1**. Due to the extremely brief relaxation periods for these mechanisms, they are more often referred as resonance peaks rather than relaxation, as they make no contribution to losses in the relevant frequency range for electronics ( $< 10^9$  Hz).<sup>27</sup> As such these forms of polarisation are not usually utilised to increase energy storage capabilities in polymers. Molecular polarisation is however very relevant for polymers containing molecular dipoles, ferroelectric polymers in particular. The substantial contribution of molecules to the net polarisation in these polymer dielectrics arises from the orientation of these polymer molecular dipoles along an applied field. So, for the sake of simplicity, we will refer to molecular polarisation as *orientational* polarisation from here on out. Hence, the three most relevant forms of polarisation – *ionic*, *interfacial* and *orientational* – will be discussed here.

These 3 forms of polarisation are seen at far lower frequencies than the electronic and atomic polarisations and may substantially vary between polymers and composites with changes in processing methodology and material structure.<sup>15,39,41</sup> As such these are the primary phenomena of interest for enhancing capacitive polymers. Firstly, it should be noted that ionic and interfacial contributions are often a function of material structure and defect/inclusion density. Dielectric spectroscopy and ferroelectric testing together may probe the extent of these contributions, especially when paired with nanostructure probe techniques to gain insight into the structural origins of the material's polarisation behaviour. It should be noted however that relaxation processes which occur on extremely long timescales (i.e. with low frequency signatures in the  $\epsilon''(\omega)$  loss spectrum) produce very low power outputs even for materials with high energy storage densities due to this long discharge period. As such, these mechanisms are not practical for pulsed energy devices, and focus is typically shifted to enhancing the discharge efficiency and storage capabilities of mechanisms in the  $\sim 10^0$ - $10^9$  Hz range. Molecular dipole polarisation is therefore the main target for enhancing power density in polymers, as the response frequencies lie in this frequency range. In particular, the power density attainable from molecular dipole and interfacial polarisations in may be significantly enhanced with changes in the molecular structure all the way to the macrostructure of the material, which has led to research into a wide array of structuring approaches.<sup>42-45</sup> But first, each of these forms of polarisation must be well understood in order to interpret P-E data and its relationship to material structure.

#### **2.4.1. Ionic Polarisation**

The contribution of ionic polarisation to the net polarisation of dielectric polymer systems is one of the most difficult to manipulate and control. Ionic relaxation is a function of the often long migration time along the field within the material, and so can appear at frequencies far lower than the Hz-kHz range.<sup>14</sup> Although, the real possibility of sub-second ion migration in a material – dependent on multiscale structural order amongst other things – will lead to a relaxation in a similar frequency range to the molecular dipoles. Ions may act as mobile charge carriers under an applied field, similar to free electrons. Hence a high ion mobility or concentration can increase conductive losses. Mobile charge carriers in semi-crystalline polymers contribute to conduction mainly by hopping transport, whereby the ions ‘hop’ between free energy states around adjacent polymer chains.<sup>40,46,47</sup> Due to their mobility, ions may easily polarise across amorphous/crystalline interfaces in the microstructure, leading to charge separation at these interfaces. This is a rather lossy process due to the low conductivity of amorphous polymer phases and will incur higher losses than the polarisation of molecular dipoles in these regions.

However, it should be noted that the range over which these amorphous phase molecular dipoles can interact is limited. This nanometre scale ‘co-operative rearranging region’ (CRR) is a

function of temperature, enlarging at lower temperatures due to increased order, and reaching a minimum at the glass transition temperature,  $T_g$ .<sup>48</sup> For low  $T_g$  polymers, the CRR will be small at typical operating temperatures. For example, PVDF, with  $T_g = -35^\circ\text{C}$ , will have a small CRR from room temperature up to its melting temperature  $T_m \sim 165^\circ\text{C}$ , and so little amorphous region polarisation due to interacting molecular dipoles is expected. High ion densities in the CRR may alter this. The activation energy  $E_a$  associated with this rearrangement may be significantly lowered with increasing ion concentration, making the presence of high ionic polarisation in a polymer dielectric seem more appealing. Although, a lower  $E_a$  also leads to an increased electrical conductivity as this energy may also describe that required for hopping transport, inevitably increasing conductive losses. In contrast, lower temperatures – which extend the CRR – will lead to increases in  $E_a$ , reducing losses from ion transport. Conversely, at high temperatures, impeded ion mobility may lead ions to agglomerate at the electrodes due to their coulombic attraction to them.<sup>49</sup> This ‘electrode polarisation’ describes charge transport at the electrode-polymer interface, and results in large losses due to leakage currents; an effect exacerbated by high ion concentrations and low frequencies (i.e. in the d.c. regime). For example, Correia *et al.* investigated how the concentration of ionic liquids (ILs) in PVDF affected the dielectric properties and found that an increased IL concentration resulted in both an increased dielectric permittivity and losses.<sup>50</sup> They outline the key contributing effects to these losses; (i) an increased d.c. conductivity; (ii) increased charge mobility; and (iii) increased electrode polarisation.

Hence, in practise, ionic polarisation is, in general, not ideal for dielectric polymer devices. While the ionic polarisation obtained with high ion concentrations can significantly contribute to the net polarisation in the material, associated losses are prominent at all temperatures and frequencies and cannot be sufficiently suppressed by controlling ion concentration. Energy barriers preventing charge transport along the electric field direction are an effective way to mitigate these problems, particularly as ions may become trapped at these interfaces and contribute to a higher  $P_{max}$ .<sup>51,52</sup> However, regulation of ion concentration in the material should be the first port of call, as ionic polarisation will almost always incur energy losses of greater magnitude than losses caused by interfacial and orientational polarisation mechanisms.

#### 2.4.2. Orientational polarisation

Orientational polarisation in ferroelectric polymers refers to polarisation arising from the alignment of molecular dipoles due to an applied electric field. This is the primary mechanism for energy storage in dielectric polymers with a high permittivity, and typically polymers with high molecular dipole moments will exhibit the strongest orientational polarisation.<sup>22,53</sup> Polymer molecular dipoles are often strong enough to produce high local electric fields, and as such are effective sites for storing significant amount of energy. However, this also means they may

experience strong coupling to neighbouring polymer chains. Hence these dipoles may co-orientate, ‘dragging’ each other with them as they rotate in response to an applied field. Similarly, when the field is relaxed, the polymer chains may ‘pull’ neighbouring dipoles with them into the relaxed, unoriented state. Although as they produce strong local fields, in many cases molecular dipoles may act to shield neighbours from the external field, raising the threshold field – the coercive field,  $E_c$  – required to orientate a given dipole.<sup>22,40</sup> The manner in which dielectric materials express this behaviour entirely depends on the material’s microstructure, which determines how dipoles interact and hence orientate along an applied field.

As seen in **Figure 2.1**, while the contribution arising from molecular dipole co-orientation can usually be seen somewhere in the low Hz-kHz range, it can appear much higher depending on the microstructure and nanostructure of the polymer. The form of  $\epsilon'(\omega)$  will depend on a multitude of factors and is usually best interpreted from empirical data due to the multifaceted mechanisms that polymorphic polymers may experience. This is due to their complex structure making it difficult to foresee if mechanisms impeding or promoting polymer dipole orientation will typically arise.<sup>54,55</sup>

Returning to **Figure 1.3**, one may infer some behaviour of dipoles not only from the  $\epsilon'(\omega)$  spectrum, but also from the form of P-E loops. As previously noted, a low remnant polarisation  $P_r$  and high discharge efficiency  $\eta$  implies mobile polymer molecules, leading to easy dipole reorientation after removal of the applied field. This may come in the form of dipole reorientation of single molecules in amorphous (or sometimes crystalline) nanoregions, or in the form of large crystalline domain reorientation.<sup>22</sup> In contrast, linear dielectric materials do not usually show nearly as much propensity for orientational polarisation, typically due to the lack of polar features in the microstructure. This is evident in the low  $P_r$  seen in these materials. Despite having a near zero dielectric loss, this lack of orientational polarisation substantially limits their net polarisability.<sup>27,56</sup>

In the paraelectric case, as dipoles are not ordered in crystalline domains, there is a lack of co-ordinated alignment in response to an applied field, producing a low net polarisation. Dipoles in this case are not coupled, and instead may act to oppose each other’s orientation to minimise the local free energy.<sup>22,57</sup> Thus, the total energy required to orientate a set of adjacent dipoles is higher. At low fields however, many isolated dipoles will easily orientate along the applied field, leading to an initial linear-like response. Additionally, paraelectric materials may exhibit very low loss as independent dipoles reverse readily upon removal of the electric field, contributing to a high  $\eta$ .<sup>1,58</sup> A partially oriented structure such as that seen in **Figure 1.3** will typically arise at high fields, with the applied field providing sufficient energy for many dipoles to reorientate, causing a strong local electric field along the direction of the applied field. Some remaining dipoles in the microstructure will oppose this orientation to minimise the local free energy,

limiting the total stored energy and increasing the energy required to orientate more dipoles, resulting in increased losses.

In contrast, the behaviour of dipoles in ferroelectric materials, with microstructures optimised for attaining high orientational polarisation, are worth investigating in some detail. The manner in which dipoles orientate in response to an applied field will have strong dependence on the various aspects of the ferroelectric microstructure.<sup>16,17,59–62</sup> In this case, while individual dipoles are still affected by their neighbours, this framework should be applied to ferroelectric domains as a whole.

Domains form in ferroelectrics due to the strong coupling between dipoles during crystallisation. The energy required to orientate an entire domain will therefore be lower than the sum of energies needed to orientate all the domain's dipoles individually, as would be required in the case of a dipolar glass. The capacity for ferroelectric domains to produce a high net polarisation with low associated losses mainly depends on the way in which domains are organised within the crystalline microstructure of the material. Due to their far larger size and the resultant high local electric fields they produce, domains are far more liable to remaining 'frozen-in' after they have been polarised and the polarising applied field has been removed. That is, they do not depolarise to their resting state easily, leading to a decreased discharge efficiency  $\eta$ . Polymers containing particularly large crystallites may show a superior *stored* energy density,  $U_s$ , due to strong interactions between domains within the crystallites.<sup>16</sup> However, this structure will not produce a high *discharged* energy density  $U_e$  if the domains remain frozen-in and produce a low  $\eta$ .

In particular, the thermal history of a crystalline ferroelectric polymer will determine the nature of its domain structure, so fabrication methodologies which maximise the potential orientational polarisation should be utilised. In particular, minimising the size of crystallites during crystallisation is often optimal as it may produce the ferroelectric nanodomains which cause the aforementioned desired relaxor ferroelectric (RFE) behaviour.<sup>19,61</sup> While producing ferroelectric nanodomains can provide large enhancements to polarisability, the interaction between these nanodomains is crucial for taking full advantage of the polar nanostructure and for orientating as many domains as possible. Due to the semi-crystalline nature of ferroelectric polymers, the size, relaxed-state orientation and packing structure of crystallites can have a sizable impact on the interactions between domains.<sup>20,21,63</sup> The direction of application of the electric field must also be considered when designing the architecture of the polymer, since if the processing method mainly produces a domain orientation in one direction or plane in the ambient state, an electric field applied along this plane or axis will do little to induce polarisation. For example, in the case of a ferroelectric polymer thin film, it should be ensured that domains are as perpendicular to the through-plane direction as possible, such that when an electric field is applied along this direction, the net reorientation of domains will be maximised.<sup>13</sup> Essentially,

the manufacturing process of ferroelectric polymers should ensure the creation of a microstructure comprising of a high density of small crystallites and nanodomains which are naturally oriented against the desired direction of polarisation, allowing for a potentially large orientational polarisability.

However, polymer crystallites containing small nanodomains within large crystallites do not form spontaneously, and as such most bulk processing methods will not return such structures. Processing techniques which involve or cause high in-plane mechanical stress (such as melt-pressing) have been found to induce the break-up of crystallites and domains, forming nanodomains.<sup>36</sup> Guo *et al.* measured the crystalline long period – the spacing between adjacent crystal structures – and orientation of crystals in PVDF samples which had been stretched at various temperatures in the melt-phase.<sup>64</sup> Stretching at higher temperatures increased the elasticity of the polymer, allowing amorphous phases between crystals to comfortably expand at low strains, leading to an initial increase in the crystalline long period along the stretching

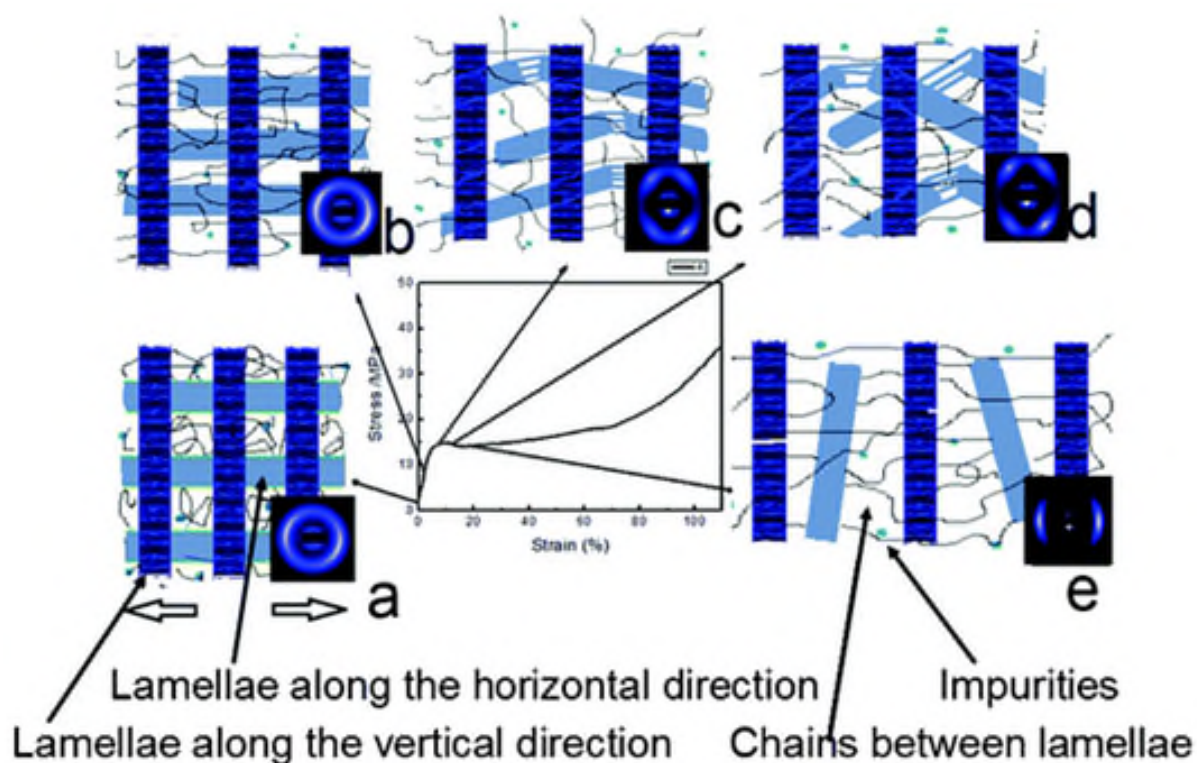


**Figure 0.2.** Crystalline lamellae as a function of strain. Initially, tie molecules – amorphous phase polymer chains which hold adjacent crystalline lamellae together – elongate as the amorphous phase expands, leading to an increase in long period along the stretching direction (**a**=>**b**). Lamellae then begin to break up along the stretching direction (**b**=>**c**), where the polymer reaches its yield point. Then, the long period reaches a maximum (**c**=>**d**), and finally the lamellae are forced to orientate in the same direction as the long period decreases (**d**=>**e**). After this point, the amorphous phase is stretched to its maximum and voids and cavities will nucleate at higher strains. Reproduced from Ref. <sup>64</sup> with permission from the Royal Society of Chemistry.

direction. After reaching a maximum, the long period begins to decrease as crystallites are broken up with increasing strain, which correlates with the breakup of the amorphous phase and subsequent nucleation of voids and cavities in the microstructure.<sup>65</sup> This process is shown in **Figure 2.2**, where the lamellae – regions of polymer molecule crystallinity – become increasingly aligned as the polymer is stretched, as uniaxial deformation forces an eventual rotation of crystallites off-axis. Furthermore, continuing the stretching process after reaching a maximum in crystallite alignment causes recrystallisation. Hence exerting mechanical stress along a given plane may also have the beneficial secondary effect of inducing the desired crystalline properties in the polymer matrix, including a potential enhancement of desired crystalline polymer phases.<sup>65–68</sup> For example, in the case presented in **Figure 2.2**, Guo *et al.* found that the electroactive  $\beta$ -phase in PVDF is formed during the stretching process. Since the  $\beta$ -phase in PVDF also packs more closely than other crystalline phases, the density of ferroelectric domains is also seen to increase. This process is usually exacerbated at high temperatures as crystallites may transition into melt-phase, but this is also encouraged under the exertion of high strains. Applying intense shearing forces under the application of heat is therefore an effective approach to induce the desired crystal structure in ferroelectric polymers.<sup>69</sup>

#### 2.4.3. Interfacial Polarisation

While manipulating the crystalline polymorphism of electroactive polymers is key to inducing a high orientational polarisation and thus attaining a large net polarisability, this is not the only factor that may lead to a high  $U_e$ .<sup>14,16,17,53,70</sup> The microstructure of polymers will affect the polarisability of the electroactive crystallites, as the environment around material dipoles and ferroelectric domains will affect how easily they orientate along an applied field. Optimising microstructure may be taken further than domain structure however by utilising hierarchical designs, most notably the use of interfaces. Interfaces can achieve two core goals. Firstly, interfaces are highly effective at impeding electrical breakdown, which can significantly enhance the maximum polarisation in a dielectric as well as largely enhancing the lifetime of a pulsed power device.<sup>71</sup> This will be explored in more detail later. Just as importantly however, interfaces can act as their own sites for energy storage and offer substantial enhancements to material polarisability.

Interfaces in a polymer dielectric may act as energy barriers for charge transport, and so will naturally act as a site for free charge accumulation.<sup>7,8,15,20,45,72–74</sup> This naturally occurs at the polymer-electrode interface regardless of material microstructure and can contribute to the discharged energy density, but notably also exacerbates losses via leakage currents when charge carriers are able to overcome the polymer/electrode energy barrier.<sup>75</sup> Tailored microstructural and design however can produce a multitude of other sites for this charge storage, such as grain boundaries between crystallites and at interfaces between different polymers. Space charges will



form on both sides of a given interface, forming an effective micro-capacitor where opposing charges agglomerate on either side of the boundary, causing a local electric field across the interface. The formalism for understanding how these mechanisms operate was developed by Maxwell and later optimised by Wagner and Sillars, and so interfacial polarisation is often termed Maxwell-Wagner-Sillars (MWS) polarisation.<sup>76</sup>

In comparison to other polarisation mechanisms, the discharge period of interfacial polarisations *can* be extremely long, as can be seen by the low frequency response peak in **Figure 2.1**.<sup>22,77</sup> Charge carriers may find metastable states near the interfaces depending on the energy band structure of the polymers. Hence the recombination time of these charge carriers can be quite long, even after the applied field is removed. This relaxation may be modelled in a similar manor to the Debye model – an idealised dielectric response where the dipoles are not considered to interact with an external applied field of frequency  $\omega$ . This leads to the dielectric function

$$\epsilon_{int}(\omega) = \epsilon_{\infty} + \frac{\Delta\epsilon}{1 + i\omega\tau_{int}} \quad (0.2)$$

Where  $\tau_{int}$  is the interfacial polarisation relaxation period of interfacial charges,  $\epsilon_{\infty}$  is the permittivity at the high frequency limit,  $\Delta\epsilon$  is the permittivity across the interface and  $\epsilon_{int}$  is the component of the material's overall dielectric function arising from interfacial polarisation.<sup>40</sup> In the simplest case, it can be shown that for a two-component layered dielectric containing materials with permittivities and conductivities  $\epsilon_1, \epsilon_2, \sigma_1$  and  $\sigma_2$

$$\tau_{int} = \frac{\epsilon_1 + \epsilon_2}{\sigma_1 + \sigma_2} \quad (0.3)$$

Which is intuitively analogous to the relation  $\tau = l/\omega = \epsilon/\sigma$ , implied by **equation 1.6**. From this it can be understood that only one of the materials requires a strong enhancement to drastically change the relaxation period. For example, in the case  $\sigma_2 \gg \sigma_1$ , i.e. an insulating layer combined with a conductive layer, the discharge time will be dominated by the conductive layer's conductivity. In contrast, enhancing either  $\epsilon_1$  or  $\epsilon_2$  will result in a far longer charge retention time at the interface. Hence for highly polarisable (high  $\epsilon$ ) multi-component polymer systems containing insulating components in an effort to impede electrical breakdown,  $\tau_{int}$  will typically be very high. Due to this, interfacial polarisation may act to slow discharge – a problem for pulsed power systems which require fast energy delivery.<sup>78</sup> Taking advantage of interfacial polarisation is therefore tricky as ensuring the polarisation translates to both an enhanced  $U_e$  and  $\eta$  is a complex process typically involving many steps of experimental trial and error.

Conceiving a thinly layered 3-layer structure containing a ferroelectric layer surrounded by two insulating outer layers – as many research groups have – one would expect the main sites for interfacial polarisation to be at the two interfaces at either side of the ferroelectric layer. Due to the charge accumulation at either side of this layer, a capacitive affect *across* the layer will

manifest.<sup>15</sup> This can lead to the interfacial polarisation inducing orientational polarisation, which will discharge at more practical rates. This effect may be even more pronounced at the boundaries between crystalline and amorphous phases.<sup>16</sup> Any electric field across a crystalline-amorphous boundary will be met by a compensating electric field within the given phases, orienting dipoles in turn. However, since the difference in permittivities and conductivities are far lower across this boundary than across boundaries between different polymers, the build-up of charge on either side of the interface will be far less significant, as will the induced dipole orientation. This may also be achieved in nanocomposites at the boundaries between nanofillers and the polymer matrix, which may often be heavily exacerbated by the large interfacial surface area in composites with well-dispersed nanoparticles, as well as the often large discrepancy in permittivity between the polymer and the nanofiller.<sup>79,80</sup> Wang *et al.* for example found that introducing ceramic barium titanate (BaTiO<sub>3</sub>) nanoparticles into their solution cast layered PVDF films, featuring sequential layers of PVDF and PVDF/BaTiO<sub>3</sub>, significantly enhanced their composite permittivity when compared to the expected value calculated by a serial capacitor model.<sup>7</sup> This enhancement is expected in systems with high interfacial polarisation and is presumed to contribute to the impressive  $U_e$  of 7.02 J/cm<sup>3</sup> at 3900 kV/cm observed in their many-layered composites.<sup>15,20</sup>

As discussed in this section, a high polarisation in a given region of a dielectric will lead to a high local electric field. This is representative of substantial charge storage, but may also be a sign of impending sample failure due to electric breakdown as the maximum electrical stress of the material is approached.

## 2.5. Electrical breakdown in polymers

As previously mentioned, enhancing the electrical breakdown strength  $E_B$  in polymer-based dielectrics is essential for maximising the discharged energy density  $U_e$  due the roughly quadratic dependence of the latter on the former. Thus, one key question must be answered; what causes electrical breakdown to occur? The short answer is that it occurs when the material begins conducting, but the causes of conduction in otherwise insulating polymer systems is far more complex, and heavily depends on the macrostructural architecture of the material, as well as its microstructure and nanostructure.<sup>33,35</sup>

Breakdown is a phenomenon seen in all materials and will occur in polymers and composites without truly ‘conductive’ components. What drives breakdown to occur – and equivalently what prevents it from occurring – varies wildly with material components and microstructure. Analogous to a fork lighting strike, when electrical breakdown occurs, charge carriers find the route of least electrical resistance in an insulator between two opposing charge reservoirs. Most commonly an ‘electron avalanche’ is caused by a runaway effect initiated by a small number of

extremely high energy conduction electrons. First, a high energy conduction band electron collides with atoms in the polymer matrix, ionising them and liberating electrons into the conduction band. If this initial electron is of sufficient energy, both free electrons may then go on to repeat this process.<sup>81</sup> Ultimately this results in an ‘electrical treeing’ effect, seen in **Figure 2.3**, which is demonstrative of how the charge carriers attempt to find the path of least resistance through the structure. This process will be accelerated in the case of electrode charge injection, as high energy electrons which penetrate the polymer from the metallic conduction band are likely to have high energies.<sup>82</sup> Hence insulating the electrodes from the dielectric can assist in preventing electrical breakdown, as well as reducing losses due to leakage currents.<sup>83</sup>

The likelihood of this occurring at a given applied field is largely dependent on what the constituents of the material are, but **Figure 2.3** also clearly highlights how the microstructure impacts the path of least resistance through a material. In the absence of conductive components, in a polymer this path will pass through any voids and defects present in the microstructure. This is due to the local electric field around such sites, which may exceed the bulk applied field. Near a defect, void or inclusion in a polymer matrix, there will be a marked change in local permittivity, and an accompanying large electric field gradient, i.e., a high potential difference.<sup>84</sup> This leads to enhanced charge transport across these sites, which at the ultrahigh electric fields applied in these systems leads to local breakdown – also known as partial breakdown. This causes a slew of knock-on effects including local heating, leading to melting and material deformation, electrochemical changes, and build-up of space charges in the newly enlarged void.<sup>45,85</sup> With prolonged exposure to high alternating electric fields, these local breakdown effects will worsen and proliferate, increasing the likelihood of full breakdown. Hence the higher the density of these microstructural irregularities throughout the matrix, the higher the

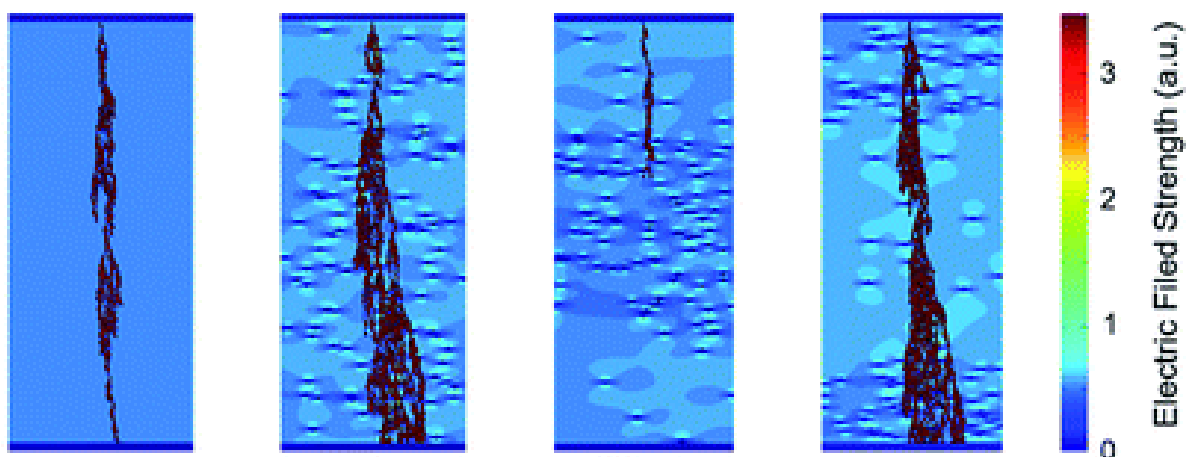


**Figure 0.3.** Schematic of the development of electrical trees through the neat ferroelectric polymer, followed by composites containing ceramic nanofillers in various distributions, which significantly impacts how the trees propagate through the material structure. Left to right: no nanofillers, randomly distributed nanofillers, nanofillers distributed near the composite centre, nanofillers distributed near the composite edges. Reproduced from Ref. <sup>72</sup> with permission from the Royal Society of Chemistry.

probability of breakdown, as currents may find a path through these features to bridge the length of the bulk material. In all-polymer systems, the breakdown field is hard to predict as the presence of voids and defects will likely substantially reduce  $E_b$  from its theoretical upper limit. The measured value of  $E_b$  is therefore highly dependent on the details of the fabrication process, as this will determine the density of these abnormalities.

It should be noted that, the probability of failure of a polymer is highly sensitive to the area of testing employed.<sup>86</sup> Increasing the area of testing leads to a higher likelihood that somewhere between the testing electrodes there is a network of weak links that is sufficient to cause breakdown at a given applied field. Smaller electrode areas will have fewer weak links in the area between the electrodes, and hence will usually survive to higher fields. For the best estimation of an intrinsic  $E_b$  – that is the breakdown strength in an ideal sample of the material with few weak links – small area electrodes should be used over multiple areas to find the maximum possible  $E_b$ . Similarly, the sample thickness must also be considered, as this will affect the number of defects within the chosen area of a sample.<sup>34,87</sup> The sample microstructure will of course be intrinsically linked to the fabrication process, which will in turn impact the sample thickness. In many cases, it may be that thicker testing areas are more likely to contain large defects due to the higher chance of sample inhomogeneities. In fact, it may only take one large defect like this to initiate breakdown in a thick sample.<sup>86</sup> However, the dependence of  $E_b$  on thickness may wildly vary with material architecture. Different material and composite designs will have differing mechanisms liable for triggering breakdown, which may be hard to predict.<sup>88</sup> Hence the relationship of thickness to these mechanisms is best determined empirically rather than employing pre-conceived models to drive material design.

Polymer interphases and interfaces are also an effective way to maximise energy storage without significantly increasing the risk of electrical breakdown. This is because they may act as scattering sites for electrons, reducing their mean free path and hence also reducing the energy gained from traversing the electric field.<sup>9,71,89,90</sup> Multi-phase all-polymer systems have hence become a popular choice of dielectric polymer material, especially considering their additional benefit of promoting interfacial polarisation. They will be explored more later.

In the field of polymer nanocomposites, a commonly encountered phenomenon is that of the percolation threshold; the nanofiller loading at which nanoparticles form a continuous network through the material structure.<sup>91</sup> This may lead to the manifestation of a conductive pathway through the material in the case of certain nanofillers. As many composites seek to avoid this scenario, nanofiller loadings are usually targeted just below the percolation threshold. In this case, the small gaps between nanofillers act as insulating barriers for charge transport which must be overcome. Alternatively, more complex solutions may be utilised, such as those seen in **Figure 2.3**, where the nanofillers have been situated further from the edges of the composite to insulated them from the electrodes. Of course, increasing the applied field across the

composite will increase the mean energy of charge carriers and assist charges in surpassing the energy barrier which otherwise prevents them from hopping between states in defects, voids and/or inclusions. So, in any case, at some threshold field, all energy barriers in the system will be overcome and bulk conduction will manifest, leading to total electrical breakdown.

Now, having discussed the variety of mechanisms in polymers which contribute to a high  $U_e$ , it is worth reviewing the selection of polymers which may be incorporated into dielectric devices. As polymers may have linear or non-linear dielectric responses under an electric field, these different classes of dielectric will be reviewed independently.

## **2.6. Effects of processing methodologies on the properties of dielectric polymers**

### **2.6.1. Linear polymers**

Polymer chains possessing molecular dipoles are not particularly common, making choice limited with respect to highly polarisable polymers.<sup>77</sup> **Table 2.1** provides a list of polymers with a variety of dielectric properties extracted from various works. It can be seen here that the vast majority of dielectric polymers exhibit linear behaviour. Other properties such as electrochemical stability, bulk conductivity and processability may also affect their capacitive performance.<sup>92</sup> As was previously mentioned, due to their typically low permittivity and lack of polar features in their structure, linear dielectric polymers are rarely used in energy storage applications. To make up for their low polarisability, extremely high electric fields must be applied. As such, the key to high performance in linear polymers is their ability to survive these high electric fields without breaking down. As per the quadratic dependence of **equation 2.1**, a high  $E_b$  can lead to a surprisingly high  $U_e$  even with a low permittivity. Polar linear polymers are few and far between since, typically, molecular dipoles lead to substantial orientational polarisation, which is usually a non-linear function of the magnitude of the applied field. However, the few polar linear polymers that do exist have been explored for their energy storage properties. Polyurea for example has a very high dipole moment of 4.56 Debye, and despite the lack of crystalline structure can reach a permittivity of  $>4$ .<sup>58,93,94</sup>

Because of this, even after decades of research into alternatives, BOPP still stands as the most promising linear dielectric for use in pulsed power systems. In fact, besides polymers used in high temperature applications such as polytetrafluoroethylene (PTFE) and polysulfones (PSU), BOPP dominates the market for linear polymer-based capacitors.<sup>95</sup> Orienting the polymer chains in a polypropylene film leads to a homogenous microstructure, lacking in weak points at which electrical breakdown events would occur. After biaxial orientation – usually imposed by mechanical stretching of a thin film – polypropylene possesses an extremely homogenous, densely packed nanostructure consisting of lamellar crystallites which lie along the axes of

stretching (i.e. in plane).<sup>33,35</sup> Hence upon application of a through-plane electric field, the crystallites are oriented perpendicular to the field lines.

Polymer	$E_b$ (kV/mm)	$\epsilon_r$	$U_e$ (J/cm <sup>3</sup> )	Reference
Polyurea	800	4.2	12	58
Polythiourea	1000	4.5	22	96
Polycarbonate	528	2.8	0.5-1	4,29
Polyethylene terephthalate	570	3.3	1-1.5	4,29
Polyethylenimine	460, 450	3.2, 2.7	2.3, 1.6	51,97 *
Polyimide	310	3.4	1.42	98
Polyether ether ketone	320	3.1	1.4	97 *
Polyphenylene sulfide	550	3.1	1-1.5	4,29
Polypropylene	640	2.2	1-1.2	4,29
Biaxially oriented Polypropylene	700	2.25	5	97 *
Polyethylene naphthalate	550	3.2	1-1.5	4,29
Polyvinylidene difluoride	600	12	11	84
P(VDF-CTFE)	618	13	25	99
P(VDF-HFP)	600, 700	12, 15	6.5, 25	100,101
P(VDF-TrFE-CTFE)	300	40	7.2	102

**Table 0.1.** A variety of polymers, linear and non-linear, listed with their key dielectric properties. Polymers in bold are linear dielectrics. \*  $U_e$  values calculated via **equation 2.1** using data extracted from the source paper. All data in this table was collected in experiments performed at room temperature. Permittivity measurements were typically taken at ~1 kHz.

Methodologies for fabricating BOPP continue to attempt to optimise the microstructure for both high polarisability and high insulation. This has led to the breakdown strength of BOPP being pushed to extremely high values while retaining low losses, producing remarkable discharged energy densities.<sup>55</sup> Of course, a higher crystallinity may lead to a higher carrier concentration due to the altered band structure and will also contribute to a higher carrier mobility.<sup>103</sup> Ho *et al.* concluded that breakdown in BOPP occurs due to hopping conduction, and that breakdown in BOPP is a thermally activated process.<sup>104</sup> While low field hopping conduction in highly insulating polymers is dominated by ionic impurities and as such is typically low, high field conduction is dominated by electrons and holes. These charges occupy amorphous phase defect states and chemical impurity states in the large insulator bandgap, which can produce much stronger conduction effects.<sup>105</sup>

Due to this, operation at ultrahigh electric fields over long periods of time is not such a reliable strategy, as breakdown becomes increasingly likely.<sup>94</sup> To add to this, it is also now thought that further increases to the breakdown field (particularly without significant detriment to material lifetime) are becoming unattainable, as the highest breakdown strengths now achieved are approaching estimated theoretical limits.<sup>53,106</sup> Hence attention has shifted to improving the polarisability of BOPP such that its performance is improved outside of the ultrahigh field regime. Chemical modifications have shown some promise for this.<sup>107,108</sup>

### 2.6.2. Ferroelectric polymers

While ferroelectric polymers are not too common, there are still a number which have been explored for use in capacitive systems besides the notorious PVDF, which will be explored in greater detail later. For example, variants of nylon are similar in dipolar structure to the PVDF  $\beta$ -phase, with  $\text{C=O}$  groups occupying one side of the chain and  $\text{CH}_2$  groups on the other. However, it does not exhibit such a coherent response to an applied field due to the hydrogen bonding present between its  $\text{C=O}$  and  $\text{CH}_2$  groups, impeding molecular polarisation.<sup>109,110</sup> Cyanopolymers however also contain a molecular dipole and exhibit some ferroelectric-like behaviour in their crystalline structure. As the cyano ( $\text{C}\equiv\text{N}$ ) group exhibits a  $\sim 3.5\text{--}4.5$  Debye dipole moment when coupled with opposing  $\text{CH}_2$  groups.<sup>111,112</sup> Polyvinylidene cyanide (PVDCN), the cyanopolymer analogue of PVDF, is chemically unstable in ambient conditions and so must be chemically modified to become viable. Polymethyl vinylidene cyanide (PMVC) may form an all-trans conformation similar to  $\beta$ -phase PVDF, which readily polarises and holds polarisation on the timescale of days.<sup>113</sup> Several co-polymers of PMVC have been investigated over the years and may possess dielectric constants closer to that of PVDF than typical non-ferroelectric polymers.<sup>114</sup> Molecular dipoles seem to interact in some of these vinylidene cyanide copolymers, forming paracrystals – crystallites that exhibit short range but not long-range structural order – which polarise in unison in response to an applied field.<sup>115–117</sup>

Polyacrylonitrile (PAN) is another semi-crystalline polymer which also holds promise due to its ferroelectric all-trans planar zigzag phase.<sup>113,118–122</sup> The polymer matrix is thought to form in a hexagonal structure, although the chains seem to have kinks randomly placed along their axis, causing deviation from the all-trans structure, and producing some disorder. Mechanical stretching or the application of a strong electric field at high temperature may undo these kinks, often resulting in a simultaneous increase in total crystallinity.<sup>123,124</sup> PAN co-polymers have attracted similar interest. In particular, poly(acrylonitrile-allylcyanide) PAN-AL, is seen to kink less due to higher rotational freedom of the polymer chain without sacrificing the tight chain-packing. It is not certain however that PAN-AL is ferroelectric, as it only exhibits ferroelectric-like behaviour around and above its  $T_g$ , and even in this case the energy discharges extremely quickly.<sup>124,125</sup>

## 2.6.3. PVDF and it's copolymers

### 2.6.3.1. Crystalline structure of PVDF

Compared to all these polymers, PVDF and its copolymers have consistently attracted more interest due to their consistent ability to deliver a high energy storage density and the plethora of routes that have been forged to enhance its dielectric properties.<sup>70</sup> The ferroelectric crystal physics of PVDF has now become very well understood, and as such PVDF now paves the way for high  $U_e$  polymer-based materials for pulsed power systems. The total crystallinity of PVDF may reach 50-70%, although it is limited to this due to end-to-end chain linkage, in which inevitable head-to-head and tail-to-tail defects will surface.<sup>126,127</sup> The duality of the tight packing of PVDF chains due to its small molecular cross-section produces an interplanar spacing of 0.847 nm and an end-to-end chain spacing of 0.49 nm.<sup>128</sup> Thus, along with its large molecular dipole, PVDF achieves a high dipole density making it immediately promising for obtaining a large energy storage density.<sup>116</sup> Furukawa *et al.* calculated a nominal dipole density of 0.13 C/m<sup>2</sup> in PVDF by assuming a dipole moment of  $\sim 2$  Debyes ( $7 \cdot 10^{-30}$  C m) and summing this over a unit volume of the lattice.<sup>129,130</sup> For a benchmark comparison, the unit cell of ferroelectric ceramic Barium Titanate comparatively has a dipole density of 0.26 C/m<sup>2</sup>.<sup>131</sup>

In total, PVDF expresses 5 core crystalline phases, 3 of which are commonly expressed in its crystal structure. Of these, the ferroelectric  $\beta$ -phase exhibits the highest polarity. As seen in **Figure 2.4**, the all-*trans*  $\beta$ -phase is the only phase in which the hydrogen and fluorine groups are always on opposing sides of the chain. Hence when chains crystallise into this phase conformation, the dipole formed between the extremely electronegative fluorine and the  $-\text{CH}_2$

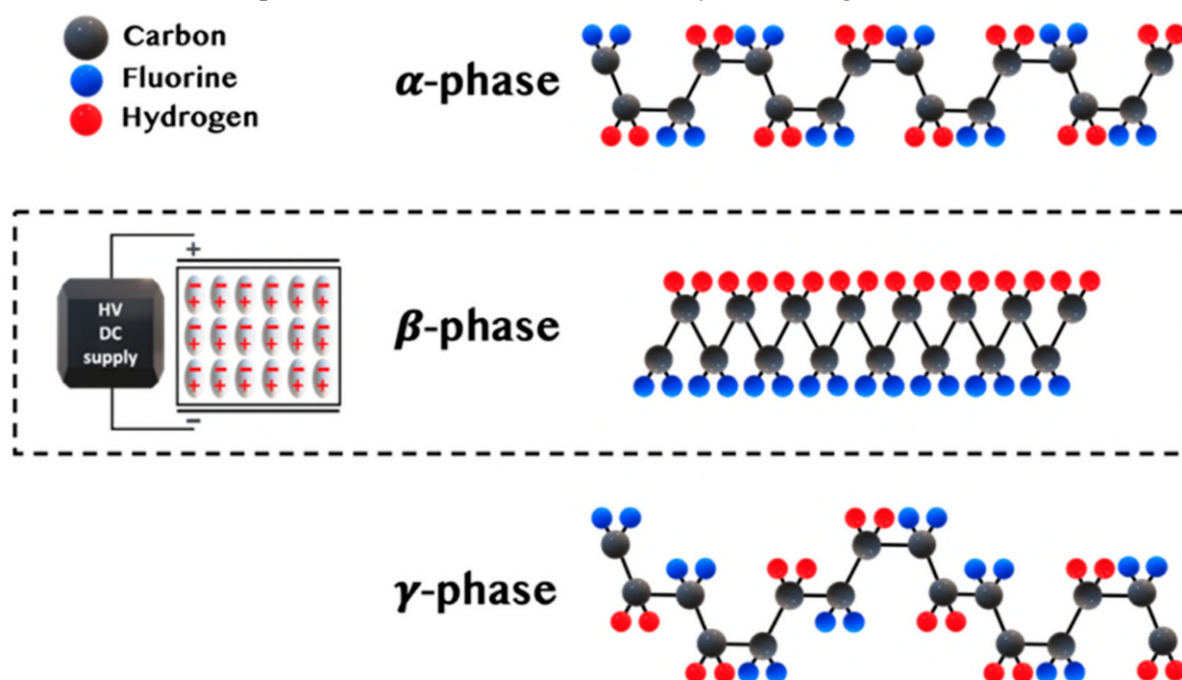


**Figure 0.4.** Diagram of PVDF molecules in the 3 key crystalline phases, showing the polarity of the  $\beta$ -phase in particular.<sup>209</sup>



group is at its strongest, with the net dipole moment per unit increasing by 10% when in the  $\beta$ -phase crystal form.<sup>130,132</sup> Conversely the  $\alpha$  and  $\epsilon$  phases (the latter of which has been seldom observed) possess *trans-gauche* antiparallel chain packing conformations, which leads to a net cancellation of dipole moment.<sup>133</sup> Hence these crystalline morphologies form paraelectric crystals, and as such their formation should be suppressed if possible. Little is known about the  $\epsilon$ -phase of PVDF – an analogue of  $\gamma$ -PVDF – as it is extremely difficult to form. Hence, there is next to no experimental characterisation of its properties, with the vast majority of the interest in it originating from theoretical studies.<sup>133,134</sup> Even still, most computational research has found little of note regarding the  $\epsilon$ -phase. The  $\alpha$ -phase – by far the most commonly observed PVDF phase due to its stability – is generally formed above the Curie temperature of PVDF (170 °C), or at rapid cooling rates.<sup>135,136</sup> The  $\delta$ -phase is also similar to the  $\alpha$ -phase but with every other chain oriented in reverse, resulting in a net dipole moment. However, this dipole is still lower than that attained by  $\beta$ -PVDF. Additionally, forming  $\delta$ -phase crystallites can be difficult and is only practically realised by exposing  $\alpha$ -PVDF to high electric fields.<sup>137</sup> This significantly hinders the processability of  $\delta$ -PVDF, as this manufacturing process – called electroforming – often results in electrical breakdown of the system.<sup>138</sup> Hence, while it can exhibit some ferroelectric properties, the difficulty of forming a  $\delta$ -phase dominant sample of PVDF and its general ferroelectric inferiority to the  $\beta$ -phase has meant it has rarely been investigated as a viable alternative, especially when considering industrial scalability. Finally, the *trans-trans-gauche*  $\gamma$ -phase is electroactive and does possess a dipole moment. However, unlike the all-trans  $\beta$ -phase, the gauche bond in every fourth monomer unit weakens this dipole and so its presence is often undesirable for attaining the highest net polarisation.<sup>133,137</sup> Although it should be noted that the interactivity of different phases in PVDF is often quite complex and depends on the specifics of the crystal nanostructure, so a polymorphic crystal structure can come with its advantages.<sup>15–17,45,139,140</sup>

Reaching similar polarisations to PVDF with alternative polymers usually requires chemical modifications to artificially enhance the polarisability of the polymer chains. This typically comes with a slew of associated issues, including decreased electrochemical stability, increased cost and lower processability.<sup>36,95</sup> Additionally, capacitive performance may turn out to be worse, as more complex polymers may incur higher losses due to more complicated interchain interactions, for example due to increased remnant polarisation as dipoles are more easily frozen-in.<sup>6,77,102</sup> In fact, compared to other ferroelectric polymers,  $\beta$ -PVDF chains readily switch orientation upon electric field application due to the small interplanar spacing and end-to-end gauche bonds. This leads to strong molecular coupling and so as one molecular chain is polarised by the applied field, it ‘pulls’ neighbouring chains with it. This effect manifests as a kink wave propagating along the molecular axis of the PVDF, rotating the chain dipoles to align with the electric field.<sup>141</sup>

Chemical modification of PVDF has been used to enhance its dielectric properties, although the viability of these polymers for energy storage is tenuous. The molecular structure of some of the most commonly used PVDF copolymers is given in **Figure 2.5**. These polymers may possess the substantial advantage of exhibiting relaxor ferroelectric behaviour, usually attributed to their low crystallite size and moderate total crystallinity, which can assist in preventing ‘frozen-in’ polarisation and promote relaxation.<sup>14,57,81,142</sup> Although, while PVDF copolymers and terpolymers with large side groups (such as those shown in the final columns of **Table 2.1**, i.e., PVDF-trifluoroethylene {PVDF-TrFE}, PVDF-TrFE-chlorotrifluoroethylene {PVDF-TrFE-CTFE}), can have extraordinary dielectric permittivities and associated polarisability, their cost of manufacture, poor electrochemical stability and generally subpar operative lifetimes render them quite inconvenient for practical applications.<sup>1,30,143–145</sup> There is substantial ongoing interest into the use of these polymers, but in general, the more straightforward copolymer of PVDF-co-hexafluoropropylene (PVDF-HFP) has been more commonly utilised. Having a similar molecular structure to regular PVDF, PVDF-HFP is known to have a higher electrical breakdown strength and a lower dielectric loss than PVDF, while also possessing a slightly higher dielectric permittivity, induced by the more heavily fluorinated polymer backbone.<sup>31</sup> Its dielectric properties and crystal structure don’t substantially differ from PVDF, meaning it may often be substituted for PVDF without having to account for any differences, but with hope of slightly enhanced ferroelectric properties, which has led to increased interest in it as a reasonably cheap alternative to regular PVDF.<sup>16,17,32,146–149</sup> To make the most of these properties, the processing methodology should be tailored to ensure the desired crystalline structure can be obtained. This begins with trying to obtain PVDF-HFP with a high  $\beta$ -phase content, which requires control of the crystallisation process.

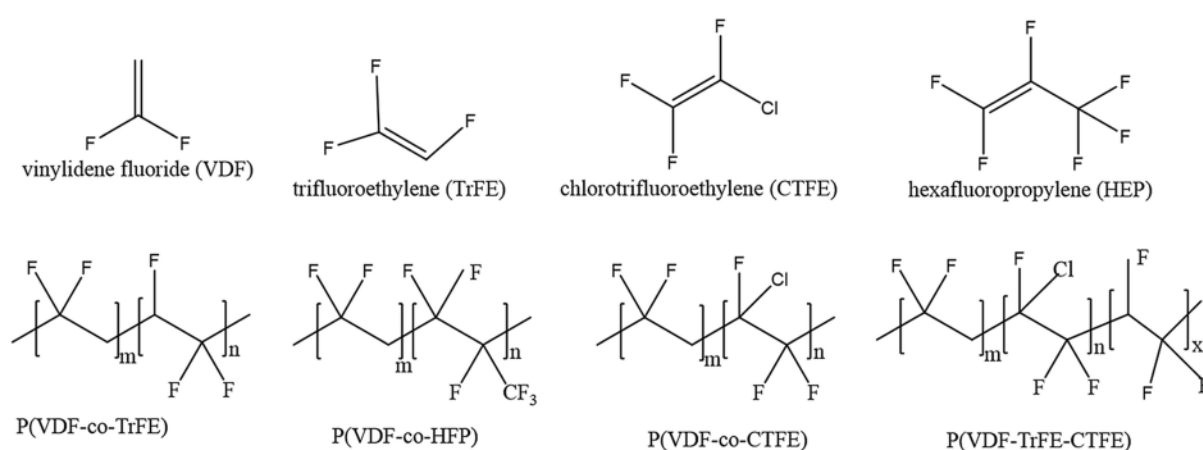


**Figure 0.5.** Monomer molecular structures of commonly utilised ferroelectric copolymers of PVDF. Reproduced from Ref. <sup>43</sup> with permission from the Royal Society of Chemistry.

### 2.6.3.2. Effect of processing methods on the structure of PVDF and its copolymers

Specialised processing techniques can be used to form  $\beta$ -PVDF, with some methods pushing the crystalline fraction to almost 100% with specialised processing approaches.<sup>59,150–153</sup> Generally, the polymer chains must have some form of mechanical or electrical stress exerted on them during processing to induce alignment of the chains in the resultant crystalline form. In fact, it is often speculated that the formation of the  $\alpha$ -phase and subsequent relaxation to the  $\beta$ -phase is a primary mechanism for  $\beta$ -phase formation.<sup>154</sup> For example, as previously discussed, the  $\alpha$ -phase may be transformed into the  $\beta$ -phase under mechanical deformation, high pressure and temperatures and applying high electric fields during processing.<sup>59,64,155</sup> This is usually achieved in either in solution or in the melt, in which the PVDF chains may reorganise and crystallise easily. The  $\gamma$ -phase can also be obtained from the  $\alpha$ -phase but requires high annealing temperatures and again mechanical deformation.<sup>155,156</sup> In previous studies, the relationships between processing parameters and crystalline transitions in PVDF have been investigated both theoretically and experimentally. Alternatively, in solution, the  $\alpha$  and  $\beta$ -phases may relax to the  $\gamma$ -phase when using highly polar solvents or high casting.<sup>150,157,158</sup> The addition of polar additives to melts or solutions of PVDF or application of electric fields are seen to amplify this relaxation process.<sup>151</sup>

Melt-phase processing methods for producing electroactive PVDF usually involve either melt extrusion or hot-pressing.<sup>36,94,151,159</sup> Typically, melt-processing means PVDF crystallises into the most kinetically stable  $\alpha$ -phase, as the opposing molecular dipoles in  $\alpha$ -crystallites minimises the system's free energy.<sup>14,160,161</sup> However, hot-pressing methodologies effectively employ biaxial or uniaxial stretching on extruded thin films during processing, which can partially prevent the need for stretching the films post-processing to transform  $\beta$ -PVDF to  $\alpha$ -PVDF.<sup>162</sup> This is not the only advantage of stress exertion, as the ferroelectric domains may also be oriented along the direction perpendicular to the plane of the produced thin film, increasing the film's through-plane polarisability.<sup>20</sup> Additionally, the size of domains may be broken down promoting relaxor-like ferroelectric behaviour. In fact, partial melt-phase stretching may be preferred to solid state stretching to ensure the microstructural integrity of the film, preventing the formation of voids and cracks which may enhance losses and lead to early electrical breakdown, while also avoiding entering a completely melted state in which the PVDF is likely to crystallise into the  $\alpha$ -phase.<sup>77</sup> Ren *et al.* found that *decreasing* the pressing temperature during hot-pressing of their PVDF thin films produced smaller crystallites and larger interchain distances due to an increased induced stress compared to the high temperature pressing.<sup>21</sup> Heating to 60 °C under the high applied pressure likely increased the plasticity of the PVDF and hence it may flow as if in a partial melt-phase allowing for the crystal structure to change. Additionally, the rate of cooling of the PVDF film *after* leaving the hot-press can substantially affect its phase composition and crystallinity. In general, a lower quenching temperature (i.e. a

faster rate of cooling) will result in a higher crystallinity, with many studies finding that  $\beta$ -phase formation is also promoted.<sup>148,163–166</sup>

When casting PVDF from solution however, the crystallisation mechanism is quite different. Polarity of the solvent molecules, concentration of the polymer and the rate of evaporation may all substantially affect the crystallisation process.<sup>167–169</sup> In general, a higher evaporation rate will promote less selective crystallisation and result in a low  $\beta$ -phase crystallinity.<sup>157</sup> Although, whilst forming the  $\alpha$ -phase is more kinetically favourable than forming the  $\beta$ -phase,  $\beta$ -PVDF is more entropically (thermodynamically) stable than the  $\alpha$ -phase due to its all-trans conformation. Hence at low crystallisation rates, the  $\beta$ -phase easily forms, whereas higher crystallisation rates suppress its formation, as thermal barriers prevent it from crystallising quickly enough, instead producing a high  $\alpha$ -phase content. Hence a low evaporation rate is generally favourable for solution casting ferroelectric PVDF thin films. Additionally, the formation of the  $\gamma$ -phase is a common result of solution casting, as an  $\alpha$  to  $\gamma$ -phase transformation is commonplace in this crystallisation environment.<sup>161</sup> Overall, the crystalline polymorphism which ultimately arises from solution crystallisation largely depends on the crystallisation rate.

One final method for producing ferroelectric PVDF is that of electrospinning.<sup>158,170–172</sup> While not capable of producing the higher throughput of hot-pressing and solution casting, the high electric fields implicit to the electrospinning process ensure a unique crystal structure in the produced polymer fibre membrane. The process is shown in **Figure 2.6**. First, a highly homogeneous polymer solution is created before being fed into a thin plastic tube by a syringe, which is compressed at a given rate. This tube connects to a hollow metallic needle – the spinneret – which is held above a metallic plate – the collector. A voltage is held between the

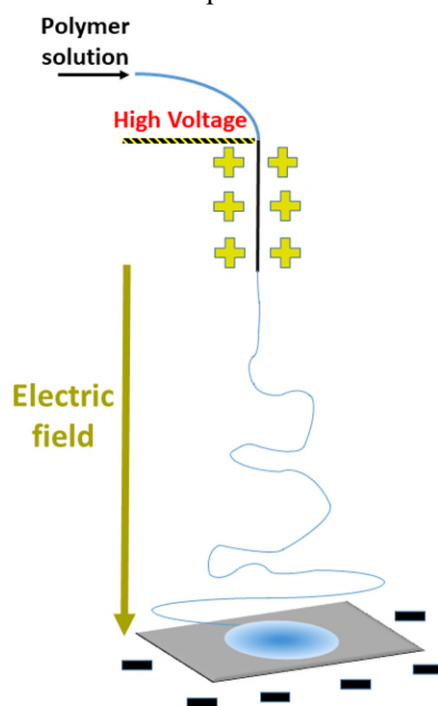


**Figure 0.6.** Schematic of the electrospinning process.

two metallic components, which exerts a force on the slightly polar polymer solution emitting from the spinneret. This results in a force balance between the surface tension of the droplet sitting on the periphery of the metallic spinneret, and the electrical stress exerted on the droplet by the applied voltage. This forms a ‘Taylor cone’, which, in a steady state, rips solution off the droplet at the same rate the droplet is fed solution by the compression of the syringe. This forms an extremely thin jet of polymer solution being pulled towards the metallic collector, which subsequently undergoes substantial ‘whipping’ instabilities due to the various forces exerted on it. Simultaneously, the solution jet dries up, in part due to the extreme electric fields the solution is exposed to. Ultimately this produces a porous, low density thin film of randomly oriented polymer nanofibres on the collector. Due to the extreme electrical forces exerted on the solution jet, the crystallisation that occurs between the spinneret and the collector often results in a degree of molecular orientation, as well as a preference for regular orientation of molecular dipoles in the crystallites as they form.<sup>173</sup> Hence, a high  $\beta$ -phase crystallinity often manifests in PVDF, making electrospun PVDF nanofibre membranes suitable for ferroelectric applications.<sup>174</sup>

## **2.7. Polymer/inorganic nanoparticle composites**

In recent years there has been significant exploration in the field of polymer nanocomposites for pulsed energy storage devices. Due to their competitiveness with polymers with respect to ferroelectric properties, ceramic nanofillers are popular for use in nanocomposites with polymers to create highly polarisable materials. Their high dielectric constant and thus polarisability can lend significant performance enhancements to energy storage in a polymer matrix. To understand the nature of these composites, it is first helpful to consider the properties of all-ceramic ferroelectrics.<sup>24,85,140</sup>

Compared to the complex, disordered, semicrystalline polymorphic structure of polymers, ceramics tend to have an ordered, highly crystalline structure, which leads to a higher electrical conductivity compared to their polymer counterparts. Most notably, this leads to all-ceramic ferroelectrics possessing a substantially reduced electrical breakdown strength. Due to the far higher conductivity in all-ceramic systems, a conducting pathway which initiates a breakdown event is far more likely to form at lower fields.<sup>175–177</sup> Since the permittivity of the nanoparticles incorporated into these ceramic nanoparticle polymer composites are typically far higher than the surrounding matrix, they take on a minimal electric field load.<sup>52</sup> As such, around the site of a nanoparticle, the electric field will be drastically enhanced on a local scale as there is a step local change in permittivity.<sup>28,88,178</sup> This allows the nanoparticles to become effective potential wells.

To effectively marry the properties of polymers and ceramics, it is imperative to avoid the formation of percolative conductive pathways in the composite. At the percolation threshold,

the internal field within nanofillers increases substantially, and whilst this leads to a large increase in the composite's dielectric constant, it significantly reduces the electrical breakdown strength, ultimately leading to a far lower  $U_e$ .<sup>52,179</sup> How to avoid this is a function of the target macroscale structure, and how to attain it with the available processing methodologies. For example, co-extruding – the process of simultaneously melt-extruding two plastic materials into a single structure – is a popular scalable method for producing polymer/nanoparticles nanocomposites with easily tailorable layered macrostructures. In co-extruded polymer/ceramic blend composites, high shearing rates and long shearing periods are necessary to prevent the formation of agglomerates, which could be sites for initiating breakdown as well as dampening the enhancements the ceramics may offer.<sup>180</sup> Tomer *et al.* and others have taken this further by using electrophoresis; the act of applying an electric field during processing to align randomly dispersed ceramic fillers into chainlike structures.<sup>181,182</sup> Solution casting – sometimes followed by hot-pressing – is another popular route to forging well dispersed nanocomposites.<sup>88,183,184</sup> For example, Mao *et al.* used the common approach of a two-step mixing method in which the nanoparticles are first dispersed and ultrasonicated in a solution, which is then added to a separate solution including PVDF and further mixed.<sup>185</sup>

A somewhat unique advantage of employing nanofillers in some composites is the enhanced interfacial polarisation which may arise due to the agglomeration of particles at phase interfaces in the composite.<sup>79,92,186</sup> This interfacial agglomeration of nanofillers is often imposed intentionally during processing due to the potential well effect of nanoparticles. This is helpful for trapping mobile charges which may otherwise contribute to losses and breakdown, leading to an increased accumulation of charge at these interfaces. Hence despite their higher conductivities, inorganic nanofillers can actually suppress the overall carrier mobility in the composite below percolation, as well as producing large interfacial polarisations.<sup>187</sup> The changes in dielectric properties around an interface can also be tailored in detail by altering the intrinsic nanoparticle properties, such as their surface chemistry, size and concentration, or by altering the morphology of the interface itself.<sup>185,188</sup>

Of course, the properties of the nanofiller will also affect the nanocomposite properties in many other ways. Chemical modifications in particular can provide improved adhesion between the nanoparticles and the polymer matrix.<sup>88,189</sup> This can provide significant enhancements to breakdown strength as it eliminates inhomogeneities which would otherwise arise in the matrix due to the incompatibility between the nanofiller and polymer. Similarly, ceramics in polymer systems are also often doped to prevent high leakage currents.<sup>190,191</sup> In any case, their presence will generate an 'interaction zone' around the interface which will have different dielectric properties to both the polymer matrix and any nanoparticle dominant regions.<sup>91</sup>

Non-ceramic nanofillers have also attracted some interest to enhance energy storage properties of polymers.<sup>77,179,192,193</sup> Graphene nanoplatelets for example have been implemented in

ferroelectric composites to enhance their permittivity. Due to their 2D topology, nanoplatelets may exhibit strong interfacial effects with the polymer matrix especially for surface modified graphene.<sup>194</sup> Carbon nanotubes and inorganic nanowires (such as Titanium dioxide,  $\text{TiO}_2$ , and Barium Titanate,  $\text{BaTiO}_3$ ) are also a popular choice of nanofiller due to their high aspect ratio, which produces a higher dielectric permittivity.<sup>79,88,195</sup> This higher permittivity creates a larger disparity between the nanoparticle and surrounding matrix, leading to interfacial effects which make the nanowires effective site for energy storage.<sup>28,110,182</sup> Additionally, due to their 1D morphology, orienting nanowires within the polymer matrix can lead to some impressive enhancements to the dielectric properties.<sup>33,196</sup> All in all, however, the trade-offs when implementing inorganic nanofillers into polymer composites means they do not consistently outperform all-polymer systems, particularly at ultrahigh electric fields. Hence there is still significant interest in all-polymer materials for pulsed energy devices.

## 2.8. All-polymer dielectrics

All-polymer dielectrics containing combinations of different polymers are becoming increasingly popular as the methodologies involving tailoring their nanostructure have developed.<sup>29</sup> Like the case of nanocomposites, the difference in dielectric properties between polymers in an all-polymer structure is the key to developing a material with both enhanced permittivity and breakdown strength. Strong energy storage capabilities rely on the intrinsic electrical properties of polymer chains and the crystalline polymorphism they exhibit, as these are the sources of polarisability in these materials.<sup>62</sup> The most common approaches to processing either utilise chemical modification of polymers to enhance their permittivity and/or processing approaches which produce nanostructures which exhibit ideal ferroelectric behaviour.<sup>36,197,198</sup> In any case, the *compatibility* of the polymers must be heavily considered.<sup>156</sup> Immiscibility between polymers may result in microstructural defects, which may in turn initiate early breakdown. Additionally, differences in melt properties can make it difficult to acquire the desired nanomorphology in all the polymers at once, particularly in the case of hot-pressing approaches. How polymers condense into their polymorphic phases often has a strong dependence on temperature, which could mean certain processing conditions are necessary for one polymer to which may not be suitable for another. Hence emphasis is often placed on the fine details of the processing methodology for producing all-polymer dielectrics.

### 2.8.1. PVDF blends

Various processing methodologies have been employed to try to enhance  $U_e$  in PVDF-based dielectrics via formation of specialised structures.<sup>143</sup> One of the most popular and straightforward ways to process a multi-polymer system is to use a blending process in which

polymers are either heated into the melt phase or combined in solution and mixed to form a randomly structured multi-phase system.<sup>10,39,149,199</sup> This simple approach is favourable for cheap, high throughput production, but bypasses any tailored mesoscale structuring which may offer performance enhancements. Ensuring miscibility of the polymer phases is of paramount importance as there will be a large number of interfaces between the polymers throughout the blend, and so low compatibility will lead to a high likelihood of electrical breakdown.<sup>50,200</sup> If good miscibility between the polymer phases is achieved however, desirable interfacial effects may arise, giving blends an advantage over other macrostructures.

The aforementioned triblock copolymer PVDF-trifluoroethylene-chlorotrifluoroethylene (PVDF-TrFE-CFE) exhibits higher polarisability than the PVDF homopolymer and a relative permittivity of over 50, dwarfing regular PVDF (~10-12).<sup>201</sup> While PVDF-TrFE-CFE exhibits relaxor ferroelectric behaviour, it typically experiences polarisation saturation – in which the material is unable to further polarise – often well before its breakdown field  $E_b$ , limiting its supremacy over regular PVDF.<sup>99</sup> Zhang *et al.* found that their PVDF-TrFE-CFE/PVDF blends achieved a higher maximum polarisability than the neat terpolymer at high fields.<sup>10</sup> The terpolymer side groups effectively act as molecular defects which may break up the ferroelectric domains, producing nanodomains and leading to relaxor ferroelectric behaviour. In these blends both the maximum polarisation  $P_{max}$  and  $E_b$  are enhanced at high fields compared to the neat terpolymer due to interfacial interactions between the polymer phases producing a higher discharged energy density  $U_e$ . Increasing the proportion of PVDF-TrFE-CFE in the blends produced a higher rate of polarisation, with saturation being reached at a lower field, but also produces an increased  $P_{max}$ . Polarisation saturation is suppressed in the blends by interfacial interactions between the polymer phases, so the large total phase interface area in the blend induced by a high degree of mixing leads to a significant increase in  $P_{max}$ . Due to the increase in  $E_b$  with higher PVDF content, the maximum  $U_e$  is lower in neat PVDF-TrFE-CFE than in the 80/20 PVDF-TrFE-CFE/PVDF blends, which exhibit the best performance.

Similarly, Peng *et al.* investigated their PMMA/PVDF-hexafluoropropylene (PVDF-HFP) blend films to discern how the crystallinity varies with processing methodology and how this correlates with energy storage performance.<sup>32</sup> Of course, increasing the proportion of PMMA in the blends resulted in a decreased total crystallinity, and a resultant lower overall dielectric constant due to the lower permittivity of PMMA. A low PMMA content of 5% was found to be the most effective proportion to acquire the largest  $U_e$ , implying the PMMA was contributing mainly to increasing discharge efficiency rather than the polarisability of the blend. The authors postulate that this may be to do with hydrogen bonding between the C=O group in the PMMA with the CH<sub>2</sub> group in the PVDF-HFP, resulting in restricted chain movement. They also note that their PVDF exhibits more  $\gamma$ -phase crystallinity in the blends, postulating that the PMMA may initiate its formation. This increase in  $\gamma$ -phase crystallinity also translated to a lower  $\beta$ -



PVDF content, which, due the lower polarity of the  $\gamma$ -phase, will reduce energy losses and produce a larger  $\eta$ .

R. Li *et al.* fabricated polyamide 11(PA11)/PVDF blend 3 mm films by employment of hot-pressing and subsequent quenching, which exhibit an ultralow dielectric loss along with a high relative permittivity of 40. This is four times higher than typical neat PVDF films, and nearly 8 times higher than neat PA11.<sup>202</sup> The authors attribute this to effects arising at the interface between the polymers, as high phase compatibility between the two polymers may lead to high polarisations at their interfaces. This is evidenced by their addition of the compatibiliser styrene maleic anhydride (SMA), which acts to further enhance crystalline structure at these interfaces, improving the electron mobility along them. SMA addition also acted to decrease the dielectric loss, reducing it by 2/3rds, potentially by confining electrons to these interfacial areas rather than traversing the film with lossy transport mechanisms. This demonstrates how interfacial effects are key to high performance in all-polymer dielectric materials, as the nature and pervasiveness of these interfaces will determine how both charge transport and charge storage mechanisms behave in the structure.<sup>15</sup> If the intention of using contrasting polymers is to enhance the properties of the overall structure by obtaining the advantages of both an insulator and a ferroelectric, interfaces will determine how these properties superpose. Hence, structuring approaches revolving around this principle can be extremely effective.

Blends involving ionic liquids (ILs) – large molecule ionic compounds which are easily dispersed in polymer solutions – are becoming increasingly popular for inducing polar crystalline formations in dielectric polymers.<sup>50,203,204</sup> Upon adding the IL tributyl(tetradecyl)phosphonium dodecylbenzene-sulfonate, Soares *et al.* describe the enhancement in  $\beta$ -PVDF fraction and increased melt viscosity of their polymer blends containing PVDF-HFP and dodecylbenzene sulfonic acid doped polyaniline (PANI:DBSA).<sup>149</sup> The eased processing was found to produce highly dielectric homogenous polymer blends. This was also observed by Meher *et al.* in their PVDF/PANI blends incorporating the room temperature ionic liquid 1-butyl-3-methylimidazolium hexa-fluoro phosphate.<sup>11</sup> The authors in these cases used high ionic liquid loadings as their stated aims are to attain high electrical conductivity in the blends.<sup>205</sup> In the case of PVDF-based dielectrics for pulsed power systems, low conductivity is of course desired to minimise loss. Hence the lowest proportion of ionic liquids possible to induce  $\beta$ -PVDF formation and enhance  $U_e$  are most desirable.<sup>150</sup>

### 2.8.2. Multilayer polymer dielectrics

Multilayer polymer dielectrics contain layers of different polymer thin films, stacked alternately in order to take advantage of the differing properties of the selected polymers. Typically, ferroelectric polymer layers are fabricated in tandem with insulating polymer layers using methods including multilayer thin film co-extrusion and compression moulding, both of which

can ensure the most homogenous and cohesive structure with the fewest defects or voids, warding off the potential for early electrical breakdown.<sup>71,100,159</sup> Like in the blends, high miscibility is paramount for the laminate to obtain a high  $U_e$ . Although, multilayer laminates offer a variety of distinct advantages over blends, and as such are becoming an increasingly popular alternative structuring approach.<sup>20,206,207</sup> For example, the insulating layers in multilayer laminates will take on most of the electric field load, shielding the electroactive layers and hence reducing the field within these layers.<sup>9</sup> This key structural difference that multilayer laminates have over blends – that the interfaces are oriented perpendicular to the applied field – is far more effective for enhancing  $E_b$  compared to the randomly oriented interfaces present in polymer blends. This is because the boundaries between the polymer layers tend to prevent the formation of conductive channels *along the direction of the applied field*, making it difficult for electrical stress to propagate and cause a breakdown event.<sup>8,206</sup> In contrast, in blends, as interfaces are sometimes parallel to the electric field, they provide conducting channels *along* the direction of the field, decreasing  $E_b$ .<sup>15,52</sup>

Additionally, an increased interfacial surface area in the laminate – particularly perpendicular to the applied field – will produce a significantly enhanced interfacial polarisation.<sup>15,71</sup> Mobile charges, which may otherwise propagate through the structure and cause an electron avalanche, are instead trapped at the layer interfaces. As the hottest mobile electrons (which usually penetrate the laminate at the electrodes) move through the structure and liberate other electrons, the ensuing high density of free electrons will diffuse along the field lines and build up at the interfaces as they struggle to pass through them.<sup>74</sup> Hence this both impedes the propagation of electrical trees and leads to agglomeration of space charges at the interfaces. Hot electrons may still possess enough energy to overcome the interfacial energy barrier however, and so employment of multiple interfaces can lead to the highest enhancement to breakdown strength as well as maximising the interfacial polarisation.<sup>1</sup> As this also leads to lower conductive losses as conduction is impeded, multilayer polymer laminates are extremely effective at minimising dielectric loss and hence maximising the discharge efficiency,  $\eta$ .<sup>90</sup> Space charge accumulation at multilayer interfaces will lead to a charge separation geometry like that seen in **Figure 2.7**. Thicker insulating layers will therefore lead to both a greater separation of charge *and* a higher breakdown strength, as the energy required for a charge carrier to overcome the energy barrier provided by the insulating layer increases with layer thickness. Thicker electroactive layers (independent of insulating layer thickness) also allow for a higher accumulation of space charges, as charges are typically more numerous and mobile. In contrast however, incorporating electroactive layers far thinner than their insulating counterparts makes ionic migration across the laminate far more difficult, reducing dielectric losses.<sup>20</sup>

As the source of polarisation, selecting an electroactive layer for a multilayer laminate is the first port of call. Appropriate ferroelectric polymers are few and far between, and at present the majority of research focuses on PVDF and its copolymers.<sup>10,96,102,144,198</sup> Insulating polymers which are melt-phase miscible with PVDF and its copolymers must therefore be selected, which provides an even narrower set of choices. Polycarbonates, polysulfones and polymethacrylates are all common choices which meld well with PVDF and its copolymers. For example, Wolak *et al.* produced layered polycarbonate (PC)/PVDF copolymer {structure  $-(CH_2-CF_2)_{85}-(CFCF_3CF_2)_{15}$ } thin films (overall thickness  $\sim 500\ \mu\text{m}$ ) via co-extrusion, with the number of layers investigated alternating between 2 and 256.<sup>100</sup> The PVDF copolymer possessed a relative permittivity of 10-15, contrasting with PC, which has a value of  $\sim 3$ . Due to the high breakdown strength of PC ( $\sim 6000\ \text{kV/cm}$ ) and the large contrasts in both permittivity and conductivity between PC and the PVDF copolymer, the propagation of electrical trees was impeded substantially. Due to the permittivity contrast between the layers, electrons, holes, and ions accumulated at the interfaces as they struggled to penetrate the insulating PC layers, leading to a large interfacial polarisation. In a later study, the authors found that increasing the number of layers of each polymer (and hence the number of interfaces) while keeping the overall laminate thickness identical led to a decreased electric field in the PVDF copolymer layers, and hence a

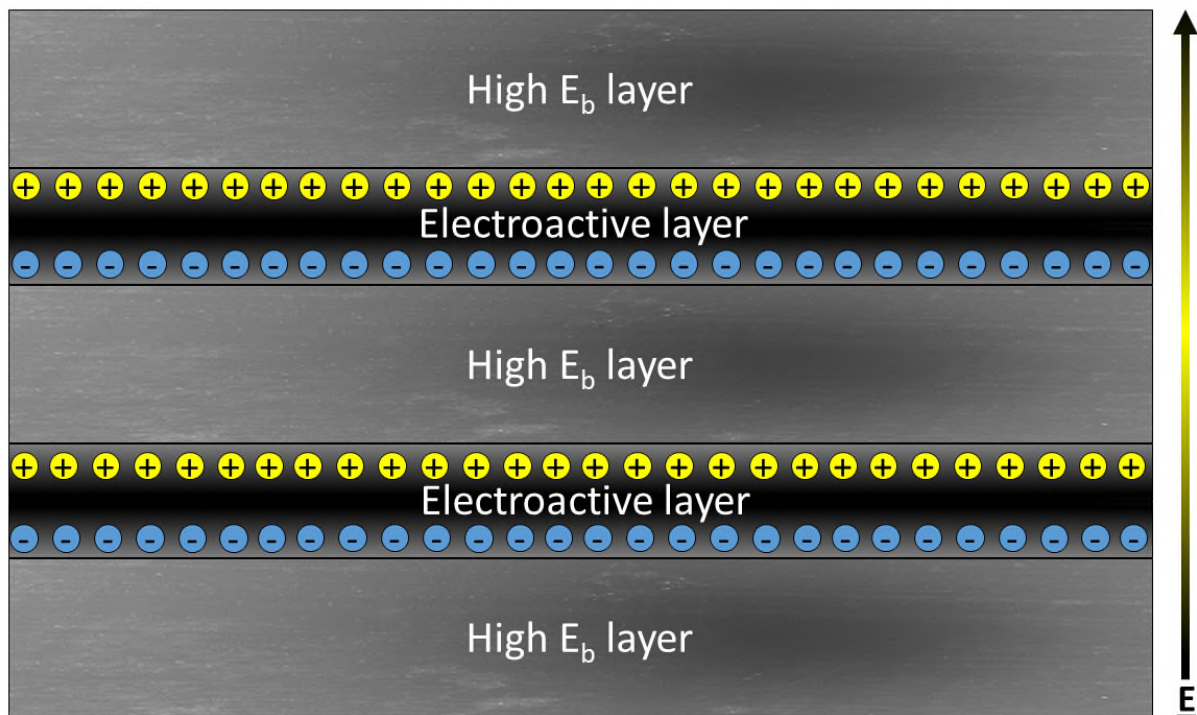


**Figure 0.7.** A schematic of the cross-sectional structure of a multilayer polymer composite, incorporating a polarisable nanofibre layer alongside an insulating, non-porous polymer layer. reduction in ionic conduction. This suppressed the irreversible dipolar switching of crystallites, reducing dielectric loss significantly.<sup>90</sup>

However, it is also possible to incorporate two immiscible polymers by employing so called ‘tie materials’. Yin *et al.* improved interlayer adhesion in their PET/PVDF-HFP multilayer films by incorporating PMMA; a polymer miscible with both polyethylene terephthalate (PET) and PVDF-HFP.<sup>20</sup> They saw an increase in the discharged energy density  $U_e$  of 40% at 5000 kV/cm at the optimal loading of 8 vol% PMMA, reaching a  $U_e$  of almost 8 J/cm<sup>3</sup>. The breakdown strength was also seen to increase by up to 25% at 20 vol% PMMA and observed a 20% increase at the optimal loading of 8 vol% PMMA. The authors further enhanced their laminate performance with use of lateral biaxial stretching. This was seen not only to increase the crystallinity and conformity of crystallite orientation in the PVDF-HFP, but also increased the lateral size to layer thickness aspect ratio. Hence, the interfacial polarisation – and thus  $U_e$  – is enhanced as the overall interfacial area to total film thickness ratio increases.

Zhou *et al.* also constructed PC/PVDF-HFP layered films – in the case without any tie materials – in order to investigate the mechanisms behind and effect of poor interfacial adhesion and associated electrical breakdown in multilayer polymer laminates.<sup>89</sup> In these laminates, electrical stress leads to the formation of a ‘pinhole’ in the structure, indicative of local electron avalanche which superheats the polymer, melting it and forming a void. This avalanche is more easily impeded in multilayer laminate architectures by the barriers between layers, although it will negatively affect the laminate lifetime by making future electrical treeing more likely to proliferate through the layered structure.<sup>52,81,82,208</sup> At fields high enough to induce electrical trees which pervade the entire laminate, breakdown occurs, and the pinhole will penetrate the entire film. The authors observed by SEM that the pinholes generated upon breakdown in the insulating PC layer occurred in regions of delamination, where interfacial adhesion is poor. They go on to speculate that as the breakdown occurred, the vaporised material around the pinhole formed a pressure front which pushed neighbouring layers apart, causing further delamination. Electrical trees then propagate in-plane around the pinhole along the voids between the delaminated films. Furthermore, in laminates with lower layer thickness, the mechanical damage caused by pinhole formation can permeate adjacent layers, making electrical trees more likely to penetrate multiple layers. An intermediate layer thickness of 160 nm was found to be optimal by constraining breakdown to a single layer while also providing many interfaces to impede it.

The phenomenon of interfacial treeing in multilayer dielectric laminates was also studied in depth by Mackey *et al.*, who observed interface treeing effects in their multilayer PC/PVDF-HFP films.<sup>82,90</sup> They observed that their single layer films and blends showed pinholes without electrical treeing at breakdown sites. In contrast, treeing tended to occur either on the surface layer or at interfaces in the first few layers of their multilayer laminates due to the significant resistance interfaces provide. The authors inferred that charge injected from the electrodes spread *along* these layers rather than penetrating many layers, preventing the single pinhole

breakdown effect they observed in their monolayer films. When breakdown does occur in the multilayer laminates, the electric field arcs *through* the layers, forming through-plane pinholes which allow the charge previously constrained in layers due to interfacial treeing to discharge through the layers. Again, a many layered composition with low layer thickness was seen to provide the best enhancement to breakdown strength,  $E_b$ . In a later study, the authors observed a similar effect in their 32 layered, laterally stretched PET/poly(vinylidene fluoride-co-tetrafluoroethylene) (PVDF-TrFE) multilayer films.<sup>159</sup> While their multilayers lacked a tie material between the PET and PVDF-TrFE, biaxial stretching provided a large enhancement in  $E_b$  and thus a large increase in the discharged energy density  $U_e$ , reaching an impressive  $16 \text{ J/cm}^3$  at over  $8000 \text{ kV/cm}$  in their best sample. Varying layer composition of samples revealed that the biaxially stretched films had the largest lateral extent of electrical trees around a breakdown site, which was correlated with a larger  $E_b$ . It was deduced that this was due to an enhanced orientation of the PET layer and in-plane crystallisation of PVDF-TrFE induced by stretching, reducing through-layer treeing and increasing mechanical integrity respectively.

Additionally, the choice of outer layer of the laminate – i.e. the layer contacting the electrode – can strongly influence breakdown and charge storage properties.<sup>83</sup> Lean *et al.* produced a model to simulate field distributions in their PC/PVDF-HFP multilayers to investigate this effect.<sup>9</sup> In their previous works, the authors found empirically that breakdown in these films predominantly occurs on the surface layers. Using this evidence as the basis for the model, they found that when using PC as the outer layer, the electric field load taken on by the PC layer contacting the anode is much higher than the breakdown strength of PC monolayers. They also found that the field in the adjacent PVDF-HFP layer was very low. Conversely, using PVDF-HFP as the surface layer, the breakdown effects were mainly observed deeper into the film. In the former case, the field gradient between the electrode and the low permittivity PC layer is extremely high, putting high electrical stress on the film. This caused heavy charge injection from the anode, which also explains the surface treeing observed on the outer layers of the laminates observed in the studies by Mackey *et al.*<sup>82,90</sup> Similarly, in the case of PVDF-HFP as the outer layer, the interfacial breakdown observed deeper in the laminate is explained by the high field predicted at these interfaces due to interlayer fracturing and the ensuing large internal voids.

Additionally, the use of an insulating layer as the outermost can prevent a significant leakage current, which would otherwise negatively impact charge retention and increase the dielectric loss.<sup>83</sup> The previously discussed 3-component laminate created by Yin *et al.* is particularly effective in this respect, as the interfaces between miscible PMMA and PVDF-HFP layers become difficult boundaries for impurity ions to traverse, *and* act as sites for charge build-up.<sup>20</sup> Their high miscibility also ensures good cohesion, preventing interlayer fracturing and void formation, while the highly insulating PET outer layer will take on a large electric field load and prevent leakage current. Simultaneously the progression between the vastly differing polymer

layers ensures the field gradient between layers is not too large, preventing high electrical stresses at the interfaces. Altogether, this system is very effective at producing a high discharge efficiency, low dielectric losses, and a high electrical breakdown strength. All that remains is to maximise the polarisability of the PVDF layers.

## 2.9. Conclusions

While there are a variety of dielectric polymers which possess a degree of polarisability, the majority of them have various issues ranging from high cost, processing difficulties, low polarisability, and high dielectric loss. For this reason, PVDF and its similar copolymer counterpart PVDF-HFP are selected for investigation in this work due to both their excellent dielectric properties and processability, allowing them to be fabricated with various different methodologies. In particular, the ferroelectric properties of PVDF can be readily tuned by varying processing conditions such as solvents employed, processing temperature and by applying electrical fields. For example, when producing PVDF by electrospinning, a near 100% ferroelectric  $\beta$ -phase can be formed in the nanofibres by optimising the processing conditions.

PVDF's good processability also extends to its good miscibility with polymers such as polycarbonate and polymethyl methacrylate, which are great partners in composites and hybrid polymer systems as their insulating properties can reduce ferroelectric losses and increase its breakdown strength. This has led to the development of a multitude of ferroelectric polymer blends and multilayer laminates, the latter of which have proved particularly successful at withstanding electrical breakdown at ultrahigh electric fields while producing extraordinarily high energy discharged densities and impressive discharge efficiencies. The use of finely tuned distributions of nanoparticles in some of these composites has also seen some success, although often at the expense of the electrical breakdown resistance.

Additionally, the impressive ferroelectric performance of PVDF and its copolymers in a variety of works has spurred significant interest in its crystalline structure. Electrospinning in particular has proven an effective approach to creating high  $\beta$ -phase content PVDF, and the incorporation of ionic liquids into the processing methodology may also act to increase the polar  $\beta$ -phase content. Since ionic liquids offer a straightforward processing route to produce PVDF with a  $\beta$ -phase dominant crystalline microstructure, the first endeavours in this work were to investigate the potential of electrospinning PVDF with an ionic liquid additive.

## 2.10. References

1. Jiang, J. *et al.* Ultrahigh discharge efficiency in multilayered polymer nanocomposites of high energy density. *Energy Storage Mater.* **18**, 213–221 (2019).

2. Karanja, P. & Nath, R. Study of Charge Storage Properties in Biaxially Oriented Polypropylene. *IEEE Trans. Electr. Insul.* **28**, 294–298 (1993).
3. Zheng, F. *et al.* Space charge characterization in biaxially oriented polypropylene films. *IEEE Trans. Dielectr. Electr. Insul.* **23**, 3102–3107 (2016).
4. Picci, G. & Rabuffi, M. Status quo and future prospects for metallized polypropylene energy storage capacitors. *PPPS 2001 - Pulsed Power Plasma Sci. 2001* **1**, 417–420 (2002).
5. Hamza, A. M., Han, J. K., Bu, S. D., Seo, J. M. & Lee, J. K. Relaxation currents from macroscopic depolarization in poly-4-vinylphenol dielectrics. *Synth. Met.* **161**, 698–703 (2011).
6. Chu, B., Zhou, X., Neese, B., Zhang, Q. M. & Bauer, F. Relaxor ferroelectric polymer-poly(vinylidene fluoride-trifluoroethylene- chlorofluoroethylene) terpolymer high electric energy density and field dependent dielectric response. *Ferroelectrics* **331**, 35–42 (2006).
7. Wang, Y. *et al.* Compositional tailoring effect on electric field distribution for significantly enhanced breakdown strength and restrained conductive loss in sandwich-structured ceramic/polymer nanocomposites. *J. Mater. Chem. A* **5**, 4710–4718 (2017).
8. Wang, Y. *et al.* Ultrahigh electric displacement and energy density in gradient layer-structured BaTiO<sub>3</sub>/PVDF nanocomposites with an interfacial barrier effect. *J. Mater. Chem. A* **5**, 10849–10855 (2017).
9. Lean, M., Wolak, M., Mackey, M. & Baer, E. Internal field distributions in multilayer polycarbonate/poly(vinylidene fluoride)-hexafluoropropylene films at onset of breakdown. *IEEE Trans. Dielectr. Electr. Insul.* **21**, 800–808 (2014).
10. Zhang, X. *et al.* Achieving High Energy Density in PVDF-Based Polymer Blends: Suppression of Early Polarization Saturation and Enhancement of Breakdown Strength. *ACS Appl. Mater. Interfaces* **8**, 27236–27242 (2016).
11. Meher, D., Suman, Karna, N. & Sahoo, B. P. Development of Poly (vinylidene fluoride) and Polyaniline blend with high dielectric permittivity, excellent electromagnetic shielding effectiveness and Ultra low optical energy band gap: Effect of ionic liquid and temperature. *Polymer (Guildf)*. **181**, 121759 (2019).
12. Grimnes, S. & Martinsen, Ø. G. Dielectrics. in *Bioimpedance and Bioelectricity Basics* vol. 17 37–75 (Elsevier, 2015).
13. Sencadas, V., Lanceros-Méndez, S., Sabater I Serra, R., Andrio Balado, A. & Gómez Ribelles, J. L. Relaxation dynamics of poly(vinylidene fluoride) studied by dynamical mechanical measurements and dielectric spectroscopy. *Eur. Phys. J. E* **35**, (2012).
14. Xia, W., Lu, J., Tan, S., Liu, J. & Zhang, Z. *Manipulating dielectric properties by modifying molecular structure of polymers. Dielectric Polymer Materials for High-Density Energy Storage* (Elsevier Inc., 2018). doi:10.1016/B978-0-12-813215-9.00004-X.
15. Chen, X. *et al.* Enhanced dielectric properties due to space charge-induced interfacial

- polarization in multilayer polymer films. *J. Mater. Chem. C* **5**, 10417–10426 (2017).
16. Guan, F., Wang, J., Pan, J., Wang, Q. & Zhu, L. Effects of polymorphism and crystallite size on dipole reorientation in poly(vinylidene fluoride) and its random copolymers. *Macromolecules* **43**, 6739–6748 (2010).
  17. Guan, F., Pan, J., Wang, J., Wang, Q. & Zhu, L. Crystal orientation effect on electric energy storage in Poly(vinylidene fluoride-co-hexafluoropropylene) copolymers. *Macromolecules* **43**, 384–392 (2010).
  18. Ranjan, V., Yu, L., Nardelli, M. B. & Bernholc, J. Phase equilibria in high energy density PVDF-based polymers. *Phys. Rev. Lett.* **99**, 1–4 (2007).
  19. Liu, Y. *et al.* Relaxor Ferroelectric Polymers: Insight into High Electrical Energy Storage Properties from a Molecular Perspective. *Small Sci.* **1**, 2000061 (2021).
  20. Yin, K. *et al.* Effects of Interphase Modification and Biaxial Orientation on Dielectric Properties of Poly(ethylene terephthalate)/Poly(vinylidene fluoride-co-hexafluoropropylene) Multilayer Films. *ACS Appl. Mater. Interfaces* **8**, 13555–13566 (2016).
  21. Ren, X. *et al.* Giant energy storage density in PVDF with internal stress engineered polar nanostructures. *Nano Energy* **72**, 104662 (2020).
  22. Zhu, L. & Wang, Q. Novel Ferroelectric Polymers for High Energy Density and Low Loss Dielectrics. *Macromolecules* **45**, 2937–2954 (2012).
  23. Black, C. T., Farrell, C. & Licata, T. J. Suppression of ferroelectric polarization by an adjustable depolarization field. *Appl. Phys. Lett.* **71**, 2041–2043 (1997).
  24. Peng, B. *et al.* Large Energy Storage Density and High Thermal Stability in a Highly Textured (111)-Oriented Pb<sub>0.8</sub>Ba<sub>0.2</sub>ZrO<sub>3</sub> Relaxor Thin Film with the Coexistence of Antiferroelectric and Ferroelectric Phases. *ACS Appl. Mater. Interfaces* **7**, 13512–13517 (2015).
  25. Yang, L. *et al.* Perovskite lead-free dielectrics for energy storage applications. *Prog. Mater. Sci.* **102**, 72–108 (2019).
  26. Bonardd, S. *et al.* Dipolar glass polymers containing polarizable groups as dielectric materials for energy storage applications. A minireview. *Polymers (Basel)*. **11**, 1–10 (2019).
  27. Zhu, L. Exploring strategies for high dielectric constant and low loss polymer dielectrics. *J. Phys. Chem. Lett.* **5**, 3677–3687 (2014).
  28. Dang, Z. M., Yuan, J. K., Yao, S. H. & Liao, R. J. Flexible nanodielectric materials with high permittivity for power energy storage. *Adv. Mater.* **25**, 6334–6365 (2013).
  29. Fan, B., Zhou, M., Zhang, C., He, D. & Bai, J. Polymer-based materials for achieving high energy density film capacitors. *Prog. Polym. Sci.* **97**, 101143 (2019).
  30. Yang, L. *et al.* Relaxor ferroelectric behavior from strong physical pinning in a poly(vinylidene fluoride-co-trifluoroethylene-co-chlorotrifluoroethylene) random terpolymer. *Macromolecules* **47**, 8119–8125 (2014).
  31. Chen, J. *et al.* Multilayered ferroelectric polymer films incorporating low-dielectric-constant



- components for concurrent enhancement of energy density and charge–discharge efficiency. *Nano Energy* **54**, 288–296 (2018).
32. Peng, G. *et al.* New crystal structure and discharge efficiency of poly(vinylidene fluoride-hexafluoropropylene)/poly(methyl methacrylate) blend films. *RSC Adv.* **4**, 16849–16854 (2014).
  33. Fillery, S. P. *et al.* Nanolaminates: Increasing dielectric breakdown strength of composites. *ACS Appl. Mater. Interfaces* **4**, 1388–1396 (2012).
  34. Diaham, S. *et al.* Dielectric breakdown of polyimide films: Area, thickness and temperature dependence. *IEEE Trans. Dielectr. Electr. Insul.* **17**, 18–27 (2010).
  35. Gao, L. Y., Tu, D. M., Zhou, S. C. & Zhang, Z. L. The Influence of Morphology on the Electrical Breakdown Strength of Polypropylene Film. *IEEE Trans. Electr. Insul.* **25**, 535–540 (1990).
  36. Ren, X., Meng, N., Yan, H., Bilotti, E. & Reece, M. J. Remarkably enhanced polarisability and breakdown strength in PVDF-based interactive polymer blends for advanced energy storage applications. *Polymer (Guildf)*. **168**, 246–254 (2019).
  37. Kasap, S. O. Principles of Electronic Materials and Devices. 240 p. (2004).
  38. Teixeira, S. S., Dias, C. J., Dionisio, M. & Costa, L. C. New method to analyze dielectric relaxation processes: A study on polymethacrylate series. *Polym. Int.* **62**, 1744–1749 (2013).
  39. Zhao, X. *et al.* Exploring the relationship of dielectric relaxation behavior and discharge efficiency of P(VDF-HFP)/PMMA blends by dielectric spectroscopy. *Mater. Res. Express* **3**, (2016).
  40. Schönhal, A. & Kremer, F. *Broadband Dielectric Spectroscopy. Broadband Dielectric Spectroscopy* (Springer Berlin Heidelberg, 2003). doi:10.1007/978-3-642-56120-7.
  41. Mishra, S. *et al.* Effect of multi-step processing on the structural, morphological and dielectric behaviour of PVDF films. *Ionics (Kiel)*. **26**, 6069–6081 (2020).
  42. Pan, H., Kursumovic, A., Lin, Y. H., Nan, C. W. & MacManus-Driscoll, J. L. Dielectric films for high performance capacitive energy storage: Multiscale engineering. *Nanoscale* **12**, 19582–19591 (2020).
  43. Wan, C. & Bowen, C. R. Multiscale-structuring of polyvinylidene fluoride for energy harvesting: the impact of molecular-, micro- and macro-structure. *J. Mater. Chem. A* **5**, 3091–3128 (2017).
  44. Wang, J., Adami, D., Lu, B., Liu, C. & Maazouz, A. Multiscale Structural Evolution and Its Relationship. *Polymers (Basel)*. **12**, (2020).
  45. Jiang, J. *et al.* Synergy of micro-/mesoscopic interfaces in multilayered polymer nanocomposites induces ultrahigh energy density for capacitive energy storage. *Nano Energy* **62**, 220–229 (2019).
  46. Jonscher, A. K. review article The 'universal' dielectric response. *Nature* **267**, 673–679

- (1977).
47. Lunkenheimer, P. *et al.* Origin of apparent colossal dielectric constants. *Phys. Rev. B - Condens. Matter Mater. Phys.* **66**, 521051–521054 (2002).
  48. Donth, E. The size of cooperatively rearranging regions at the glass transition. *J. Non. Cryst. Solids* **53**, 325–330 (1982).
  49. Serghei, A., Tress, M., Sangoro, J. R. & Kremer, F. Electrode polarization and charge transport at solid interfaces. *Phys. Rev. B - Condens. Matter Mater. Phys.* **80**, 1–5 (2009).
  50. Correia, D. M. *et al.* Ionic and conformational mobility in poly(vinylidene fluoride)/ionic liquid blends: Dielectric and electrical conductivity behavior. *Polymer (Guildf)*. **143**, 164–172 (2018).
  51. Marwat, M. A. *et al.* Sandwich structure-assisted significantly improved discharge energy density in linear polymer nanocomposites with high thermal stability. *Colloids Surfaces A Physicochem. Eng. Asp.* **581**, 123802 (2019).
  52. Huan, T. D. *et al.* Advanced polymeric dielectrics for high energy density applications. *Prog. Mater. Sci.* **83**, 236–269 (2016).
  53. Wei, J. & Zhu, L. Intrinsic polymer dielectrics for high energy density and low loss electric energy storage. *Prog. Polym. Sci.* **106**, 101254 (2020).
  54. Barber, P. *et al.* *Polymer composite and nanocomposite dielectric materials for pulse power energy storage. Materials* vol. 2 (2009).
  55. Ritamaki, M., Rytoluoto, I. & Lahti, K. Performance metrics for a modern BOPP capacitor film. *IEEE Trans. Dielectr. Electr. Insul.* **26**, 1229–1237 (2019).
  56. Baer, E. & Zhu, L. 50th Anniversary Perspective: Dielectric Phenomena in Polymers and Multilayered Dielectric Films. *Macromolecules* **50**, 2239–2256 (2017).
  57. Sun, W., Mao, J., Wang, S., Zhang, L. & Cheng, Y. Review of recent advances of polymer based dielectrics for high-energy storage in electronic power devices from the perspective of target applications. *Front. Chem. Sci. Eng.* **15**, 18–34 (2020).
  58. Wang, Y., Zhou, X., Lin, M. & Zhang, Q. M. High-energy density in aromatic polyurea thin films. *Appl. Phys. Lett.* **94**, 20–23 (2009).
  59. Martins, P., Lopes, A. C. & Lanceros-Mendez, S. Electroactive phases of poly(vinylidene fluoride): Determination, processing and applications. *Prog. Polym. Sci.* **39**, 683–706 (2014).
  60. Setter, N. *et al.* Ferroelectric thin films: Review of materials, properties, and applications. *J. Appl. Phys.* **100**, 0–46 (2006).
  61. Meng, N. *et al.* Ultrahigh  $\beta$ -phase content poly(vinylidene fluoride) with relaxor-like ferroelectricity for high energy density capacitors. *Nat. Commun.* **10**, 1–9 (2019).
  62. Gomes, J., Nunes, J. S., Sencadas, V. & Lanceros-Mendez, S. Influence of the  $\beta$ -phase content and degree of crystallinity on the piezo- and ferroelectric properties of poly(vinylidene fluoride). *Smart Mater. Struct.* **19**, (2010).

63. Li, Y., Xu, C. Y., Zhang, B. Y. & Zhen, L. Work function modulation of bilayer MoS<sub>2</sub> nanoflake by backgate electric field effect. *Appl. Phys. Lett.* **103**, (2013).
64. Guo, H. *et al.* In-situ synchrotron SAXS and WAXS investigations on deformation and  $\alpha$ - $\beta$  transformation of uniaxial stretched poly(vinylidene fluoride). *CrystEngComm* **15**, 1597 (2013).
65. Castagnet, S., Girault, S., Gacougnolle, J. L. & Dang, P. Cavitation in strained polyvinylidene fluoride: Mechanical and X-ray experimental studies. *Polymer (Guildf)*. **41**, 7523–7530 (2000).
66. Gebrekstos, A., Prasanna Kar, G., Madras, G., Misra, A. & Bose, S. Does the nature of chemically grafted polymer onto PVDF decide the extent of electroactive  $\beta$ -polymorph? *Polymer (Guildf)*. **181**, 121764 (2019).
67. Ran, S., Wang, Z., Burger, C., Chu, B. & Hsiao, B. S. Mesophase as the precursor for strain-induced crystallization in amorphous poly(ethylene terephthalate) film. *Macromolecules* **35**, 10102–10107 (2002).
68. Zuo, F. *et al.* The role of interlamellar chain entanglement in deformation-induced structure changes during uniaxial stretching of isotactic polypropylene. *Polymer (Guildf)*. **48**, 6867–6880 (2007).
69. Brunengo, E. *et al.* Double-step moulding: An effective method to induce the formation of  $\beta$ -phase in PVDF. *Polymer (Guildf)*. **193**, (2020).
70. Xia, W. & Zhang, Z. PVDF-based dielectric polymers and their applications in electronic materials. *IET Nanodielectrics* **1**, 17–31 (2018).
71. Tseng, J. K. *et al.* Interfacial polarization and layer thickness effect on electrical insulation in multilayered polysulfone/poly(vinylidene fluoride) films. *Polymer (Guildf)*. **55**, 8–14 (2014).
72. Wang, Y. *et al.* Multilayered hierarchical polymer composites for high energydensity capacitors. *J. Mater. Chem. A* **7**, 2965–2980 (2019).
73. Zhang, K., Qiu, J. & Wang, S. Thermoelectric properties of PEDOT nanowire/PEDOT hybrids. *Nanoscale* **8**, 8033–8041 (2016).
74. Wang, Y., Hou, Y. & Deng, Y. Effects of interfaces between adjacent layers on breakdown strength and energy density in sandwich-structured polymer composites. *Compos. Sci. Technol.* **145**, 71–77 (2017).
75. Samet, M. *et al.* Electrode polarization vs. Maxwell-Wagner-Sillars interfacial polarization in dielectric spectra of materials: Characteristic frequencies and scaling laws. *J. Chem. Phys.* **142**, (2015).
76. Sillars, R. W. The properties of a dielectric containing semiconducting particles of various shapes. *Inst. Electr. Eng. - Proc. Wirel. Sect. Inst.* **12**, 139–155 (1937).
77. Prateek, Thakur, V. K. & Gupta, R. K. Recent Progress on Ferroelectric Polymer-Based Nanocomposites for High Energy Density Capacitors: Synthesis, Dielectric Properties, and

- Future Aspects. *Chem. Rev.* **116**, 4260–4317 (2016).
78. Liu, S., Xue, S., Shen, B. & Zhai, J. Reduced energy loss in poly(vinylidene fluoride) nanocomposites by filling with a small loading of core-shell structured BaTiO<sub>3</sub>/SiO<sub>2</sub> nanofibers. *Appl. Phys. Lett.* **107**, (2015).
  79. Zhang, X. *et al.* Ultrahigh energy density of polymer nanocomposites containing BaTiO<sub>3</sub>@TiO<sub>2</sub> nanofibers by atomic-scale interface engineering. *Adv. Mater.* **27**, 819–824 (2015).
  80. Wu, C. M. & Chou, M. H. Polymorphism, piezoelectricity and sound absorption of electrospun PVDF membranes with and without carbon nanotubes. *Compos. Sci. Technol.* **127**, 127–133 (2016).
  81. Zhang, H. *et al.* A review on the development of lead-free ferroelectric energy-storage ceramics and multilayer capacitors. *J. Mater. Chem. C* **8**, 16648–16667 (2020).
  82. MacKey, M. *et al.* Enhanced breakdown strength of multilayered films fabricated by forced assembly microlayer coextrusion. *J. Phys. D: Appl. Phys.* **42**, (2009).
  83. Liu, L., Qu, J., Gu, A. & Wang, B. Percolative polymer composites for dielectric capacitors: a brief history, materials, and multilayer interface design. *J. Mater. Chem. A* **8**, 18515–18537 (2020).
  84. Zhang, X. *et al.* Polymer Nanocomposites with Ultrahigh Energy Density and High Discharge Efficiency by Modulating their Nanostructures in Three Dimensions. *Adv. Mater.* **30**, 1–10 (2018).
  85. Palneedi, H., Peddigari, M., Hwang, G. T., Jeong, D. Y. & Ryu, J. High-Performance Dielectric Ceramic Films for Energy Storage Capacitors: Progress and Outlook. *Adv. Funct. Mater.* **28**, 1–33 (2018).
  86. Laihonon, S. J., Gustafsson, A., Gäfvert, U., Schütte, T. & Gedde, U. W. Area dependence of breakdown strength of polymer films: Automatic measurement method. *IEEE Trans. Dielectr. Electr. Insul.* **14**, 263–274 (2007).
  87. Wu, K., Wang, Y., Cheng, Y., Dissado, L. A. & Liu, X. Statistical behavior of electrical breakdown in insulating polymers. *J. Appl. Phys.* **107**, (2010).
  88. Han, K. *et al.* A Hybrid Material Approach Toward Solution-Processable Dielectrics Exhibiting Enhanced Breakdown Strength and High Energy Density. *Adv. Funct. Mater.* **25**, 3505–3513 (2015).
  89. Zhou, Z. *et al.* Fracture phenomena in micro- and nano-layered polycarbonate/poly(vinylidene fluoride-co-hexafluoropropylene) films under electric field for high energy density capacitors. *J. Appl. Polym. Sci.* **131**, n/a-n/a (2014).
  90. Mackey, M. *et al.* Reduction of dielectric hysteresis in multilayered films via nanoconfinement. *Macromolecules* **45**, 1954–1962 (2012).
  91. Pourrahimi, A. M., Olsson, R. T. & Hedenqvist, M. S. The Role of Interfaces in

- Polyethylene/Metal-Oxide Nanocomposites for Ultrahigh-Voltage Insulating Materials. *Adv. Mater.* **30**, 1–25 (2018).
92. Zhou, L. & Jiang, Y. Recent progress in dielectric nanocomposites. *Mater. Sci. Technol. (United Kingdom)* **36**, 1–16 (2020).
  93. Kumlar, W. & Fohlen, G. M. The Dipole. 1944–1948 (1944).
  94. Chen, Q., Shen, Y., Zhang, S. & Zhang, Q. M. Polymer-Based Dielectrics with High Energy Storage Density. *Annu. Rev. Mater. Res.* **45**, 433–458 (2015).
  95. Ho, J. S. & Greenbaum, S. G. Polymer Capacitor Dielectrics for High Temperature Applications. *ACS Appl. Mater. Interfaces* **10**, 29189–29218 (2018).
  96. Wu, S. *et al.* Aromatic polythiourea dielectrics with ultrahigh breakdown field strength, low dielectric loss, and high electric energy density. *Adv. Mater.* **25**, 1734–1738 (2013).
  97. Ho, J. & Jow, R. Characterization of High Temperature Polymer Thin Films for Power Conditioning Capacitors. *U.S. Army Res. Lab. Res. report, Adelphi, MD, ARL-TR-4880* 1–28 (2009).
  98. Wang, J. *et al.* Enhanced energy density and thermostability in polyimide nanocomposites containing core-shell structured BaTiO<sub>3</sub>@SiO<sub>2</sub> nanofibers. *Appl. Surf. Sci.* **426**, 437–445 (2017).
  99. Zhou, X., Chu, B., Neese, B., Lin, M. & Zhang, Q. M. Electrical energy density and discharge characteristics of a poly(vinylidene fluoride-chlorotrifluoroethylene) copolymer. *IEEE Trans. Dielectr. Electr. Insul.* **14**, 1133–1138 (2007).
  100. Wolak, M. A. *et al.* Dielectric response of structured multilayered polymer films fabricated by forced assembly. *Appl. Phys. Lett.* **92**, 1–4 (2008).
  101. Zhou, X. *et al.* Electrical breakdown and ultrahigh electrical energy density in poly(vinylidene fluoride-hexafluoropropylene) copolymer. *Appl. Phys. Lett.* **94**, 5–8 (2009).
  102. Zhang, Z. & Chung, T. C. M. Study of VDF/TrFE/CTFE terpolymers for high pulsed capacitor with high energy density and low energy loss. *Macromolecules* **40**, 783–785 (2007).
  103. Lu, J., Zhu, B., Zhang, X. & Wang, X. Dielectric Strength Structure-Activity Relationship of BOPP Film for High Energy Density Pulse Capacitor. *IEEE Trans. Plasma Sci.* **47**, 4342–4349 (2019).
  104. Ho, J. & Jow, T. R. High field conduction in biaxially oriented polypropylene at elevated temperature. *IEEE Trans. Dielectr. Electr. Insul.* **19**, 990–995 (2012).
  105. Teyssedre, G. & Laurent, C. Charge transport modeling in insulating polymers: From molecular to macroscopic scale. *IEEE Trans. Dielectr. Electr. Insul.* **12**, 857–874 (2005).
  106. Umran, H. M., Wang, F. & He, Y. Ageing: Causes and Effects on the Reliability of Polypropylene Film Used for HVDC Capacitor. *IEEE Access* **8**, 40413–40430 (2020).
  107. Han, C. *et al.* Enhanced dielectric properties of sandwich-structured biaxially oriented polypropylene by grafting hyper-branched aromatic polyamide as surface layers. *J. Appl.*

- Polym. Sci.* **137**, 1–12 (2020).
108. Qiao, Y., Yin, X., Zhu, T., Li, H. & Tang, C. Dielectric polymers with novel chemistry, compositions and architectures. *Prog. Polym. Sci.* **80**, 153–162 (2018).
  109. Mei, B. Z., Scheinbeim, J. I. & Newman, B. A. The Ferroelectric Behavior of Odd-Numbered Nylons. *Ferroelectrics* **144**, 51–60 (1993).
  110. Jing, Q. & Kar-Narayan, S. Nanostructured polymer-based piezoelectric and triboelectric materials and devices for energy harvesting applications. *J. Phys. D. Appl. Phys.* **51**, (2018).
  111. Wang, W. & Fan, H. Structures and piezoelectric properties of substituted  $\beta$  PVDF-based polymers studied by density functional theory. *Ferroelectrics* **409**, 41–44 (2010).
  112. Wang, Z. Y., Su, K. H., Fan, H. Q. & Wen, Z. Y. Possible reasons that piezoelectricity has not been found in bulk polymer of polyvinylidene cyanide. *Polymer (Guildf)*. **49**, 2542–2547 (2008).
  113. Poulsen, M. *et al.* Investigation of ferroelectricity in poly(methyl vinylidene cyanide). *Ferroelectr. Lett. Sect.* **32**, 91–97 (2005).
  114. Raihane, M., Zerroukhi, A., Kaddami, H., Lahcini, M. & Boiteux, G. Dielectric properties of copolymers based on cyano monomers and methyl  $\alpha$ -acetoxyacrylate. *Polym. Int.* **62**, 684–692 (2013).
  115. Tasaka, S., Inagaki, N., Okutani, T. & Miyata, S. Structure and properties of amorphous piezoelectric vinylidene cyanide copolymers. *Polymer (Guildf)*. **30**, 1639–1642 (1989).
  116. Poulsen, M. & Ducharme, S. Why ferroelectric polyvinylidene fluoride is special. *IEEE Trans. Dielectr. Electr. Insul.* **17**, 1028–1035 (2010).
  117. Lindenmeyer, P. H. & Hosemann, R. Application of the theory of paracrystals to the crystal structure analysis of polyacrylonitrile. *J. Appl. Phys.* **34**, 42–45 (1963).
  118. Liu, X. D. & Ruland, W. X-ray Studies on the Structure of Polyacrylonitrile Fibers. *Macromolecules* **26**, 3030–3036 (1993).
  119. Wang, W. *et al.* Unexpectedly high piezoelectricity of electrospun polyacrylonitrile nanofiber membranes. *Nano Energy* **56**, 588–594 (2019).
  120. Cetiner, S. *et al.* Polypyrrole/polyacrylonitrile composite films: Dielectric, spectrophotometric and morphologic characterization. *Fibers Polym.* **11**, 843–850 (2010).
  121. Liao, X. *et al.* Polyacrylonitrile-derived polyconjugated ladder structures for high performance all-organic dielectric materials. *Chem. Commun.* **51**, 10127–10130 (2015).
  122. Su, R. *et al.* Polarity-induced ferroelectric crystalline phase in electrospun fibers of poly(vinylidene fluoride)/polyacrylonitrile blends. *J. Mater. Res.* **27**, 1389–1398 (2012).
  123. Ueda, H. & Carr, S. H. Piezoelectricity in polyacrylonitrile. *Polym. J.* **16**, 661–667 (1984).
  124. von Berlepsch, H., Künstler, W., Wedel, A., Danz, R. & Geiß, D. Piezoelectric Activity in a Copolymer of Acrylonitrile and Methylacrylate. *IEEE Trans. Electr. Insul.* **24**, 357–362 (1989).

125. Tasaka, S., Nakamura, T. & Inagaki, N. Ferroelectric Behavior in Copolymers of Acrylonitrile and Allylcyanoide. *Jpn. J. Appl. Phys.* **31**, 2492–2494 (1992).
126. Ebnesajjad, S. *Introduction to Fluoropolymers. Applied Plastics Engineering Handbook* (Elsevier, 2011). doi:10.1016/B978-1-4377-3514-7.10004-2.
127. Lin, Y. Non-Isothermal Crystallization Behavior of Poly(vinylidene fluoride) in Dialkyl Phthalate Diluents during Thermally Induced Phase Separation Process. **11** (2020).
128. Lando, J. B., Olf, H. G. & Peterlin, A. Nuclear magnetic resonance and x-ray determination of the structure of poly(vinylidene fluoride). *J. Polym. Sci. Part A-1 Polym. Chem.* **4**, 941–951 (1966).
129. Furukawa, T. Ferroelectric properties of vinylidene fluoride copolymers. *Phase Transitions* **18**, 143–211 (1989).
130. Wang, Z. Y., Fan, H. Q., Su, K. H. & Wen, Z. Y. Structure and piezoelectric properties of poly(vinylidene fluoride) studied by density functional theory. *Polymer (Guildf)*. **47**, 7988–7996 (2006).
131. Burcsu, E., Ravichandran, G. & Bhattacharya, K. Large electrostrictive actuation of barium titanate single crystals. *J. Mech. Phys. Solids* **52**, 823–846 (2004).
132. Gianetti, E. Semi-crystalline fluorinated polymers. *Polym. Int.* **50**, 10–26 (2001).
133. Lovinger, A. J. Annealing of Poly(vinylidene fluoride) and Formation of a Fifth Phase. *Macromolecules* **15**, 40–44 (1982).
134. Pelizza, F. & Johnston, K. A density functional theory study of poly(vinylidene difluoride) crystalline phases. *Polymer (Guildf)*. **179**, 1–16 (2019).
135. Green, J. S., Farmer, B. L. & Rabolt, J. F. Effect of thermal and solution history on the Curie point of VF 2-TrFE random copolymers. *J. Appl. Phys.* **60**, 2690–2693 (1986).
136. Teyssedre, G., Bernes, A. & Lacabanne, C. Cooperative movements associated with the Curie transition in P(VDF-TrFE) copolymers. *J. Polym. Sci. Part B Polym. Phys.* **33**, 879–890 (1995).
137. Martín, J. *et al.* Solid-state-processing of  $\delta$ -PVDF. *Mater. Horizons* **4**, 408–414 (2017).
138. Li, M. *et al.* Revisiting the  $\delta$ -phase of poly(vinylidene fluoride) for solution-processed ferroelectric thin films. *Nat. Mater.* **12**, 433–438 (2013).
139. Li, Y. *et al.* Understanding Nonlinear Dielectric Properties in a Biaxially Oriented Poly(vinylidene fluoride) Film at Both Low and High Electric Fields. *ACS Appl. Mater. Interfaces* **8**, 455–465 (2016).
140. Zhang, Y. *et al.* Enhanced electric polarization and breakdown strength in the all-organic sandwich-structured poly(vinylidene fluoride)-based dielectric film for high energy density capacitor. *APL Mater.* **5**, (2017).
141. Dvey-Aharon, H., Sluckin, T. J., Taylor, P. L. & Hopfinger, A. J. Kink propagation as a model for poling in poly(vinylidene fluoride). *Phys. Rev. B* **21**, 3700–3707 (1980).

142. Ribeiro, C. *et al.* Electroactive poly(vinylidene fluoride)-based structures for advanced applications. *Nat. Protoc.* **13**, 681–704 (2018).
143. Qi, L., Petersson, L. & Liu, T. Review of Recent Activities on Dielectric Films for Capacitor Applications. *J. Int. Counc. Electr. Eng.* **4**, 1–6 (2014).
144. Zhu, Y., Jiang, P. & Huang, X. Poly(vinylidene fluoride)terpolymer and poly(methyl methacrylate)composite films with superior energy storage performance for electrostatic capacitor application. *Compos. Sci. Technol.* **179**, 115–124 (2019).
145. Yang, L. *et al.* Novel polymer ferroelectric behavior via crystal isomorphism and the nanoconfinement effect. *Polymer (Guildf)*. **54**, 1709–1728 (2013).
146. Maeda, K., Tasaka, S. & Inagaki, N. Ferroelectric Behavior of Vinylidene fluoride-Trifluoroethylene-Hexafluoropropylene Terpolymers. *Jpn. J. Appl. Phys.* **30**, 716–719 (1991).
147. Aldas, M., Boiteux, G., Seytre, G. & Ghallabi, Z. Dielectric behaviour of BaTiO<sub>3</sub> / P (VDF-HFP) composite thin films prepared by solvent evaporation method. *Proc. 2010 IEEE Int. Conf. Solid Dielectr. ICSD 2010* (2010) doi:10.1109/ICSD.2010.5568042.
148. Divya, S. & Hemalatha, J. Study on the enhancement of ferroelectric  $\beta$  phase in P(VDF-HFP) films under heating and poling conditions. *Eur. Polym. J.* **88**, 136–147 (2017).
149. Soares, B. G. *et al.* Poly(vinylidene fluoride-co-hexafluoropropylene)/polyaniline blends assisted by phosphonium - Based ionic liquid: Dielectric properties and  $\beta$ -phase formation. *Eur. Polym. J.* **73**, 65–74 (2015).
150. Xing, C., Guan, J., Li, Y. & Li, J. Effect of a room-temperature ionic liquid on the structure and properties of electrospun poly(vinylidene fluoride) nanofibers. *ACS Appl. Mater. Interfaces* **6**, 4447–4457 (2014).
151. Li, Y. *et al.* Polymorphic Extended-Chain and Folded-Chain Crystals in Poly(vinylidene fluoride) Achieved by Combination of High Pressure and Ion-Dipole Interaction. *Macromolecules* **48**, 8565–8573 (2015).
152. He, L. *et al.* Facile and effective promotion of  $\beta$  crystalline phase in poly(vinylidene fluoride) via the incorporation of imidazolium ionic liquids. *Polym. Int.* **62**, 638–646 (2013).
153. Ruan, L. *et al.* Properties and applications of the  $\beta$  phase poly(vinylidene fluoride). *Polymers (Basel)*. **10**, 1–27 (2018).
154. Kim, W. J., Han, M. H., Shin, Y. H., Kim, H. & Lee, E. K. First-Principles Study of the  $\alpha$ - $\beta$  Phase Transition of Ferroelectric Poly(vinylidene difluoride): Observation of Multiple Transition Pathways. *J. Phys. Chem. B* **120**, 3240–3249 (2016).
155. Cui, Z., Hassankiadeh, N. T., Zhuang, Y., Drioli, E. & Lee, Y. M. Crystalline polymorphism in poly(vinylidene fluoride) membranes. *Prog. Polym. Sci.* **51**, 94–126 (2015).
156. Li, M. *et al.* Ferroelectric phase diagram of PVDF:PMMA. *Macromolecules* **45**, 7477–7485 (2012).
157. Gregorio, R. & Borges, D. S. Effect of crystallization rate on the formation of the polymorphs



- of solution cast poly(vinylidene fluoride). *Polymer (Guildf)*. **49**, 4009–4016 (2008).
158. Zhong, G. *et al.* Understanding polymorphism formation in electrospun fibers of immiscible Poly(vinylidene fluoride) blends. *Polymer (Guildf)*. **52**, 2228–2237 (2011).
  159. Carr, J. M. *et al.* Effect of biaxial orientation on dielectric and breakdown properties of poly(ethylene terephthalate)/poly(vinylidene fluoride-co-tetrafluoroethylene) multilayer films. *J. Polym. Sci. Part B Polym. Phys.* **51**, 882–896 (2013).
  160. Jurczuk, K., Galeski, A., Mackey, M., Hiltner, A. & Baer, E. Orientation of PVDF  $\alpha$  and  $\gamma$  crystals in nanolayered films. *Colloid Polym. Sci.* **293**, 1289–1297 (2015).
  161. Gregorio, R. Determination of the  $\alpha$ ,  $\beta$ , and  $\gamma$  crystalline phases of poly(vinylidene fluoride) films prepared at different conditions. *J. Appl. Polym. Sci.* **100**, 3272–3279 (2006).
  162. Hartono, A. *et al.* Effect of Mechanical Treatment Temperature on Electrical Properties and Crystallite Size of PVDF Film. *Adv. Mater. Phys. Chem.* **03**, 71–76 (2013).
  163. Shi, F., Ma, J., Wang, P. & Ma, Y. Effect of quenching temperatures on the morphological and crystalline properties of PVDF and PVDF-TiO<sub>2</sub> hybrid membranes. *J. Taiwan Inst. Chem. Eng.* **43**, 980–988 (2012).
  164. Song, D., Yang, D. & Feng, Z. Formation of  $\beta$ -phase microcrystals from the melt of PVF<sub>2</sub>-PMMA blends induced by quenching. *J. Mater. Sci.* **25**, 57–64 (1990).
  165. Yang, D. & Chen, Y. B-Phase Formation of Poly(Vinylidene Fluoride) From the Melt Induced By Quenching. *J. Mater. Sci. Lett.* **6**, 599–603 (1987).
  166. He, X., Yao, K. & Gan, B. K. Phase transition and properties of a ferroelectric poly(vinylidene fluoride-hexafluoropropylene) copolymer. *J. Appl. Phys.* **97**, 084101 (2005).
  167. Chinaglia, D. L. *et al.* Influence of the solvent evaporation rate on the crystalline phases of solution-cast poly(vinylidene fluoride) films. *J. Appl. Polym. Sci.* **116**, 785–791 (2010).
  168. Gradys, A. & Sajkiewicz, P. Determination of the melting enthalpy of  $\beta$  phase of poly(vinylidene fluoride). *E-Polymers* (2013) doi:10.1515/epoly-2013-0119.
  169. Ma, W., Zhang, J., Chen, S. & Wang, X. Crystalline phase formation of poly(vinylidene fluoride) from tetrahydrofuran/N,N-dimethylformamide mixed solutions. *J. Macromol. Sci. Part B Phys.* **47**, 434–449 (2008).
  170. Shin, Y. M., Hohman, M. M., Brenner, M. P. & Rutledge, G. C. Experimental characterization of electrospinning: the electrically forced jet and instabilities. *Polymer (Guildf)*. **42**, 09955–09967 (2001).
  171. Zander, N. E. Hierarchically structured electrospun fibers. *Polymers (Basel)*. **5**, 19–44 (2013).
  172. Dong, Z., Kennedy, S. J. & Wu, Y. Electrospinning materials for energy-related applications and devices. *J. Power Sources* **196**, 4886–4904 (2011).
  173. Ma, X. *et al.* Molecular orientation in electrospun poly(vinylidene fluoride) fibers. *ACS Macro Lett.* **1**, 428–431 (2012).
  174. Yee, W. A., Kotaki, M., Liu, Y. & Lu, X. Morphology, polymorphism behavior and molecular

- orientation of electrospun poly(vinylidene fluoride) fibers. *Polymer (Guildf)*. **48**, 512–521 (2007).
175. Zhang, Y., Li, Y., Zhu, H., Fu, Z. & Zhang, Q. Sintering temperature dependence of dielectric properties and energy-storage properties in (Ba,Zr)TiO<sub>3</sub> ceramics. *J. Mater. Sci. Mater. Electron*. **28**, 514–518 (2017).
  176. Puli, V. S., Pradhan, D. K., Riggs, B. C., Chrisey, D. B. & Katiyar, R. S. Investigations on structure, ferroelectric, piezoelectric and energy storage properties of barium calcium titanate (BCT) ceramics. *J. Alloys Compd*. **584**, 369–373 (2014).
  177. Hall, D. A. & Stevenson, P. J. High field dielectric behaviour of ferroelectric ceramics. *Ferroelectrics* **228**, 139–158 (1999).
  178. Yu, K., Bai, Y., Zhou, Y., Niu, Y. & Wang, H. Poly(vinylidene fluoride) polymer based nanocomposites with enhanced energy density by filling with polyacrylate elastomers and BaTiO<sub>3</sub> nanoparticles. *Appl. Phys. Lett*. **104**, (2014).
  179. Zhao, X. *et al.* Tuning the dielectric properties of polystyrene/poly(vinylidene fluoride) blends by selectively localizing carbon black nanoparticles. *J. Phys. Chem. B* **117**, 2505–2515 (2013).
  180. Subodh, G., Deepu, V., Mohanan, P. & Sebastian, M. T. Dielectric response of high permittivity polymer ceramic composite with low loss tangent. *Appl. Phys. Lett*. **95**, 210–212 (2009).
  181. Tomer, V., Randall, C. A., Polizos, G., Kostelnick, J. & Manias, E. High- and low-field dielectric characteristics of dielectrophoretically aligned ceramic/polymer nanocomposites. *J. Appl. Phys*. **103**, 1–7 (2008).
  182. Lin, Y., Wu, G. S., Yuan, X. Y., Xie, T. & Zhang, L. D. Fabrication and optical properties of TiO<sub>2</sub> nanowire arrays made by sol-gel electrophoresis deposition into anodic alumina membranes. *J. Phys. Condens. Matter* **15**, 2917–2922 (2003).
  183. Liu, S., Xue, S., Zhang, W. & Zhai, J. Enhanced dielectric and energy storage density induced by surface-modified BaTiO<sub>3</sub> nanofibers in poly(vinylidene fluoride) nanocomposites. *Ceram. Int*. **40**, 15633–15640 (2014).
  184. Mayeen, A. *et al.* Flexible dopamine-functionalized BaTiO<sub>3</sub>/BaTiZrO<sub>3</sub>/BaZrO<sub>3</sub>-PVDF ferroelectric nanofibers for electrical energy storage. *J. Alloys Compd*. **837**, (2020).
  185. Mao, Y. P., Mao, S. Y., Ye, Z. G., Xie, Z. X. & Zheng, L. S. Size-dependences of the dielectric and ferroelectric properties of BaTiO<sub>3</sub>/polyvinylidene fluoride nanocomposites. *J. Appl. Phys*. **108**, (2010).
  186. Feng, Y., Deng, Q., Peng, C. & Wu, Q. High dielectric and breakdown properties achieved in ternary BaTiO<sub>3</sub>/MXene/PVDF nanocomposites with low-concentration fillers from enhanced interface polarization. *Ceram. Int*. **45**, 7923–7930 (2019).
  187. Tian, F., Lei, Q., Wang, X. & Wang, Y. Effect of deep trapping states on space charge suppression in polyethylene/ZnO nanocomposite. *Appl. Phys. Lett*. **99**, (2011).

188. Dang, Z. M., Wang, H. Y., Peng, B. & Nan, C. W. Effect of BaTiO<sub>3</sub> size on dielectric property of BaTiO<sub>3</sub>/PVDF composites. *J. Electroceramics* **21**, 381–384 (2008).
189. Zhou, T. *et al.* Improving dielectric properties of BaTiO<sub>3</sub>/ferroelectric polymer composites by employing surface hydroxylated BaTiO<sub>3</sub> nanoparticles. *ACS Appl. Mater. Interfaces* **3**, 2184–2188 (2011).
190. Zhang, H. *et al.* Polymer Matrix Nanocomposites with 1D Ceramic Nanofillers for Energy Storage Capacitor Applications. *ACS Appl. Mater. Interfaces* **12**, 1–37 (2020).
191. Chen, G. *et al.* Effects of Sintering Method and BaTiO<sub>3</sub> Dopant on the Microstructure and Electric Properties of Bi (Fe<sub>0.9</sub>Al<sub>0.05</sub>Yb<sub>0.05</sub>) O<sub>3</sub>-Based Ceramics. *J. Electron. Mater.* **49**, 2608–2616 (2020).
192. Ponnamm, D., Aljarod, O., Parangusan, H. & Ali Al-Maadeed, M. Al. Electrospun nanofibers of PVDF-HFP composites containing magnetic nickel ferrite for energy harvesting application. *Mater. Chem. Phys.* **239**, 122257 (2020).
193. Al-Saleh, M. H. & Abdul Jawad, S. Graphene Nanoplatelet–Polystyrene Nanocomposite: Dielectric and Charge Storage Behaviors. *J. Electron. Mater.* **45**, 3532–3539 (2016).
194. Lin, B. *et al.* Enhanced dielectric permittivity in surface-modified graphene/PVDF composites prepared by an electrospinning-hot pressing method. *Compos. Sci. Technol.* **172**, 58–65 (2019).
195. Huang, X., Jiang, P., Kim, C., Liu, F. & Yin, Y. Influence of aspect ratio of carbon nanotubes on crystalline phases and dielectric properties of poly(vinylidene fluoride). *Eur. Polym. J.* **45**, 377–386 (2009).
196. Shen, Y. *et al.* Modulation of topological structure induces ultrahigh energy density of graphene/Ba<sub>0.6</sub>Sr<sub>0.4</sub>TiO<sub>3</sub> nanofiber/polymer nanocomposites. *Nano Energy* **18**, 176–186 (2015).
197. Cozza, E. S., Monticelli, O., Marsano, E. & Cebe, P. On the electrospinning of PVDF: Influence of the experimental conditions on the nanofiber properties. *Polym. Int.* **62**, 41–48 (2013).
198. Xia, W., Xu, Z., Zhang, Q., Zhang, Z. & Chen, Y. Dependence of dielectric, ferroelectric, and piezoelectric properties on crystalline properties of p(VDF-co-TrFE) copolymers. *J. Polym. Sci. Part B Polym. Phys.* **50**, 1271–1276 (2012).
199. Koseki, Y., Aimi, K. & Ando, S. Crystalline structure and molecular mobility of PVDF chains in PVDF/PMMA blend films analyzed by solid-state <sup>19</sup>F MAS NMR spectroscopy. *Polym. J.* **44**, 757–763 (2012).
200. Kumar, K. K. *et al.* Electrical conduction mechanism in NaCl complexed PEO/PVP polymer blend electrolytes. *J. Non. Cryst. Solids* **358**, 3205–3211 (2012).
201. Wu, S. *et al.* A high-K ferroelectric relaxor terpolymer as a gate dielectric for organic thin film transistors. *Appl. Phys. Lett.* **102**, (2013).

202. Li, R. *et al.* Polyamide 11/Poly(vinylidene fluoride) Blends as Novel Flexible Materials for Capacitors. *Macromol. Rapid Commun.* **29**, 1449–1454 (2008).
203. Xing, C. *et al.* Ionic liquid modified poly(vinylidene fluoride): Crystalline structures, miscibility, and physical properties. *Polym. Chem.* **4**, 5726–5734 (2013).
204. Wang, P., Xu, P., Wei, H., Fang, H. & Ding, Y. Effect of block copolymer containing ionic liquid moiety on interfacial polarization in PLA/PCL blends. *J. Appl. Polym. Sci.* **135**, 6–11 (2018).
205. Xing, C., You, J., Li, Y. & Li, J. Nanostructured Poly(vinylidene fluoride)/Ionic Liquid Composites: Formation of Organic Conductive Nanodomains in Polymer Matrix. *J. Phys. Chem. C* **119**, 21155–21164 (2015).
206. Zhou, Z. *et al.* Interphase/interface modification on the dielectric properties of polycarbonate/poly(vinylidene fluoride-co-hexafluoropropylene) multilayer films for high-energy density capacitors. *J. Polym. Sci. Part B Polym. Phys.* **51**, 978–991 (2013).
207. Wolak, M. A. *et al.* Imaging the effect of dielectric breakdown in a multilayered polymer film. *J. Appl. Polym. Sci.* **123**, 2548–2557 (2012).
208. Guo, M. *et al.* High-Energy-Density Ferroelectric Polymer Nanocomposites for Capacitive Energy Storage: Enhanced Breakdown Strength and Improved Discharge Efficiency. *Mater. Today* **29**, 49–67 (2019).
209. Kalimuldina, G. *et al.* A review of piezoelectric pvdf film by electrospinning and its applications. *Sensors (Switzerland)* **20**, 1–42 (2020).

## Chapter 3

### Electrospinning of PVDF nanofibres

#### 3.1. Introduction

In the endeavour to produce highly ferroelectric PVDF, the effect of processing methodology on nanostructural morphology of PVDF must be carefully considered. As explored in the previous chapters, electrospinning is a highly effective single processing step that may produce highly ferroelectric PVDF due to the crystallite morphology it tends to produce. The high shearing and electrostatic forces exerted on the polymer jet by the electrostatic field promotes  $\beta$ -phase crystallisation within the PVDF nanofibres whereby the negatively charged  $\text{CF}_2$  groups align themselves within the solution stream as it travels toward the collector, enhancing the *trans*  $\beta$ -phase formation.<sup>1</sup> This eliminates the need for post-processing shearing and annealing, often used to increase the piezoelectric and ferroelectric activity of PVDF films.<sup>2–4</sup> In contrast, hot-pressed (also referred to as “melt-compressed”) PVDF typically contains a high proportion of the paraelectric  $\alpha$ -phase with a low total crystallinity, whereas solution-cast PVDF contains a high proportion of the somewhat polar  $\gamma$ -phase, some  $\beta$ -phase PVDF, and a comparable total crystalline fraction to electrospun PVDF.<sup>5–7</sup>

The key challenge with electrospinning PVDF is in optimising the processing parameters to maximise the  $\beta$ -phase content, which largely involves achieving stable spinning at high voltages to form thin nanofibres. Spinning thin fibres causes the formation of nanoscale ordered crystalline domains within the nanofibres oriented along the fibre axis.<sup>8,9</sup> Similarly, the solution properties must be fine-tuned to achieve high quality fibres, as balancing the viscosity and conductivity of the solution in turn determines the flow rate-voltage balance. Ionic liquids (ILs), can also significantly ease electrospinning and improve nanofibre morphologies even at these low loadings, while also increasing conductivity of the nanofibre membranes due to their ionic nature.<sup>10–12</sup> ILs are also easily dispersed in comparison to many solid nanofillers, which tend to agglomerate or stack in the electrospinning solution, and also alter the morphology of the nanofibres.

However, the relationship between processing parameters and optimal crystallisation conditions is still not fully understood, particularly when incorporating ILs into processing techniques. Hence, in this chapter, the effects of three processing methods on the crystalline structure evolution of PVDF were investigated; electrospinning, solution-casting and hot-pressing. An ionic liquid (1-allyl-3-methylimidazolium chloride, AMIM), used as an additive in aiding the electrospinning process, also affected the crystalline structure of the electrospun PVDF nanofibers. The total crystallinity, crystalline phase content and dielectric properties of the PVDF samples prepared under different processing conditions were evaluated by Fourier

transform infrared spectroscopy (FTIR) and differential scanning calorimetry (DSC), and impedance spectroscopy. Small- and wide-angle X-ray scattering (SAXS/WAXS) analyses were used to refine the crystal phase contents estimated by FTIR, while also determining the morphology formed by the three processing techniques.

## 3.2. Experimental

### 3.2.1. Materials and characterisation

Commercial PVDF pellets (Kynar 740,  $T_m = 168\text{ }^{\circ}\text{C}$ ) and PVDF-HFP (Sigma-Aldrich 427179,  $T_m = 155\text{--}160\text{ }^{\circ}\text{C}$ ) were used for creating the solution cast, hot-pressed and electrospun samples. Dimethylformamide, DMF (>99%) was purchased from Fisher Scientific UK. Acetone was purchased from Sigma-Aldrich, UK and 1-allyl-3-methylimidazolium chloride (AMIM, 98%) was purchased from Alfa Aesar. Carbon black grease, used for electrical impedance spectroscopy, was purchased from MG Chemicals, UK.

FTIR was performed on all samples using a Bruker Tensor 27 in a wavenumber range of 500–4000  $\text{cm}^{-1}$ . Samples were cut and removed from substrates, and an ambient background reading was subtracted from each spectrum. Phase content may be estimated with the method detailed by Cai *et al.*<sup>13</sup> Firstly, a total ‘electroactive’ (EA) phase content – the sum of  $\beta$  and  $\gamma$ -phase contents,  $F(\text{EA})$  – is firstly found by comparing the strong ( $\beta + \gamma$ ) peak at 840  $\text{cm}^{-1}$  to the  $\alpha$ -phase peak at 763  $\text{cm}^{-1}$ . This can be determined according to the Beer–Lambert law as shown in **equation 3.1**

$$F(\text{EA}) = \frac{A_{\text{EA}}}{(K_{\text{EA}}/K_{\alpha})A_{\alpha} + A_{\text{EA}}} \quad (10.1)$$

where  $K_{\text{EA}}$  ( $7.7 \times 10^4\text{ cm}^2\text{ mol}^{-1}$ ) and  $A_{\text{EA}}$  are the absorption coefficient and relative intensity of the peak at 840  $\text{cm}^{-1}$ , respectively, and  $K_{\alpha}$  ( $6.1 \times 10^4\text{ cm}^2\text{ mol}^{-1}$ ) and  $A_{\alpha}$  are equivalent for the peak at 763  $\text{cm}^{-1}$ .<sup>14</sup> Since exclusive peaks exist for the  $\beta$ -phase at 1275  $\text{cm}^{-1}$  and the  $\gamma$ -phase at 1234  $\text{cm}^{-1}$ , the individual phases may be estimated from the strength of these peaks relative to the nearby troughs. This is possible for most of the  $\beta$  and  $\gamma$ -phase peaks, although in some samples the stronger peak obscures the other, preventing quantification of the two phases.

2D small-angle X-ray scattering and 2D wide-angle X-ray scattering (2D SAXS/WAXS) data was collected using a Xenocs Xeuss 2.0 X-ray instrument operating with a copper (Cu)  $K_{\alpha}$  source ( $\lambda = 1.54\text{ \AA}$ ). The 2D SAXS/WAXS data were collected on the Pilatus 300 K and Pilatus 100 K detector systems, respectively. Both detectors were calibrated with silver behenate. An evacuated chamber of 1.2 m was situated between the sample and SAXS detector to reduce air scattering and absorption. The WAXS detector was positioned in the evacuated sample chamber at a distance of 162 mm. The neat PVDF and PVDF/AMIM samples were positioned vertically in the evacuated sample chamber and static 2D SAXS/WAXS data was

taken with a collection time of 120 s. All SAXS/WAXS data were normalized for sample thickness, transmission and background scattering. X-ray data reduction and analysis was performed using the Xeuss 2.0 instrument data processing and analysis software. The 2D SAXS/WAXS data were reduced to 1D scattering profiles of intensity ( $I$ ) versus scattering vector ( $q$ ) for SAXS and  $2\theta$  for WAXS (where  $q = (4\pi/\lambda) \sin(\theta)$ ,  $2\theta$  is the scattering angle and  $\lambda$  is the X-ray wavelength), by sector averaging around the beam stop by a fixed angle and radius,  $q$ . To determine information on the long-range ordering in the samples, 1D correlation functions were computed from the 1D SAXS profiles using the Corfunc software incorporated into the SasView SAXS analysis package.<sup>15,16</sup> The 1D correlation function,  $\gamma(R)$  is expressed as

$$\gamma(R) = \frac{1}{Q_s} \int_0^\infty I(q) q^2 \cos(qR) dq \quad (0.2)$$

where  $I(q)$  is the scattering intensity and  $Q_s$  is the experimental invariant obtained from the 1D SAXS profile between the experimental limits of  $q_1$  (first data point) and  $q_2$  (region where  $I(q)$  is constant). The scattering invariant  $Q_s$  is expressed as:

$$Q_s(t) = \int_0^\infty q^2 I(q) dq \approx \int_{q_1}^{q_2} q^2 I(q) dq \quad (0.3)$$

The 1D correlation functions were computed by the extrapolation of the 1D SAXS profile ( $q \rightarrow \infty$ ) according to Porod's law and a Guinier model back extrapolation ( $q \rightarrow 0$ ). The correlation function analysis assumes an ideal two-phase lamellar morphology of the PVDF polymer and various parameters including long period  $L_p$ , crystalline layer thickness  $H_b$ , amorous layer thickness  $S_b$ , and estimated bulk percent crystallinity  $\chi_c$ , can be extracted.<sup>15,17,18</sup>

SEM imaging was performed using a Carl Zeiss Sigma field SEM. Samples were sputter coated using an Au/Pd target to a thickness of  $\sim 5$  nm. Images were taken using accelerating voltages between 3-10 kV, and fibre diameters were calculated using point-to-point measurement tools in the Zeiss SEM software, using a sample size of roughly 10-20 nanofibres. DSC was performed using a Mettler Toledo STAR<sup>e</sup>1 instrument on samples weighing  $\sim 10$  mg under a nitrogen atmosphere at a flow rate of  $20 \text{ cm}^3 \text{ min}^{-1}$ . Samples were subjected to a heating and cooling cycle between  $-50$  to  $230$  °C at a rate of  $10$  °C  $\text{min}^{-1}$ . Impedance spectroscopy was carried out using a Princeton Applied Research Parstat MC with a PMC-2000 card and a two-point probe. Samples were coated with silver paint in order to fix the conductive area. Measurements were taken between  $10^0$  to  $10^5$  Hz.

### 3.2.2. PVDF production methods

PVDF samples were prepared by three different methods: solution-casting, hot-pressing and electrospinning. For solution-casting, PVDF and PVDF/AMIM (1 wt%) solutions were directly cast onto glass dishes and dried under vacuum at  $60$  °C for 24 hours. The resulting film thickness

was approximately  $120 \pm 50 \mu\text{m}$ . Dried PVDF and PVDF/AMIM films were further hot-pressed at  $190^\circ\text{C}$ , under 8 MPa for 5 minutes. The thickness of resultant samples was approximately  $120 \pm 50 \mu\text{m}$ .

Electrospun PVDF nanofibres were prepared with the Spraybase CAT000001 electrospinning instrument. Firstly, PVDF pellets were dissolved in DMF at  $60^\circ\text{C}$  for at least 6 hours under magnetic stirring to form a homogeneous solution. After cooling down to room temperature, acetone was added to form a 3:7 volumetric ratio to DMF, and the solution was stirred for further 12 hours. To study the effects of additives, AMIM was added at 1 wt% and 3 wt% to the solutions during the stirring process. PVDF fibre membranes were electrospun with a spinneret–collector distance of 15 cm with a range of voltage and spinning rates in order to determine the optimal spinning conditions for stable fibres.

### 3.3. Results and discussion

#### 3.3.1. Effects of an ionic liquid on the morphology of electrospun PVDF nanofibres

The processing conditions for the electrospinning of our PVDF nanofibres first had to be determined. In particular, the concentration of PVDF in the spinning solution determines the viscosity and surface tension of the spinning solution, which has a significant influence on the morphology of electrospun fibres. Additionally, the selection of solvents and the ratio in which to employ them will have a strong effect on these solution characteristics. Here, DMF was selected due to its moderate boiling point and evaporation rate which stabilises the solution jet during electrospinning and promotes the production of homogenous fibres. Acetone was initially added to increase the solvent volatility and in turn the rate of fibre formation, and may also serve to promote  $\beta$ -phase formation due to rapid solvent evaporation.<sup>7,19–22</sup> PVDF nanofibre membranes produced with acetone and DMF with varying PVDF solution concentrations are shown in the SEM images in **Figure 3.1**.

First attempts at electrospinning involved mixing PVDF into DMF/Acetone (7:3 ratio) at 20 wt% (**Figure 3.1(a)**). This produced a highly beaded nanofibre membrane via rather unstable electrospinning, suggesting the solution was too volatile. Thus, electrospinning was attempted using DMF alone, employing several PVDF concentrations to find an optimal solution viscosity with this change of solvent. When the concentration of PVDF/DMF solution was reduced to 10 wt% or 15 wt% (**Figure 3.1(b, c)** respectively), beads were generated to an even greater extent. These low viscosity solutions have low surface tension, which results in the spinning solution being directly sprayed onto the collector under the electric field without jet elongation, producing a film of polymer beads rather than a nanofibre membrane. In contrast, the PVDF/DMF (20 wt%) solution was electrospun into more homogeneous nanofibres with relatively few beads, with average diameter of 50–200 nm (**Figure 3.1(d)**). In this case, a more



stable jet was formed producing a more uniform fibre morphology, although even these fibres are not seen to be completely beadless despite the seemingly stable electrospinning (**Figure 3.1(d)**). It should also be noted that the relationship between solution flow rate and electric field strength (the ratio of applied voltage to tip-collector distance) determines the balance between the electric force on the polymer solution and the surface tension on the droplet of solution formed at the spinneret end. At first, a high production rate for our nanofibres was prioritised, which requires a high solution flow rate. In turn, a high electric field is needed to maintain the aforementioned force balance. For our nanofibres, this balance was reached at  $\sim 12.7$  kV voltage, 15 cm tip-collector distance and a flow rate of  $3 \text{ ml hr}^{-1}$  when using a PVDF/DMF (20 wt%) solution. However, even under these optimised conditions, the Taylor cone was clearly unstable during electrospinning, leading to the production of the beads observable in **Figure 3.1(d)**. A more stable, steady state of force balance hence must be reached. Using a lower solution flow rate was therefore deemed necessary, but this must be accompanied by a lower electric field. This had already been attempted during the parameter optimisation process, and produced very unstable electrospinning, as the field was not strong enough to shape the solution and form a

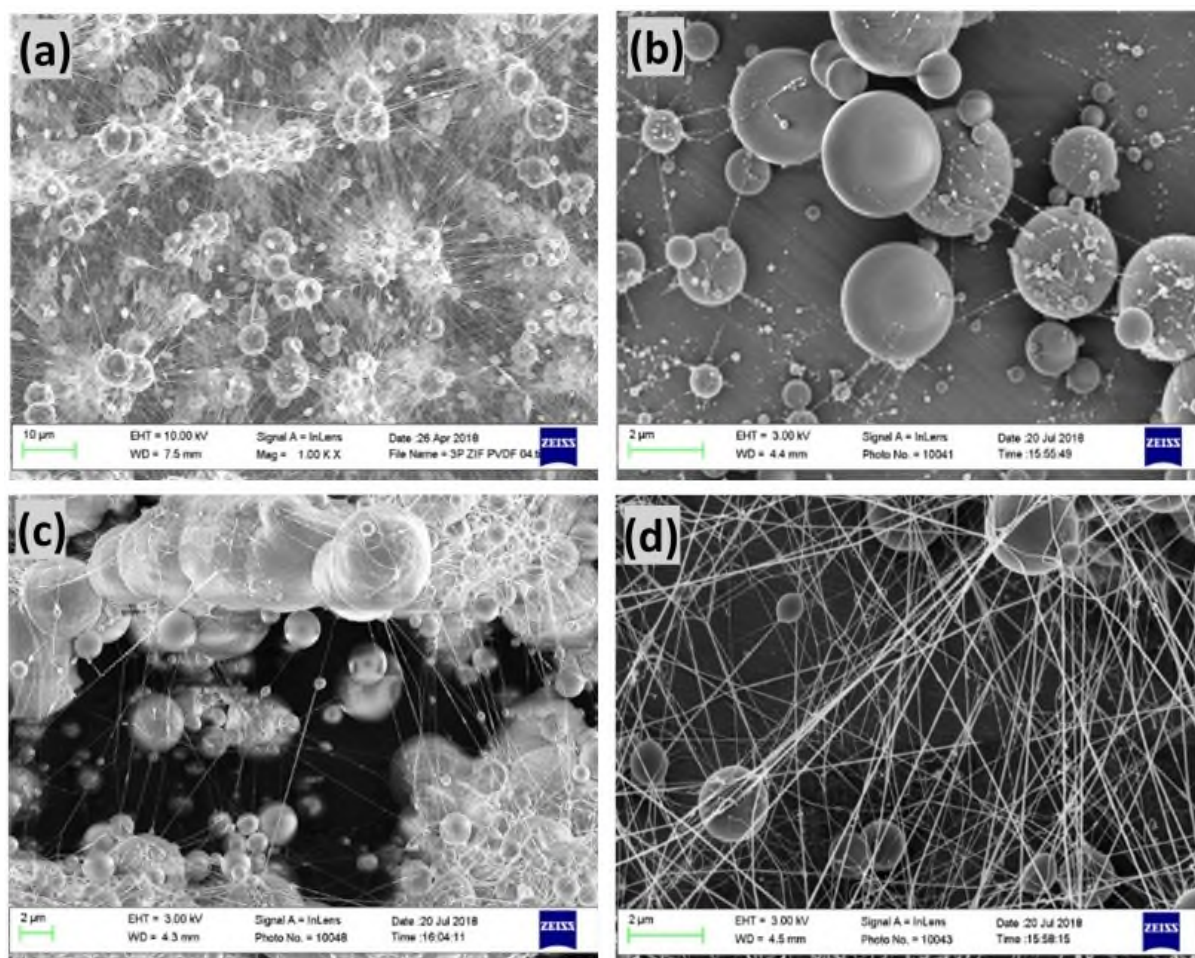


**Figure 0.1.** SEM images of PVDF nanofibers: (a) PVDF 20 wt% in 7:3 DMF/acetone (b-d) PVDF in DMF with different concentrations of (b) 10 wt%; (c) 15 wt% and (d) 20 wt%. The fibres shown in (d) were formed at a flow rate of  $3 \text{ ml hr}^{-1}$ , a voltage of 12.7 kV and a tip-collector distance of 15 cm.

stable Taylor cone. To mitigate this, the response of the solution to the electric field, i.e. its conductivity, must be enhanced.

To achieve this, the ionic liquid 1-allyl-3-methylimidazolium chloride (AMIM) was incorporated into the PVDF/DMF solution to improve the conductivity of the solution and assist the electrospinning process. The morphologies of the electrospun PVDF fibres are shown in **Figure 3.2**. The resultant fibre diameters were  $\sim 100$  nm in all samples, although the range distribution of diameters became more uniform upon the addition of AMIM,  $100 \pm 30$  nm (**Figure 3.2(b, c)**), compared to the neat PVDF fibres which are in the range of 50 nm up to 200 nm **Figure 3.2(a)**. AMIM clearly improves the nanofibre morphology, with fewer beads compared with the neat PVDF nanofibre. Moreover, the PVDF/AMIM nanofibres possess a more uniform diameter distribution of 50–150 nm with a lower mean diameter of  $\sim 90$  nm. It was found that 1 wt% AMIM addition was sufficient to form (almost) beadless fibres (**Figure 3.2(b)**). Increasing the amount of AMIM to 3 wt% (**Figure 3.2(c)**) adversely affects the fibre quality, with more beads and lower uniformity seen in the membrane. This may be due to the limited compatibility of AMIM with PVDF, leading to inhomogeneity in the solution conductivity and the fibre formation process at higher AMIM content.<sup>8</sup> Even with the increased solution conductivity, the flow rate was maintained at a relatively high  $1.5 \text{ ml hr}^{-1}$ , providing a decently high nanofibre formation rate.

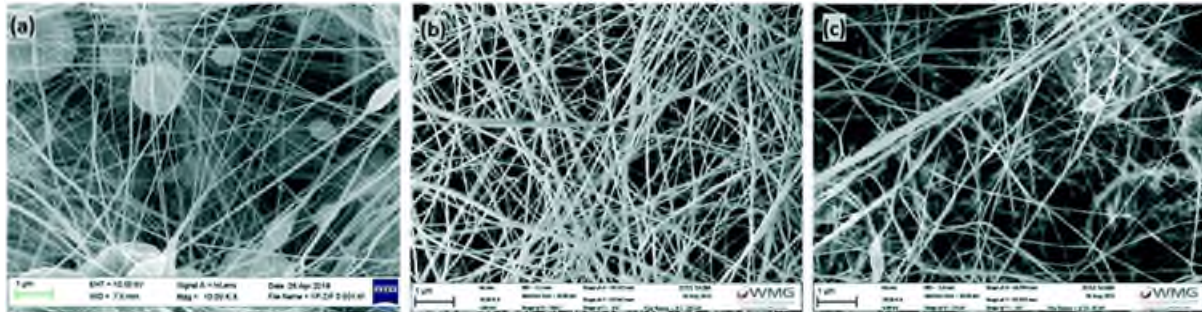


**Figure 0.2.** SEM micrographs of electrospun PVDF fibres containing (a) no additives, spun at a flow rate  $3 \text{ ml hr}^{-1}$  and a voltage of 12.7 kV; (b) 1 wt% AMIM and (c) 3 wt% AMIM, both electrospun at a flow rate of  $1.5 \text{ ml hr}^{-1}$  with a voltage of 7.4–8 kV.

### 3.3.2. Thermal analysis of PVDF and PVDF/AMIM composites

DSC was used to calculate the overall crystallinity of the PVDF and PVDF/AMIM samples. The crystallinity  $\chi_{dsc}$  of a sample with melting enthalpy  $\Delta H_m$ , is calculated from **equation 3.4**

$$\chi_{dsc} = \frac{\Delta H_m}{\Delta H_0} \quad (0.4)$$

where  $\Delta H_0$  (104.6 J/g) is the melting enthalpy of 100% crystalline PVDF.<sup>23</sup> The values of the melting point  $T_m$ , crystallization point  $T_c$ , and total crystallinities  $\chi_{dsc}$ , of the neat PVDF and PVDF/AMIM samples are collated in **Table 3.1**. **Figure 3.3** shows the heating and cooling

thermograms of the pure PVDF and PVDF/AMIM samples produced by the three different processing techniques.

Comparing the values of  $T_m$ , the PVDF/AMIM hot-pressed and solution-cast samples peaked at  $\sim 173^\circ\text{C}$ , while the corresponding neat PVDF solution-cast and hot-pressed samples peaked at  $\sim 170^\circ\text{C}$  and  $\sim 167^\circ\text{C}$ , respectively. A higher  $T_m$  is often referred to as being indicative of the  $\beta$ -phase.<sup>12,24</sup> However, the value of  $T_m$  is dependent on the crystallisation history of the material, and so  $T_m$  alone does not provide a complete qualitative description of the phase content.<sup>19,25</sup>

In **Figure 3.3(a)**, the melting peak of all the pure PVDF samples are relatively broad indicating a range of crystallize sizes, crystal perfection and phases are present. In **Figure 3.3(b)** and **Table 3.1**, AMIM is also seen to increase  $T_m$  by  $\sim 3^\circ\text{C}$  in all of the samples, and thus AMIM is seen to unilaterally increase  $T_m$  compared to the neat PVDF samples. However, it should be noted that the electrospun PVDF/AMIM melting peak (**Figure 3.3(b)**) is quite broad (consisting of several shoulders) compared with the neat electrospun PVDF sample, implying a more diverse

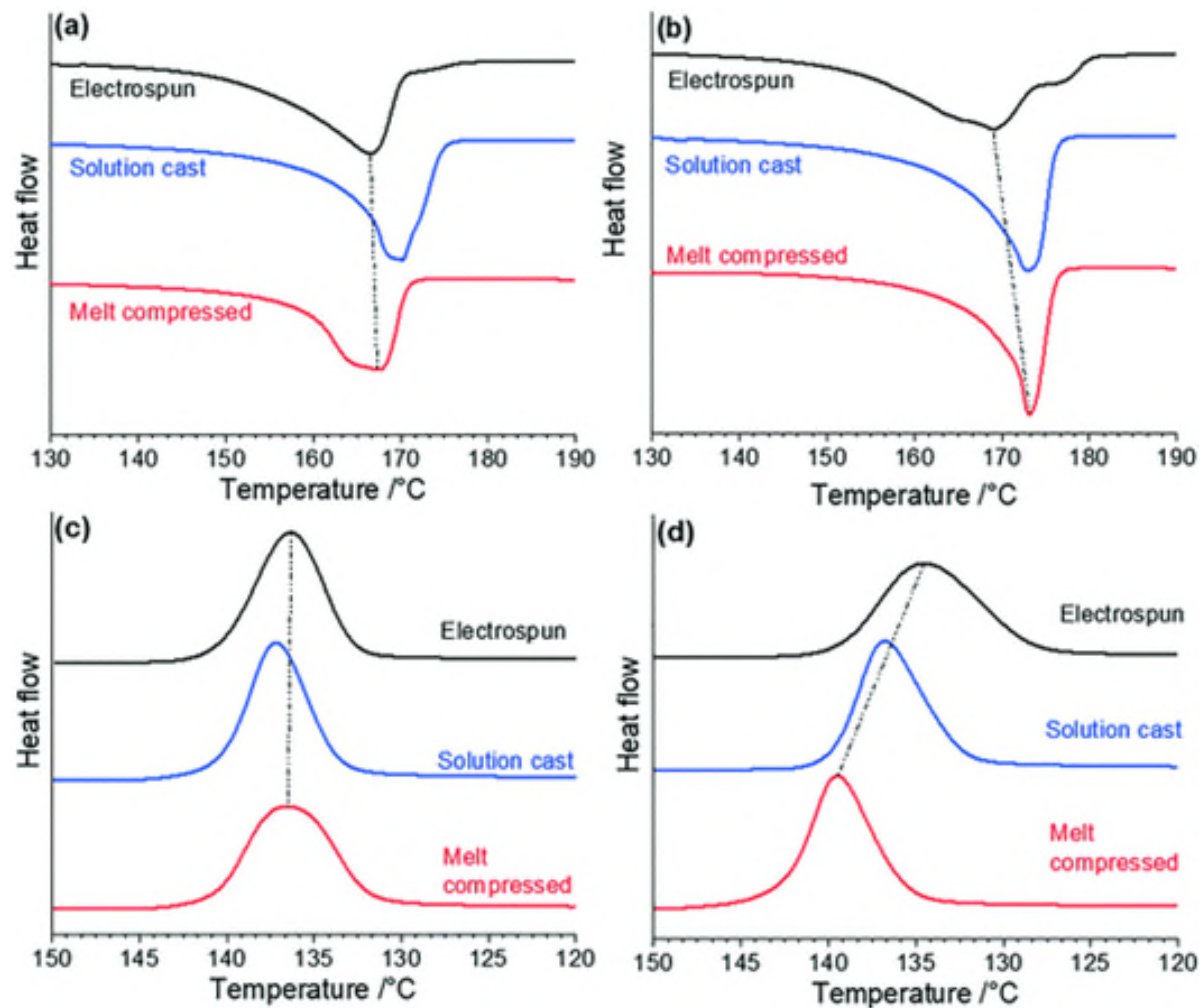


**Figure 0.3.** DSC heating thermograms of (a) neat PVDF and (b) PVDF/AMIM; and cooling thermograms of (c) neat PVDF and (d) PVDF/AMIM fabricated by various processing methods (note that the absolute value of the heat flow is arbitrary).

crystallite structure. Anousheh *et al.* suggest that in pure crystals  $\alpha$ -phase PVDF displays a higher temperature melting peak, but that regioisomeric defects in the material will influence the melting peak of the  $\alpha$ -phase more so than the  $\beta$ -phase.<sup>26</sup> Hence, greater disorder may shift the  $\alpha$ -phase melting peak down towards that of the  $\beta$ -phase, causing the illusion of a high  $\beta$ -phase content. We expect that in the PVDF/AMIM electrospun sample, the defect proportion will be lower than that of the other samples, leading to an initial  $\beta$ -phase melting peak at 169 °C, and an  $\alpha$ -phase peak at 173 °C, matching the hot-pressed and solution-cast PVDF/AMIM melting peaks (**Figure 3.3(b)**).

From the data in **Table 3.1** and melting enthalpies of the DSC thermograms, it was found that the addition of AMIM to the electrospun PVDF enhances  $\chi_{dsc}$  by 5%. The improved fibre morphology consisting of thinner fibres and a low number of beads likely induces a higher degree of molecular ordering in the fibres correlating with a higher  $\chi_{dsc}$ . The  $\beta$ -phase content will also be higher in the more uniform nanofibres as the large electrostatic forces exerted on the polymer during fibre formation induces the formation of the polar  $\beta$ -phase. This is seen as a shoulder in the melting thermogram of electrospun PVDF/AMIM (**Figure 3.3(b)**).

**Table 0.1.** Melting point  $T_m$ , crystallization point  $T_c$  and total crystallinities  $\chi_{dsc}$  determined by DSC. \*Very broad melting peak seen due to presence of multiple phases. Value given is taken at the peak's maximum.

Sample	$T_m$ (°C)	$\chi_{dsc}$ (%)	$T_c$ (°C)
PVDF hot-pressed	167.3	39	136.5
PVDF solution-cast	170.2	50	137.2
PVDF electrospun	166.5	47	136.3
PVDF electrospun	173.1	44	139.5
PVDF/AMIM solution-cast	173.0	54	136.8
PVDF/AMIM electrospun	169*	52	134.5

Xing *et al.* observed a broadening in their melting peaks as the concentration of the ionic liquid in their melt blended PVDF increases, although this is only observed in our electrospun sample.<sup>27</sup> In fact, the inverse is seen in our solution-cast and hot-pressed samples; the peaks are made thinner with the addition of AMIM, and the melting enthalpy gives a higher  $\chi_{dsc}$ . The low  $\chi_{dsc}$  and spread of crystalline phases in the neat PVDF hot-pressed sample will contribute to



the broader peak. Furthermore, the hot-pressed samples (with and without AMIM), showed noticeably lower values of  $\chi_{\text{dsc}}$  than samples made by other processing methods. This may be due to the high temperature used in the process, which keeps the PVDF in a less viscous solution during crystallisation, promoting the formation of the high bonding energy and kinetically favourable  $\alpha$ -phase.<sup>26,28</sup>

The solution-cast samples show similar or higher crystallinity than those which were electrospun, although the sharp peaks in both samples indicates a low variation in crystallite sizes and greater crystalline perfection. This is supported by the  $\chi_{\text{dsc}}$  values being the greatest from this method within the neat PVDF and PVDF/AMIM sample sets. The solution-cast samples show a sharpening and an upward shift of the melting peak by 3 °C with the addition of AMIM. The broader form and small hump on the neat solution-cast melting peak is likely due to the lower crystallinity measured in this sample.<sup>19</sup> Surprisingly however, there is no indication of the  $\gamma$ -phase in the melting peak, as this generally appears between 180–190 °C. This may indicate a transition of the  $\gamma$ -phase to the  $\alpha$ -phase during the heating or melting process. Generally, the high temperature and sharp form of the solution-cast melting peak compared to the other methods with and without AMIM, may also imply a lack of the  $\beta$ -phase compared to the other samples.

The crystallisation peaks (**Figure 3.3(c, d)**) offer some insight into the effects of AMIM on the nucleation and crystal phase formation in the samples. The electrospun samples show only a slight difference in  $T_c$  on the addition of AMIM, although the peak broadens considerably, implying that AMIM slows and diversifies the nucleation processes. As for the solution-cast samples, the addition of AMIM has a less significant effect on  $T_c$  and has little effect on the form of the peak, thus AMIM seems to make a minimal difference to nucleation and recrystallisation process. Conversely, the hot-pressed samples show a large increase in  $T_c$  of 3.0 °C and a sharper peak with AMIM addition. This implies that the AMIM has acted as a nucleating agent and has induced a crystallisation process not seen in the other samples to any extent.

### 3.3.3. Identification of PVDF crystal phases by FTIR.

FTIR analysis was used to characterise the crystal phase formation in PVDF samples prepared by the three different methods. The spectra are shown in **Figure 3.4**, while the differences in crystalline phase composition with each processing method are collated in **Table 3.2**. For the neat PVDF samples (**Figure 3.4(a, b)**), comparing the hot-pressed and electrospun samples, while they show similar  $\alpha$ -phase and  $\beta + \gamma$ -phase fractions, the electrospun sample lacks signatures of the  $\gamma$ -phase. It can be inferred that the  $\beta$  to  $\gamma$ -phase relaxation is occurring in the hot-pressed samples before a significant proportion of the solvent has boiled off, but not enough to have removed all the  $\beta$ -phase content. Conversely, this relaxation is being inhibited in the

electrospun samples in the early stages of fibre formation, preventing the formation of any significant amount of the  $\gamma$ -phase. This can be concluded from the presence of the peak at  $833\text{ cm}^{-1}$  shown in **Figure 3.4(c)** – ascribed to  $\gamma$ -phase crystallites formed by this relaxation – which is seen in the hot-pressed but not in the electrospun sample.<sup>13</sup> The electric field poling during electrospinning may prevent this relaxation, while the faster solvent evaporation rate in hot-pressed likely assists in stopping  $\gamma$ -phase formation as solution viscosity increases too quickly for the  $\beta$  to  $\gamma$ -phase relaxation to occur. As a result, the  $\beta$ -phase content by hot-pressing is  $\sim 18\%$  lower than neat PVDF obtained by electrospinning. However, the high-pressure forces exerted on the PVDF during hot-pressing facilitates the confirmation from  $\alpha$ -phase to  $\beta$ -phase, meaning the  $\beta$ -phase content is still significant.<sup>5,29</sup>

When comparing the neat PVDF solution-cast sample to both the hot-pressed and electrospun PVDF (**Figure 3.4(a, b)**), the  $\alpha$ -phase signatures at  $763$  and  $614\text{ cm}^{-1}$  are both diminished, while the  $833\text{ cm}^{-1}$  and  $1234\text{ cm}^{-1}$   $\gamma$ -phase peaks dominate the  $840\text{ cm}^{-1}$  and  $1275\text{ cm}^{-1}$   $\beta$ -phase peaks respectively. Due to the slow evaporation rate during solution-casting, the  $\beta$  to  $\gamma$ -phase relaxation occurs considerably, resulting in a high  $\gamma$ -phase content and the strong  $833\text{ cm}^{-1}$   $\beta$  to  $\gamma$ -phase relaxation peak.

In the PVDF/AMIM samples, shown in **Figure 3.4(c)**, the  $833\text{ cm}^{-1}$   $\beta$  to  $\gamma$  relaxation peak is not seen in either the hot-pressed or electrospun sample. In fact, in the hot-pressed samples, the electroactive phase content was decreased as a result of AMIM addition. The solution-cast samples, both with and without AMIM, instead show strong peaks in the  $\gamma$ -phase. It is likely  $\alpha$  or  $\beta$  to  $\gamma$ -phase transitions are prominent during the crystallisation process and that the solvent conditions did not encourage  $\beta$ -phase formation.<sup>30</sup> This is confirmed by the strong  $833\text{ cm}^{-1}$   $\gamma$  peak seen in the neat solution-cast sample. Interestingly, the phase content shows no change when AMIM is added to the solution, and the  $833\text{ cm}^{-1}$  peak is far less prominent. A low rate of solvent evaporation is likely to have occurred in these samples, providing an environment for  $\gamma$ -phase formation. Since there are no other processing conditions during solution-casting which promote the formation of other phases (such as the lack of mechanical stress), the  $\gamma$ -phase seems

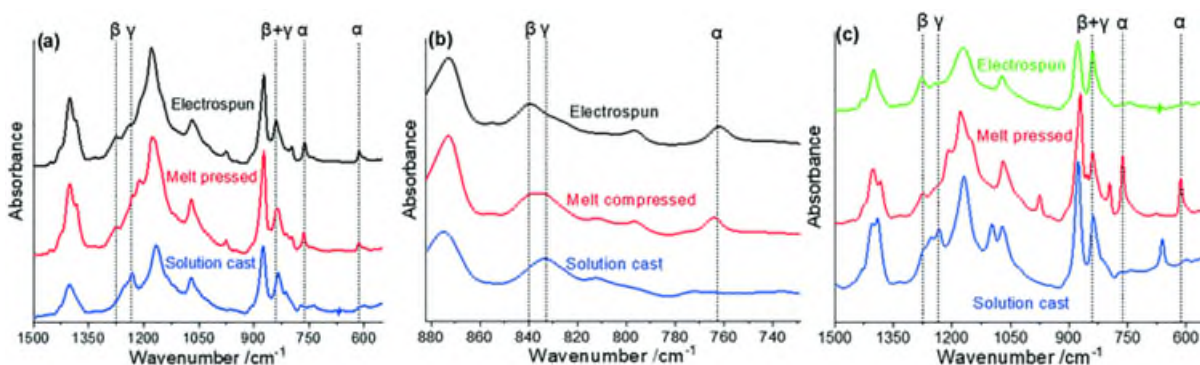


**Figure 0.4.** (a) FTIR of neat PVDF made with various processing methods; (b) expanded FTIR region between  $740$  and  $880\text{ cm}^{-1}$  (c) equivalent FTIR for PVDF/AMIM samples

to completely dominate these samples. However, the lack of detectability of the  $\beta$ -phase from this FTIR likely means that its content is underestimated.

As seen in **Table 3.2**, the addition of AMIM to the electrospinning solution clearly increases the electroactive phase composition, with  $\beta + \gamma$ -phase contents of over 70%. As expected, the highest  $\alpha$ -phase content is in the neat PVDF electrospun sample, whereas the lowest is seen in the PVDF/AMIM samples.

**Table 0.2.** Phase contents of electrospun PVDF samples containing AMIM.

Sample	$\alpha$ (%)	$\beta$ (%)	$\gamma$ (%)	$\beta + \gamma$ (%)
PVDF electrospun	41	$\lesssim 59$	—	59
PVDF/AMIM electrospun	26.5	68	5.5	73.5
PVDF melt-compressed	41	41	18	57
PVDF/AMIM melt-compressed	55	$\lesssim 45$	—	45
PVDF solution-cast	26	—	$\lesssim 74$	74
PVDF/AMIM solution-cast	27	—	$\lesssim 73$	73

### 3.3.4. Identification of PVDF crystal phases by 2D SAXS/WAXS

**Figure 3.5** shows the 2D SAXS/WAXS data for the pure PVDF and PVDF/AMIM composite samples prepared by the three different processing techniques. SAXS gives information on the macromorphology of the sample, that is, the long-range ordering and dimensions of the amorphous and crystalline lamellar layers, whereas WAXS probes the unit cell dimensions and crystal phases (micromorphology), present in the PVDF. The 2D SAXS shows isotropic scattering around the central beam stop for all samples, confirming that there was no preferred orientation of the crystalline structure induced by any of the processing methods. The 2D SAXS for pure PVDF shows that the macroscale crystalline structure is affected by the processing conditions; the solution-cast and electrospun samples have broad diffuse scattering ring whereas the hot-pressed sample has an intense more concentrated scattering ring. The scattering rings also change on addition of AMIM, making the ring more diffuse in all cases.

The corresponding isotropic 2D WAXS scattering for the pure PVDF and PVDF/AMIM, have some of the major Bragg reflections indexed on the patterns for the  $\alpha$ ,  $\beta$  and  $\gamma$  crystal phases of the polymer.<sup>31</sup> Again, the different processing methods affect the major crystalline phase occurring in the polymer. The solution-cast samples (with and without AMIM) shows mainly the  $\beta$  and  $\gamma$  crystal phases predominate in the PVDF. However, both the pure PVDF hot-pressed and electrospun samples are predominantly composed of the  $\alpha$  and  $\gamma$  crystal phases. On addition of AMIM, the crystal phase shifts largely to the  $\beta$  and  $\gamma$  crystal phases. To gain further insight in to both the macro and micromorphology of the PVDF and composites 1D SAXS/WAXS profiles were obtained from the 2D patterns in **Figure 3.5**.

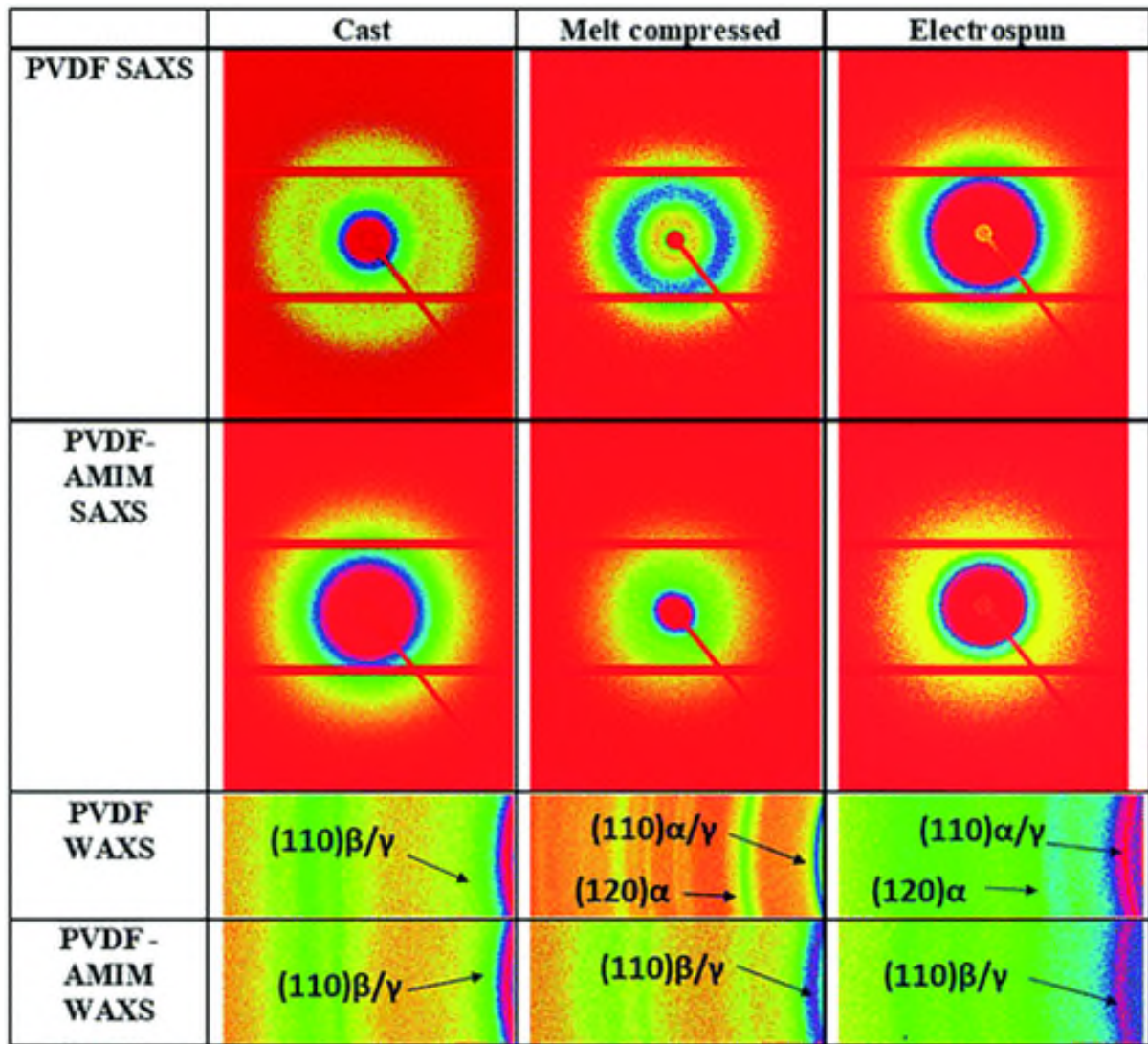


**Figure 0.5.** 2D SAXS/WAXS data of pure PVDF and PVDF/AMIM composites from the three different processing techniques (casting, hot-pressing and electrospinning). Major Bragg reflections are indexed on the 2D WAXS patterns for the  $\alpha$ ,  $\beta$  and  $\gamma$  crystal phases of PVDF.



### 3.3.5. Identification of PVDF crystal phases by 1D SAXS/WAXS

**Figure 3.6(a)** compares the 1D Lorentz corrected SAXS profiles for the pure PVDF from the three different processing conditions. The scattering peak relates to the average crystalline and amorphous layer periodicity or long period ( $L_p$ ) of the PVDF. The scattering peak in the profiles is seen to broaden and shift to higher  $q$  range with the different processing techniques. The solution-cast and electrospun SAXS profiles give a peak maximum at  $q \sim 0.1 \text{ \AA}^{-1}$ , correlating to a  $L_p = 63 \text{ \AA}$ ; whereas the hot-pressed sample gives a peak maximum at  $q \sim 0.055 \text{ \AA}^{-1}$  and  $L_p = 114 \text{ \AA}$ . The scattering peak tends to broaden can shift to lower  $q$  slightly on addition of AMIM in all samples as show in **Figure 3.6(b)**. Furthermore, for the solution cast sample, a very broad and weak second peak is observed between  $q \sim 0.03\text{--}0.06 \text{ \AA}^{-1}$ , which is likely to be the scattering from the AMIM additive.

To obtain details about the crystalline macrostructure of the PVDF, 1D correlation functions were computed from the 1D SAXS profiles. **Figure 3.6(c)** shows an example 1D correlation function for pure solution-cast PVDF. This allows the extraction of parameters (as labelled in **Figure 3.6(c)**) such as a more accurate determination of the long period,  $L_p$ , the crystalline and amorphous layer thicknesses,  $H_b$  and  $S_b$  respectively, and estimated bulk percent crystallinity  $\chi_c$ , to be obtained.<sup>15</sup> The bulk crystallinity  $\chi_c$ , is determined from the correlation function by way of **equation 3.5**

$$\chi_c = \gamma_{\min}/(\gamma_{\min} + \gamma^*) \quad (0.5)$$

where  $\gamma_{\min}$  is the first minimum in the correlation function profile and  $\gamma^*$  is the value where the linear fit to the initial part of the curve is extrapolated to  $R = 0$  (as annotated on **Figure 3.6(c)**). **Table 3.3** collates the correlation function analysis data from the 1D SAXS profiles. However, some of the data did not give reliable fits to the model and so the lamellar parameters could not be extracted in those cases from the correlation function. Comparing the results for the pure PVDF hot-pressed and solution-cast samples, the  $L_p$  is clearly reduced in the solution-cast sample and there is a reduction in the amorphous layer thickness but no real change in the crystalline lamellae layer. This results in an increased bulk crystallinity,  $\chi_c$ . Hence, the solution-casting processing technique tends to induce more crystallinity in the PVDF sample compared

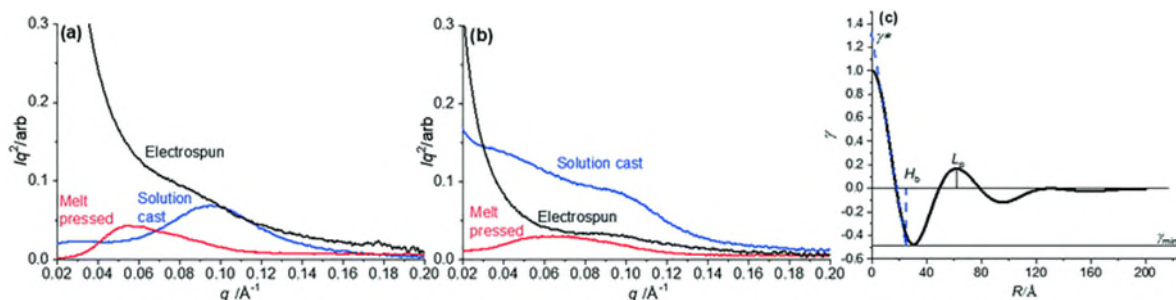


**Figure 0.6.** 1D SAXS profiles of (a) pure PVDF and (b) PVDF–AMIM composites prepared by different processing conditions; (c) corresponding 1D correlation function of solution cast pure PVDF.

with the in the hot-pressed processing technique.<sup>25</sup> However, with the addition of AMIM to the hot-pressed sample, we observe a decrease in  $L_p$ , which is due to an increase in crystalline layer thickness (and reduction of amorphous layer thickness), which increases  $\chi_c$  slightly. Similarly, Xing *et al.* showed that the addition of ILs in to PVDF, increased the scattering intensity of SAXS and shifted the  $L_p$  to lower  $q$  values and concluded that the ILs reside in the amorphous fraction of the macrostructure.<sup>11</sup> Here, the addition of AMIM influences the total crystallinity (as seen in DSC, **Figure 3.3**) and crystallite size, potentially acting as a nucleating agent as well as inducing  $\beta$ -phase formation.

**Table 0.3.** 1D SAXS correlation function results for PVDF and AMIM composites where the fits were reliable and lamellar parameters could be extracted

Sample	$L_p$ (Å)	$H_b$ (Å)	$S_b$ (Å)	$\chi_c \pm 2$ (%)
PVDF melt-compressed	99	24	75	49
PVDF solution-cast	62	24	38	55
PVDF/AMIM melt-compressed	82	29	53	51

**Table 0.4.** Crystallographic planes identified for each phase from the 1D-WAXS data, for the  $\alpha$ ,  $\beta$  and  $\gamma$  phases of PVDF. Planes denoted in bold are observed as strong peaks in the WAXS data, whereas others are smaller, less distinct peaks. The (132) and (211)  $\gamma$ -phase signatures are difficult to separate, and so are grouped.

Crystal phase	$\alpha$	$\beta$	$\gamma$
Neat PVDF electrospun	<b>(110)</b> , <b>(021)</b> , <b>(120)</b> , <b>(200)</b>	(110), <b>(310)</b> , (020), (101)	<b>(110)</b> , <b>(022)</b> , <b>(200)</b> , (132)/(211)
PVDF/AMIM electrospun	(110), <b>(140)</b> , <b>(200)</b>	<b>(110)</b> , <b>(001)</b> , <b>(310)</b> , <b>(020)</b> , <b>(101)</b>	<b>(110)</b> , (200), (132)/(211)
Neat PVDF solution-cast	(110), (002)	<b>(110)</b> , <b>(310)</b>	<b>(110)</b> , <b>(004)</b> , <b>(132)</b> / <b>(211)</b>
PVDF/AMIM solution-cast	(110), (002)	<b>(110)</b> , <b>(310)</b>	<b>(110)</b> , <b>(004)</b> , <b>(132)</b> / <b>(211)</b>
Neat PVDF melt-compressed	<b>(110)</b> , <b>(021)</b> , <b>(120)</b> , <b>(200)</b> , <b>(040)</b> , <b>(002)</b>	(110)	<b>(110)</b> , <b>(022)</b> , <b>(200)</b> , (041), (132)/(211)
PVDF/AMIM melt-compressed	(110)	<b>(110)</b> , (020)	<b>(110)</b> , (004)

1D WAXS is used to confirm the prominence of the different crystal phases, which have been identified with FTIR, for the three processing methods and addition of AMIM. **Figure 3.7** shows the 1D WAXS for all samples highlighting the major peaks for the  $\alpha$ ,  $\beta$  and  $\gamma$ -phases. A full

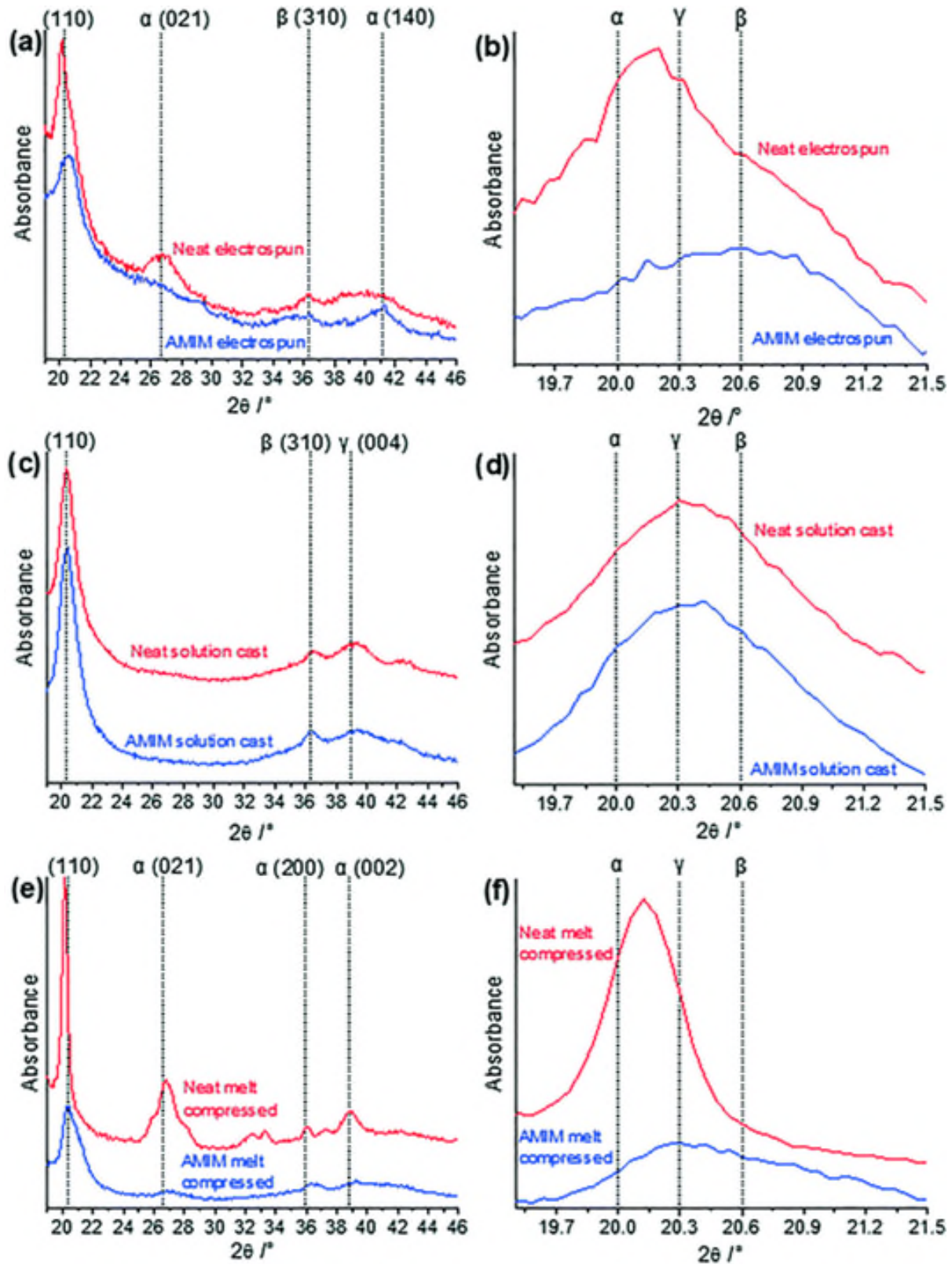


**Figure 0.7.** (a, b) Electrospun; (c, d) solution-cast and (e, f) melt-compressed 1D-WAXS spectra (note that the absolute value of the absorbance is arbitrary).is arbitrary).

breakdown of the crystallographic planes identified from the 1D WAXS profiles for all samples is provided in **Table 3.4**.<sup>31</sup> From the data in **Table 3.4**, while it is clear that the three different processing methods of neat PVDF influence the crystal phase content, it is seen that all samples have mixtures of the three major crystalline phases. Typically, the  $\alpha$ -phase tends to dominate in the electrospun and melt-compressed neat PVDF samples, whereas the  $\beta$ -phase is dominant in the electrospun PVDF/AMIM samples.<sup>11,19,25,32</sup> The solution-cast neat PVDF and PVDF/AMIM show that the  $\beta$ - and  $\gamma$ -phases are prevalent in these samples due to the fast solvent evaporation at low temperatures.<sup>19</sup> The 1D WAXS profiles for the electrospun samples are shown in **Figure 3.7(a, b)**. The  $\alpha$ -phase signature in both samples is present but appears to be more dominant in the neat PVDF sample. The  $\alpha$ -phase (120)/(012) peak at  $26.6^\circ$  in particular is absent in the PVDF/AMIM sample, but strong in the neat PVDF. Conversely, the  $\gamma$  phase peaks in the region of  $38.8^\circ$  to  $42^\circ$  are enhanced the PVDF/AMIM sample. **Figure 3.7(b)** displays the form of the peaks around  $20^\circ$ . The  $\beta$ -phase signature is identified by the (110) peak at  $20.6^\circ$ , which is partially obscured by peaks at  $20.0^\circ$  and  $20.3^\circ$ , representing the (110)  $\alpha$ -phase and  $\gamma$ -phase respectively. The PVDF/AMIM sample clearly shows a broader form to this peak, implying significant amounts of all three crystalline phases are present but the  $\beta$ -phase is mainly dominant, which agrees with the FTIR analysis. The 1D-WAXS profiles of the solution-cast samples (**Figure 3.7(c, d)**) show a high proportion of the  $\gamma$ -phase with little to no  $\alpha$ -phase signature, again supported by the FTIR data. The position of the (110) peak at  $20\text{--}21^\circ$ , shown in **Figure 3.7(d)**, highlights the  $\gamma$ -phase is dominant in in both samples. The data also shows the (310)  $\beta$ -phase peaks in both samples, confirming at least a partial split in the electroactive phase content undetectable by FTIR. Therefore, the addition of AMIM to the casting solution seems to have little effect on the phase content of PVDF, again this agrees with the FTIR data.

The 1D-WAXS profiles of both melt-compressed samples in **Figure 3.7(e, f)**, predominantly show  $\alpha$ -phase signatures. These are more prominent in the neat PVDF data. On the addition of AMIM the proportion of the  $\beta$ -phase content is increased, where the combined  $\alpha$ – $\beta$  peaks around  $35.9\text{--}36.3^\circ$  are shifted toward higher  $2\theta$ , implying a high proportion of the  $\beta$ -phase is present. Similarly, the combined peaks around  $20.0\text{--}20.6^\circ$  (shown in **Figure 3.7(f)**) are shifted toward higher  $2\theta$ , also confirming a  $\beta$  and/or  $\gamma$ -phase enhancement. Again, the addition of AMIM was seen to increase  $\beta$ -phase content in our FTIR data. Finally, the peaks around the  $32\text{--}34^\circ$  region in the neat melt-compressed sample correspond with the (121) and (130) crystallographic planes of the  $\delta$ -phase; a more elusive phase similar to the  $\alpha$  conformation, but with alternate molecules rotated by  $180^\circ$  in the unit cell.<sup>6</sup> Similarly, the neat PVDF solution-cast sample shows (041) and (221)  $\delta$ -phase signatures around  $42\text{--}43^\circ$ .

The 1D WAXS data (**Figure 3.7, Table 3.4**) confirms that the AMIM is effective at inducing the  $\alpha$ – $\beta$  crystal phase relaxation of PVDF in both the electrospun and melt-compressed samples but does not alter the unit cells associated with these forms, (monoclinic to orthorhombic

respectively). Therefore, it is reasonable to assume that the AMIM is not incorporated into the PVDF unit cell but will be part of the amorphous region in the lamellar macrostructure.<sup>13</sup> From the FTIR and SAXS/WAXS data here, it can be concluded that while the solution-cast samples have an electroactive phase content just as high as the best electrospun samples, electrospinning with an ionic substance remains the most reliable method for producing a high  $\beta$ -phase fraction.

### 3.3.6. Electrical properties of PVDF nanofibre membranes

The effect of AMIM on the electrical properties of the PVDF nanofibres was investigated, shown in **Figure 3.8**. Circular pieces of aluminium foil were coated with a thin layer of carbon black grease and attached to either side of the nanofibre membranes. It was ensured that this layer was applied homogeneously such that no grease could penetrate the porous membrane, which would lead to erroneous measurements and the potential for shorting if the grease were to penetrate the whole membrane.

It was found that both the conductivity and relative permittivity of the PVDF nanofibres increase by almost an order of magnitude when spun with AMIM. The more homogenous fibre structure of the PVDF/AMIM samples forms due to stable electrospinning in which the electric field exerts a force on the polymer jet constant in time and position. This should increase the degree of crystalline order within the fibres, likely contributing to the higher conductivity, as demonstrated by the larger crystallinity seen in **Table 3.1**. Similarly, the electroactive phase content of the AMIM incorporated fibres, shown in **Table 3.2**, will be a key component of this enhancement.

The incorporation of an ionic substance into the fibres leads to a higher charge mobility, as their presence in the polymer matrix should impede the accumulation of static charges on the polymer surface.<sup>7</sup> Xing *et al.* report an order of magnitude decrease to the volume resistivity of their PVDF/ionic liquid melt mixed blends when increasing their ionic liquid concentration from 2 wt% to 4 wt%, and further order of magnitude drops when increased to 10 wt% and 20 wt% in

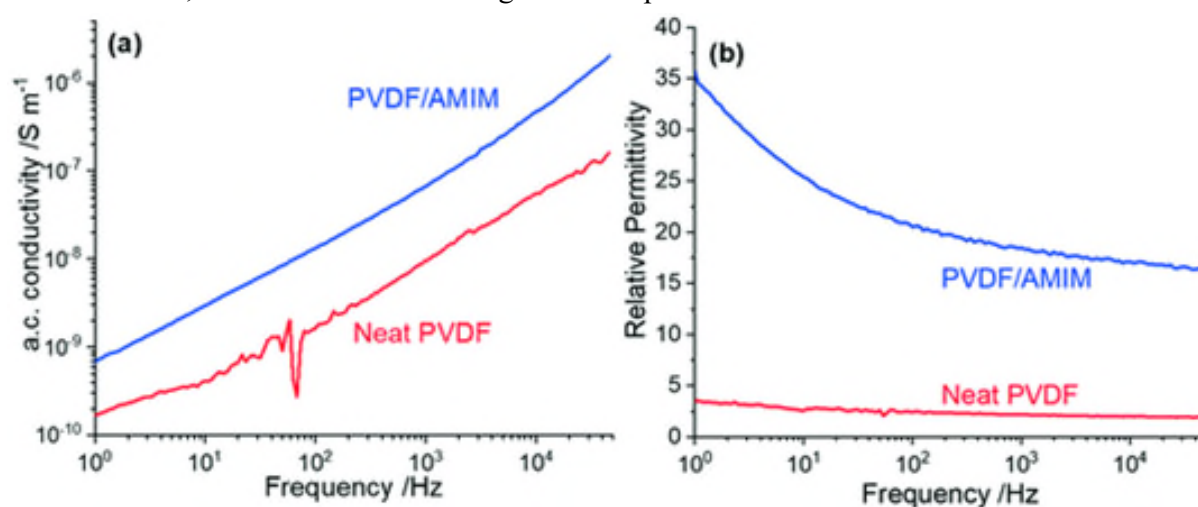


**Figure 0.8.** (a) a.c. conductivity and (b) relative permittivity of the PVDF nanofibre membranes.

turn, while they were unable to probe the conductivity in their neat PVDF, which they attribute to electrostatic charge build-up.<sup>11</sup> They later report that similar conductivity enhancements were seen in their PVDF/ionic liquid electrospun fibres at the same ionic liquid contents due to a decrease in surface charge accumulation. This leads to a conductive, hydrophobic, porous and piezoelectric polymer membrane, highlighting the multifunctional potential of these materials.<sup>10</sup> Hence, increasing the proportion of AMIM in our PVDF samples to similar concentrations (e.g. 10 wt%) could lead to further increases in conductivity. However, it should be noted that the conductivity of the polymer solution needs to be well balanced in the case of electrospinning. A higher conductivity of the solution may cause the solution jet to fall back on to itself between the collector and the spinneret due to charge movement within the jet, inhibiting the formation of beadless, thin and well dispersed fibres.

### 3.3.7. Optimisation of nanofibre production

Further attempts were made to create the most stable electrospinning process at the highest flow rate possible in order to maximise high  $\beta$ -phase PVDF nanofibre throughput. Since stable Taylor cone formation relies on the inverse dependence of electrical stress and surface tension, a balance between solution flow rate and solution conductivity must be found to ensure stable spinning.<sup>1</sup> This was executed by attempting loadings below 1 wt% AMIM concentration in the polymer solution, as a lower solution conductivity would lead to lower electrical shear stresses on the Taylor cone at a given electrospinning voltage. This results in a lower rate of removal of solution from the Taylor cone, allowing for the application higher solution flow rates, resulting in a higher nanofibre throughput. Additionally, to maximise the ferroelectric potential of the nanofibres, PVDF-HFP was substituted for regular PVDF, which was shown to exhibit almost identical behaviour in terms of the electrospinning process, as well as the resultant nanofibre properties.

A variety of AMIM concentrations below 1 wt% were mixed into 20 wt% PVDF-HFP/DMF solutions to produce the nanofibre membranes, ranging from 0.5 wt% down to 0.02 wt%. Firstly, the phase content of the produced nanofibres were estimated by FTIR, shown in **Figure 3.9**. Evidently, even at the low 0.02 wt% AMIM loading, the electrospinning process was capable of producing  $\beta$ -phase dominant PVDF-HFP nanofibres, with no sign of  $\gamma$ -phase content whatsoever in any of the membranes according to the peak at  $1234\text{ cm}^{-1}$ . However, a strange trough just below the usual position of the  $\alpha$ -phase signature at  $763\text{ cm}^{-1}$  seemed to become significantly pronounced at the low AMIM loadings of 0.1 and 0.02 wt%. Additionally, a tiny trough at  $763\text{ cm}^{-1}$  seemed to be rearing its head at around this wavenumber. Nonetheless, even at these low loadings, the nanofibres were clearly extremely  $\beta$ -phase dominant, and no pattern of noticeable decrease in  $\beta$ -phase content was detected by use of **equation 3.1**.



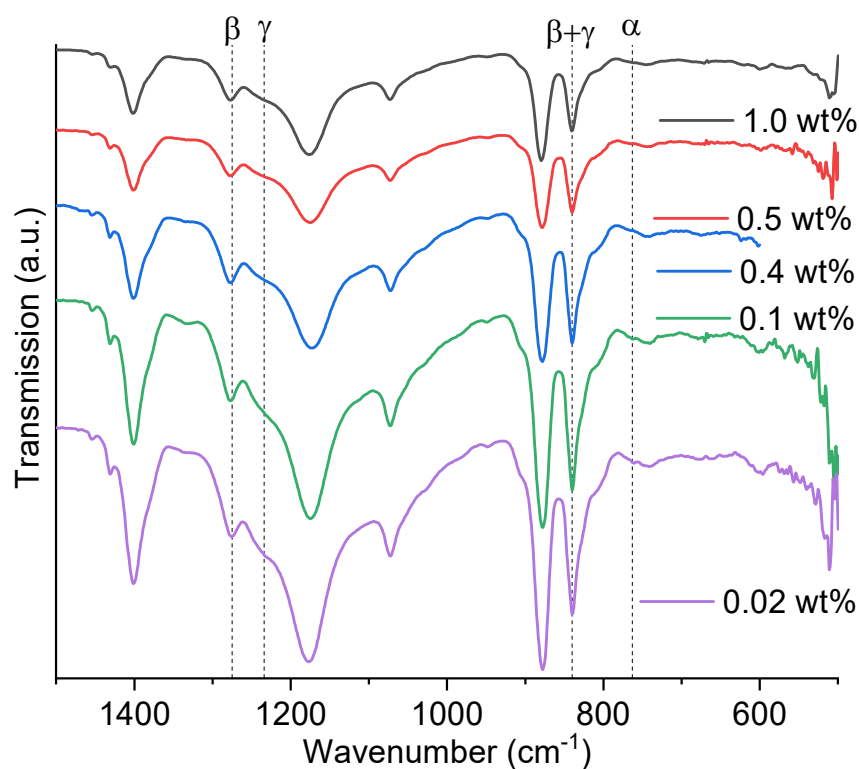


**Figure 0.9.** FTIR of PVDF-HFP nanofibre membranes electrospun with various AMIM concentrations

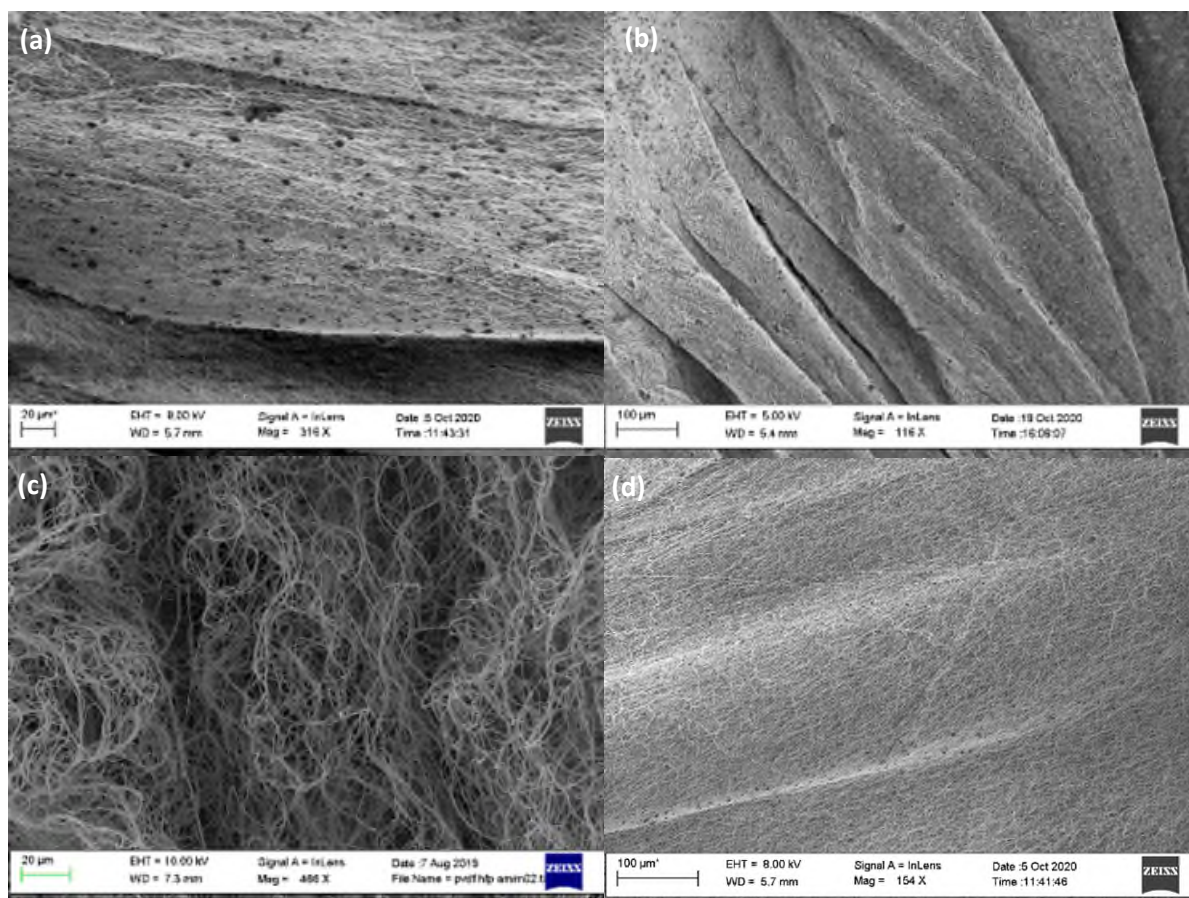


**Figure 0.10.** PVDF-HFP/AMIM nanofibres with AMIM loadings of (a,b) 0.02 wt%, (c) 0.1 wt% and (d) 0.5 wt%.

However, SEM imaging of the produced fibres raised questions about electrospinning at these lower loadings. Micrographs of various low AMIM content nanofibres are given in **Figure 3.10**. At 0.1 wt% AMIM loading and below (**Figure 3.10(a - c)**), there are clear beads appearing in the nanofibre membranes, whereas at 0.5 wt% AMIM loading (**Figure 3.10(d)**), the nanofibres appear completely smooth, as in the 1 wt% case. The 0.4 wt% case also appeared beadless. Along with the potential presence of higher  $\alpha$ -phase content in the 0.1 wt% and below suggested by **Figure 3.10**, it seemed unwise to proceed using nanofibres with lower AMIM content. This transition allowed for a rough doubling in nanofibre production rate by doubling the usable flow rate during electrospinning, achieved by lowering the AMIM loading from 1 wt% to 0.5 wt%. Hence, an AMIM concentration of 0.5 wt% was utilised going forwards.

### 3.4. Conclusions

The advantages of electrospinning have been demonstrated by producing neat PVDF nanofibres which exhibit higher  $\beta$ -phase content compared to melt-compressed and solution-cast samples. The analysis showed that the melt-compressed PVDF contains a high proportion of the paraelectric  $\alpha$ -phase with a low total crystallinity, rendering them impractical for ferroelectric applications. Conversely, the solution-cast PVDF films show high  $\gamma$ -phase content but similarly lacked a significant  $\beta$ -phase crystalline fraction. Since the solution-cast sample has a slightly higher total crystallinity than the electrospun sample, the technique may be useful if highly crystalline  $\gamma$ -phase PVDF films are desired.

Furthermore, the ionic liquid AMIM has been shown to assist the electrospinning of PVDF by producing more homogeneous nanofibres with a higher proportion of the electroactive  $\beta$ -phase. As seen in DSC, AMIM has also had a positive impact on total crystallinity of samples made *via* solution-casting and melt-compression as well as electrospinning. Interestingly, the solution-cast samples show the highest crystallinity, and the PVDF/AMIM electrospun samples also show a high total crystallinity. Combined with the high  $\beta$ -phase contents of the samples, electrospinning of PVDF with AMIM at around 0.5 wt% concentration is found to be the optimal method of producing crystalline, ferroelectric phase-dominant PVDF whilst maximising the production rate of the nanofibres. Electrical impedance spectroscopy also revealed that AMIM enhanced the a.c. conductivity and relative permittivity of the electrospun PVDF nanofibres by an order of magnitude, showing the effect of using AMIM on not just the morphology of the nanofibres, but also their electrical properties. Finally, PVDF-HFP is also shown to be a completely viable substitute for regular PVDF when producing electrospun nanofibres, raising hopes for the prospect of these nanofibres as ferroelectric materials.



### 3.5. References

1. Shin, Y. M., Hohman, M. M., Brenner, M. P. & Rutledge, G. C. Experimental characterization of electrospinning: the electrically forced jet and instabilities. *Polymer (Guildf)*. **42**, 09955–09967 (2001).
2. Nunes-Pereira, J., Sencadas, V., Correia, V., Rocha, J. G. & Lanceros-Méndez, S. Energy harvesting performance of piezoelectric electrospun polymer fibers and polymer/ceramic composites. *Sensors Actuators, A Phys*. **196**, 55–62 (2013).
3. Sharma, M., Srinivas, V., Madras, G. & Bose, S. Outstanding dielectric constant and piezoelectric coefficient in electrospun nanofiber mats of PVDF containing silver decorated multiwall carbon nanotubes: Assessing through piezoresponse force microscopy. *RSC Adv*. **6**, 6251–6258 (2016).
4. Guo, H. *et al.* In-situ synchrotron SAXS and WAXS investigations on deformation and  $\alpha$ - $\beta$  transformation of uniaxial stretched poly(vinylidene fluoride). *CrystEngComm* **15**, 1597 (2013).
5. Wan, C. & Bowen, C. R. Multiscale-structuring of polyvinylidene fluoride for energy harvesting: the impact of molecular-, micro- and macro-structure. *J. Mater. Chem. A* **5**, 3091–3128 (2017).
6. Ma, W., Zhang, J., Chen, S. & Wang, X. Crystalline phase formation of poly(vinylidene fluoride) from tetrahydrofuran/N,N-dimethylformamide mixed solutions. *J. Macromol. Sci. Part B Phys*. **47**, 434–449 (2008).
7. Yee, W. A., Kotaki, M., Liu, Y. & Lu, X. Morphology, polymorphism behavior and molecular orientation of electrospun poly(vinylidene fluoride) fibers. *Polymer (Guildf)*. **48**, 512–521 (2007).
8. Fan, L., Xu, Y., Zhou, X., Chen, F. & Fu, Q. Effect of salt concentration in spinning solution on fiber diameter and mechanical property of electrospun styrene-butadiene-styrene tri-block copolymer membrane. *Polymer (Guildf)*. **153**, 61–69 (2018).
9. Ma, X. *et al.* Molecular orientation in electrospun poly(vinylidene fluoride) fibers. *ACS Macro Lett*. **1**, 428–431 (2012).
10. Xing, C., Guan, J., Li, Y. & Li, J. Effect of a room-temperature ionic liquid on the structure and properties of electrospun poly(vinylidene fluoride) nanofibers. *ACS Appl. Mater. Interfaces* **6**, 4447–4457 (2014).
11. Xing, C. *et al.* Ionic liquid modified poly(vinylidene fluoride): Crystalline structures, miscibility, and physical properties. *Polym. Chem*. **4**, 5726–5734 (2013).
12. He, M. *et al.* Thermopower enhancement in conducting polymer nanocomposites via carrier energy scattering at the organic-inorganic semiconductor interface. *Energy Environ. Sci*. **5**, 8351–8358 (2012).

13. Cai, X., Lei, T., Sun, D. & Lin, L. A critical analysis of the  $\alpha$ ,  $\beta$  and  $\gamma$  phases in poly(vinylidene fluoride) using FTIR. *RSC Adv.* **7**, 15382–15389 (2017).
14. Martins, P. *et al.* Local variation of the dielectric properties of poly(vinylidene fluoride) during the  $\alpha$ - to  $\beta$ -phase transformation. *Phys. Lett. Sect. A Gen. At. Solid State Phys.* **373**, 177–180 (2009).
15. Ryan, A. J. SAXS Correlation Function: New Software at Daresbury. *Fibre Diffraction Review* vol. 3 25 (1994).
16. SasView SAXS analysis software. <https://www.sasview.org/>. (Accessed 21/04/2022)
17. Balta-Calleja, F. J. J. & Vonk, C. G. X-ray scattering of synthetic polymers. *Elsevier* **8**, 317 (1989).
18. Porod, G. Die Röntgenkleinwinkelstreuung von dichtgepackten kolloiden Systemen. *Kolloid-Zeitschrift* **124**, 83–114 (1951).
19. Cui, Z., Hassankiadeh, N. T., Zhuang, Y., Drioli, E. & Lee, Y. M. Crystalline polymorphism in poly(vinylidene fluoride) membranes. *Prog. Polym. Sci.* **51**, 94–126 (2015).
20. Cozza, E. S., Monticelli, O., Marsano, E. & Cebe, P. On the electrospinning of PVDF: Influence of the experimental conditions on the nanofiber properties. *Polym. Int.* **62**, 41–48 (2013).
21. Wang, Y. R., Zheng, J. M., Ren, G. Y., Zhang, P. H. & Xu, C. A flexible piezoelectric force sensor based on PVDF fabrics. *Smart Mater. Struct.* **20**, (2011).
22. Zheng, J., He, A., Li, J. & Han, C. C. Polymorphism control of poly(vinylidene fluoride) through electrospinning. *Macromol. Rapid Commun.* **28**, 2159–2162 (2007).
23. Gomes, J., Nunes, J. S., Sencadas, V. & Lanceros-Mendez, S. Influence of the  $\beta$ -phase content and degree of crystallinity on the piezo- and ferroelectric properties of poly(vinylidene fluoride). *Smart Mater. Struct.* **19**, (2010).
24. Andrew, J. S. & Clarke, D. R. Effect of electrospinning on the ferroelectric phase content of poly(vinylidene difluoride) fibers. *Langmuir* **24**, 670–672 (2008).
25. Martins, P., Lopes, A. C. & Lanceros-Mendez, S. Electroactive phases of poly(vinylidene fluoride): Determination, processing and applications. *Prog. Polym. Sci.* **39**, 683–706 (2014).
26. Anousheh, N. & Soldera, A. Influence of regio-irregular structures on thermal behaviour of PVDF. *Polymer (Guildf)*. **125**, 154–160 (2017).
27. Xing, C. *et al.* Novel multifunctional nanofibers based on thermoplastic polyurethane and ionic liquid: towards antibacterial, anti-electrostatic and hydrophilic nonwovens by electrospinning. *Nanotechnology* **26**, 105704 (2015).
28. Kim, W. J., Han, M. H., Shin, Y. H., Kim, H. & Lee, E. K. First-Principles Study of the  $\alpha$ - $\beta$  Phase Transition of Ferroelectric Poly(vinylidene difluoride): Observation of Multiple Transition Pathways. *J. Phys. Chem. B* **120**, 3240–3249 (2016).
29. Song, D., Yang, D. & Feng, Z. Formation of  $\beta$ -phase microcrystals from the melt of PVDF2-

- PMMA blends induced by quenching. *J. Mater. Sci.* **25**, 57–64 (1990).
30. Gregorio, R. & Borges, D. S. Effect of crystallization rate on the formation of the polymorphs of solution cast poly(vinylidene fluoride). *Polymer (Guildf)*. **49**, 4009–4016 (2008).
  31. Jurczuk, K., Galeski, A., Mackey, M., Hiltner, A. & Baer, E. Orientation of PVDF  $\alpha$  and  $\gamma$  crystals in nanolayered films. *Colloid Polym. Sci.* **293**, 1289–1297 (2015).
  32. Martins, P., Costa, C. M., Benelmekki, M., Botelho, G. & Lanceros-Mendez, S. On the origin of the electroactive poly(vinylidene fluoride)  $\beta$ -phase nucleation by ferrite nanoparticles via surface electrostatic interactions. *CrystEngComm* **14**, 2807–2811 (2012).

## Chapter 4

### Electrospun polymer nanocomposite dielectrics

#### 4.1. Introduction

Metal organic frameworks (MOFs) are an emerging class of nanoparticles which are garnering increasing attention for use in various green technologies due to their unique combination of properties.<sup>1-3</sup> They are formulated by use of a metal complex as a nucleating agent for organic ligands to co-ordinate and form a core-shell structure. The stability and highly porous, tunable structures of MOFs have led to significant interest for use in applications including gas adsorption and storage, drug delivery, catalysis, and sensing technologies.<sup>4-8</sup> As the necessity to decrease environmental impact in energy production, storage and conversion mechanisms has become increasingly clear, demand for clean electrocatalysts for use in fuel cells has increased. For example, in recent years, traditional platinum-based oxygen reduction reaction (ORR) catalysts have become increasingly scarce and expensive.<sup>3,9</sup>

Zeolitic imidazole frameworks (ZIFs) have high chemical and thermal stabilities that make them applicable in a wide variety of hostile environments.<sup>9-12</sup> This is especially useful for cleaning contaminated water from nuclear plants or reducing greenhouse gas emissions from power stations and industry.<sup>13-16</sup> This property had led to great interest in ZIF coated nanofibres, which maybe formed by nucleating ZIF growth in a solution in which a nanofibre membrane is submerged. For these reasons, ZIF-coated nanofibre membranes are garnering increasing attention as durable, predominately organic alternatives to traditional filtration devices. Their ability to capture and store a variety of gas molecules, metal ions and hydrocarbons make them highly effective for cleaning gaseous and liquid wastes, as well as separating mixtures.<sup>2,17-21</sup>

Two of the most investigated and utilised ZIF structures are the Zinc based ZIF-8 and the Cobalt based ZIF-67. ZIF-67 crystals are preferred for adsorption in highly acidic environments due to its high stability and unhindered adsorption capabilities in such conditions.<sup>16,22</sup> ZIF-8 is renowned for its particularly high thermal stability and resistance to hydrolysis, slightly more so than ZIF-67.<sup>10,23</sup> The selection of the ZIF MOF to be used in a given application is largely down to the crystal size, with ZIF-8 having a typically smaller size in given growth conditions than ZIF-67. When coating electrospun nanofibres, this is of utmost importance, as the ZIF must adhere sit on the surface of the nanofibres, otherwise the composite becomes more akin to a ZIF mat than a porous membrane. Niu *et al.* also developed a method to construct ZIF MOFs utilising both Cobalt and Zinc core metal complexes, forming what we denote as BiZIF, which has properties intermediate of ZIF-8 and ZIF-67.<sup>9,24</sup>

In this work, multilayer polymer composites incorporating polyacrylonitrile (PAN) and PVDF-HFP/AMIM (henceforth denoted as PVFHA nanofibres) with ZIF were constructed. ZIF-8, ZIF-

67 and BiZIF nanoparticles have been directly grown on PAN and PVFHA nanofibre membranes of PAN, and the previously developed PVFHA nanofibres. The most appropriate ZIF for each nanofibre was selected after observing their growth. These fibre membranes were then incorporated into multilayer polymer laminates to evaluate their capacity for energy storage. To ensure a minimum degree of ferroelectricity and potentially initialise polarisation in the ZIF nanoparticles, PVFHA nanofibres are utilised in all the composites constructed here. Additionally, when determining an appropriate layer structure for these multilayer laminates, the layer contacting the electrode must be carefully selected. Due to its thermal properties, PAN will not enter the melt phase during hot-pressing, so if used as an outer layer, it would likely lead to the laminate having poor structural integrity. Conversely, the PVDF-HFP layer should not be substantially melted by the hot-pressing process as to avoid destroying the high  $\beta$ -phase content imbued by electrospinning. Additionally, if the intention is for ZIF to become a site for charge storage, the ZIF crystals should not be adjacent to electrodes where that stored charge may easily leak. Rather free charges should be able to travel through the layered structure reasonably easily such that it can reach the ZIF. Hence neither nanofibre membrane is considered suitable as an electrode contacting layer, and instead a solution cast PVDF film is selected as the most suitable alternative to ensure high structural integrity of the laminates produced.

## **4.2. Experimental**

### **4.2.1. Materials**

PAN powder (Sigma-Aldrich 181315) was used for electrospinning PAN nanofibres, and PVDF powder (Solef 5130) was utilised for casting the thin film outer layers of the laminate structures. Cobalt(II) nitrate hexahydrate ( $\text{Co}(\text{NO}_3)_2 \cdot 6\text{H}_2\text{O}$ , Alfa-Aesar 36418), zinc nitrate hexahydrate ( $\text{Zn}(\text{NO}_3)_2 \cdot 6\text{H}_2\text{O}$ , Acros Organics 211662500) and 2-methylimidazole (2MI, Sigma-Aldrich M50850) were used to create the ZIF metal-organic frameworks. Methanol (MeOH), used as the solvent for ZIF growth, was purchased from Sigma-Aldrich.

### **4.2.2. Electrospinning**

Electrospun PAN/2MI nanofibres were prepared with the Spraybase CAT000001 electrospinning instrument. Using similar ratios to Niu *et al.*, PAN powder was dissolved in DMF at a 10 wt% ratio, along with 2MI at 4 wt%.<sup>9</sup> Pure PAN nanofibres were constructed from the same solution, simply without adding 2MI. This solution was stirred at 60 °C for 36 hours to form a completely homogeneous solution. PAN fibre membranes were electrospun for between 1-3 hours with a spinneret-collector distance of 10 cm at voltages from 8 to 9 kV

(resulting in electric fields of 80-90 kV/m) and a spinning rate of 1 ml/hr. Fabrication of the PVFHA nanofibres is as described in the previous chapter.

#### 4.2.3. Synthesis of ZIF coated nanofibre membranes

BiZIF coating of PAN nanofibres was performed in a similar manor to that described by Niu *et al.*<sup>9</sup> A bimetal solution containing 148.5 mg  $\text{Zn}(\text{NO}_3)_2 \cdot 6\text{H}_2\text{O}$ , 291.0 mg  $\text{Co}(\text{NO}_3)_2 \cdot 6\text{H}_2\text{O}$  and 15 ml of methanol was first fabricated. After a few minutes of room temperature stirring to ensure homogenous dissolution of the metal complexes, the PAN/2MI fibre membrane was dipped in the solution for 1 hour to nucleate the ZIF formation. The solution beaker was lightly mixed by hand periodically during this period to ensure the solution permeated the membrane as thoroughly as possible. Meanwhile, a 5 ml solution of methanol containing 492.0 mg of 2MI was prepared with room temperature stirring, resulting in a total 1:2:12:494 Zn:Co:2MI:MeOH molar ratio in the solution. After the initial hour of exposure, this was then added dropwise to the metal solution to accelerate the BiZIF formation. ZIF-8 and ZIF-67 coated PAN nanofibres were prepared in a similar manor. PAN/2MI nanofibres were dipped in either a solution of  $\text{Zn}(\text{NO}_3)_2 \cdot 6\text{H}_2\text{O}$  or  $\text{Co}(\text{NO}_3)_2 \cdot 6\text{H}_2\text{O}$ , but this time at a molar ratio of 1:4:625 Zn/Co:2MI:MeOH, inspired by Gao *et al.*<sup>13</sup> In any case of ZIF growth, the ZIF was allowed to grow for various periods to discern how long it would take for the MOFs to fully grow, but not too long that oversized MOFs coat and smother the fibres. In the end, a growth period of 3-4 hours was found to be sufficient to for full growth of any of the ZIF MOFs. The PAN fibre membrane was then removed from the solution and washed at least 3 times with methanol, until the washing solution lost any cloudy (ZIF-8) or purple (ZIF-67 and BiZIF) tint. The membrane was then dried by vacuum filtration to remove any remaining solution within pockets of the nanofibre membrane, and then placed in an oven overnight at 40 °C. Additionally, PVDF-HFP/AMIM (PVFHA) nanofibres were coated in ZIF-8 and BiZIF MOFs by the same method, with the notable difference that the nanofibres do not contain any 2MI. Hence the PVFHA nanofibres were only exposed to the metal solution for 10 minutes (with mild stirring) to ensure penetration of the metal ions far into the membrane. ZIF growth was nucleated once the 2MI/methanol solution had been added. Again, MOFs were allowed to grow for 3-4 hours, and the same washing and drying procedure was applied.

#### 4.2.4. Processing of PAN/ZIF/PVFHA multilayer composites

To investigate the polarisability of ZIF coated nanofibres, multilayer dielectric polymer composites incorporating PAN/ZIF and PVFHA/ZIF have been constructed. A few compositions were initially attempted to discern which would produce the most cohesive and efficient energy storage structure. Of course, these come hand in hand; good structural integrity

ensures that breakdown events struggle to trigger due to the lack of voids and defects in the structure, meaning higher electric fields can be applied and the sample may be polarised further. Two kinds of multilayer polymer laminates were thus fabricated from the various nanofibres by a hot-pressing process. First, a five-layer structure incorporating both PAN/ZIF and PVFHA nanofibres was constructed as shown in **Figure 4.1(a)**. The outer PVDF solution cast layers were first made by a doctor blading process. This provides protection to the inner fibre layers during hot-pressing and effectively seals the laminate together. PVDF powder was added to a

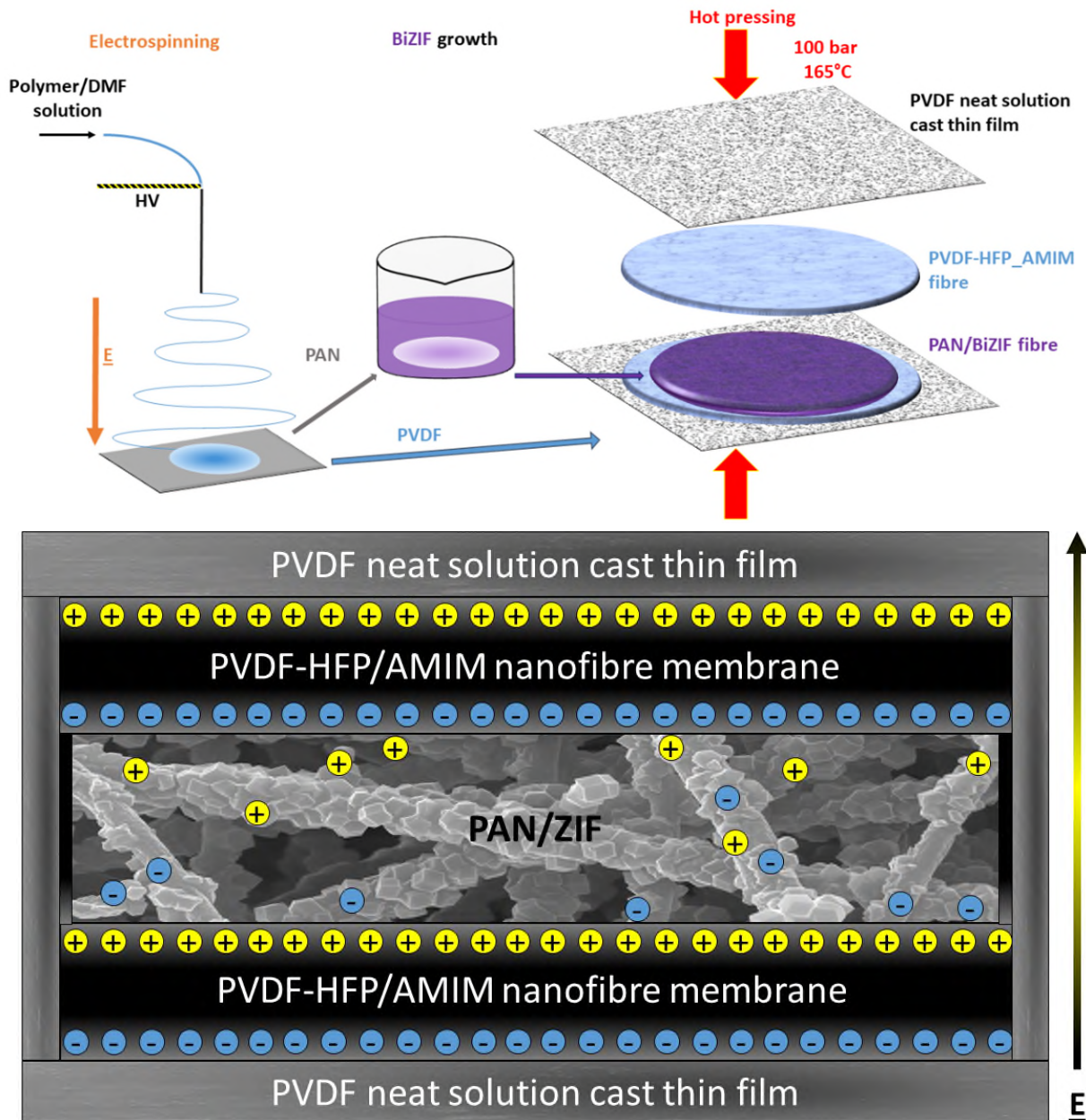


**Figure 0.1. (a)** Schematic showing how the sandwich structured laminate ZIFLAM is formed. After the electrospinning process, the PAN fibres are coated with the BiZIF nanoparticles and pressed into the sandwich structure with the PVDF-HFP/AMIM (PVFHA) fibres and the solution cast PVDF films as shown. PANLAM was fabricated with an identical method without ZIF growth. **(b)** provides a schematic of the cross-section of the resulting laminate, with charge storage sites indicated.

DMF solution at 10 wt% loading, then stirred overnight at 60 °C in an oil bath. This was then cast onto a Teflon sheet and smoothed into a 200 µm solution layer and allowed to dry overnight at room temperature with the assistance of fans built into the doctor blade apparatus. The produced films were  $\leq 50$  µm thick and had large lateral size, exceeding that of the inner layers, meaning the outside of the laminate will be sealed during pressing. The individual layers of the sandwich structure were placed on top of each other between two Teflon sheets, ensuring that the layers became sequentially larger in area from the centre outwards to prevent the layers from overlapping at a weight ratio of 1:10:20 PVDF:PVFHA: PAN/BiZIF. The stack was then hot-pressed at 165 °C for 20 seconds after a degassing phase intended to remove any gas between the layers of the composite, as well as to provide some initial melting. For the first ten seconds of continuous pressing, the sandwich structure was pressed at 40 bar, followed by 100 bar for a further 10 seconds. The short period of pressing was used to prevent the PVFHA nanofibre membrane from melting, halting the transformation from the  $\beta$ -phase to the  $\alpha$ -phase, while still melting the outer PVDF solution cast layers. Since the outer layers are in closer contact to the heated metal plates, these should melt most easily, so the short pressing period should ensure this layer takes on the bulk of the heat and melt together at the edges of the laminate, providing structural integrity. Their  $\leq 50$  µm thickness means this happens readily upon pressing, despite the low pressing period. The sample is then quenched in an ice bath upon removal from the hot-press to maximise the PVDF crystallinity and  $\beta$ -phase (re)-formation during cooling from the melt. The high temperature (near the  $\sim 170$  °C melting point of PVDF-HFP) used to form the laminate was considered necessary to make the potentially immiscible layers as structurally cohesive as possible, as well as to reduce the number of defects in the sample. Two laminates were produced for comparison; one with a neat PAN membrane (named PANLAM) and one with PAN/ZIF (named ZIFLAM). As shown in **Figure 4.1(b)**, the concept here is that the ZIF nanoparticles in the central layer may act as sites for charge storage, in a similar manner to their ability to capture gas molecules, increasing net polarisation. This may be particularly pronounced near to the interface between the highly polar PVFHA nanofibre layers. Interfacial polarisation in the PVFHA nanofibres – which in turn produces increased orientational polarisation in the PVDF-HFP near the PVFHA-PAN/ZIF interface – will lead to space charge accumulation near this interface. Hence, nearby ZIF particles may act as charge storage banks, increasing the overall polarisation around the interface. This could also decrease the free charge density in the laminate, potentially impeding electrical breakdown, which may be further pronounced by the electrically insulating nature of ZIF. Additionally, similar to the previous chapter, PVFHA nanofibres were pressed into 3-layer laminate structures utilising polymethyl methacrylate (PMMA) as an outer layer to insulate the PVFHA nanofibres electrically and physically. The 3-layer laminates were pressed at the somewhat low temperature of 140 °C such



that much of the PVDF-HFP crystallinity induced by electrospinning is retained, and significant disruption of the ZIF coated nanofibre structure in the central layer is avoided.

#### **4.2.5. Characterisation**

Scanning electron microscopy (SEM) imaging was performed with the same method as described in section 3.2.1. Energy dispersive x-ray spectroscopy (EDS) was also performed alongside SEM with an Oxford Instrument Xmax<sup>N</sup> 80 SDD (silicon drift detector) EDS detector. X-Ray diffraction measurements were made on a 3rd generation Malvern Panalytical Empyrean equipped with multicore (iCore/dCore) optics and a Pixcel3D detector operating in 1D scanning mode. A copper tube was used giving Cu K <sub>$\alpha$ 1/2</sub> radiation (1.5419Å) and a beam knife was used to reduce air scatter at the low angles. Scans were made in the range  $2\theta = 5 - 70^\circ$  with a step size of  $0.0263^\circ$  and a counting time of  $\sim 334$  s/step.

Impedance spectroscopy was carried out with the same method as described in section 3.2.1, except that samples were coated with carbon black grease (MG Chemicals) instead of silver paint. Measurements were taken between  $10^0$  and  $10^6$  Hz. A Precision LCII Ferroelectric Test System from Radiant technologies was used to measure the polarisation of the samples and determine their ferroelectric and charge storage properties by use of monopolar displacement electric field (P-E) hysteresis loops. Samples had small pieces of carbon black tape applied to each side of the composite to decrease contact resistance between the tape and the electrodes of the testing apparatus. The maximum electric field applied in these loops was taken from 10 kV/cm up to the electrical breakdown field of the samples, with all fields applied at a frequency of 10 Hz.

### **4.3. Results and Discussion**

#### **4.3.1. Electrospinning**

Multiple solvents are often used for electrospinning PAN, notably DMF, THF and acetone.<sup>25,26</sup> Usually, a solvent mixture is used to hit a sweet spot of solution volatility, which is largely dependent on the boiling points of the solutions. During our attempts to spin from a solution of PAN powder dissolved in DMF/acetone mixtures at DMF:acetone solution ratios of 50:50, 70:30 and 80:20, we found issues with the stability of the solution. It appeared that the high volatility of the solution induced by the acetone lead to unstable spinning, as intermittently the solution jet would begin spraying with seemingly no cause. Adding THF to the solution had a similar, but less extreme affect. Even when only utilising 10% THF in the solution, the solution droplet is clearly unstable. The PAN/DMF solution in contrast spun very stably once a suitable balance between electric field and solution flow rate was reached such that the solution is drawn from the spinneret at the same rate it is fed in. Hence, an 100% DMF solution was ultimately

used with a ratio of 10 wt% PAN. Once this method had been established, PAN was also electrospun with 2MI to promote nucleation of ZIF growth on the surface of the nanofibres upon exposure to a solution containing the cobalt and/or zinc metal complexes. 4 wt% 2MI was added to the PAN/DMF solution, similar to the ratios used by Niu *et al.*<sup>9</sup> The fibres as produced are shown in **Figure 4.2**. In the case of either pure PAN or PAN/2MI, the nanofibres possessed similar morphologies, both on their surface and in terms of their diameter. Typically, the fibre diameters vary between 500-800  $\mu\text{m}$ , extremely large compared to the PVFHA nanofibres, which have an average diameter closer to 200  $\mu\text{m}$ . The morphology of the PVFHA nanofibres is as described in chapter 3.

Non-polar PVDF (e.g.  $\alpha$ -phase PVDF) and PAN are immiscible in the melt phase, owing to the difference in their solubility parameters.<sup>27</sup> However, both polymers may be polar (with PAN possessing a dipole due to its -CN group), and hence the miscibility may be improved by enhancing this interaction. For example, polar solvents may be used to form a miscible solution.<sup>28</sup> However, as the polymer layers are to be hot-pressed to form the multilayer laminate, the use of a solvent is not possible. Additionally, due to the relative thermal stability of PAN over PVDF, developing a hot-pressing method which produces a cohesive multilayer structure is difficult. PAN does not undergo any phase changes before the threshold of PVDF melting at  $\sim 170^\circ\text{C}$ , at which point the  $\beta$ -PVDF formed by electrospinning will be lost to the melt phase, likely producing  $\alpha$ -PVDF upon recrystallisation from the melt instead. In fact, PVDF-HFP may begin phase transitions as it enters a partial melt phase prior to this threshold at around  $145^\circ\text{C}$  and upwards.<sup>29</sup> So, hot-pressing a structure involving both materials will inevitably produce some issues of structural integrity. The polar ionic liquid 1-allyl-3-methylimidazolium chloride (AMIM) utilised for electrospinning may help to enhance interactions between the two polymer layers, as this has been shown to help with miscibility in solution.<sup>30</sup> As the PVDF-HFP nanofibres should enter a partial melt-phase, the interactions between AMIM and the surrounding polymer layers may be enhanced.

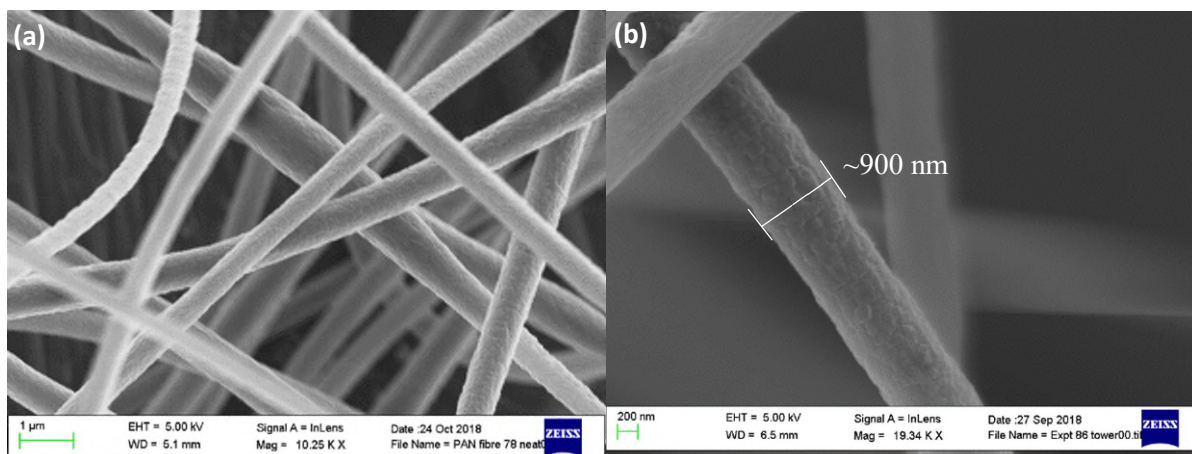


**Figure 0.2.** SEM images of as spun (a) PAN nanofibres and (b) PAN-2MI nanofibres.

#### 4.3.2. Morphology of PAN/ZIF

PAN/ZIF fibres were prepared by both the in-situ technique, in which PAN/2MI fibres being exposed to a solution containing the metal complexes, and the extrinsic technique, in which neat PAN nanofibres are exposed to a solution containing metal complexes first, followed by addition of 2MI to the solution to initiate ZIF growth. All 3 forms of ZIF are grown on the nanofibres, with SEM images of all 3 shown in **Figure 4.3**. From initial attempts at coating pure PAN nanofibres with ZIF particles, it seems the ZIF-67 coating is the least suitable for PAN nanofibres. Despite their much larger size than the PVFHA nanofibres, the PAN nanofibres are still far too small in comparison to typical ZIF-67 MOFs for them to coat the fibres homogeneously. In contrast, at their best, both ZIF-8 and BiZIF very effectively coat the PAN nanofibres. In the case of ZIF-8 however, the ZIF particles have not formed complete ZIF particles such as those seen in the case of ZIF-67. The ZIF-8 MOFs seem to have nucleated in numerous locations along the surface of the nanofibres and have impeded each other's growth due to how closely the individual particles are packed. This results in a loss of the polyhedral structure of ZIF and forms an intergrown structure of ZIF MOFs instead.<sup>2,20,31</sup> The BiZIF crystals show a similar phenomenon, with clear intergrowing of ZIF nanoparticles around the nanofibre surface, although on this occasion the ZIF crystals were far larger in size and seem to have attained some form of polyhedral structure.

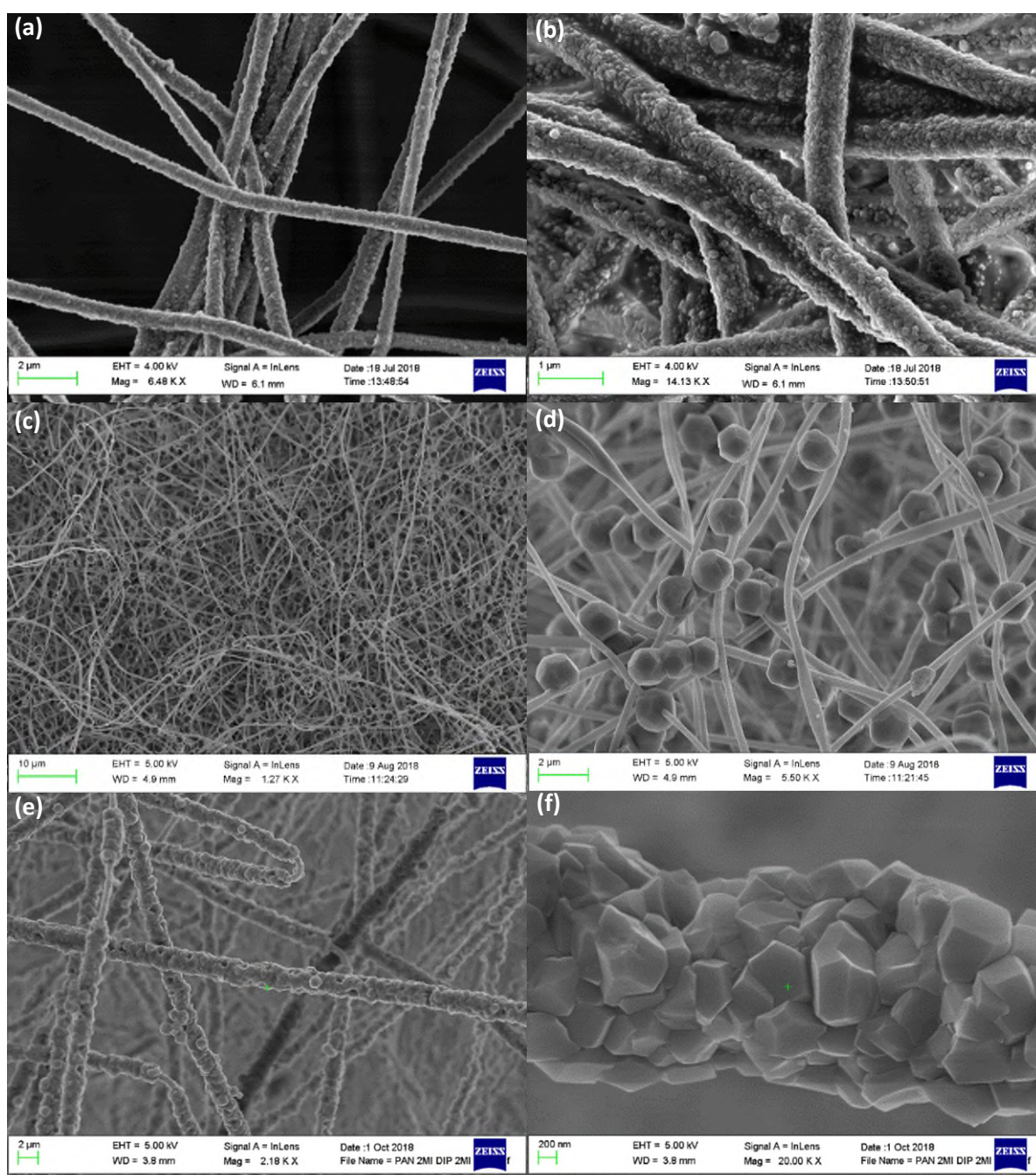


**Figure 0.3.** SEM images showing the morphology of PAN/ZIF-8 nanofibres (a, b), PAN/ZIF-67 nanofibres (c, d) and PAN/BiZIF nanofibres (e, f), all grown for 3 hours. ZIF-8 showed good adherence of ZIF to the nanofibres, although in many regions ZIF agglomerates between fibres built up, and in general zeolitic structure was not predominantly present. ZIF-67 crystals proved too large to coat the nanofibres once grown into fully zeolitic form, with sizes larger than individual nanofibres. BiZIF samples typically showed the best ZIF-fibre adherence across the whole sample, with less agglomeration and a more polyhedral structure than that seen in the PAN/ZIF-8 nanofibre composites.



### 4.3.3. Crystalline structure of PAN/ZIF nanofibres

To investigate the crystalline structure of the produced BiZIF and the effect of the PAN nanofibres on the produced nanoparticles, precipitates of the ZIF growth solution containing the polymer nanofibres were acquired and characterised by XRD. After the newly coated ZIF nanofibers are sufficiently washed, precipitates were formed by centrifuging a portion of the methanol solution used to wash the fibres, producing a ZIF powder once the solution had evaporated. Two precipitates are developed; one from the solution in which the BiZIF was grown with the PAN nanofibre present, and another from a solution without any nanofibres. The aim was to evaluate if the structure of the BiZIF had been altered due to the presence of the nanofibres. The difference between the ZIFs grown with and without the nanofibres is clear in the SEM micrographs shown in **Figure 4.4(c, d)**. The BiZIF grown with the PAN nanofibre clearly has a more regular external structure, implying the growth has largely saturated, which is supported by the merging of crystals at the regular interfaces and edges of the ZIFs. In contrast

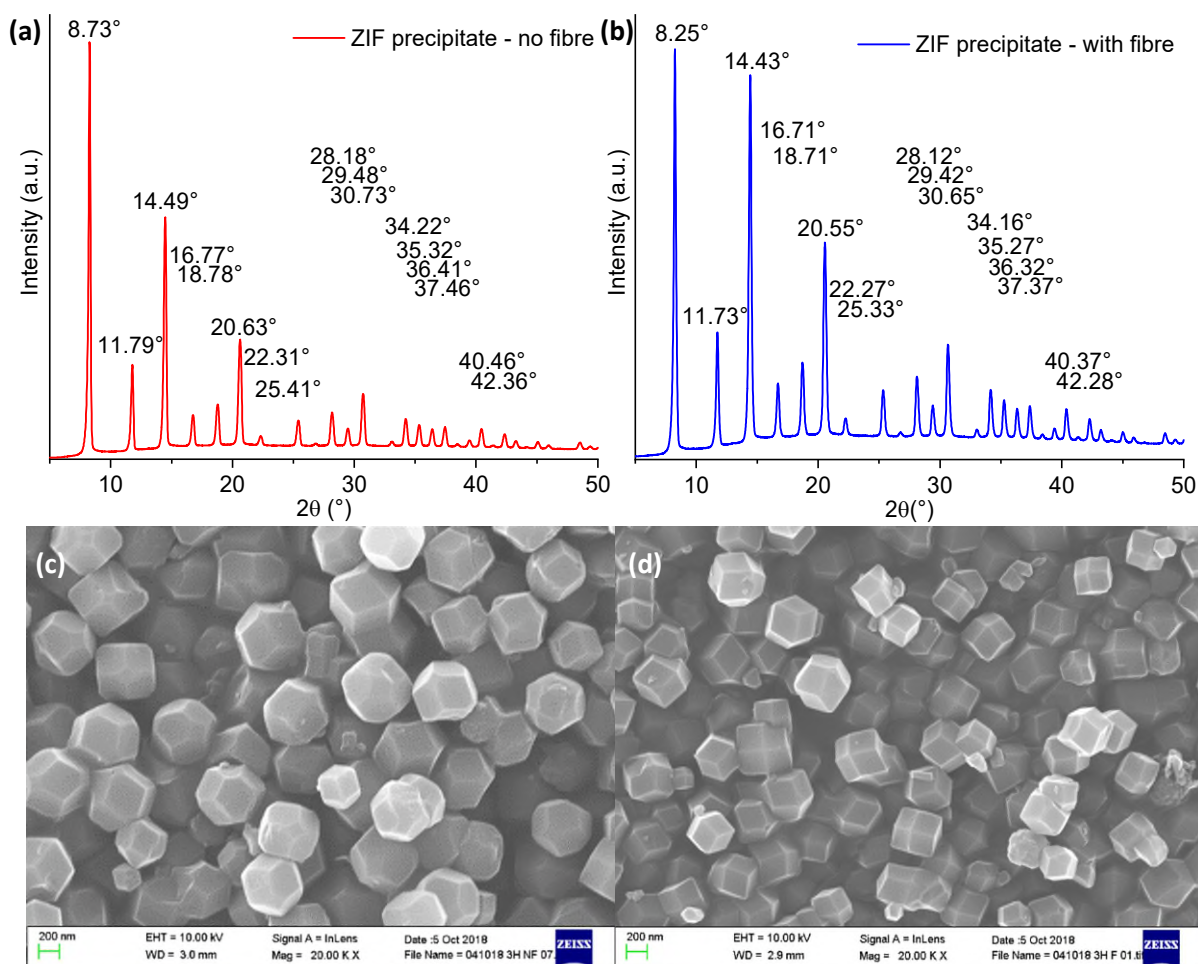


**Figure 0.4.** X-ray diffraction spectra and SEM images of BiZIF precipitates from samples grown without (a) and with (b) PAN nanofibres, along with SEM images of the resultant BiZIF precipitates with (c) and without (d) the nanofibre present. The peak shift from 8.73° to 8.25° shows a substantial shift in crystal structure due to the change in crystal structure with fibre addition.

the ZIF grown in isolation are largely still growing themselves, indicated by their larger number of edges, smoother vertices on the MOF surface and – in the case of the ZIF nanoparticles exhibiting these behaviours – a lower degree of merging. The XRD spectra (**Figure 4.4 (a, b)**) confirm this, as the ‘with fibre’ precipitate shows a systematic minor shift of peaks to lower  $2\theta$ , indicative of a larger crystal size.<sup>14</sup> Additionally, the relatively stronger set of peaks observed in the spectra of the ZIF grown on the PAN nanofibre surface are evidence that the growth is more matured, with a multitude of crystallographic planes giving comparably strong signatures in the spectra.<sup>13</sup> For comparison, **Figure 4.5** gives XRD spectra of the PAN nanofibres in isolation alongside the PAN/BiZIF nanofibres. The broad hump imposed on the spectra of the PAN/ZIF nanofibre by the presence of PAN is clearly visible and may also be contributing to a lesser extent to the spectra in **Figure 4.5(b)**. This PAN/ZIF spectra also shows similar signatures to the ZIF precipitate grown with the fibre, showing a similar shift to lower  $2\theta$  values, along with a similar broad intensity of a variety of peaks, validating the result in **Figure 4.4(b)**. It is hoped that the more developed crystallinity of the ZIF MOFs also results in a higher dipole moment, and hence a potentially higher polarisability.

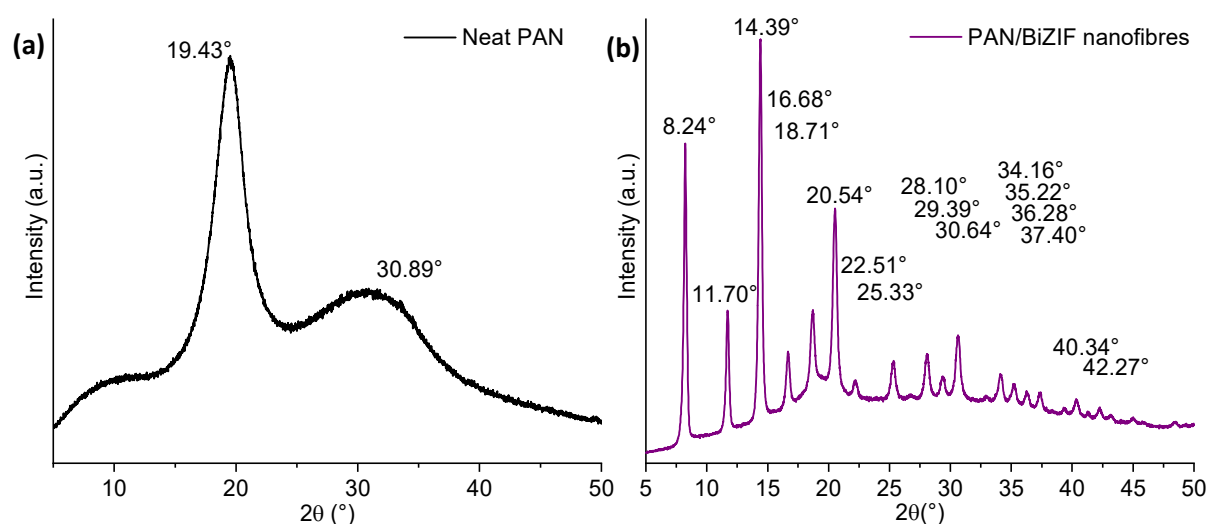


**Figure 0.5.** XRD spectra of (a) a PAN nanofibre and (b) a PAN/BiZIF composite membrane

#### 4.3.4. ZIF growth on PVDF-HFP/AMIM (PVFHA) nanofibres

Once the growth conditions of ZIF on PAN nanofibres had been optimised, growth of ZIF MOFs was also attempted on the PVFHA nanofibres. It was anticipated that developing this growth methodology would be more difficult, as the PVFHA nanofibres are typically much smaller in diameter than PAN, so developing a homogenous coating of fully grown ZIF crystals is not necessarily straightforward. Since the ZIF-67 MOFs were too large to form homogenous coatings of the thicker PAN nanofibres, this was not attempted on PVFHA nanofibres. SEM micrographs of the PVFHA nanofibre membranes coated with ZIF-8 are shown in Figure 26. In the case of ZIF-8, the MOFs either completely overwhelm and agglomerate in the porous

nanofibre membrane (**Figure 4.6(a)**), or they are undergrown (**Figure 4.6(b)**). Generally, ZIF-8 MOFs struggle to coat the nanofibres effectively across the sample, with very few areas showing any continuous coating and many areas showing no coating whatsoever. In general the ZIF-8 seems to have agglomerated in pores in the nanofibre membrane, possibly induced during the washing process as the poorly adhered ZIF MOFs are washed into the membrane pores. In contrast, the BiZIF MOFs seem too large to effectively coat the PVFHA fibres, similar to the case of ZIF-67 coated on PAN. Comparing the structure of the BiZIF MOFs shown in **Figure 4.6 (c, d)** to **Figure 4.6 (c, d)**, the BiZIF is clearly sufficiently grown, as well as agglomerating in many cases between the fibres, similar to the case of ZIF-8. Hence the PVFHA nanofibres overall seem less suitable for ZIF coating than PAN.

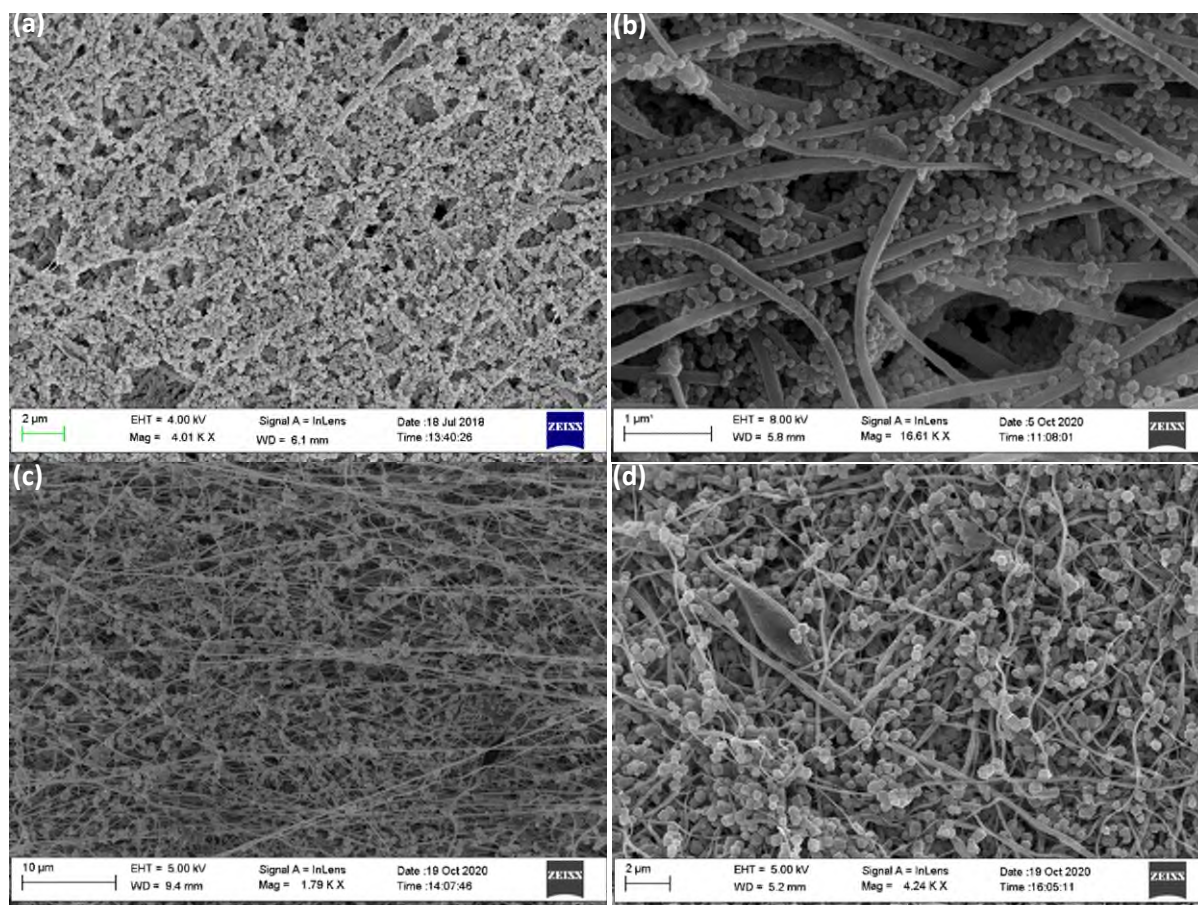


**Figure 0.6.** SEM images of PVFHA nanofibres coated in (a, b) ZIF-8 and (c, d) BiZIF nanoparticles.

#### 4.3.5. PAN/ZIF five-layer laminates

The multilayer ferroelectric composites, constructed as described in the experimental section, were firstly investigated by FTIR analysis, both on the individual components of the laminate as well as the laminates themselves. As can be seen in **Figure 4.7**, the  $\beta$ -phase seems to have been well retained in the PVDF-HFP nanofibres after incorporation into the 5-layered composite structure. There does however seem to have been a partial transition into both the  $\gamma$ -phase and  $\alpha$ -phase in these nanofibres, as a small signature not visible in the neat nanofibres is apparent in

the FTIR spectra of both PANLAM and ZIFLAM. Interestingly, the neat solution cast PVDF – used as the outer layer – seems to also be predominately  $\beta$ -phase, with a hint of the  $\alpha$ -phase also present in the spectra. FTIR was performed on the surface of the composites, meaning both the solution cast and electrospun layers are probed, so which layer is contributing to the various phase signatures is unclear. To gain further insight into potential phase changes in the various layers, SEM micrographs of the cross-sections of the laminates were taken, as shown in **Figure 4.8**. Despite the samples – by eye and physical inspection – not immediately seeming to have an issue of delamination, the SEM images reveal that layer adhesiveness is far from ideal in both composites. In either case, the PVDF and PVFHA layers seem to have stuck together as well as expected, but do not seem to have adhered well to the PAN or PAN/ZIF layers. Thus, as

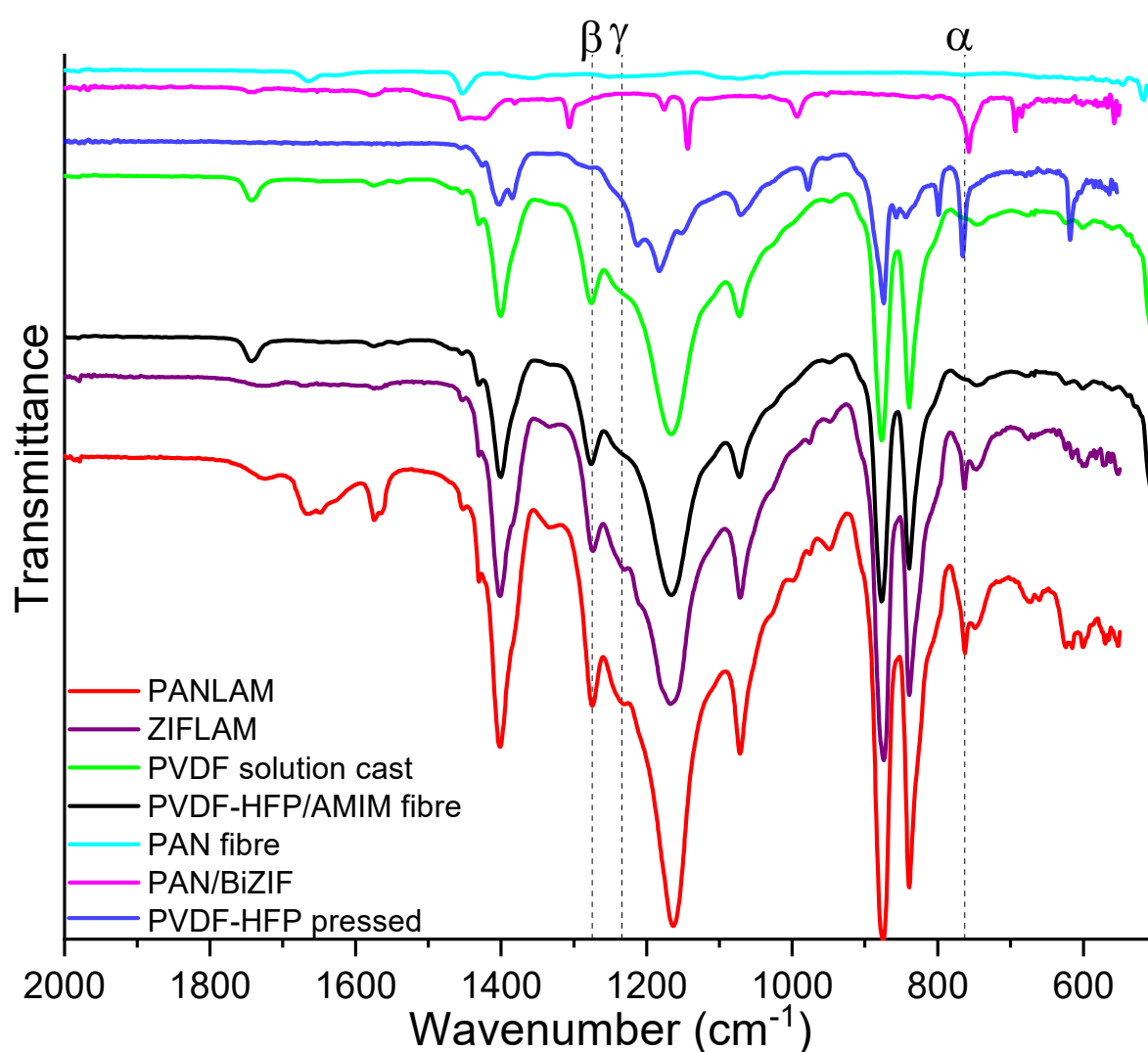


**Figure 0.7.** Fourier Transform Infrared Spectroscopy of the sandwich structured composites and their components. Peaks for the paraelectric  $\alpha$ -phase and polar  $\beta$ -phase, as well as the electroactive  $\gamma$ -phase are highlighted. Electrospun PVDF-HFP/AMIM show a clear  $\beta$ -phase signature, while the hot-pressed PVDF-HFP shows a clear  $\alpha$ -phase signature. Both composites show both  $\beta$ - and  $\alpha$ -phase signatures, implying the partial retention of the crystal structure of the fibres.



feared, this process did not ensure miscibility of the PAN and PVFHA nanofibre layers. The images do however show the unchanged morphology of the PAN and PAN/ZIF fibres, as well as providing confidence that the BiZIF MOFs have been undamaged in this process.

While MOFs have been investigated for their potential in capture of ions and other molecules, their potential for energy storage applications on electrically active nanofibre membranes. ZIF MOFs are known to possess a dipole moment. Mohajer *et al.* measured the dipole moments of various ZIF-8 and ZIF-90 MOFs with varying modifications to the organic linkers, along with their CO<sub>2</sub> uptake.<sup>22</sup> Amongst their measurements, the dipole moment of ZIF-8 was found to be 5.07 D, higher than that of  $\beta$ -PVDF, which sits at 2.1 D.<sup>32</sup> Since the polarity of the ZIF increases the electrostatic interactivity with CO<sub>2</sub> molecules, this is advantageous for their adsorption capacity, although the crystalline morphological changes will also affect this significantly. Izzaouiha *et al.* also showed that CO<sub>2</sub> adsorption in various ZIFs could substantially enhance the dipole moment, giving promise for utilising spent polymer nanofibre/ZIF gas adsorption composite membranes in energy storage applications.<sup>12</sup> However, it is worth noting that these authors measure the dipole moment of ZIF-8 as 0.11D. Considering the lack of data available in literature on the dipole moment of ZIF-8, this casts doubt on the real value, but encourages our investigation into the potential for ferroelectric applications, nonetheless. But, even if ZIF-

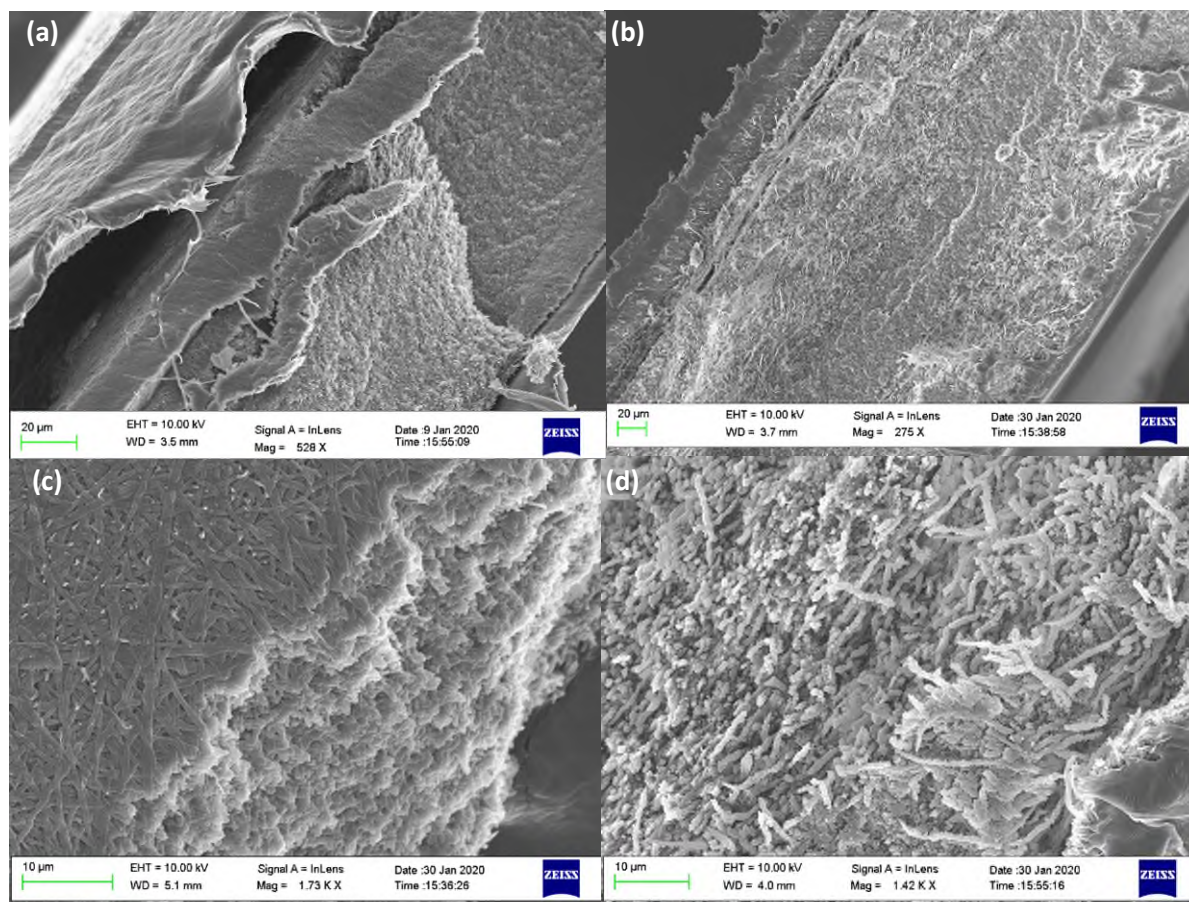


**Figure 0.8.** SEM images of the (a) PANLAM and (b) ZIFLAM cross-sections, alongside higher resolution images of the inner layers of (c) PANLAM and (d) ZIFLAM

8 is known to possess a dipole moment, the polarisability of ZIF-8 is not known too well. Knebel *et al.* measured the ferroelectric properties of a ZIF-8 single crystal, finding no ferroelectric hysteresis, but instead a ‘soft’ lattice movement in the direction of the applied field.<sup>33</sup> The  $\text{Zn}^{2+}$  ions present in the metal complex are known to contribute to polarisation as at low fields – where a net polarisation of the ZIF is observed – the activation energy for polarising the linker molecules is too high for it to manifest. Hence this polarisation must originate in the zinc metal ions. Their ferroelectric measurements show an extremely lossy capacitor, with much of the energy contributing towards shifting the crystal lattice structure, altering the porous properties of the crystal. Although, as ZIF is often used to store ions and other particles, it may be possible for it to act as a store of charge when exposed to a high electric field if ions and other free charges manage to penetrate the MOFs. As such there is hope that ZIF may contribute to the polarisability of the composite despite its seeming lack of intrinsic ferroelectricity.

Hence, despite the issues surrounding delamination, dielectric and ferroelectric testing was still performed on the laminates, the results of which are shown in **Figure 4.9** alongside a PVFHA nanofibre membrane for comparison. It is worth noting that due to the porous nature of the PVFHA nanofibre membranes, the contact area between the electrodes and the PVFHA fibres is hard to determine while using conductive carbon black grease as an electrode for the dielectric tests (**Figure 4.9 (a-c)**). Normally, carbon black grease is used as an electrode to fix this area and decrease contact resistance between the sample and electrodes. This is usually ensured by pressing two pieces of aluminium foil coated in carbon black grease around each side of the membrane, resulting in good contact between the electrodes and the sample. However, carbon black grease easily penetrates this porous membrane, and so the fibres must be allowed to contact the grease without pressing. This means that the permittivity and a.c. conductivity of this sample may be underestimated.

As seen in **Figure 4.9(a)**, the permittivity of PANLAM supersedes that of the PVFHA nanofibres, as well as ZIFLAM, across the whole frequency range of  $10\text{-}10^6$  Hz. In the low frequency regime, the composite seems to reach unreasonably high permittivities however, suggesting the presence of d.c. conduction through the sample. Conversely, ZIFLAM exhibits a permittivity signature more akin with the neat PVFHA fibre membrane, although appears more insulating overall. The a.c. conductivity data (**Figure 4.9(b)**) tells a similar story, with PANLAM exhibiting a higher conductivity than both ZIFLAM and the neat nanofibre membrane. In this case, ZIFLAM also shows a relative increase in conductivity in the low frequency regime, while mirroring the behaviour of the PVFHA membrane in the medium-high frequency range. Investigating the phase angle (**Figure 4.9(c)**), the behaviour of the composites can be better understood. As the frequency decreases, all 3 materials show similar signatures – albeit with differing magnitudes – implying that the PVFHA fibre membranes are the key contributor to the dielectric behaviour of the composites. PANLAM shows the most conductive

behaviour, appearing to respond more in phase with the applied field than its counterparts. This implies it has the most permissive structure to charge carriers, resulting in the high observed electrical conductivity and dielectric permittivity. This is also likely why the permittivity is seen to increase by so much in the low frequency ( $\approx 10^3$  Hz) regime; mobile ions and charges injected at the electrodes will become more responsive in this range, resulting a rapid increase in permittivity. No component of the composite should intrinsically exhibit such high permittivities, implying charge carriers make a significant contribution to the response in this range. These effects are not too surprising, as the outer solution cast PVDF layer is not very insulating, so charge carries may easily be injected from the electrodes, producing a quite conductive structure. Additionally, the lack of adhesion between layers likely leads to a lack of reliable barriers to charge transport in the structure. Interestingly, ZIFLAM shows an even more

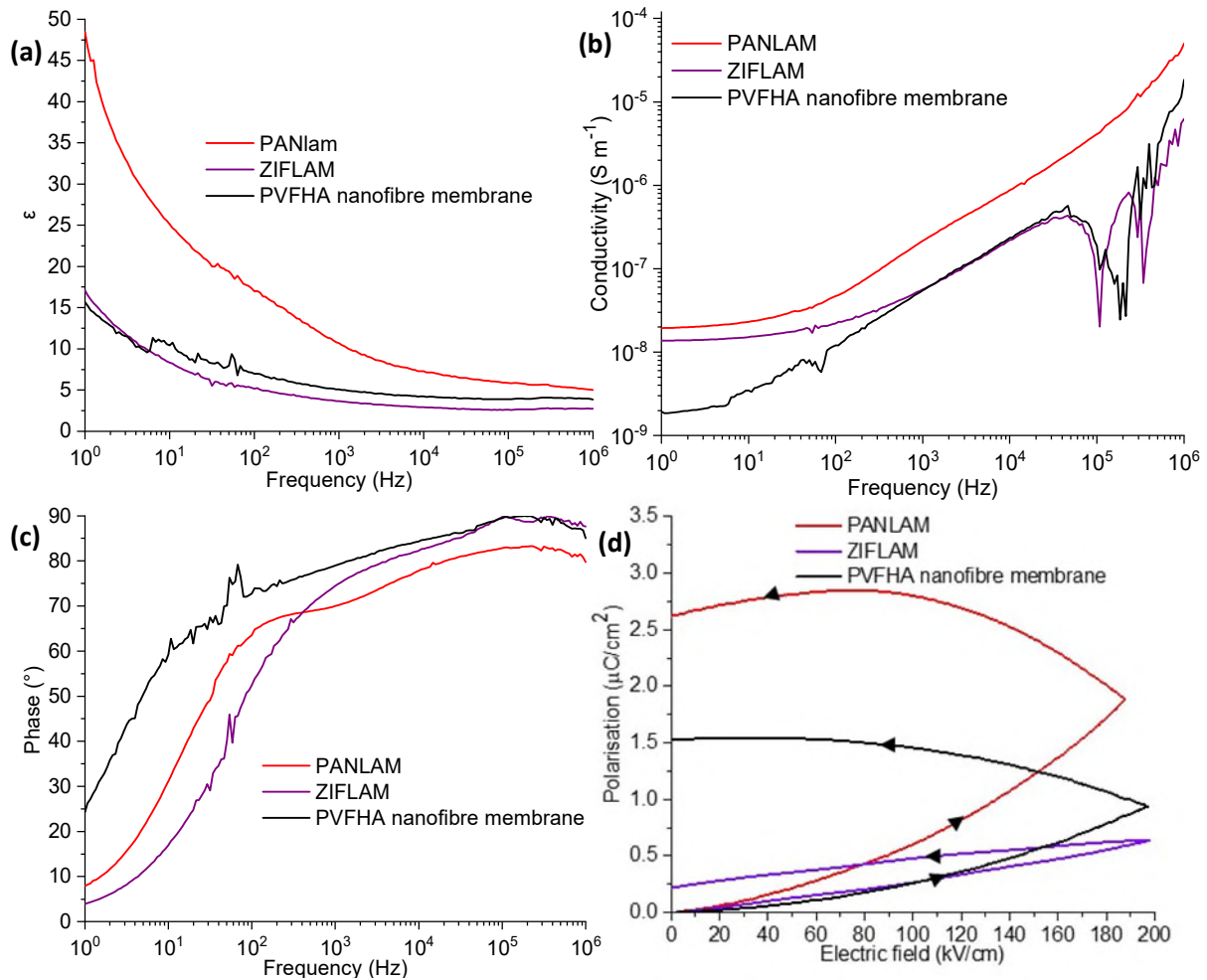


**Figure 0.9.** (a) Permittivity (b) conductivity and (c) phase angle of the PANLAM and ZIFLAM sandwich structured hot-pressed composites, as well as data for a neat PVFHA nanofibre membrane for comparison, measured by broadband impedance spectroscopy. (d) Monopolar electric displacement-field loops measured with a ferroelectric analyser. It is unlikely the behaviour seen in (d) constitutes ferroelectric behaviour, but rather just of extremely lossy dielectrics, who's signatures tend to show massive hysteresis in monopolar test data.<sup>36</sup>

rapid change in phase response to the field at low frequencies, responding more in phase with the field than PANLAM by  $\sim 300$  Hz. This would explain the relative increase in conductivity in the low frequency regime. Although, ZIFLAM also show a permittivity more in line with the neat PVFHA fibre sample, with seemingly no additional contributions in this frequency range. It may be that at these low frequencies, charges are more easily travelling through the composite, but are then being captured by the ZIF in the central layer of the composite, preventing substantial ionic and electronic polarisations and muting any increases in permittivity.

As seen in **Figure 4.9(d)**, the materials also underwent ferroelectric P-E testing, with the electrical breakdown data from these tests given in **Table 4.1**. An electric field was ramped up to a maximum and cycled back down at a frequency of 10 Hz while measuring their polarisation. The maximum polarisation realised in the samples is high for these electric fields, which are far below that of those commonly reached in comparable polymer ferroelectrics.<sup>34</sup> PANLAM manages to exceed an impressive  $2.8 \mu\text{C}/\text{cm}^2$ , whereas the neat PVFHA nanofibre reaches over  $1.5 \mu\text{C}/\text{cm}^2$  and ZIFLAM reaches  $0.64 \mu\text{C}/\text{cm}^2$ . These high polarisations come with the significant caveat that the losses are near 100% in both PANLAM and the neat PVFHA fibre. The fibre membrane exhibiting these losses is expected, as the membrane will provide a high density of mobile charges (not least due to the inclusion of the ionic liquid AMIM), and charges should find the fibre membrane easy to traverse. The remnant polarisation seen in both the PVFHA membrane and PANLAM are large, implying both structures are largely exhibiting high polarisation due to conductive effects. Additionally, the fact the maximum polarisation is reached when the field is decreasing is indicative of an unresponsive sample and an inability to discharge stored polarisation over a short timescale – even when exposed to an opposing electric field. This is obviously highly undesirable for pulsed power applications.

**Table 0.1.** Measured  $E_b$  of the composites and their components

Sample	$E_b$ (kV/cm)
PVFHA fibre	100
PAN/BiZIF fibre	70
PANLAM	150
ZIFLAM	150
PVDF-HFP hot-pressed	160

ZIFLAM in contrast seems to show quite low losses, which may be due to the capturing of charges travelling through the structure by the ZIF in the central layer, meaning the polarisation in the composite may be more easily retained. However, this results in a much more moderate maximum polarisation, and the loss is still significant at around 50%, largely down to a high remnant polarisation at around  $1/3^{\text{rd}}$  of the maximum polarisation. Due to its high thickness, only a moderate electric field of  $\sim 300$  kV/cm was reached in our tests, and ZIFLAM was not observed to experience breakdown in any of our tests. In contrast, PANLAM reliably fails to reach 200 kV/cm without undergoing electrical breakdown, significantly limiting the potential for this structure to deliver high performance at higher fields. Conversely, the PVFHA fibre breaks down over a wide variety of fields between 100 and 400 kV/cm. It is worth noting that the fibrous samples have an inhomogeneous thickness distribution across the sample, meaning electrical breakdown may find a short path through the porous membranes, leading to high variance in breakdown properties.

From this data, the structure utilised in ZIFLAM may be worth investigating further. The lower losses seen in ZIFLAM provide some promise, as they may be preventing significant conduction through the structure. Although there is little evidence here that components other than the PVFHA nanofibres increase the polarisability of the composite overall, as the polarisation reached at 200 kV/cm is higher than that seen ZIFLAM. Attempts made to coat PVFHA nanofibres with ZIF have largely failed due to the small radius of the fibres making it difficult for even the smaller ZIF-8 MOFs (as opposed to the BiZIF used in ZIFLAM) to nucleate and adhere to the surface of the nanofibres. Hence incorporating both ZIF and PVFHA fibres into the same multilayer composite structure via fibre coating may prove difficult without producing the delamination issues seen in these samples, which seem to be inducing early electrical breakdown. Additionally, the solution cast PVDF outer layers do not seem to be preventing conduction into the sample from the electrodes to an adequate extent. Hence, a more insulating substitute which is miscible with PVDF in the melt phase would be desirable.

#### **4.3.6. PVFHA/ZIF three-layer laminates**

As it became apparent that incorporating PAN – immiscible with PVDF-HFP – into the multilayer hot-pressed laminates was not feasible, focus was shifted to working with a polymer highly miscible with PVDF-HFP to ensure better cohesion between layers in the multilayer structure. Additionally, as evidenced by the extremely early breakdown of the 5-layer composites, a cohesive composite structure must be produced, the presence of any defects will result in early electrical breakdown and high energy losses. Two sets of 3-layer laminates containing PVFHA/BiZIF and PVFHA/ZIF-8 nanofibre composites were produced, each of which were evidently pristine and flexible, devoid of defects or air bubbles and cohesive in structure, with no evidence of delamination between layers. Both samples had very homogenous

thickness, and despite the extreme similarity in both the processing conditions and sample contents, the PMMA:PVFHA/ZIF-8 composite had a thickness of 185  $\mu\text{m}$ , whereas the PMMA:PVFHA/BiZIF composite had a lower thickness of 125  $\mu\text{m}$ .

Ferroelectric tests were hence performed on the laminates with the same methodology as employed previously. The results of tests on the two laminates are shown in **Figure 4.10**, alongside a 3-layer PMMA laminate containing a central PVFHA nanofibre layer without any ZIF. From the 8 tests performed on the ZIF-8 composite, the vast majority of them broke down below 300 kV/cm. The PVFHA/ZIF-8 curve given in **Figure 4.10(a)** was the only area of the sample tested which survived up to 550 kV/cm, where the voltage amplifier hit its limit. In contrast, none of the 4 tests performed on different areas of the BiZIF composite – one of which is shown in **Figure 4.10(b)** – led to electrical breakdown, with all samples surviving up to 800 kV/cm. Comparing the loops at 550 kV/cm, it seems that the PVFHA/ZIF-8 sample exhibits higher polarisability despite its inability to reach the higher electric fields like the PVFHA/BiZIF sample. However, while the maximum polarisation of the ZIF-8 laminate is clearly higher at this field, the loss is also demonstrably higher, as can be seen by the far larger loop area at this voltage. This is what leads to the identical discharged energy density, but higher discharge efficiency of the PVFHA/ZIF-8 composite in contrast to the PVFHA/BiZIF composite. Comparing the loops of both ZIF containing laminates to that of a laminate of the same construction but without ZIF, it is clear that the ZIF is not providing any enhancements to polarisability. In fact, if anything, the ZIF is diminishing the polarisability of the laminates. There is no clear disparity in discharge efficiency between the ZIF containing and ZIF absent

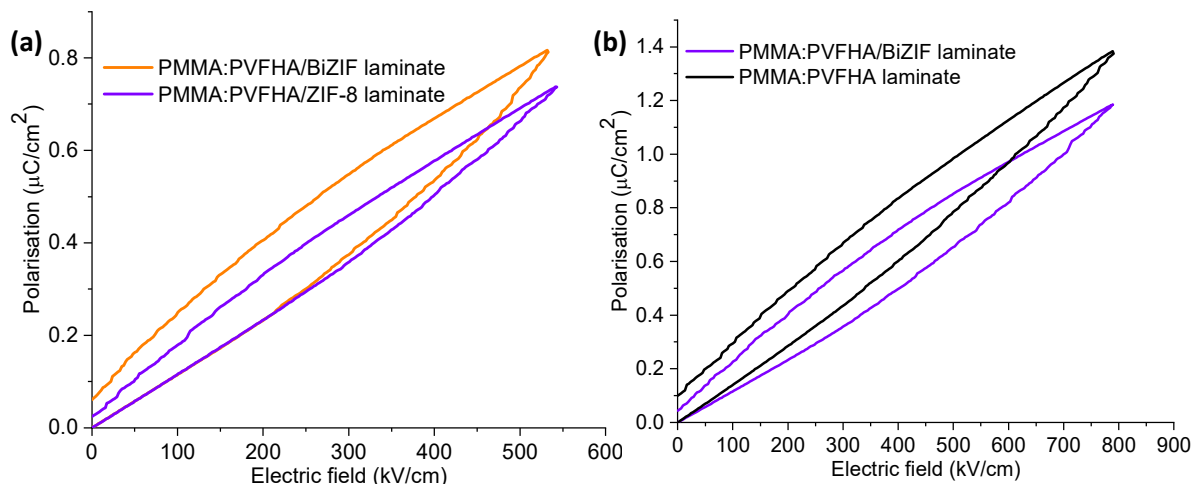


**Figure 0.10.** P-E loops of 3-layer PMMA:PVFHA laminates, containing ZIF-8, BiZIF or no ZIF. **(a)** Provides a comparison between the two laminates containing different forms of ZIF, whereas **(b)** provides a comparison between the BiZIF laminate and a laminate lacking ZIF nanofibre coatings. All composites utilised 300 mg PMMA layers alongside PVFHA nanofibre layers ranging from 60 mg (the ZIF absent case) to 90 mg in the BiZIF and ZIF-8 laminates. The ZIF absent laminate was also pressed at 160  $^{\circ}\text{C}$ , whereas the other two samples were pressed at 140  $^{\circ}\text{C}$ .

laminates at 800 kV/cm, although the ZIF lacking sample has a noticeably higher discharged energy density. Further to this, this sample has around 65% of the PVFHA content of the ZIF containing sample, which has just over 90 mg of PVFHA compared to 60 mg. From our findings in chapter 3, this could have a substantial impact on the sample polarisability, and so the detrimental effect of ZIF presence on the sample may in fact be underestimated by these curves. Thus, ZIF is not presumed to have a positive impact on the energy storage properties of PMMA/PVFHA nanofibre laminates.

#### 4.4. Conclusions

In this work, PAN and PVFHA nanofibres were successfully electrospun and subsequently coated with ZIF nanoparticles of differing varieties, so long as the size of the fully grown ZIF particles was small enough in comparison to the nanofibre diameter. Growth conditions and methodologies were optimised such that the ZIF coatings had well-developed crystal structures and morphologies, and in some cases produced nanofibres fully covered in ZIF coatings.

Although, while they may possess a potentially significant dipole moment, ZIF-8 and BiZIF nanoparticle coated polymer nanofibres have been shown here to provide no measurable enhancements in polarisability when incorporated into multilayer structures which exhibit high discharge efficiencies and low remnant polarisations.<sup>12,22</sup> The data here demonstrate that such architectures give promise for producing polymer-based ferroelectric thin films due to the low losses exhibited when employing PMMA as an outer layer of the multilayer structure. But unfortunately, the use of ZIF nanoparticles and PAN nanofibres provided no measurable benefits to this approach. While PAN nanofibres have been shown to possess a dipole if containing the ‘sawtooth’ all-trans phase conformation, but our PAN nanofibres offered no sign of this in the XRD patterns and showed no such propensity for ferroelectric behaviour in our tests.<sup>35</sup>

However, the more prominent issue with the composites produced in this chapter was the lack of miscibility between the PAN and PVFHA. Despite trying various processing methods, it was impossible to encourage these two polymers to develop sufficient miscibility such that the multilayer structures showed excellent structural integrity. This led to low extremely high loss ferroelectric behaviour and rendered them useless as ferroelectric composites. Further to this, the voids left in the structure due to the lack of cohesion between the PVFHA and PAN layers would inevitably lead to early electrical breakdown. Hence, focus is shifted to producing an analogous structure using the far more miscible PMMA layers and PVFHA nanofibres to maximise ferroelectric performance, without the use of ZIF nanoparticles.



## 4.5. References

1. Zhu, Q. L. & Xu, Q. Metal-organic framework composites. *Chem. Soc. Rev.* **43**, 5468–5512 (2014).
2. Kang, Z., Fan, L. & Sun, D. Recent advances and challenges of metal-organic framework membranes for gas separation. *J. Mater. Chem. A* **5**, 10073–10091 (2017).
3. Yang, L., Zeng, X., Wang, W. & Cao, D. Recent Progress in MOF-Derived, Heteroatom-Doped Porous Carbons as Highly Efficient Electrocatalysts for Oxygen Reduction Reaction in Fuel Cells. *Adv. Funct. Mater.* **28**, 1–21 (2018).
4. Wang, J. H., Li, M. & Li, D. A dynamic, luminescent and entangled MOF as a qualitative sensor for volatile organic solvents and a quantitative monitor for acetonitrile vapour. *Chem. Sci.* **4**, 1793–1801 (2013).
5. Peterson, G. W., Lu, A. X. & Epps, T. H. Tuning the Morphology and Activity of Electrospun Polystyrene/UiO-66-NH<sub>2</sub> Metal-Organic Framework Composites to Enhance Chemical Warfare Agent Removal. *ACS Appl. Mater. Interfaces* **9**, 32248–32254 (2017).
6. Lee, I., Choi, S., Lee, H. J. & Oh, M. Hollow Metal-Organic Framework Microparticles Assembled via a Self-Templated Formation Mechanism. *Cryst. Growth Des.* **15**, 5169–5173 (2015).
7. Yang, Y. *et al.* Hollow metal-organic framework nanospheres via emulsion-based interfacial synthesis and their application in size-selective catalysis. *ACS Appl. Mater. Interfaces* **6**, 18163–18171 (2014).
8. Kreno, L. E. *et al.* Metal-organic framework materials as chemical sensors. *Chem. Rev.* **112**, 1105–1125 (2012).
9. Niu, Q. *et al.* Bimetal-organic frameworks/polymer core-shell nanofibers derived heteroatom-doped carbon materials as electrocatalysts for oxygen reduction reaction. *Carbon N. Y.* **114**, 250–260 (2017).
10. Sun, W., Zhai, X. & Zhao, L. Synthesis of ZIF-8 and ZIF-67 nanocrystals with well-controllable size distribution through reverse microemulsions. *Chem. Eng. J.* **289**, 59–64 (2016).
11. Yu, D. *et al.* An ordered ZIF-8-derived layered double hydroxide hollow nanoparticles-nanoflake array for high efficiency energy storage. *J. Mater. Chem. A* **4**, 16953–16960 (2016).
12. Izzaoui, S., Abou El Makarim, H., Benoit, D. M. & Komiha, N. Theoretical Study of the CO<sub>2</sub> Adsorption by Zeolitic Imidazolate Frameworks (ZIFs). *J. Phys. Chem. C* **121**, 20259–20265 (2017).
13. Gao, M., Zeng, L., Nie, J. & Ma, G. Polymer-metal-organic framework core-shell framework nanofibers: Via electrospinning and their gas adsorption activities. *RSC Adv.* **6**, 7078–7085 (2016).



14. Wang, C. *et al.* In Situ Growth of ZIF-8 on PAN Fibrous Filters for Highly Efficient U(VI) Removal. *ACS Appl. Mater. Interfaces* **10**, 24164–24171 (2018).
15. Gong, X., Wang, Y. & Kuang, T. ZIF-8-Based Membranes for Carbon Dioxide Capture and Separation. *ACS Sustain. Chem. Eng.* **5**, 11204–11214 (2017).
16. Li, W., Liu, Y. Y., Bai, Y., Wang, J. & Pang, H. Anchoring ZIF-67 particles on amidoximerized polyacrylonitrile fibers for radionuclide sequestration in wastewater and seawater. *J. Hazard. Mater.* **395**, 122692 (2020).
17. Li, K. *et al.* Zeolitic imidazolate frameworks for kinetic separation of propane and propene. *J. Am. Chem. Soc.* **131**, 10368–10369 (2009).
18. Lin, K. Y. A. & Chang, H. A. Ultra-high adsorption capacity of zeolitic imidazole framework-67 (ZIF-67) for removal of malachite green from water. *Chemosphere* **139**, 624–631 (2015).
19. Wang, Y. *et al.* Ultrahigh energy density and greatly enhanced discharged efficiency of sandwich-structured polymer nanocomposites with optimized spatial organization. *Nano Energy* **44**, 364–370 (2018).
20. Guo, Y., Wang, X., Hu, P. & Peng, X. ZIF-8 coated polyvinylidene fluoride (PVDF) hollow fiber for highly efficient separation of small dye molecules. *Appl. Mater. Today* **5**, 103–110 (2016).
21. Ostermann, R., Cravillon, J., Weidmann, C., Wiebcke, M. & Smarsly, B. M. Metal-organic framework nanofibers via electrospinning. *Chem. Commun.* **47**, 442–444 (2011).
22. Mohajer, F. & Niknam Shahrak, M. Simulation study on CO<sub>2</sub> diffusion and adsorption in zeolitic imidazolate framework-8 and -90: influence of different functional groups. *Heat Mass Transf.* **55**, 2017–2023 (2019).
23. Park, K. S. *et al.* Exceptional chemical and thermal stability of zeolitic imidazolate frameworks. *Proc. Natl. Acad. Sci. U. S. A.* **103**, 10186–10191 (2006).
24. Yang, J. *et al.* Hollow Zn/Co ZIF Particles Derived from Core-Shell ZIF-67@ZIF-8 as Selective Catalyst for the Semi-Hydrogenation of Acetylene. *Angew. Chemie - Int. Ed.* **54**, 10889–10893 (2015).
25. Panapoy, M., Dankeaw, A. & Ksapabutr, B. Electrical Conductivity of PAN - based Carbon Nanofibers Prepared by Electrospinning Method. *Thammasat Int. J. Sc. Tech* **13**, 11–17 (2008).
26. Zhou, Z. *et al.* Development of carbon nanofibers from aligned electrospun polyacrylonitrile nanofiber bundles and characterization of their microstructural, electrical, and mechanical properties. *Polymer (Guildf)*. **50**, 2999–3006 (2009).
27. Anvari, A. *et al.* PVDF/PAN Blend Membrane: Preparation, Characterization and Fouling Analysis. *J. Polym. Environ.* **25**, 1348–1358 (2017).
28. Xiuli, Y., Hongbin, C., Xiu, W. & Yongxin, Y. Morphology and properties of hollow-fiber membrane made by PAN mixing with small amount of PVDF. *J. Memb. Sci.* **146**, 179–184

- (1998).
29. He, X., Yao, K. & Gan, B. K. Phase transition and properties of a ferroelectric poly(vinylidene fluoride-hexafluoropropylene) copolymer. *J. Appl. Phys.* **97**, 084101 (2005).
  30. Kong, L. & Chen, W. Ionic Liquid Directed Mesoporous Carbon Nanoflakes as an Efficient Electrode material. *Sci. Rep.* **5**, 1–9 (2015).
  31. Pan, Y., Li, T., Lestari, G. & Lai, Z. Effective separation of propylene/propane binary mixtures by ZIF-8 membranes. *J. Memb. Sci.* **390–391**, 93–98 (2012).
  32. Gan, W. C., Majid, W. H. A. & Furukawa, T. Ferroelectric polarization, pyroelectric activity and dielectric relaxation in Form IV poly(vinylidene fluoride). *Polymer (Guildf)*. **82**, 156–165 (2016).
  33. Knebel, A. *et al.* Defibrillation of soft porous metal-organic frameworks with electric fields. *Science (80-. )*. **358**, 347–351 (2017).
  34. Wei, J. & Zhu, L. Intrinsic polymer dielectrics for high energy density and low loss electric energy storage. *Prog. Polym. Sci.* **106**, 101254 (2020).
  35. Su, Y. *et al.* Flexible Reduced Graphene Oxide/Polyacrylonitrile Dielectric Nanocomposite Films for High-Temperature Electronics Applications. *ACS Appl. Nano Mater.* **3**, 7005–7015 (2020).
  36. Scott, J. F., Ferroelectrics go bananas, *J. Phys. Cond. Mat.*, **20**, 2 (2008)

## Chapter 5

### Multilayer polymer dielectrics

#### 5.1. Introduction

The production of laminate composites incorporating the produced PVDF-HFP/AMIM (PVFHA) nanofibre membranes in the previous chapter largely failed on the grounds of a lack of miscibility of the polyacrylonitrile (PAN) and PVFHA nanofibres during the hot-pressing process. Additionally, the use of ZIF nanoparticles in the PVFHA nanofibre membranes did not provide any enhancements to the polarisability of the multilayer composites. However, the incorporation of PMMA layers and the removal of PAN nanofibres proved to be very useful for enhancing the structural integrity and polarisability of the composites, while improving their discharge properties substantially. In particular, the high discharge efficiency and low remnant polarisation of the composites seen in **Figure 4.10** holds some promise for the use of a PVFHA nanofibre/PMMA thin film multilayer structure.

**Figure 5.1** provides a schematic of the proposed mechanisms for the enhancements that a multilayer PMMA/PVFHA nanofibre structure can provide. Breakdown events are impeded at interfaces between the PMMA and PVFHA nanofibre layers, while the PMMA layers

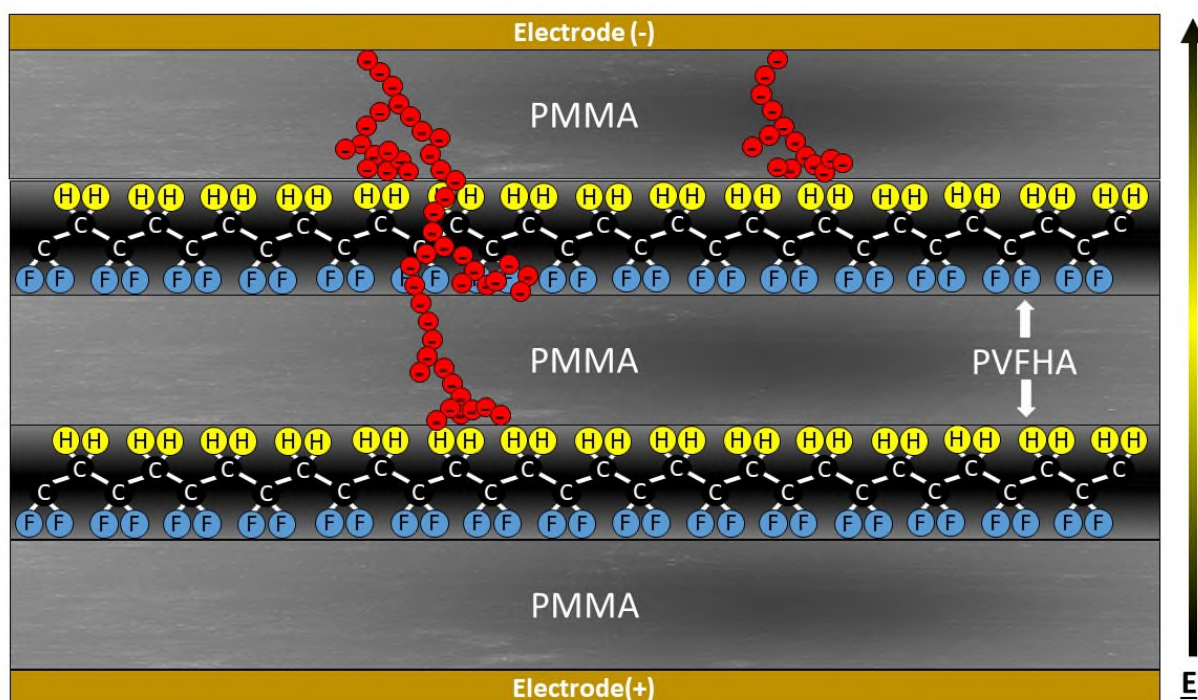


**Figure 0.1.** Schematic of the cross-section of the multilayer structure incorporating PVFHA nanofibre layers and PMMA layers, highlighting the orientational polarisation of PVDF polymer chains, the build-up of space charges at boundaries, and the impedance of breakdown events by the interfaces in the structure. Note that, for simplicity's sake, PVDF polymer chains have been shown here rather than PVDF-HFP, and the thickness of the PVFHA layers have been exaggerated.

themselves may be insulating enough to prevent conduction within the layer, preventing breakdown events from penetrating far through the structure. Additionally, the amount of space charge that accumulates at interfaces, which comprise the primary component of interfacial polarisation, will be enhanced due to the large disparity in material permittivities between the PMMA and PVFHA layers. In turn, this will increase the orientational polarisation of polar PVDF-HFP polymer chains near the interface. Hence, overall, this structure should help the composite survive to higher electric fields – increasing polarisability – and increase the polarisation at a given electric field. Furthermore, the highly compressible and innately thin PVFHA nanofibre layers are likely to be far thinner than their PMMA layer counterparts, further compounding the breakdown resistance of the structure by reducing the internal field substantially in the majority of the composite's thickness.

PVDF based multilayer laminates have proven quite successful for producing ferroelectric all-polymer dielectrics.<sup>1-5</sup> However, to our knowledge, this has not been attempted using PVDF nanofibre membranes, let alone those electrospun with an ionic additive in order to maximise the ferroelectric  $\beta$ -phase crystallinity. Hence, learning from these approaches, in this work we attempt to construct a 3-layer all-polymer laminate incorporating our PVFHA nanofibre membranes into a multilayer structure. Our straightforward and up-scalable processing approach is intended to make a high throughput manufacturing process feasible. Thus, highly insulating (i.e. high  $E_b$ ) PMMA polymer layers were used as outer layers, and the highly polarisable (i.e. high  $\epsilon_r$ ) PVFHA nanofibre membrane layers were 'sandwiched' in between. However, as the process of hot-pressing is feared to disrupt the crystallinity imposed by the optimised electrospinning process developed in chapter 3, the viability of solution casting PMMA layers around the PVFHA nanofibre membranes was attempted first.

## 5.2. Experimental

Various attempts at forming a cohesive laminate structure were attempted in this work and will be described in detail throughout this chapter. The materials and equipment used to create and characterise these laminates are as follows.

Electrospinning solutions were prepared as previously described, utilising the materials and methods described in section 3.2, with 20 wt% PVDF-HFP, 0.5 wt% AMIM and 79.5 wt% DMF. Laminates produced by hot-pressing were made in a similar manor to that described in section 4.2.4 and in **Figure 4.1**, but with the outermost layer consisting of PMMA, and alternating layers containing electrospun PVDF-HFP/AMIM (PVFHA) nanofibres.

PMMA layers for the laminates formed by hot-pressing and solution casting were sourced from Sigma Aldrich. Dichloromethane (DCM) and toluene for solution casting these PMMA layers were also acquired from Sigma Aldrich. 125  $\mu\text{m}$  Saint-Gobain Chemfluor Teflon was used to

help produce defectless hot-pressed PMMA layers for the laminates, and a doctor blade was used to produce thin PMMA layers for pressing, as was described in the section 4.2.4 in the case of PVDF films. In some cases, PVFHA nanofibres were hot-pressed in isolation before incorporation into the laminates, in which case the same Saint-Gobain Chemfluor Teflon was used to ensure effortless sample removal, and to produce pressed nanofibre membranes with high integrity.

FTIR was performed as described in section 3.2.1, using **equation 3.1** to determine phase contents of the PVFHA nanofibres at various pressing temperatures.<sup>6</sup> A heated plate built into the Bruker Tensor 27 FTIR was also used to measure crystal phase changes in the PVFHA nanofibres. WAXS and XRD studies were also performed as detailed in section 3.2.1, using a copper  $K_\alpha$  source ( $\lambda = 1.54 \text{ \AA}$ ), and producing both 2D and 1D scattering profiles. The same Carl Zeiss Sigma field SEM and EDS are employed for micrograph imaging and elemental composition analysis. Ferroelectric P-E testing was again performed on the produced laminates, as well as on pressed PVFHA nanofibre samples in some cases. Small pieces of carbon tape were again used on small regions of the samples to fix the testing area and minimise contact resistance between the samples and the sample holder electrodes, and in almost all cases the samples were tested up to their breakdown field, or up to the 10 kV limit of the testing apparatus. A 10 Hz testing frequency can be assumed unless otherwise stated.

## **5.3. Results and discussion**

### **5.3.1. Laminate structures by solution casting PMMA with PVFHA nanofibres**

When constructing this 3-layered structure, a processing route must be selected, the most obvious 3 of which were explored in processing PVDF in chapter 3. However, there are some core problems with all 3 of these processing methods that must be addressed such that the PVFHA nanofibres may perform to their highest potential. Retaining the high  $\beta$ -phase crystallinity in the PVFHA nanofibres generated by the electrospinning process is a top priority. There are a few possible solutions to this depending on the processing route selected. Solution casting insulating outer polymer layers around the PVFHA nanofibres to form a 3-layer structure is a straightforward method which should entirely avoid any structural changes to the nanofibres if performed correctly. While this avoids the nanofibres re-entering the melt phase and eliminates the possibility of losing desired crystalline properties, another problem emerges; PVDF-HFP must not dissolve in the solvent used to cast the insulating polymer, which itself of course must also be miscible with PVDF-HFP. Hence, when pursuing this processing route, a specific polymer-solvent combination must be selected that satisfies these two constraints simultaneously. PMMA is a popular choice of polymer for mixing with PVDF, as it is highly miscible with PVDF in both the melt-phase and in solution with a few solvents.<sup>7</sup> PMMA is also

insulating, largely due to its entirely amorphous structure, meaning a cohesive multilayer structure with low leakage current may be produced.<sup>8–11</sup> Unfortunately, there are very few solvents which dissolve PMMA but not PVDF-HFP. After some primary attempts with a few solvents (which had various detrimental effects on the PVFHA nanofibres) dichloromethane (DCM) was selected as the solvent which would incur the least amount of damage to the PVFHA nanofibres, whilst still being an effective solvent for dissolving the PMMA.<sup>12,13</sup>

To construct the 3-layered laminate, 5 wt% PMMA was dissolved in DCM at room temperature overnight and mixed with a magnetic stirrer bar such that a homogenous solution was formed. A glass petri dish lined with Teflon was prepared to aid with the removal of the laminate after casting. Around half of the prepared solution was then poured into the petri dish to form the bottom layer of the laminate. An as-spun PVFHA nanofibre membrane was then placed into this solution, resulting in partial submersion. The rest of the PMMA/DCM solution was then slowly poured on top to form the top layer, followed by drying at room temperature overnight in a fume hood before careful removal from the petri dish.

It was immediately clear that there were some major issues during solution casting. DCM's high volatility and low boiling point meant the solution evaporated quickly, resulting in many air pockets forming, producing many gas bubbles in the dried laminate. Since the PVFHA nanofibre membranes are extremely lightweight for both their lateral size and thickness, thin PMMA layers are also desirable. This is why a low 5 wt% loading of PMMA was chosen when preparing the casting solution. However, this also leads to a high rate of solvent evaporation, intensifying the voids produced by air pockets in the laminate. Additionally, the nanofibre membrane is liable to trapping DCM as it evaporates underneath the fibre membrane. This in essence is a good sign, as it implies the PMMA/DCM solution is not penetrating the membrane and ruining the layered structure. Although, as the solvent has such a high evaporation rate, this forms many gas bubbles in the solution beneath the membrane as it dries, producing the very high numbers of defects. Increasing the fraction of PMMA in the solution to 10 wt% and 20 wt% reduced the prevalence of these defects, but instead produced a far too thick and brittle laminate due to the high content of the more brittle PMMA. Furthermore, the microstructure of the laminates – seen in the SEM images in **Figure 5.2** – was far from ideal, as the fibrous structure was partially lost by the exposure of the nanofibres to this DCM solution. This processing method is hence far too disruptive for the PVFHA nanofibres to withstand, so a more complex methodology was attempted to form a cohesive a laminate structure from a PMMA solution.

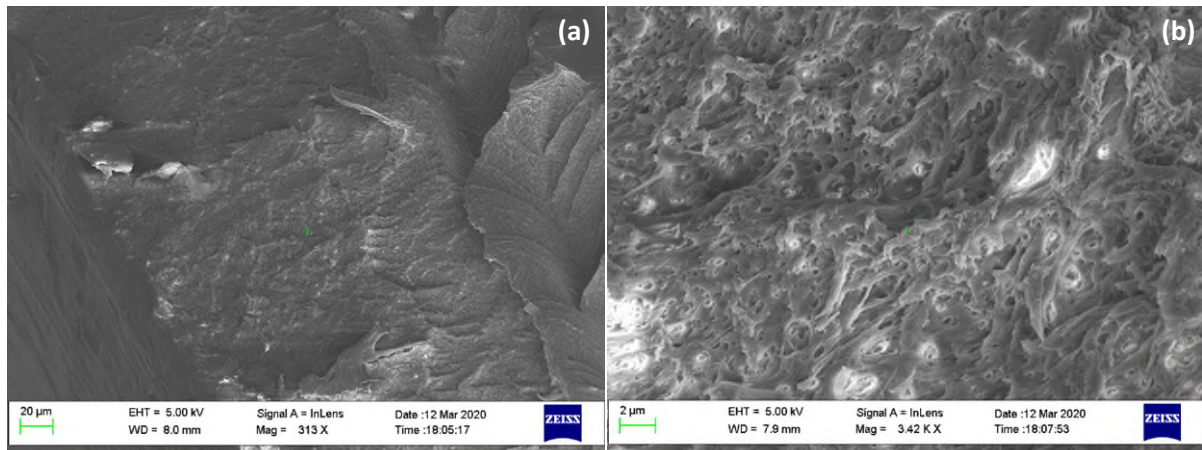


**Figure 0.2.** SEM micrographs of the solution cast PMMA/PVDF-HFP laminates. **(a)** Shows a cross-section of the structure, with no clear layered structure visible; **(b)** shows a higher resolution image of the fibrous structure, which has been partially damaged by the solution casting process.

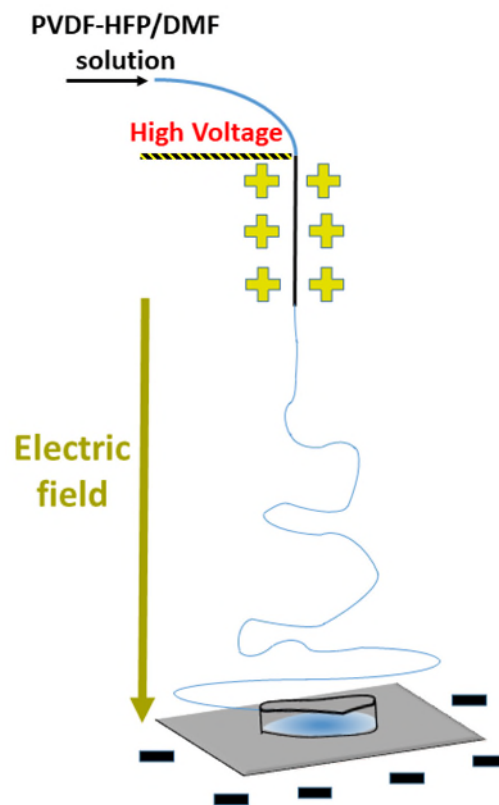


**Figure 0.3.** Schematic of nanofibre electrospinning and the chaotic form the nanofibre stream tends to exhibit. Setup identical to that **Figure 2.6**, but with a petri dish on the collector.



As casting the solution around the fibre seemed to produce a highly flawed sample due to the trapping of gas in the fibre membrane, an in-situ electrospinning method was instead attempted, in which the electrospinning setup from **Figure 2.6** was altered to that shown in **Figure 5.3**. The PVDF-HFP/AMIM/ DMF solution was spun into a glass petri dish containing freshly poured 5

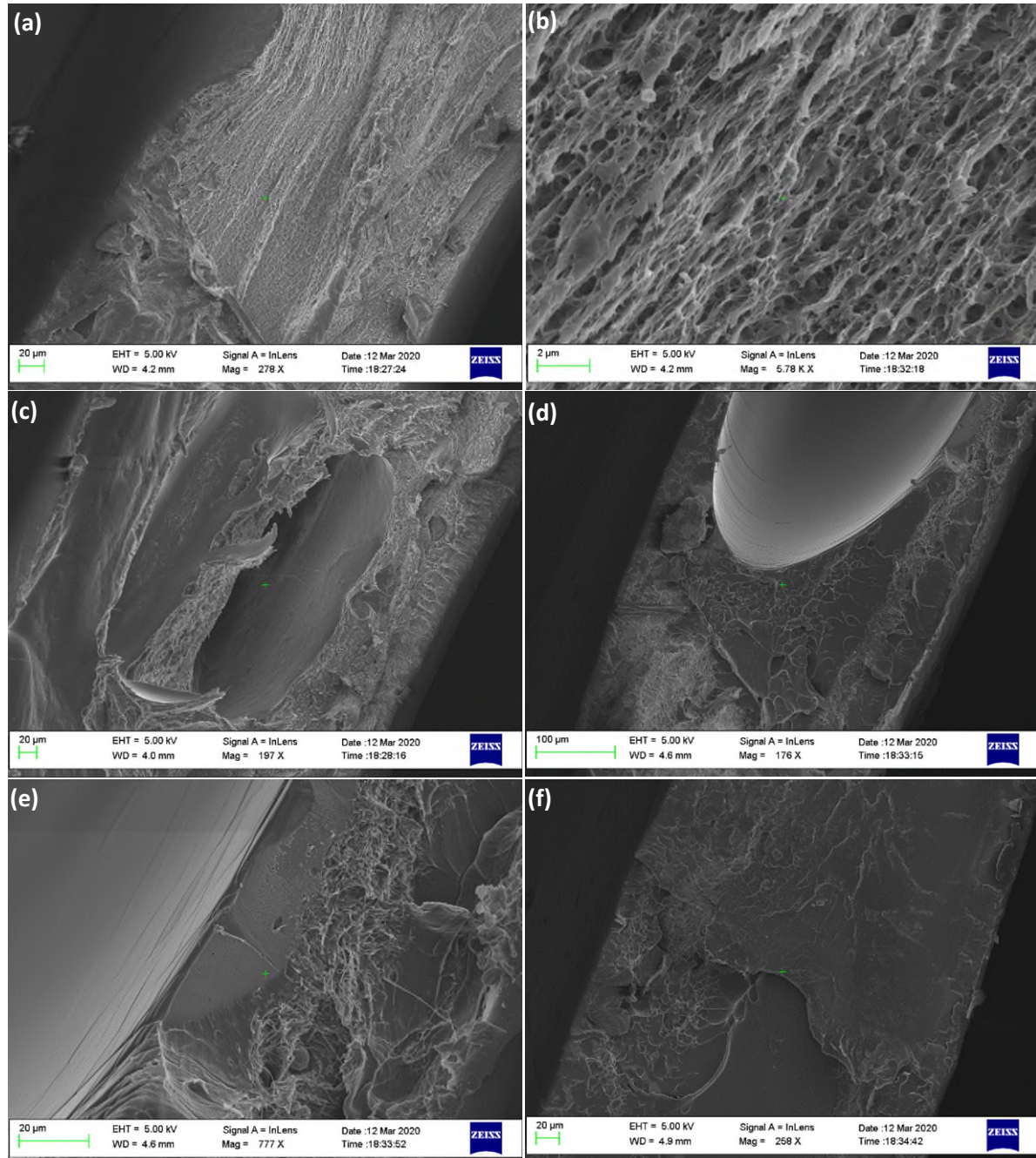


**Figure 0.4.** SEM micrographs of the in-situ electrospun PMMA/PVDF-HFP laminate. **(a)** A section of the cross-section with a clear fibrous structure; **(b)** a higher resolution image of the fibrous structure, displaying its foam like nature; **(c)** A separate part of the cross-section, showing an air pocket defect; **(d)** a second portion of the cross-section highlighting the inhomogeneity of the structure, with a lack of fibres and another large defect. **(e, f)** shows more detailed inhomogeneity in the cross-sections, where it is clear that the multilayer structure has been lost.



wt% PMMA/DCM solution. To avoid disruption in the electrospinning process, the petri dish was coated with a conductive aluminium foil substrate prior to adding the solution to act as the electrospinning collector. This foil layer was extended over the edge of the petri dish to contact the metallic plate underneath, such that a voltage was applied to the foil. Meanwhile the immediate surrounding area of the collector was covered in insulating plastic, ensuring the electrospinning jet would settle exclusively on the petri dish. Ideally, the nanofibres would condense into the solid state as they reached the PMMA/DCM solution, forming a well immersed fibrous layer. The core issue with this approach is the loss of a distinct boundary between the PMMA layers and PVFHA nanofibre layer, leading to rather the loss of the potentially advantageous interfacial structure.<sup>14</sup> This was inevitable to some extent as the nanofibres will settle in the still drying solution, although it simultaneously ensures good adhesion between the PMMA and PVFHA nanofibres. To optimise this process, prior to starting the electrospinning the solution was allowed to dry into a gel like state to avoid substantial loss of the fibrous membrane structure in the PMMA/DCM solution. Upon electrospinning, the electrospun nanofibres were clearly fully submerged in the PMMA/DCM solution, so in the end no top layer needed to be cast, and a distinct layered structure did not form. Cross-sectional SEM images of the resultant laminate are shown in **Figure 5.4**. It is clear from these images that despite the efforts made, the fibrous structure – seen clearly in both **Figure 5.2** and **Figure 3.10** – has once again been heavily disrupted. Instead, a foam-like microstructure has emerged from the altered electrospinning process. Additionally, defects arising from DCM evaporation are still commonly present, so the newly produced microstructure is still littered with defects, which would lead to early electrical breakdown and high ferroelectric energy losses. Ultimately, it was concluded that a solution casting approach is simply not viable when attempting to make a 3-layered structure involving PVFHA nanofibres as the central layer.

### **5.3.2. Hot-pressed PMMA/PVFHA nanofibre layered laminates**

After eliminating the potential of solution casting as a process to develop multilayer laminates, the potential of hot-pressing methodologies was revisited. But in contrast to chapter 4, PMMA was utilised as an insulating outer layer this time. The key advantage of hot-pressing is the ability to essentially eliminate defects with an optimised methodology. The use of high temperatures and pressures during pressing can produce extremely thin homogeneous polymer films, lacking in defects and voids. Although, the issue remains of the potential for high pressing temperatures altering the highly polarisable crystalline structure imbued in the PVFHA nanofibres by electrospinning. Hence, despite the high temperatures producing films that tend to be more durable in high electric fields, a low pressing temperature is desirable to avoid this transformation. Using PMMA makes this process easier as it enters the melt phase at a lower temperature than PVDF-HFP.<sup>9,15</sup>

Firstly, an alternate method of obtaining an outer PMMA layer is necessary as solution casting directly over the fibres is not an option. In an effort to produce the thinnest possible films at the highest production rate, a couple of methods for producing PMMA outer layers (which are subsequently hot-pressed into the multilayer laminates) were explored. A straightforward approach was first considered; hot-pressing PMMA layers. It is important to note that there must not be a significant mass difference between the insulating PMMA and electroactive PVFHA layers in these multilayer laminates, as an excess in one material may lead to a deficiency in either the breakdown strength or polarisability, impairing the maximum achievable discharged energy density,  $U_e$ , of the laminate either way. Due to this, usually only a few pellets were used to form the PMMA film when hot-pressing – this was all that was needed to reach the typical mass of the PVFHA nanofibre membranes. High pressing temperatures, ultra-smooth and thin Teflon sheets and the employment of thick hot-press plates helped to ensure these layers are homogeneous and free of defects. Hence, the films were pressed at 200 °C, 40 bar, with multiple layers of aluminium pressing plate around the outside. However, since only a few individual PMMA pellets were used to make these films, the produced PMMA layers were typically quite inhomogeneous, with thickness variances across the film. Multiple rounds of pressing helped to eliminate this somewhat, although this was not always successful and often produced more defects and inhomogeneities.

An improved methodology was thus used to combat this. The PMMA pellets were instead dissolved into solution and cast into thin films using a doctor blade apparatus. The produced PMMA thin films were then hot-pressed under the same conditions as the pellets; 200 °C, 40 bar. The first attempt was made by dissolving 20 wt% PMMA in DMF and was allowed to dry overnight. The product was a fairly homogenous, opaque, white thin film of thickness ~150 - 250 µm. However, as revealed in the SEM images in **Figure 5.5(a, b)**, the inside of the film is rather foam like in nature. This is an issue when it comes to hot-pressing, as the gas contained in the pores in the foam like structure must be removed during pressing. Even with a substantial degassing phase, this proved extremely difficult, and so resulted in defect and void laced films, even after pressing. The low volatility of DMF – even with the assistance of the in-built fans in the doctor blade apparatus used during the drying process – likely caused this structure to manifest and for gas to be trapped in the system. Toluene, a solvent with higher volatility, was hence selected instead. PMMA films were hence produced again with a doctor blade from a 20 wt% solution in toluene, produced by overnight room temperature stirring until a homogeneous solution was formed. The produced films were much thinner, typically 60-120 µm in thickness. SEM micrographs of the sample surface and cross-section are shown in **Figure 5.5(c) and (d)**. The sample is clearly far more homogenous, lacking a foam-like structure and instead having a continuous, pristine microstructure. The same hot-press process at 200 °C and 40 bar (with no need for degassing) was then applied. The output films tended to range between 40-70 µm in

thickness and had at most a ~30% variance in thickness across the film, typically without any defects or voids whatsoever near the centre of the film. Hence these films are of sufficient quality and thinness to be pressed for the outer layer of the multilayer laminates, a process which was hoped to remove the vast majority of the remaining defects around the edges of the thin film. So, with this success, effective incorporation of the PVFHA nanofibres into the hot-pressed multilayer laminates was then considered.

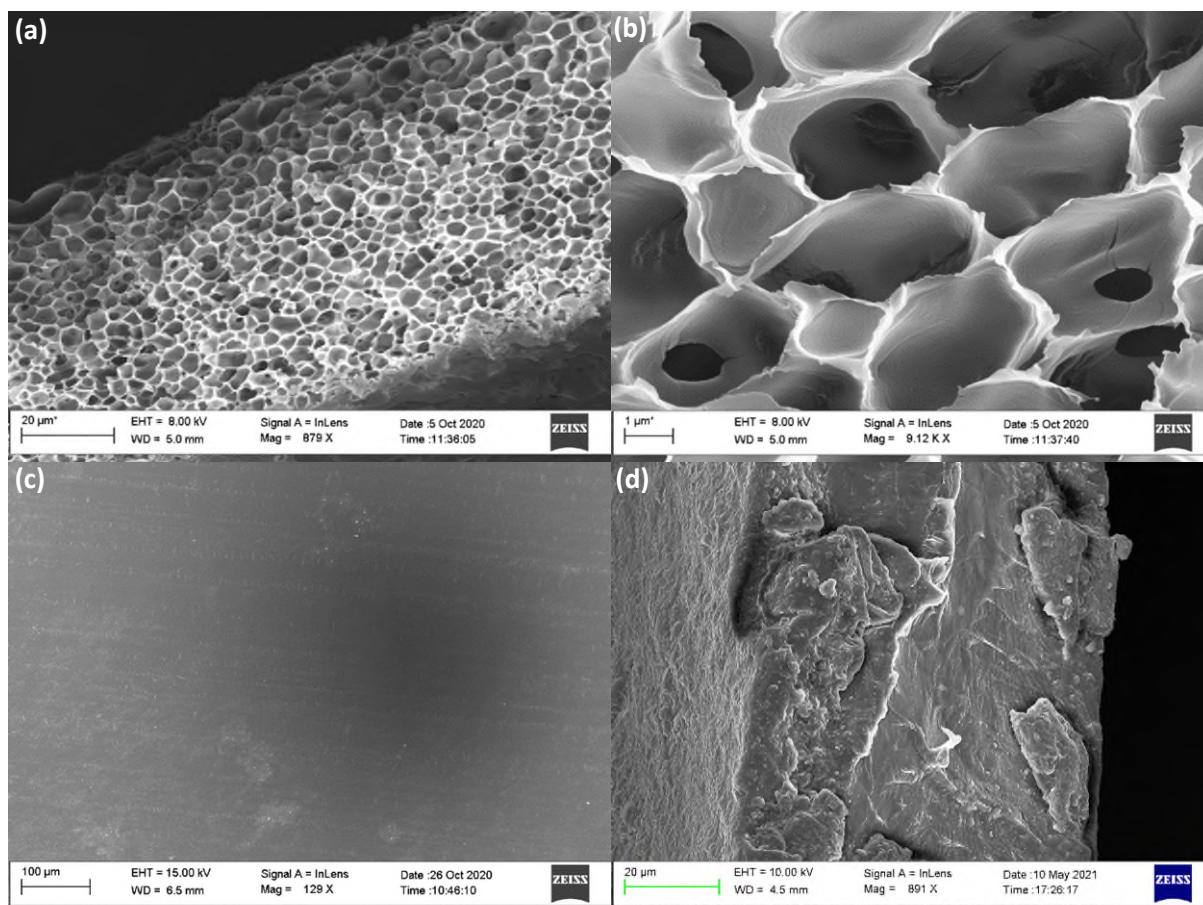


**Figure 0.5.** (a, b) the cross-section of the doctor bladed PMMA film cast from DMF, which is evidently foamy. (c) and (d) show images of the surface and cross-section of the toluene doctor bladed sample respectively, which provided no evidence of defects.

### 5.3.3. The effect of pressing temperature on PVFHA nanofibres

Since sample homogeneity and eliminating defects are of paramount importance for producing a high-performance multilayer thin film, a defect-free PVFHA nanofibre membrane must be selected for these laminates to accompany the highly homogenous PMMA outer layers. A more homogenous fibre layer may act to increase the electrical breakdown strength of the multilayer laminate due to the lower likelihood of defects and inhomogeneities persisting after pressing the layers together. Hot-pressing the neat nanofibre membrane into the layered structure may result in a more inhomogeneous pressing procedure, leaving voids in certain areas of the laminate and increasing the likelihood of electrical breakdown while also likely increasing dielectric loss.

Pre-pressing the nanofibres at lower temperatures in isolation is therefore proposed before incorporating the nanofibres into the multilayer structure. It is hoped that this may prevent the need for higher pressing temperatures (which could eliminate the unique crystal structure of electrospun PVDF-HFP) when preparing the final laminate, as this pre-pressing provides an alternate route to prevent void and defect formation in the multilayer structure. Additionally, pre-pressing PVDF into a partial melt phase at high pressures could in fact optimise the crystal structure for ferroelectric polarisation, a phenomenon observed in other works.<sup>16–19</sup> Due to the complex nano- and microstructural morphology of PVDF-HFP, the effect that the many aspects of their structure their interplay have on polarisability are not well understood, and so the details of this process are well worth exploring. The effect of pressing temperature on the morphology and crystal structure of the multilayer laminates is therefore verified by investigating the dependence of PVFHA nanofibre phase composition after being pressed at a range of temperatures.

PVFHA nanofibres were pressed at temperature increments of 5-10 °C, with the smaller 5 °C increments used around expected thresholds of phase transformations. It was decided that pressing should be performed first at temperatures lower than those required to induce a complete transition to the melt phase and should be expanded up to temperatures higher than the melting temperature of PVDF-HFP. Thus, a temperature range of 120 °C – 180°C was selected. Fibres were pressed at the given temperatures for 120s at 1 bar pressure, followed by 180s of pressing at 40 bar. The samples were then allowed to cool to around 40° C over the course of ~10 minutes before removal from the press.

Fourier transform infrared spectroscopy (FTIR) was then performed on the samples post-pressing to identify any key phase changes that may have occurred, with the curves and key signatures shown in **Figure 5.6**. Firstly, it should be noted that there is no discernible difference between the spectra for the unpressed nanofibres and the 120 °C pressed fibre, so the neat sample has not been included here for improved figure clarity. Secondly,  $\alpha$ -phase signatures are not visible for any of the pressed fibres up to ~160° C, at which point small signatures begin to appear. The  $\gamma$ -phase begins to appear at 150 °C, at which point the  $\beta$ -phase signature is also seen to decrease. As seen in chapter 3, the method developed by Cai *et al.* to discern the PVDF phases present in various samples can provide a quantitative estimate of the polymorphism in these samples.<sup>6</sup> Values deduced from the curves given in **Figure 5.6** are provided in **Table 5.1**.

From these curves, it can be deduced that the initially near 100 %  $\beta$ -phase content in the nanofibres is retained for samples pressed up to 140 °C. After this, phase transformations begin to occur.<sup>20,21</sup> Interestingly however the lack of transformation away from the electroactive  $\beta$  and  $\gamma$ -phases seems to persist until 165 °C, at which point the transformation to the  $\alpha$ -phase seems to begin. Hence in order to retain a highly polarisable material, the pressing temperature must not exceed 160 °C. Although in the 140-160° C range, the increasing  $\gamma$ -phase fraction may still

be of concern. High pressures and annealing have also been reported to induce  $\alpha \rightarrow \gamma$ -phase transformations.<sup>22,23</sup> It's possible that this polymorphic structure could lead to improved performance, as the  $\gamma$ -phase tends to exhibit lower remnant polarisation due to  $\gamma$ -crystals not having an all-trans crystal conformation, making them less susceptible to 'freezing-in'.<sup>24,25</sup> The polarisability of the  $\gamma$ -phase is of course lower than the  $\beta$ -phase however, so the estimated 67%  $\gamma$ -phase content seen in the 160 °C hot-pressed sample may prove to inhibit performance. Of course, the phases observed in these samples will not necessarily correlate with those seen in the multilayer laminates, where the nanofibres will be somewhat shielded from the heating by the outer PMMA layers, amongst other differing pressing conditions.

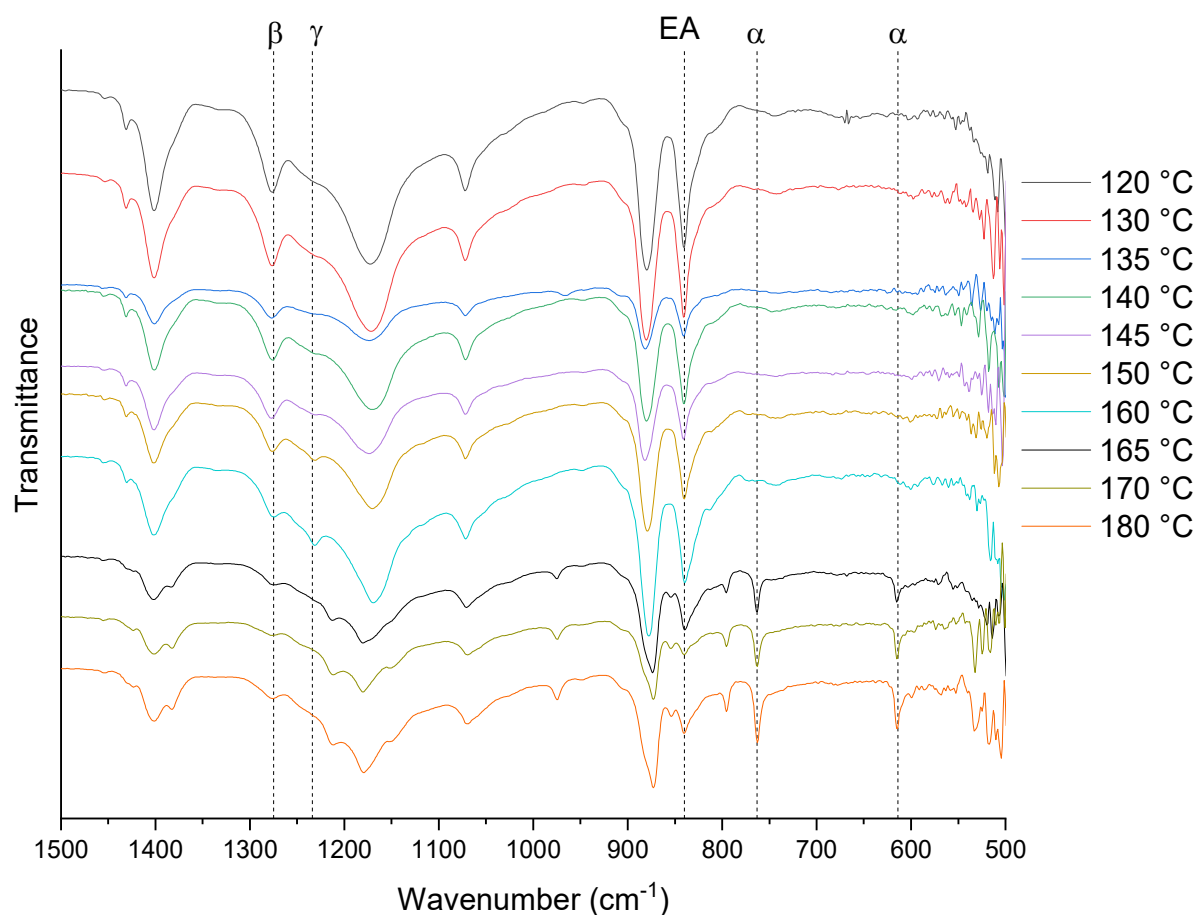


**Figure 0.6.** FTIR spectra of PVFHA nanofibres pressed at various temperatures, with key signatures of the different phases indicated. EA here indicates the 'electroactive' peak, which receives contributions from both the  $\beta$  and  $\gamma$ -phases

In situ FTIR measurements were also taken by utilising the heated plate built into the setup, providing a direct measurement of the PVFHA nanofibres in the melt phase. The curves are shown in **Figure 5.7**, and closely resemble those shown in **Figure 5.6**. Most notably, the melt phase sample shows a distinct lack of  $\gamma$ -phase, and a  $\beta$ -phase signature that more rapidly disappears around 170 °C. The  $\alpha$ -phase is clearly present in the melt, appearing even in the

lower temperature measurements. This implies that despite melting and forming the  $\alpha$ -phase in the melt, the PVDF-HFP recrystallises into the  $\beta$ -phase after cooling, most likely induced by the surrounding crystal structure remaining  $\beta$ -phase dominant. Above 160 °C, the PVDF-HFP fully enters the melt phase, causing the  $\beta$ -phase crystallinity to be entirely lost, resulting in no  $\beta$ -phase crystallite nucleation upon recrystallisation. Finally, in either case, the ‘electroactive’ phase (the combination of the  $\gamma$  and  $\beta$  phases) peak is seen to shrink drastically above 160 °C.

From these results, it seems that the phase content may be preserved in the nanofibres when pressed below 150 °C. However, this pressing procedure is likely to affect the crystallography of the nanofibres in other ways, even if the phase content itself is preserved. For example, the nanofibres pressed under high pressure at 140 °C will enter a partial melt-phase, in which some degree of change in the crystallite morphology – such as the distribution of crystallite sizes or their orientation – may be induced. This may improve performance by causing relaxor-like ferroelectric behaviour, as the average crystallite size may decrease, meaning domains are more mobile and less likely to be permanently polarised after the release of the applied field, leading to a lower remnant polarisation and high discharge efficiency.

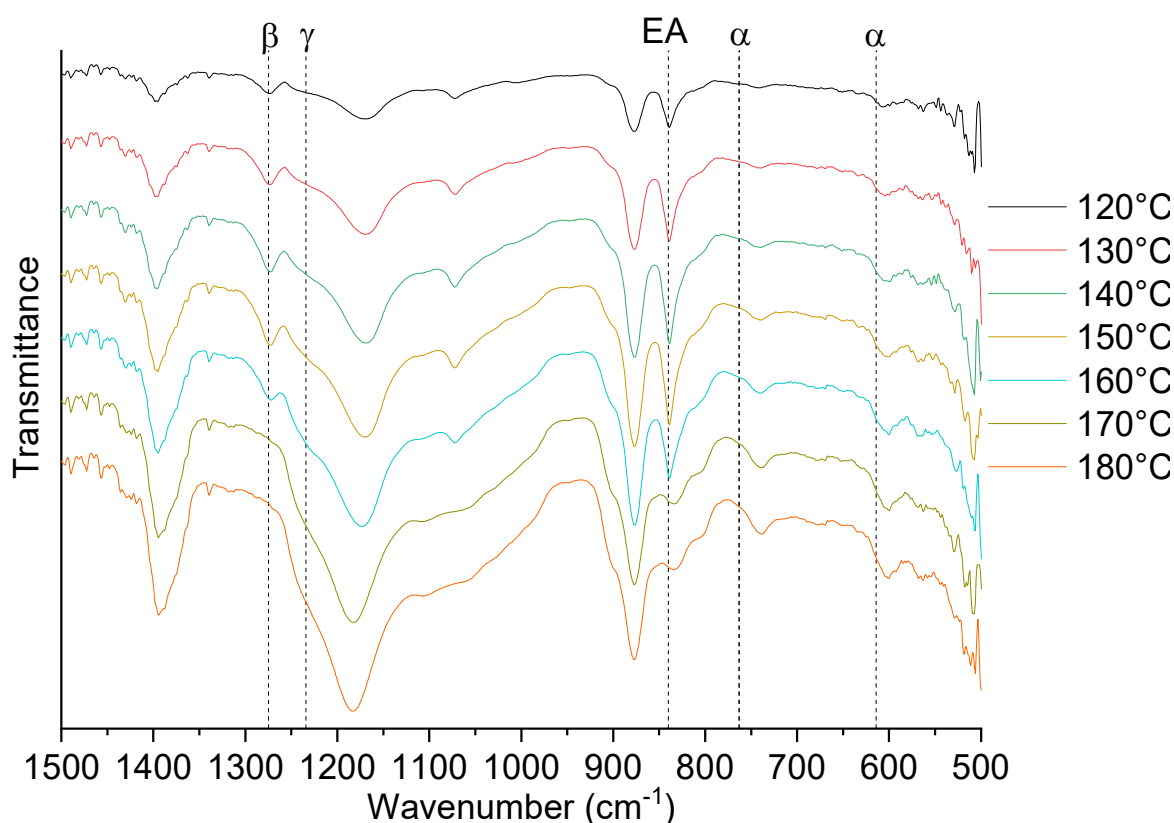


**Figure 0.7.** *In situ* FTIR measurements of a PVFHA nanofibre membrane, taken by utilising a heated plate built into the spectrometer, hence producing direct measurements of the PVDF-HFP crystal structure while it is in the melt phase

**Table 0.1.** Percentage phase content of various PVFHA nanofibers pressed at different temperatures

Temperature (°C)	Electroactive	$\alpha$ -phase	$\beta$ -phase	$\gamma$ -phase
120	100.00	0.00	100.00	0.00
130	100.00	0.00	100.00	0.00
135	100.00	0.00	100.00	0.00
140	100.00	0.00	100.00	0.00
145	100.00	0.00	96.88	3.13
150	100.00	0.00	77.78	22.22
160	100.00	0.00	33.33	66.67
165	51.17	48.83	51.17	0.00
170	38.00	62.00	38.00	0.00
180	40.86	59.14	40.86	0.00

To further investigate the crystallite structure of these pressed nanofibre membranes, WAXS and XRD studies were performed on a range of these samples to gain further insight into how their structure is affected by pressing at various temperatures. XRD plots of the various pressed

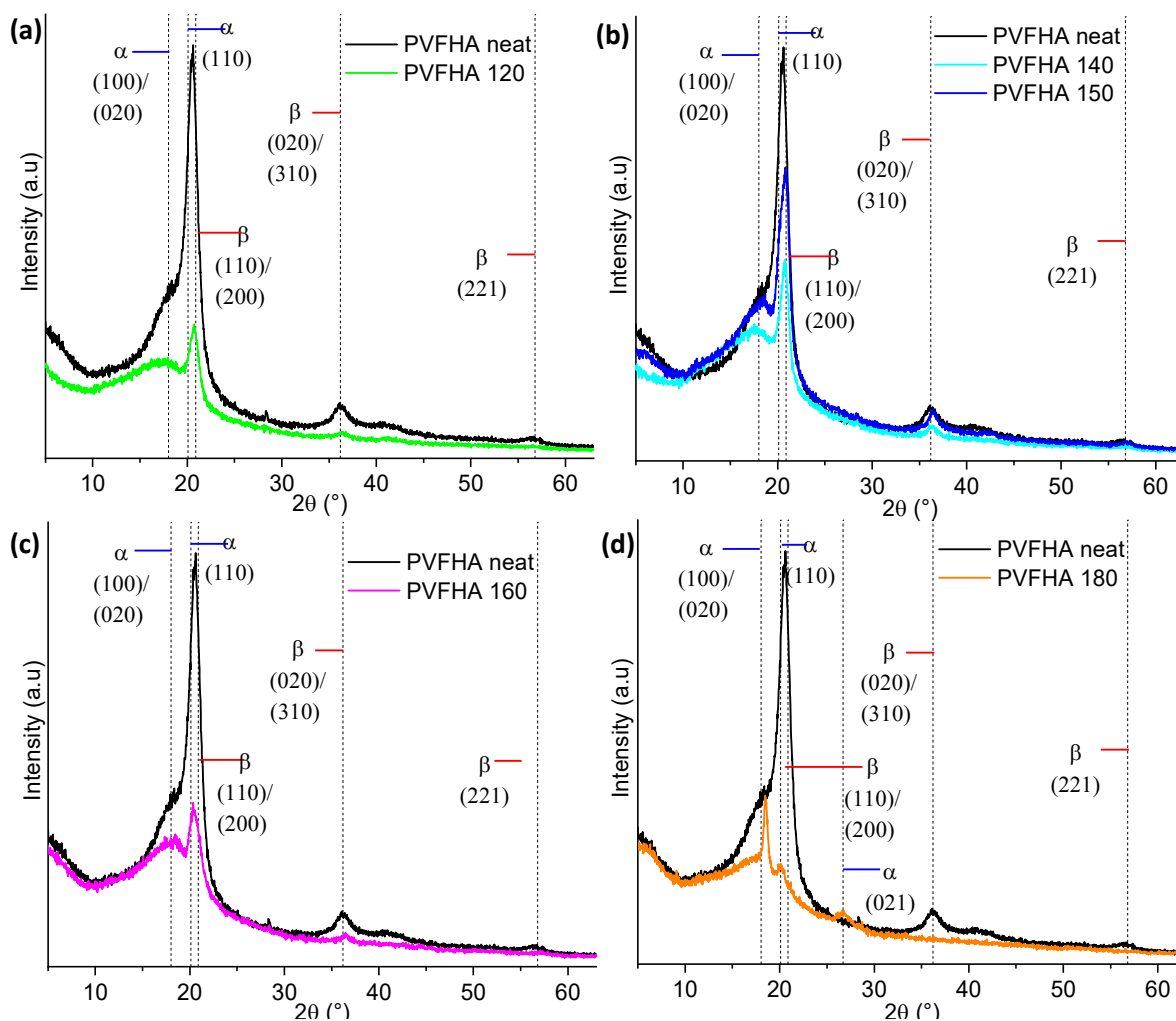


**Figure 0.8.** XRD plots of the pressed PVFHA nanofibre membranes, with key peaks indexed



nanofibre samples are presented in **Figure 5.8**, with key peaks indexed.<sup>26</sup> It is immediately apparent that at 150 °C and below, the pressing process has shifted the 20-21° peak to higher  $2\theta$ , implying an increase in the *in-plane*  $\beta$ -phase content. In fact, the peak is closest to 21° at 150 °C. **Figure 5.9** shows how this peak position shifts with pressing temperature across the whole range, along with a higher resolution image of the 20-21° peak. Above 160 °C, this peak position takes a noticeable downturn, implying the crystallites have reformed at this temperature and above, resulting in a loss of the  $\beta$ -phase content induced by electrospinning. However, since this peak only probes for the *in-plane*  $\alpha$  and  $\beta$ -phase content, other peaks must be investigated to fully understand the change of phase content with pressing temperature. By 180 °C this peak has shifted entirely to the 20°,  $\alpha$ -phase side, accompanied by a large decrease in relative intensity. Alongside  $\alpha$ -phase peaks in other parts of the spectrum becoming far more pronounced – such as the otherwise absent  $\alpha$  (021) peak at 26.7° – it is clear that at this temperature the nanofibres have completely recrystallised. Finally, it should be noted that the peak for all of the pressed nanofibres below 160 °C tend to show a slightly sharper peak than the as-spun nanofibre membrane, with the uptick of the peak beginning at a slightly later  $2\theta$  than usual. This suggests either a shift of the in-plane crystallite population towards the  $\beta$ -phase, or a decrease in the range of crystallite sizes. Either way, this shift could produce more polarisable crystallites and more efficient, relaxor-like ferroelectric behaviour, as an ideal crystallite population to exhibit this behaviour is many small, in-plane oriented  $\beta$ -phase crystallites. Investigating other peaks in the spectrum confirms these conclusions, with other  $\beta$ -phase peaks showing a noted depreciation in intensity at 160 °C and above, and  $\alpha$ -phase peaks becoming more pronounced in tandem. Noticeably, the peak at ~36°, associated with the (020)/(310) peak of the  $\beta$ -phase, seems to become more pronounced after pressing at 140-150 °C compared to pressing at 120 °C, then diminishes to a similar intensity at 160 °C, implying the pressing process may actually assist in inducing some  $\beta$ -phase crystallinity at moderate temperatures.

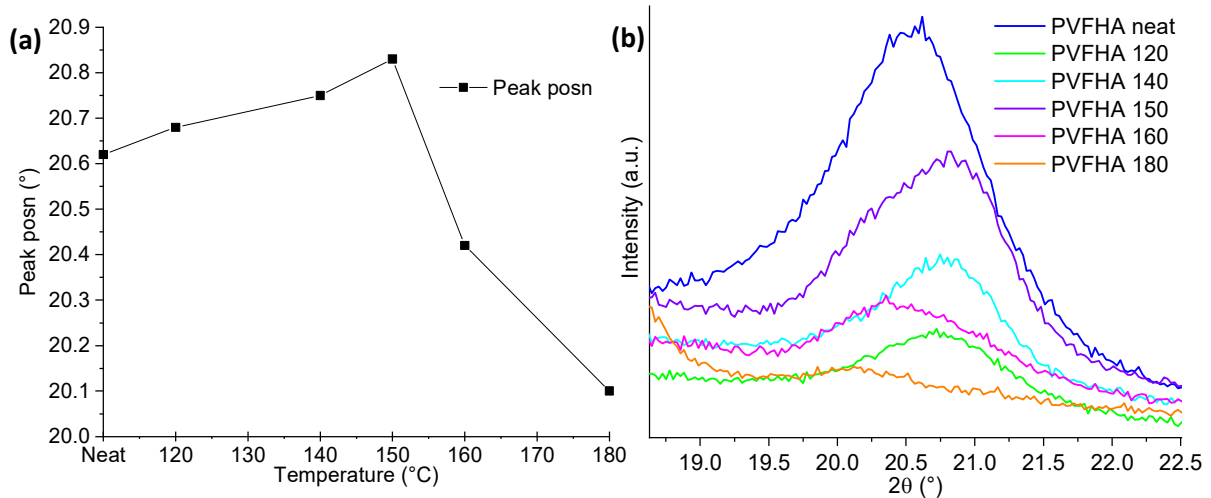


**Figure 0.9.** (a) Peak position of the in-plane crystallite 20-21° peak and (b) a higher resolution image of this peak across samples



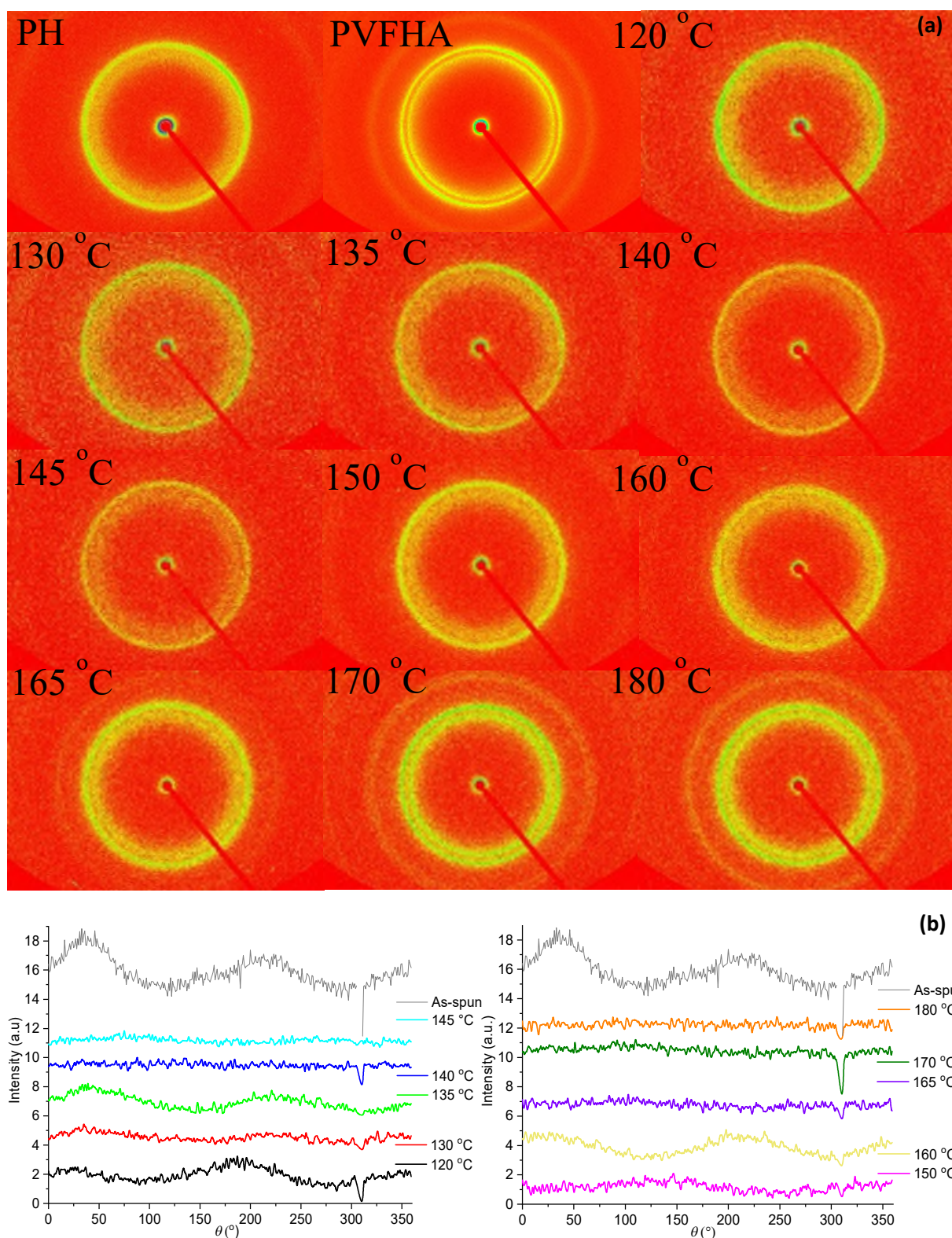


**Figure 0.10.** (a) WAXS diffraction patterns of PVDF-HFP nanofibres (PH nf) and PVFHA nanofibres (PVFHA nf), and PVFHA nanofibre membranes pressed at various temperatures and (b) associated WAXS intensity curves, showing more clearly the presence of orientation (or lack thereof) in the samples. The “as-spun sample” here is the 1D pattern for the “PVFHA nf” sample – no curve for “PH nf” is given.

WAXS diffraction patterns and associated curves are given in **Figure 5.10**. From these data, the as-spun PVFHA nanofibre) clearly displays orientation, more so than any of the other samples. After this, the 120 °C and 135 °C and 160 °C samples seem to show the most orientation, with the 130 °C and 150 °C samples also showing a small amount of orientation. Additionally, close inspection of the curves reveals a minor orientation in the 145 °C, 165 °C and 170 °C samples, whereas the 180 °C and – surprisingly – the 140 °C sample show no orientation whatsoever. If it were not for this 140 °C anomaly, one would easily assume that an increase in pressing temperature simply correlates with a decreased orientation in the nanofibres. Repeat measurements would be needed to clarify this, but in any case, the hot-pressing process seems to remove the rather significant orientation encoded into the nanofibres as they are spun.

To verify the effect of hot-pressing on the microstructure of the nanofibres, SEM imaging was performed on PVFHA nanofibres pressed between 130-160 °C; below temperatures at which they would have fully entered the melt phase, thus losing their fibrous structure almost entirely. The images are provided in **Figure 5.11**. The gradual transition from the unmelted to melted phase with increasing temperature can be seen, with an increasing number of nanofibres becoming melded together by the hot-pressing process as the temperature increases. There is some partial melting clearly occurring even at temperatures as low as 135 °C, although this is restricted to specific small areas where heat has built up during hot-pressing; otherwise, the fibres appear undamaged. By 145 °C, this effect has become much more widespread and many of the nanofibres have now been melted together. By 160 °C, the fibrous structure is almost entirely lost. While in select regions remains of the fibrous structure can be seen, broadly speaking the nanofibre membrane has been pressed into a more homogeneous thin film. Above this temperature, no fibrous structure was visible in SEM micrographs, shown in **Figure 5.12**. Invariant of temperature however, the nanofibre membranes emerge from the press as thinner, more structurally cohesive films. Hence this pressing process will enhance homogeneity of these nanofibre membranes to at least some extent before insertion into the multilayer laminates.



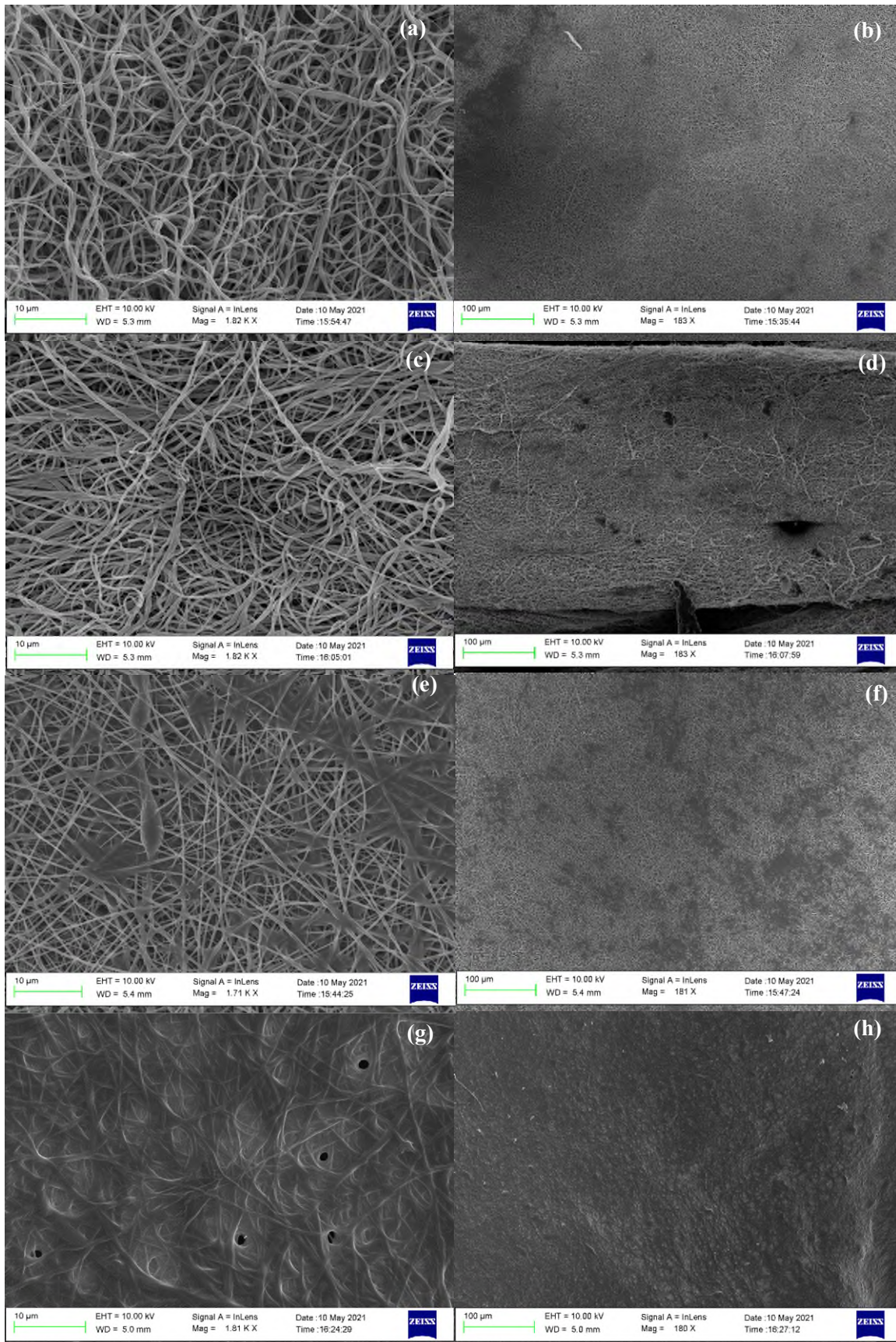


**Figure 0.11.** PVFHA nanofibres pressed at (a, b) 130 (c, d) 140 (e, f) 145 and (g, h) 160 °C

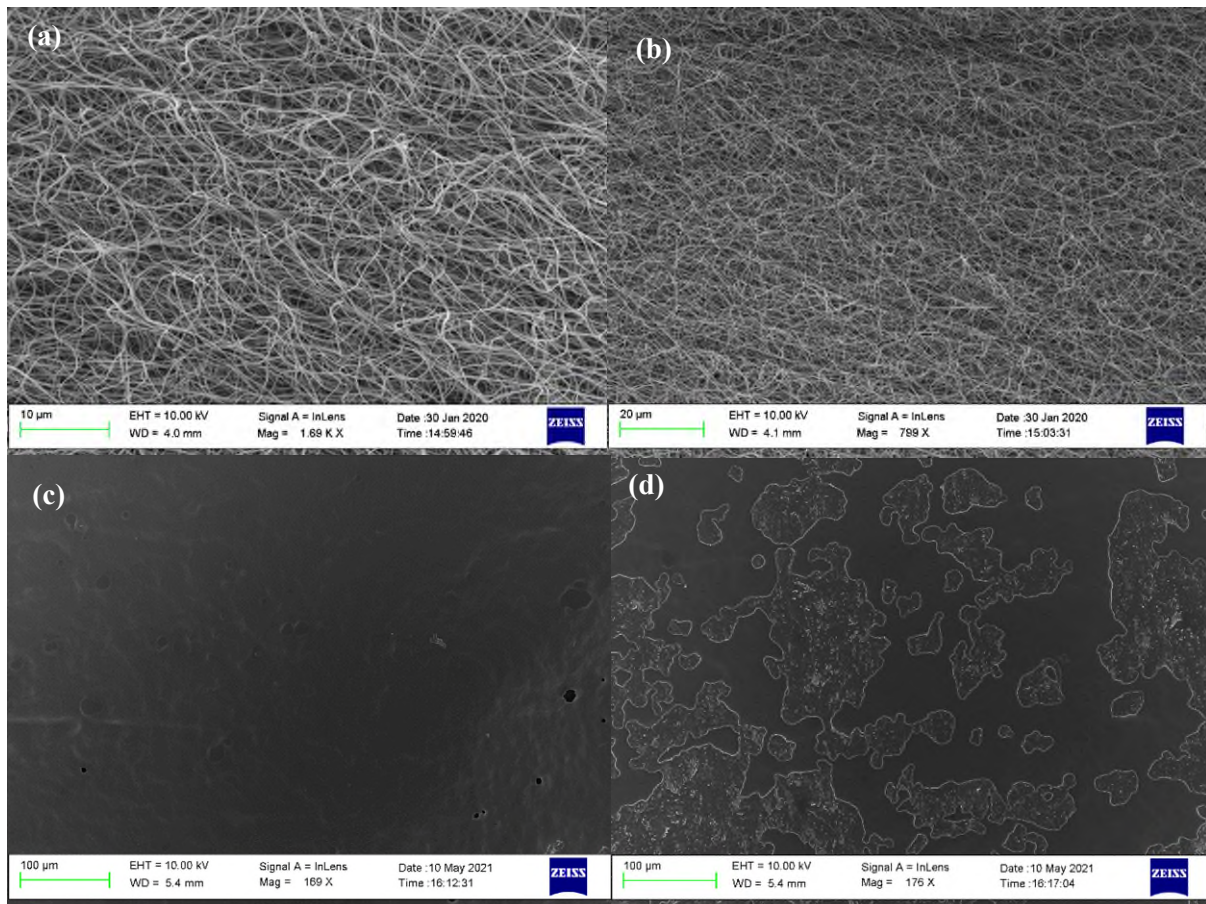


**Figure 0.12.** SEM images of (a, b) neat PVFHA nanofibres and (c, d) 180 °C pressed PVFHA nanofibres.

#### 5.3.4. The effect of pressing temperature on the morphology of laminates

To test how the previously shown results compare to nanofibre membranes incorporated into multilayer laminates for ferroelectric energy storage, similar experiments were performed on various multilayer laminates. Firstly, film morphology was considered. Measurements of PMMA film thickness for films pressed between 120-200 °C revealed that there is not a consistent dependence between temperature and PMMA film thickness. However, a dependence between total laminate thickness and pressing temperature was observed, with the largest difference in thickness observed between 140 °C and 150 °C. Hence, the key factor determining laminate thickness must be the thickness of the nanofibre layers and the temperature at which the laminate is pressed. This implies that the fibre layers undergo a large step change in morphology between pressing at 140 °C and 150 °C. **Figure 5.13** provides a comparison of the cross-sections of the multilayer laminates pressed at 135, 150 and 160 °C at a 20:1 PMMA:PVFHA weight ratio. From these images, it's clear how drastically the laminate structure changes with pressing temperature. The presence of nanofibres is visible at 140 °C, which correlates with a far higher laminate thickness. In contrast, discerning the location of the fibre layer in the 160 °C pressed laminates is extremely difficult, as the layers seem to have



become almost entirely homogenised when pressed at this temperature. This may decrease the electrical resistance between layers, possibly leading to enhanced charge transport and increased dielectric losses. This loss of the fibrous structure and an accompanying thinning of the fibre layers in tandem correlates well with the observed crystallography in the FTIR, WAXS and XRD analyses performed on the pressed nanofibres themselves (**Figures 5.6 – 5.10**), which implied crystallite structure changes at similar times to the morphological changes seen here. Therefore, despite a more homogeneous laminate structure, polarisability is expected to decrease due to the highly damaged crystalline microstructure at 160 °C and above.

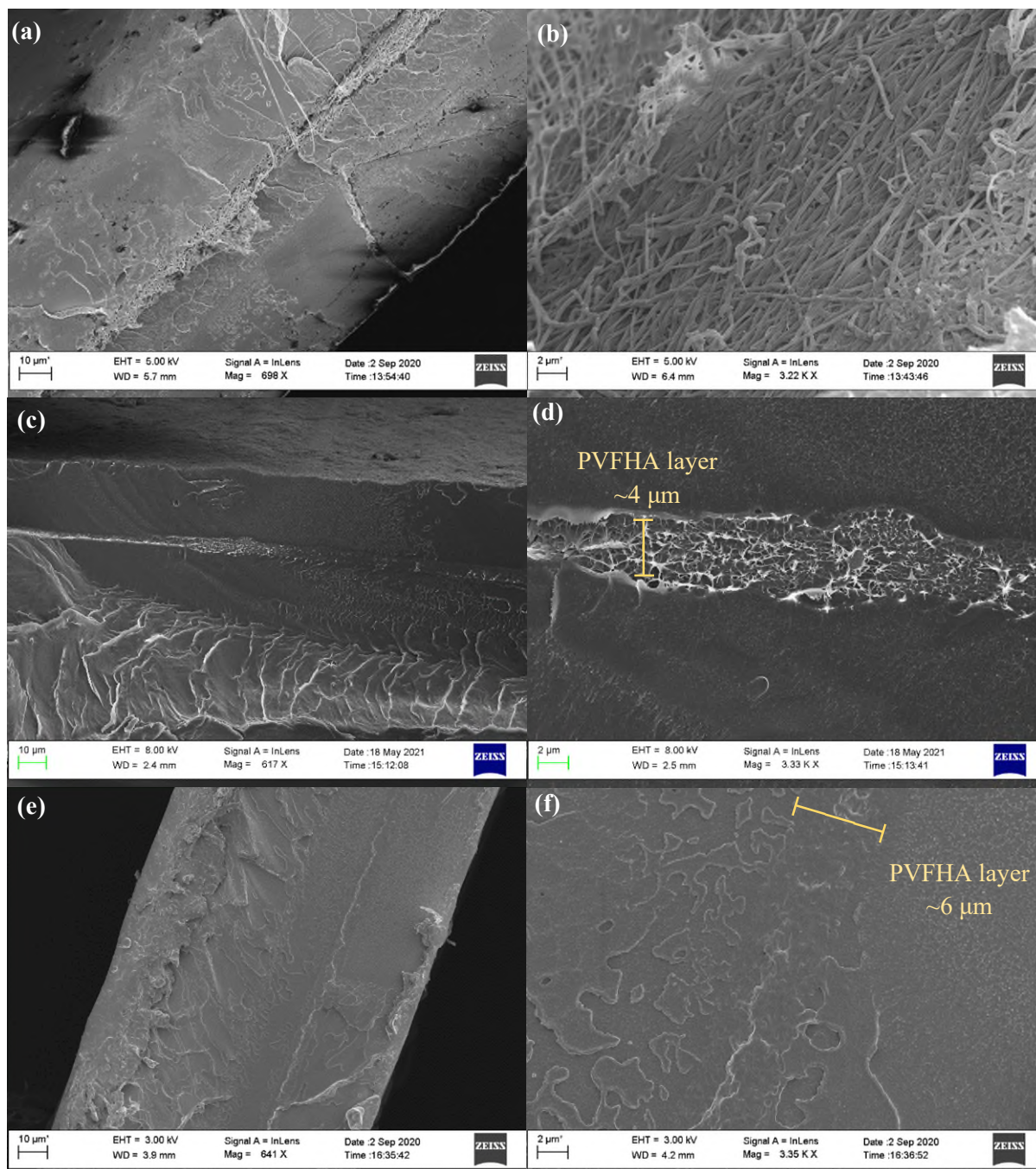


**Figure 0.13.** 3-layer 20:1 PMMA:PVFHA nanofibre laminates, pressed at (a, b) 135 °C (c, d) 150 °C (e, f) 160 °C

However, it is worth considering that the low weight ratio of PVFHA nanofibres to PMMA layers in these samples may have contributed to how easily this layer structure is lost, so the impact of this weight ratio under similar pressing conditions must also be evaluated. **Figure 5.14** provides cross-sectional images of laminates hot-pressed at 140 °C (**Figure 5.14(a-d)**) and 160 °C (**Figure 5.14(e-f)**), at higher PVFHA layer loadings of at least 50% of the PMMA layer weight. The images reveal the same, expected trends in the changes in the layered microstructure. At 140 °C, the fibre layer is still clearly visible within the laminate structure, having retained its fibrous nature on the most part. There appears to be a somewhat smooth

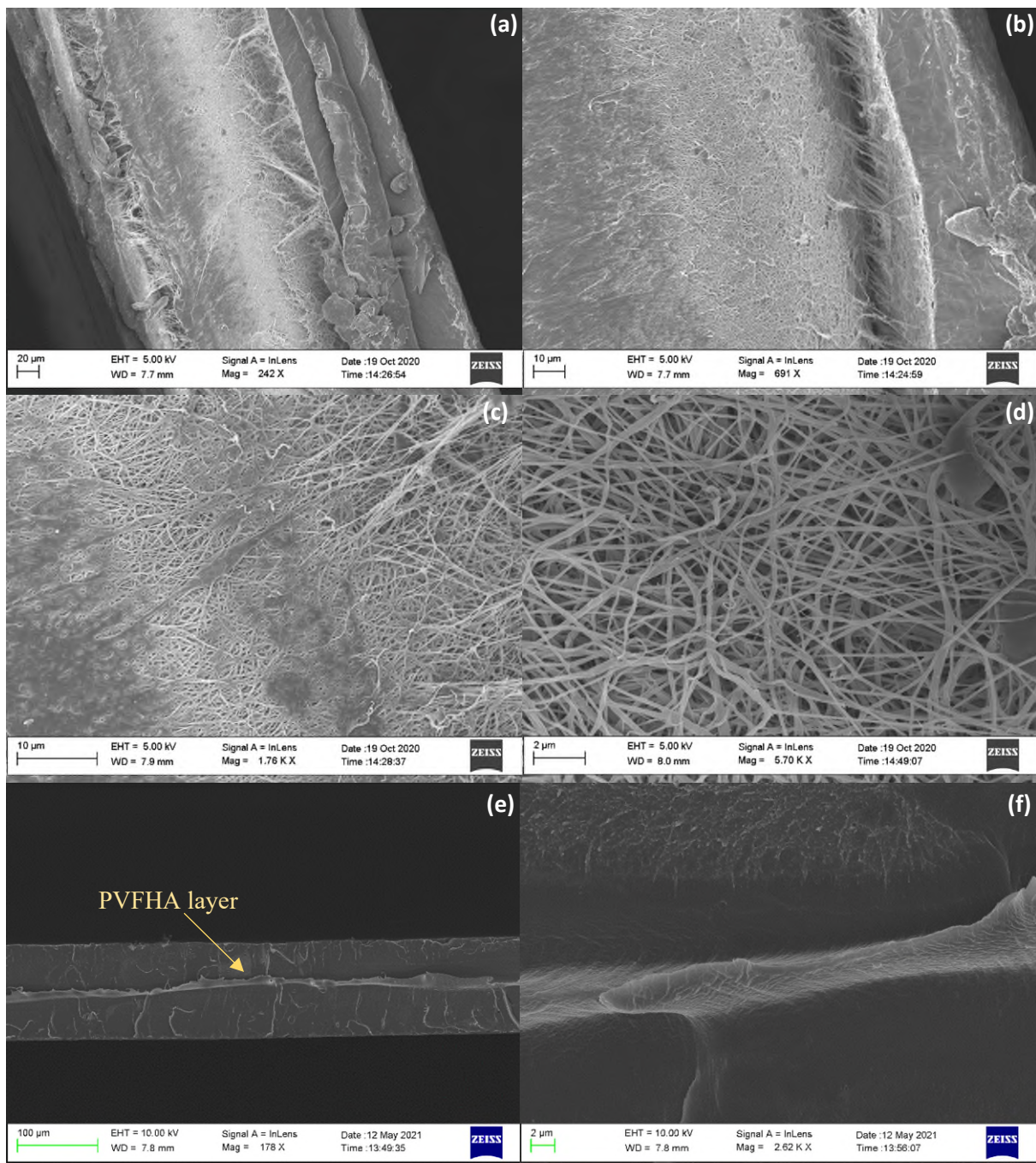


**Figure 0.14.** SEM cross-sections of laminates pressed at (a-d) 140 °C (e, f) 160 °C



transition from the clearly melted PMMA layers to the outer portions of the fibre layers, although clear inhomogeneities are present in the cross-section. These inhomogeneities may not affect polarisability of the ferroelectric domains within the nanofibres, but it does result in a thicker, mechanically substandard laminate with a less defined layer structure, potentially affecting charge transport and interfacial polarisation mechanisms. Most importantly this could lead to defects and voids within the structure, potentially acting as nucleation sites for electrical breakdown.

As the temperature gradually increases to 160 °C, a clear transition into a far more homogenous layer structure is observed. The PVFHA layers are much more easily compressed at this pressing temperature, forming a much more coherent structure and a clearly more homogenous cross-section. Further to this, even in the case of films pressed at 160 °C with a 2:1 PMMA:PVFHA weight ratio, the fibre layer is still distinctly visible, even if it's fibrous structure has been lost. **Figure 5.14(f)** provides a clear picture of how the fibre layer transitions into the PMMA layers, indicating that the layers are independent but are also merged into a continuous structure lacking

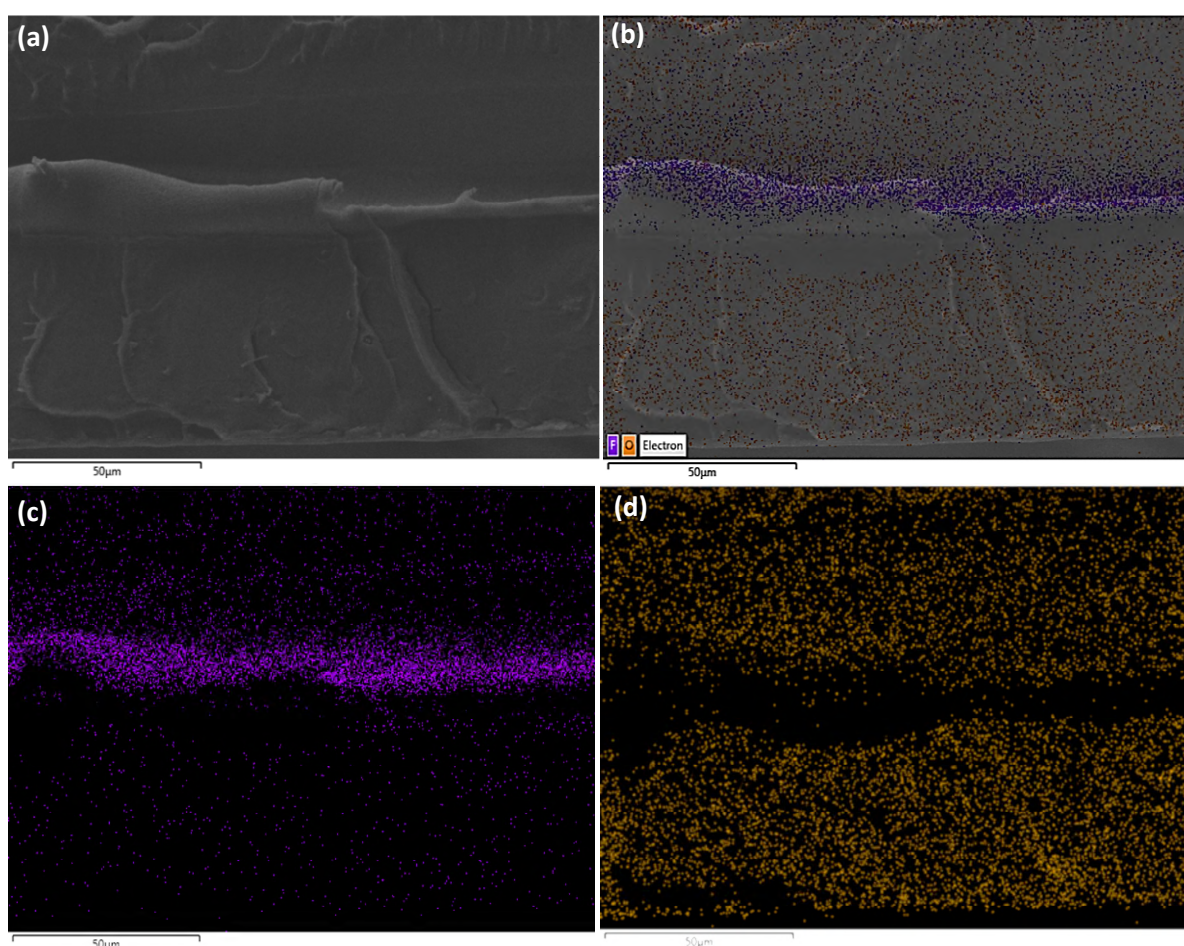


**Figure 0.15.** EDS imaging of the cross-section of the 160°C pressed sample from **Figure 5.13**. (a) Provides a plain SEM image of the sample, while (b) provides the same image with the elemental maps of fluorine and oxygen superimposed. (c) and (d) provides the fluorine and oxygen maps on their own, highlighting the location of the PMMA and PVFHA layers.

voids. To prepare this cross-section, the laminate was torn at room temperature. A blade was used to create an initial incision, and the laminate was subsequently ‘ripped’ along this fracture line. The cross-section imaged in **Figure 5.14(e, f)** was along this torn fracture. Hence, the nanofibre layer must have strongly resisted the tortional force involved in this tearing to produce the observed structure, implying it has retained its mechanical properties independent of the surrounding PMMA layers.

To provide further insight to this pressing process and the effect of temperature on the layer structure, energy-dispersive X-ray spectroscopy (EDS) was performed under the electron microscope on both the 160 °C and 180 °C pressed laminates to distinguish the layers via their elemental composition. Since the molecular structure of PMMA contains only carbon, hydrogen and oxygen, and PVDF-HFP contains only carbon, hydrogen and fluorine, the only elements that required identifying were oxygen and fluorine. **Figure 5.15** provides an SEM image of the cross-section of the 160°C pressed laminate shown in **Figure 5.14(e-f)** with elemental maps superimposed. These images provide clear evidence that the layered structure observed is indeed as predicted at this pressing temperature. However, as shown in **Figure 5.16**, the layered structure is completely lost when pressing at 180 °C – above the melting temperature of PVDF-

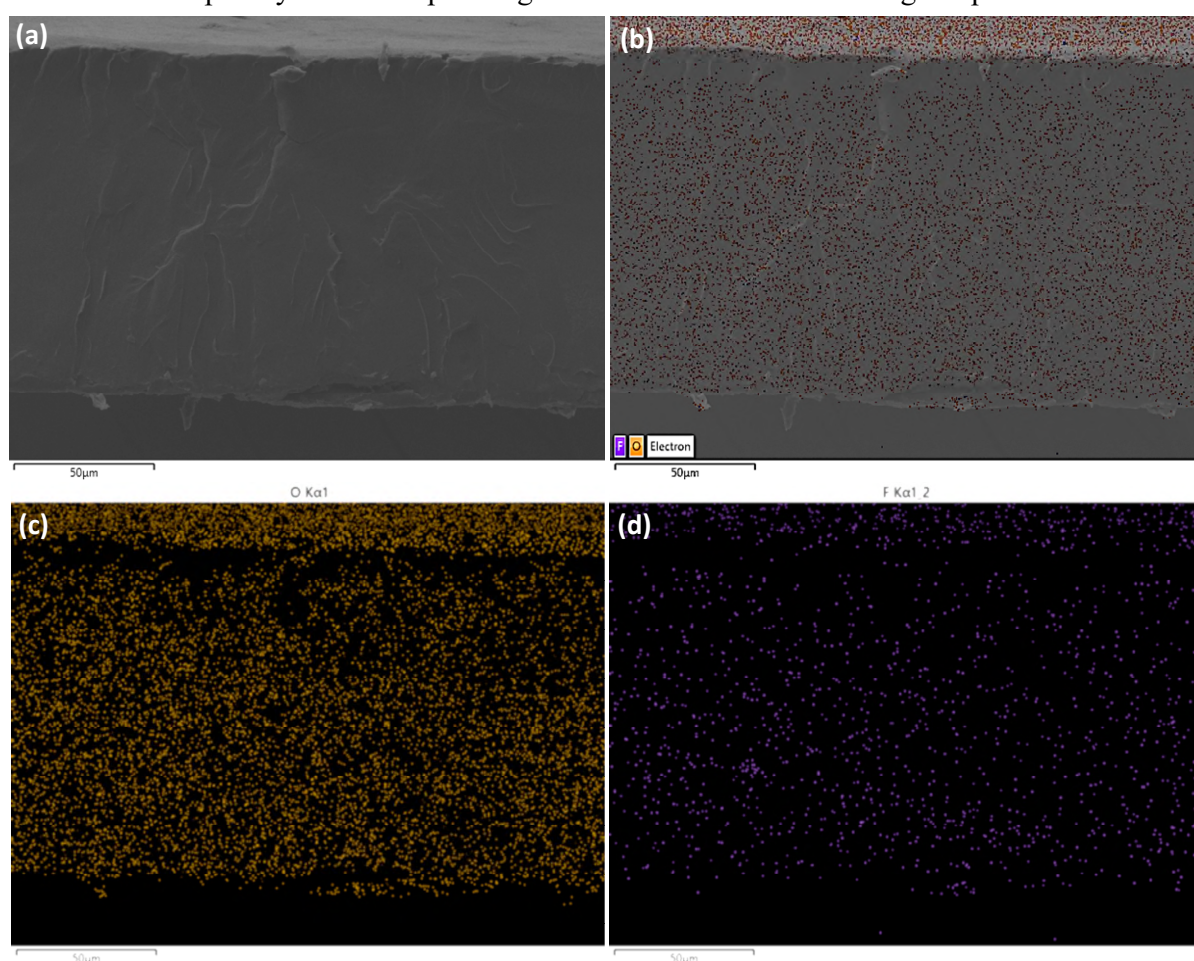


**Figure 0.16.** (a) Cross-section of a 180 °C pressed laminate with (b) showing the total elemental map, (c) showing the oxygen content and (d) showing the fluorine content. No layer structure is discernible.



HFP – and no fibre layer is identifiable either visually (**Figure 5.16(a)**) or from the EDS maps (**Figure 5.16(b-d)**). This loss of layered structure will completely remove the prospect of interfacial polarisation in the laminates due to the destruction of interfaces. Additionally, since the PVDF-HFP has likely been completely melted by the pressing process at this temperature, the crystallinity induced by electrospinning will have been entirely lost.

### 5.3.5. The effect of pressing temperature on nanofibre crystalline nanostructure

To confirm the impact of the pressing temperature on the crystalline microstructure of the fibres within the laminates, X-ray diffraction (XRD) and WAXS studies were performed on 3-layer PMMA/PVFHA nanofibre laminates pressed at 140 °C and 160 °C, similar to those performed previously on the hot-pressed nanofibre membranes. **Figure 5.17** gives a comparison of the XRD spectra between laminates pressed at these two temperatures, alongside any nanofibre peaks, with many of the key crystalline peaks indexed. It should be noted that there appears to be a large PMMA hump between 14° and 18° in the 160 °C laminate spectra. This hump is also present in the 140 °C spectra, but the (100)/(020)  $\alpha$ -phase peak at  $\sim 18.1^\circ$  is substantially more prominent in the 140 °C spectra, partially obscuring this PMMA peak. Firstly, the key 20-21° peak, containing both  $\alpha$ - and  $\beta$ -phase signatures should be investigated. Additionally, sharp peaks are associated with low crystallite sizes, whereas broad peaks are associated with large crystallites. This peak has shifted quite substantially down from 20.8° down to 20.4° – as well as undergoing substantial broadening – when increasing the pressing temperature from 140 to 160 °C. This implies a diversification of crystal phase content, as well as the formation of generally larger crystallites, hence the nanofibres must have entered the melt-phase and recrystallised to a fairly significant extent. Hence it seems that 160 °C pressing is enough to eliminate the crystal structure of the nanofibres in these laminates imposed by the electrospinning procedure. Further to this, the peak of the neat PVFHA nanofibres appears to be

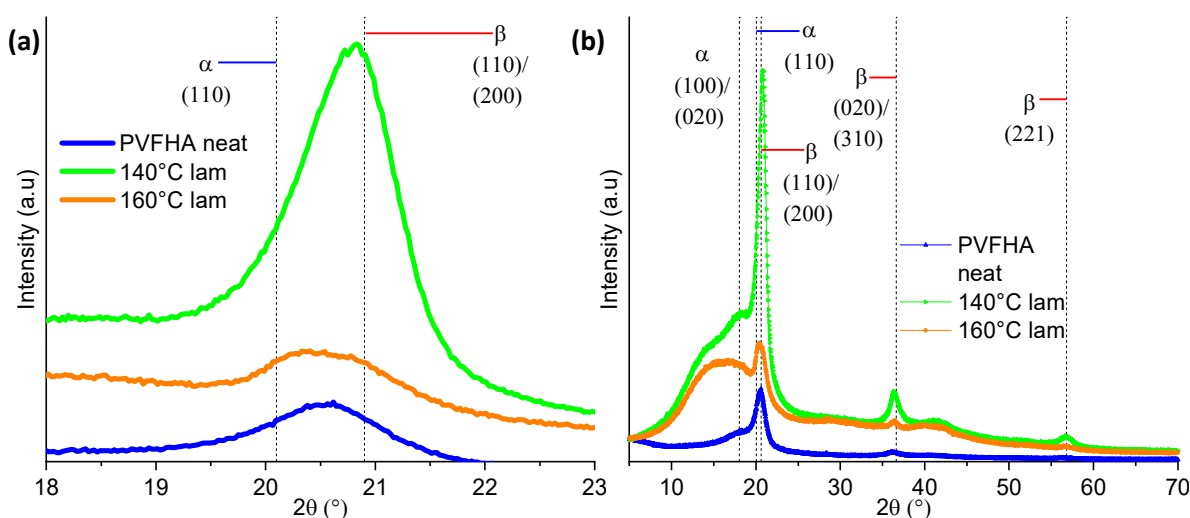


**Figure 0.17.** XRD data of laminates pressed at 140 °C and 160 °C, as well as neat PVFHA nanofibres for comparison. (a) provides the whole spectra while (b) shows only the in-plane crystallite peak.

at  $20.6^\circ$ , implying that pressing at  $140^\circ\text{C}$  may actually enhance the in-plane  $\beta$ -phase content. However the emergence of the stronger (100)/(020)  $\alpha$ -phase peak in the  $140^\circ\text{C}$  spectra implies there are still some undesirable crystal phase changes induced by the pressing process. Oddly enough this peak is lost when pressing at  $160^\circ\text{C}$ , providing further evidence that pressing at a temperature this high induces the PVDF-HFP to enter the melt-phase and recrystallise.

Secondly, it's worth investigating the  $\beta$ -phase peak at  $36\text{--}37^\circ$ . While the peak clearly appears in all three spectra, its relative intensity is at its maximum in the  $140^\circ\text{C}$  pressed laminate, and at its lowest in the  $160^\circ\text{C}$  laminate, with the unpressed nanofibre lying in between. This progression initially seems bizarre, but in the context of the  $20\text{--}21^\circ$  peak, it may be explained by the partial melt-phase entered at  $140^\circ\text{C}$ . If the nanofibres are exposed to enough heat and pressure to induce recrystallisation of only a small portion of the PVDF-HFP, the

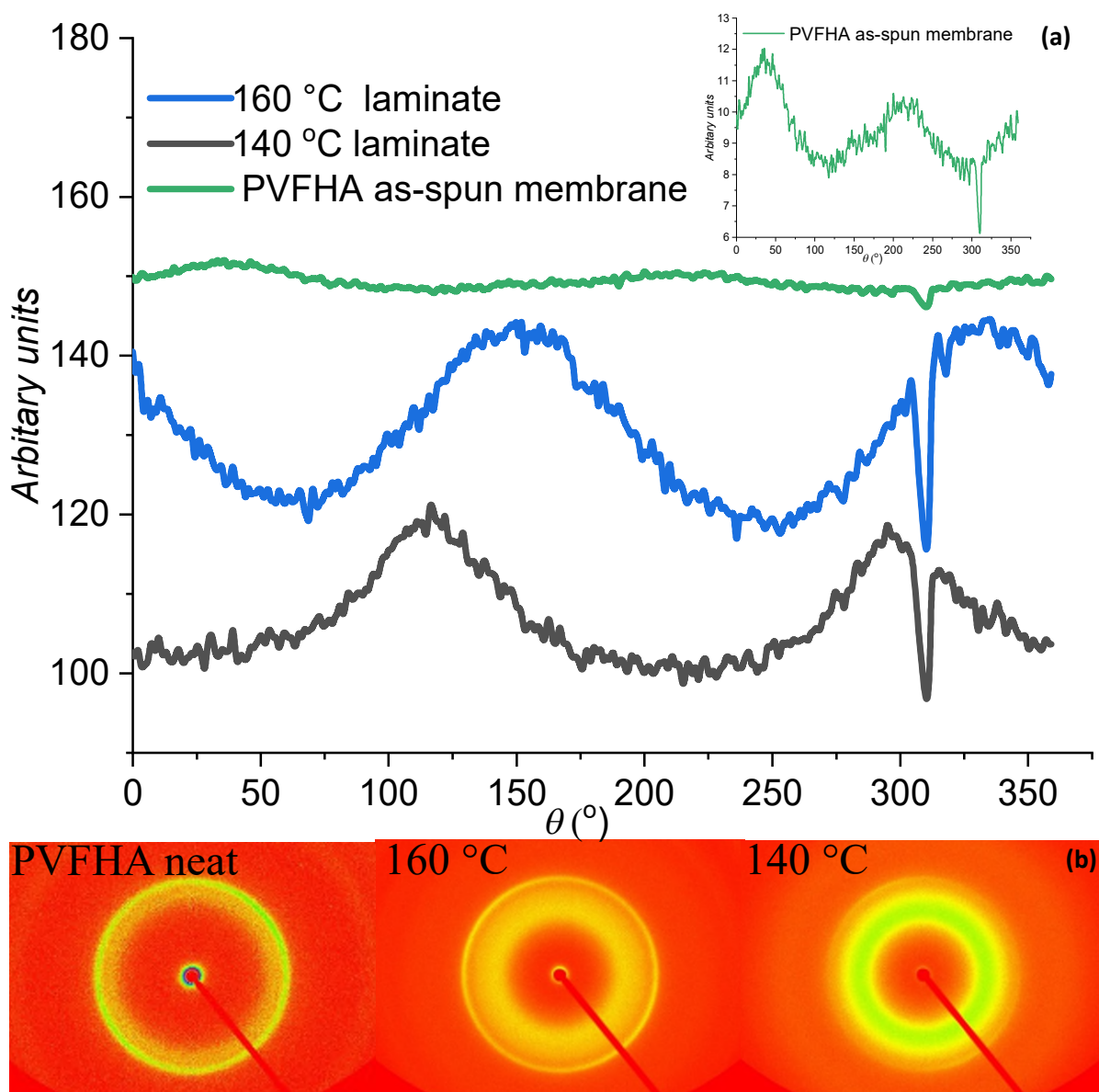


**Figure 0.18.** (a) WAXS intensity curves of laminates pressed at different temperatures, as well as an as-spun nanofibre membrane, also shown in the inset. (b) WAXS patterns of the same samples.

recrystallisation may be highly influenced by the  $\beta$ -phase dominant environment this recrystallisation occurs within. Hence, so long as only a small amount of  $\beta$ -phase PVDF-HFP is lost in the melting process, the recrystallisation should not substantially impact the overall  $\beta$ -phase crystallinity. In fact, the crystallographic planar orientation of some of the  $\beta$ -phase PVDF-HFP seems to have become more random in the 140 °C pressed laminate compared to the as-spun nanofibres, as the relative intensity of the 36.2° peak compared to the 21° is higher in the 140 °C laminate compared to the neat nanofibre. By 160 °C, the fibres in the laminate seem to have melted enough such that the  $\beta$ -phase dominance is lost, and recrystallisation into the  $\beta$ -phase will not be nearly as common. Finally, the (221)  $\beta$ -phase peak at 56.8°, comfortably at its most prominent in the 140 °C pressed laminate, provides further evidence that this pressing temperature produces the highest proportion of  $\beta$ -PVDF.

Additionally, to investigate the in-plane orientation of the crystallites, through-plane SAXS measurements on the same selection of samples were acquired to probe. The results are shown in **Figure 5.18**. Comparing the three curves, the two laminates clearly show some orientation. Additionally, from inspecting the neat PVFHA nanofibre data closely, as shown in the inset, substantial orientation is also seen in the as-spun PVFHA nanofibre membrane. These results imply that the either pressing process itself may have been effective at inducing some orientation in the crystallites present in the nanofibres, or that the orientation initially present in the nanofibres is preserved during the pressing process. The high pressure exerted on the nanofibres during the pressing process may have helped to induce some orientation with the assistance of the outer PMMA layers. Or, at the very least, the pressing process was not enough to remove the orientation of crystallites that remains in the laminates after the pressing process, regardless of the pressing temperature.

### 5.3.6. The effect of pressing temperature on energy storage in laminates

Most importantly, P-E tests were performed on these samples to discern the effects of pressing temperature on the energy storage performance of the laminates. **Figure 5.19** shows the performance of the laminates pressed at various temperatures between 140 and 180 °C, alongside a comparison to a neat PMMA sample, while **Table 5.2** provides the values attained from these tests. These curves reveal a trade-off when increasing the pressing temperature of the laminates; sample polarisability is decreased, but the electrical breakdown strength is enhanced. Both the 180 °C and 150 °C pressed samples survived up to the 10 kV voltage limit of the apparatus without undergoing breakdown over multiple tests, surviving electric fields of over 800 kV/cm. Similarly, the 160 °C sample regularly survived to over 1000 kV/cm without undergoing breakdown. The 140 °C sample however breaks down far earlier, between 450-650 kV/cm. The poor layer adhesiveness of the fibre layers compared to the PMMA layers, as can be seen in **Figure 5.13**, is likely the cause of this, as the sample is more likely to contain defects

in the area between the electrodes after pressing at these lower temperatures. From this data, there was an insufficient total area of samples to conduct enough tests to produce a data set which may have been used for Weibull breakdown analysis to discern a statistical measure of the sample reliability.<sup>27–29</sup> Although, there is sufficient data to draw some preliminary conclusions. In the case of almost any laminate pressed at 160 °C (for example, including those with lower PVFHA nanofibre contents), there was at least one test performed in which the electrical breakdown strength was far lower than seen in other tests. Since over the course of 4 tests the 180 °C sample was not observed to undergo breakdown once – even when testing areas of the sample which were not in close proximity – and the 140 °C pressed sample was observed to break down reliably between 450 and 650 kV/cm, a sensible inference is that the higher sample homogeneity produced at higher pressing temperatures increases resistance to breakdown at high fields. More tests from many samples pressed under the sample conditions would be needed to solidify these conclusions, preferably with a dataset large enough to perform Weibull analysis on to determine the true failure rate of these samples to relate to their pressing temperature.

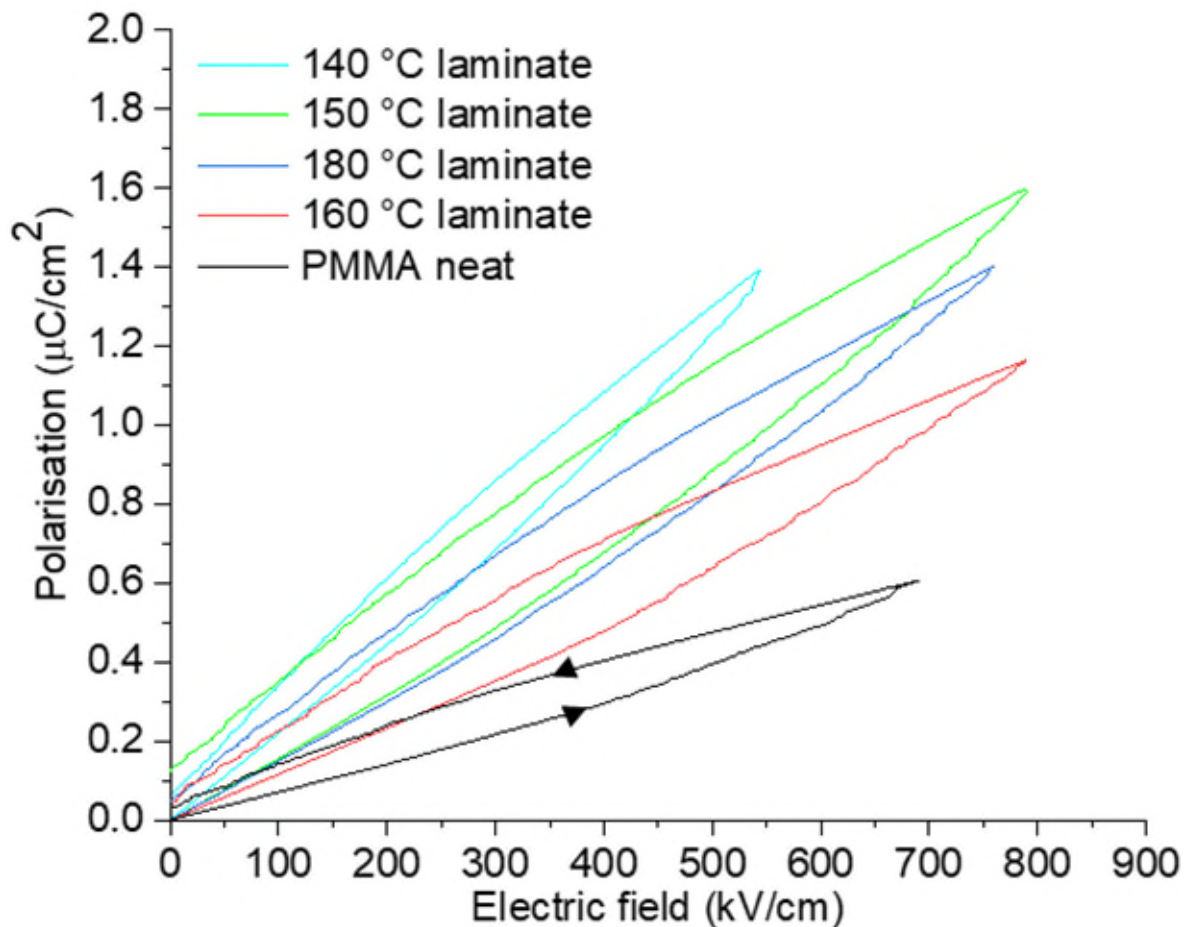


**Figure 0.19.** P-E curves for 3-layer PMMA/PVFHA laminates pressed at various temperatures, alongside a neat PMMA sample.

**Table 0.2.** Ferroelectric performance metrics for the samples provided in **Figure 5.19**, along with the electric field at which these samples were tested. Notably, a clear drop off in energy storage capacity between 150 °C and 160°C is seen

Sample	$U_e$ (mJ/cm <sup>3</sup> )	$\eta$ (%)	$E$ (kV/cm)
PMMA neat	311	73.0	700
140 °C laminate	341	82.2	550
150 °C laminate	576	75.7	800
160 °C laminate	395	76.6	800
180 °C laminate	470	78.9	770

To conclude, while it is surprising to see the strong performance of the 180 °C laminate, the studies presented so far show that a lower pressing temperature of 140 °C was able to mostly retain the crystal phase content and orientation induced in the PVFHA nanofibre membranes by the electrospinning process, which resulted in the most polarisable PMMA/PVFHA nanofibre laminates. While a higher pressing temperature may afford a higher breakdown strength by enhancing sample homogeneity, the most reliable and impressive performance is realised by utilising lower pressing temperatures whilst trying to attain the highest sample homogeneity possible in this context. An intermediate temperature of around 150 °C may also be considered as a compromise between these competing factors, and – as shown in **Table 5.2** – produces the highest discharged energy density of all the curves shown in **Figure 5.19**. Additionally, bearing in mind that higher electric fields produce higher energy losses, it does also seem that energy losses are lower when using higher pressing temperatures, which may contribute to a better performance if these pressing temperatures (most notably 150 °C) are utilised instead. So, it seems that the PVFHA nanofibres are providing a unique crystal structure which may be carried forward into the laminate structure under appropriate pressing conditions. But how do the nanofibres compare to hot-pressed PVDF-HFP in a comparable laminate structure?

### 5.3.7. The energy storage performance of PVFHA nanofibres in laminates

To verify the benefits of utilising electrospinning as a method to produce electroactive, highly polarisable PVDF in our multilayer laminates, 3-layer laminates containing a hot-pressed PVDF-HFP layer instead of the nanofibre layer were produced. Of course, hot-pressed PVDF-HFP is expected to mostly consist of the  $\alpha$ -phase and to have a lower total crystallinity, as per the results stated in chapter 3.<sup>30–32</sup> Hence, this hot-pressed PVDF-HFP laminate should show far lower polarisability than the electrospun laminates. The hot-pressed PMMA:PVDF-HFP laminate was constructed by pressing at 140 °C, the standard 40 bar pressure applied, and with PMMA and PVDF-HFP layer masses of 300 mg. SEM cross-sections provided in **Figure 5.20**. These images clearly reveal the presence of a central PVDF-HFP layer, comparable to those seen in **Figures 5.15, 5.16**, again appearing thinner than the outer PMMA ones. The more brittle

PMMA layer easily snapped when preparing this cross-section, but the PVDF-HFP seems to have been more reluctant to tear, making it easy to identify.

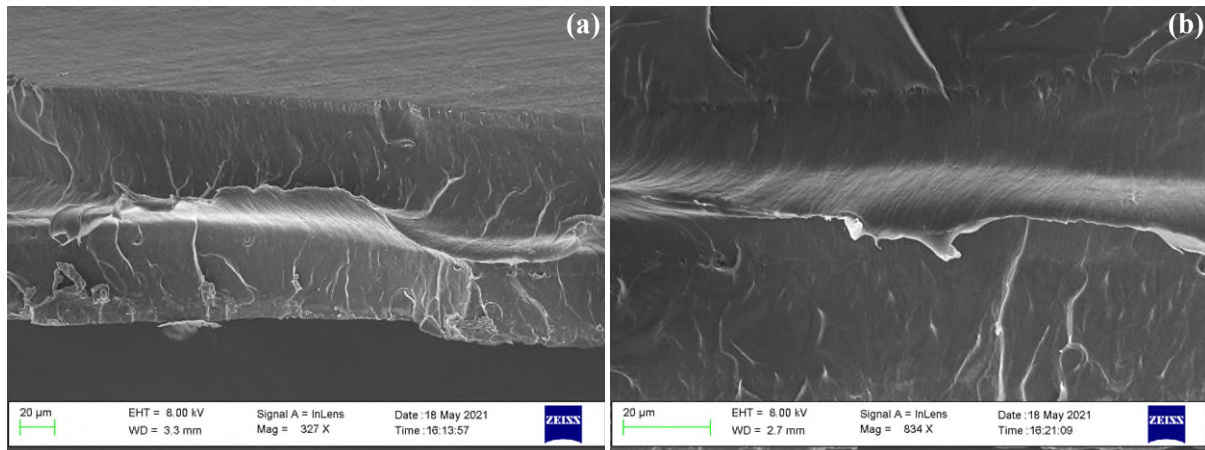


**Figure 0.21.** SEM images of a 3-layer laminate containing a hot-pressed PVDF-HFP central layer and two outer PMMA layers.

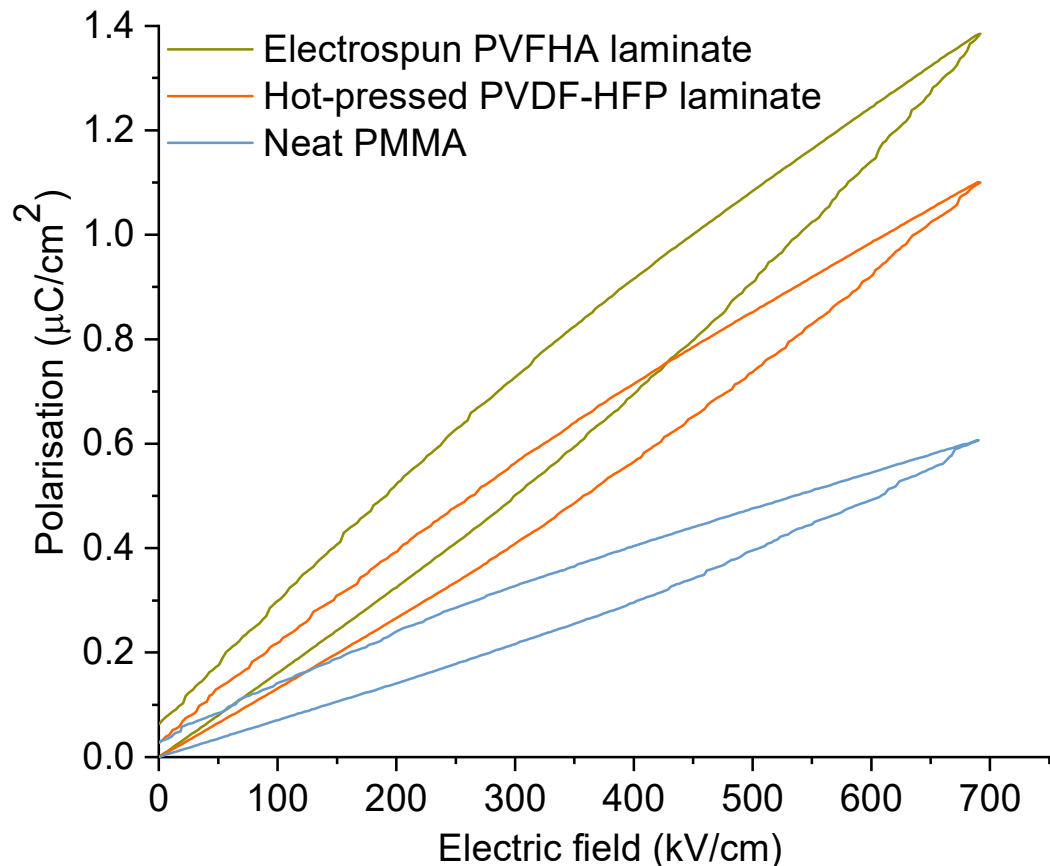


**Figure 0.20.** P-E loops of 3-layer PMMA/PVDF-HFP laminates, containing electrosun and hot-pressed PVDF-HFP, at equal weight ratios of PMMA:PVDF-HFP, tested up to a field of 700 kV/cm, with a neat PMMA sample for control. While the biggest difference in performance comes in the form of adding PVDF-HFP to form a 3-layer laminate with either production method, the nanofibres still outperform their hot-pressed counterpart by over 20% in terms of discharged energy density, while producing a similar discharge efficiency.



**Figure 5.21** gives a comparison between this laminate and a comparable multilayer laminate containing electrospun PVFHA nanofibres, with all 3 the layers weighing 300mg in both cases. A neat PMMA sample is also provided for comparison. At a moderately high electric field of 700 kV/cm, neat PMMA reaches a discharged energy density,  $U_e$ , of 179 mJ/cm<sup>3</sup> at a discharge efficiency  $\eta$  of 76.4%. The 3-layer hot-pressed PVDF-HFP laminate comparatively can discharge 340 mJ/cm<sup>3</sup> – an increase of 90% – at an efficiency of 82.7% at the same electric field. In comparison, the PVFHA nanofibre containing laminate shows a discharged energy density of 417 mJ/cm<sup>3</sup> at an efficiency of 78.2%, this time an increase of 133% compared to the neat PMMA. Additionally, the remnant polarisation,  $P_r$ , seen in all 3 of these samples is very low. Both the neat PMMA and hot-pressed PVDF-HFP multilayer show an extremely similar  $P_r$  of around 0.028  $\mu\text{C}/\text{cm}^2$ . This is compared to the fibre multilayer, which exhibits a  $P_r$  of around 0.063  $\mu\text{C}/\text{cm}^2$ ; more than double, but still very small in comparison to the maximum polarisation,  $P_{max}$ , which stands at 1.385  $\mu\text{C}/\text{cm}^2$ , 22 times higher.

Additionally, to develop on and further clarify the XRD, SAXS and WAXS analysis performed on solution-cast, hot-pressed and electrospun PVDF samples in chapter 3, XRD and WAXS data

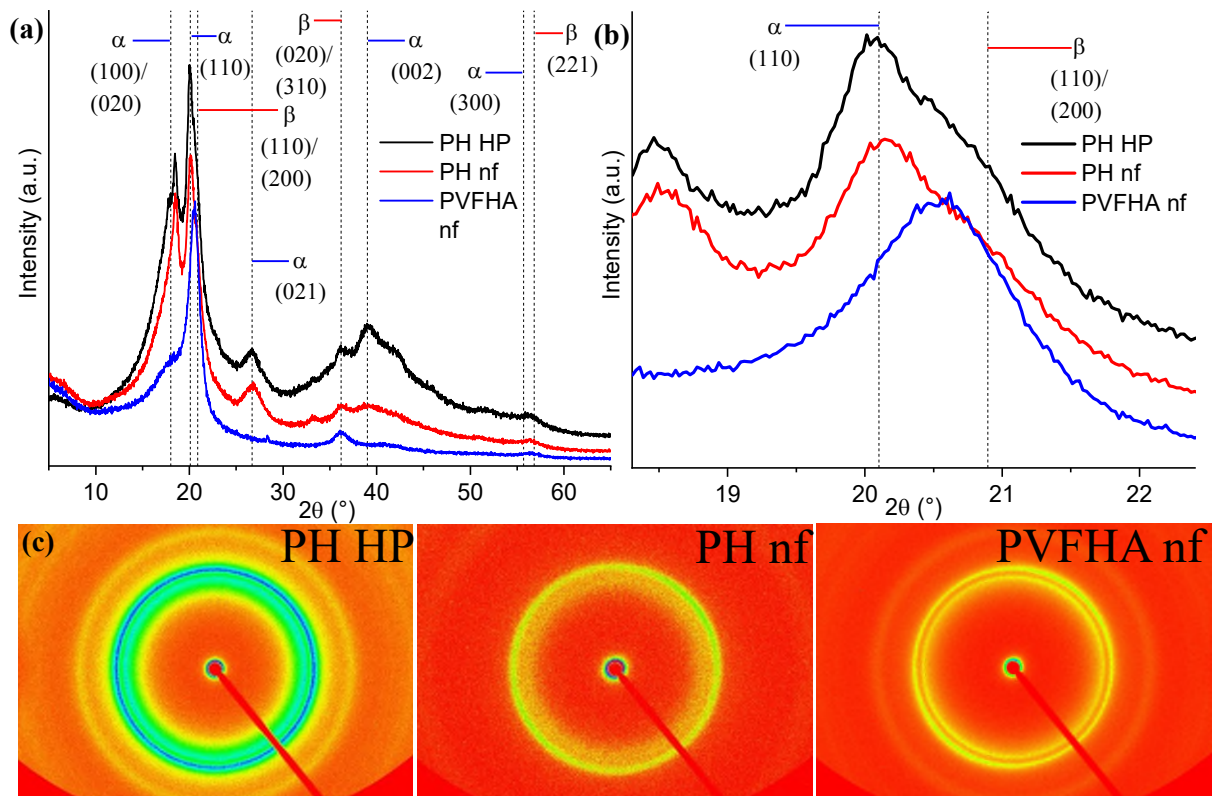


**Figure 0.22.** (a,b) XRD spectra including labelled key peaks in samples of hot-pressed PVDF-HFP (PH HP), PVDF-HFP nanofibres (PH nf) and PVFHA nanofibres (PVFHA nf) and (c) SAXS diffraction patterns of the same samples. The  $\alpha$ -phase clearly diminishes to give rise to the  $\beta$ -phase both when moving from hot-pressing to electrospinning, and when adding AMIM to the electrospinning process. Additionally, a small  $\gamma$ -phase (130) peak is seen at  $\sim 33.2^\circ$  in the two samples lacking AMIM, particularly in the electrospun sample.<sup>26</sup>

was collected to compare hot-pressed PVDF-HFP to electrospun PVDF-HFP nanofibres with and without the AMIM ionic liquid additive. Data from this study are given in **Figure 5.22**, which confirms the expected phase conformation of the 3 PVDF-HFP samples based on the data presented in chapter 3. Clear similarities are visible between the XRD spectra of the hot-pressed PVDF-HFP (PH HP) and the electrospun PVDF-HFP without AMIM (PH nf), with each sample showing strong  $\alpha$ -phase peaks, most notably at  $18.0^\circ$ ,  $26.7^\circ$  and  $39.0^\circ$  for the (100)/(020), (021) and (002) crystal planes respectively. Additionally, the  $20\text{--}21^\circ$  peak – which is indicative of planar oriented phase content – has clearly substantially shifted in the PVFHA nanofibre (PVFHA nf) sample towards the  $\beta$ -phase end of the peak compared to the other two samples. Since there is no indication of  $\alpha$ -phase presence elsewhere in the spectra, this provides confirmation that a phase makeup optimised to result in ferroelectric behaviour is present in the PVFHA sample.

Investigating the WAXS data, the PH HP sample is clearly extremely phase diverse. By inspecting its diffraction pattern, it doesn't seem to display any orientation. In contrast, both nanofibre samples show small but noticeable orientation signatures, most likely induced by the alignment of crystallites as the solution dries and the nanofibres form during electrospinning. The fact that nanofibres are oriented (randomly) in-plane in the produced membrane may also add to an orientation bias against through-plane orientation. The less diverse distribution of  $\alpha$ -phase signatures in the PH nf sample compared to the PH HP sample, particularly with respect to many of the higher deflection angle peaks, further confirms there is a greater degree of orientation induced by electrospinning compared to hot-pressing. Hence, this data shows that electrospinning as a technique is more likely to produce oriented crystallites, while the use of AMIM will induce  $\beta$ -phase formation, supporting the use of this methodology to produce ferroelectric PVDF-HFP.

### 5.3.8. The effect of PMMA layers on energy storage performance of laminates

Now the effectiveness of the central ferroelectric layer has been verified, the same should be done for the outer, insulating PMMA layers. Nanofibres alone – P-E loops of which are shown in **Figure 5.23(a)** – retain the majority of their polarisation after the field is removed. So, compared to neat PVFHA nanofibres, the remnant polarisation,  $P_r$ , seen in the laminates in **Figure 5.21** is extremely low. The fibres still show high losses even while applying a higher frequency electric field (100 Hz as opposed to the 10 Hz used in our tests on multilayer laminates) in an attempt to prevent significant semi-permanent poling due to application of a unidirectional electric field for a sustained period. To elaborate, at 10 Hz, the longer oscillatory period of the field means the ferroelectric domains of the PVDF-HFP strongly polarise along the direction of applied field and proceed to pull other domains with them as they orientate. This prolonged poling period means the nanofibres continue to polarise even after the field has



decreased to around 10% of the maximum, at which point the polarisation starts to drop, although only by  $\sim 1\text{-}2\%$  of the maximum polarisation once the field has been removed entirely. In the case of a 100 Hz field, the nanofibre begins to discharge as the field reaches 66% of the maximum field: a significant improvement over the 10 Hz case. The shorter period of unidirectional field application in the 100 Hz case leads to a less permanently poled sample, leading to easier discharge. Although, the  $P_r$  at 0 field is still  $>80\%$  of  $P_{max}$ , meaning the  $U_e$  is still extremely low. A P-E loop for a 3-layer nanofibre laminate (at a 1:1 PMMA:PVDF-HFP weight ratio) is also provided, reaching a larger  $P_{max}$  ( $\sim 18\%$  higher) while displaying far lower ferroelectric losses and a  $P_r$  of  $<4\%$  of the  $P_{max}$ . Further to this, the nanofibre membranes failed to survive fields higher than the 400 kV/cm used here without undergoing electrical breakdown, whereas the laminate managed to reach almost 800 kV/cm before reaching the voltage limit of the apparatus, avoiding breakdown entirely up to this field.

The lack of an outer insulating layer means that leakage currents between the nanofibres and the electrodes are very high in the neat PVFHA nanofibres, an effect that will have made substantial contributions to ferroelectric losses. **Figure 5.23(b)** shows the clear difference in current in this fibre sample at both 10 Hz and 100 Hz compared to the nanofibre laminate tested at 10 Hz. In all 3 cases, the samples displayed a gradual increase in current as the electric field was increased, although in the case of the neat PVFHA nanofibre being exposed to a 100 Hz applied field, there is also an initial sharp increase in current. However, the delay between the field beginning to ramp down and when the current begins to decrease varies largely between the samples. In the case of the neat nanofibre sample tested at 10 Hz, this decrease takes some time to manifest as the sample continues to polarise even after the field has begun to ramp down. Comparing this to the laminate tested at 10 Hz, besides the evidently much lower current, the

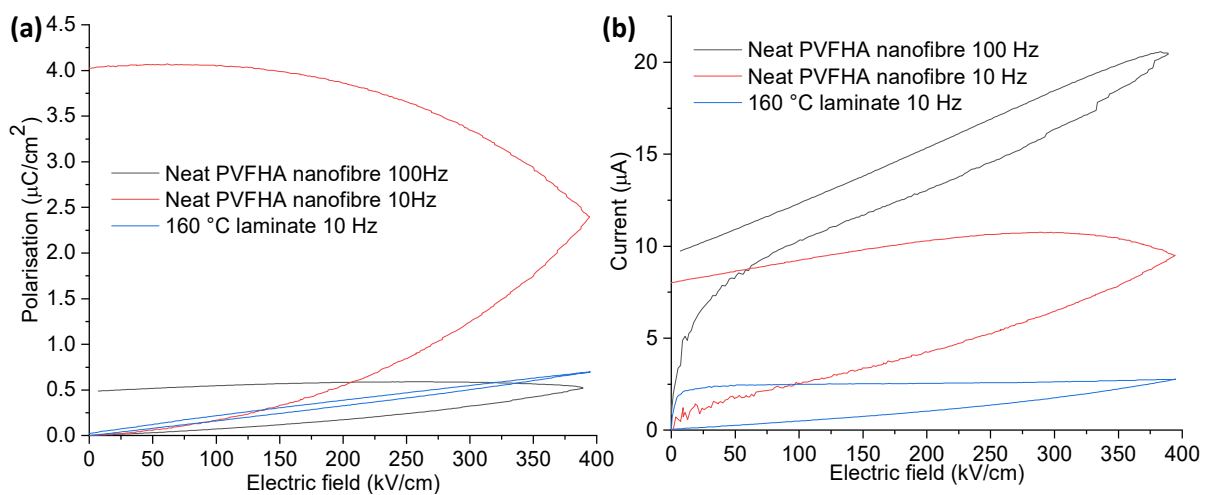


**Figure 0.23.** Polarisation and current data for a PVFHA nanofibre membrane pressed at 140 °C, alongside data for a high PVDF-HFP content PMMA/PVFHA nanofibre laminate pressed at 160 °C. 400 kV/cm was the field selected here, as the nanofibre membrane underwent electrical breakdown at 420 kV/cm.

decrease is very slow. Although, it begins this gradual decrease as soon as the field begins to ramp down. It then drops towards 0 quickly as the field nears 0, corresponding with last of the polarisation discharging, hence the low observed  $P_r$ . In contrast, the current in the neat nanofibre membrane tested at 10 Hz is still very high at 0 field, corresponding with the extremely high  $P_r$  it exhibits in **Figure 5.23(a)**. The 100 Hz neat fibre sample experiences even higher currents which – due to the faster switching of the field direction – begins to decrease almost as soon as the field begins ramping down. However, a very high current remains even at 0 field, again correlating with the previously observed high  $P_r$ . In fact, during discharge, the current in the 100 Hz case discharge is higher at all fields than in the 10 Hz case. The very different response from the material between 10 Hz and 100 Hz in terms of both polarisation and current implies that there may be components of the ferroelectric nanostructure which are responding at 10 Hz rather than 100 Hz. Unfortunately testing at 100 Hz for the multilayer laminate was not possible above 200 kV/cm, as the sample did not respond quickly enough to the applied field for the measurement apparatus to be able to obtain data. Since the loss in a dielectric includes a component proportional to d.c. conduction at low frequencies (**equation 1.6**), comparatively low resistance samples such as the neat PVFHA nanofibres will exhibit very high losses. This is what leads to the comparably large polarisation and losses seen at 10 Hz in the PVFHA nanofibres in **Figure 5.23(a)**; it is the polarisation produced by a conductive circuit. This supports the notion that the PMMA layers significantly reduce the conductivity of the sample by preventing leakage currents, thus substantially reducing the remnant polarisation in the sample after the field is removed. Without the PMMA layers, a tiny  $U_e$  will manifest instead, along with a very low discharge efficiency, as seen in the neat PVFHA nanofibres. The employment of PMMA layers to form a multilayer structure hence converts the fibres from performing as inefficient and lossy stores of polarisation into efficient capacitors capable of delivering high pulsed power outputs at high electric fields.<sup>33,34</sup>

### 5.3.9. The effect of the PHA:PMMA mass ratio on ferroelectric performance

The use of PMMA in the multilayer structure has proven effective at preventing leakage currents and dielectric losses, as well as enhancing the electrical breakdown strength. Its use also comes with the added benefit of increasing the mechanical integrity of the material, producing a tougher film with a less fragile surface while retaining the flexibility of the nanofibres. Finding the optimal ratio between the PVFHA nanofibre and PMMA layers is less dependent on these factors however, as even a thin PMMA outer layer will substantially reduce leakage currents as well as enhancing the mechanical integrity and breakdown strength. The key difference a higher PMMA ratio will have on the laminate is on the polarisability, particularly at high fields. PMMA is an amorphous polar polymer, typically exhibiting a fairly low molecular dipole moment in the range of 1.3-1.5 D depending on its tacticity.<sup>35</sup> While it does not contribute

to polarisability in the form of ferroelectricity like PVDF-HFP, the PMMA dipoles can still make significant contributions to the laminate's energy storage capabilities. Due to the lack of crystallites and associated coordinated polarisation of adjacent dipoles, PMMA dipoles are more likely to oppose each other locally, as in the case of a dipolar glass. Hence, it's possible there would be some degree of polarisation saturation in the PMMA layers at higher applied fields. In contrast, the PVFHA nanofibres are not expected to exhibit polarisation saturation until significantly higher fields and are also expected to polarise much more quickly at low fields.

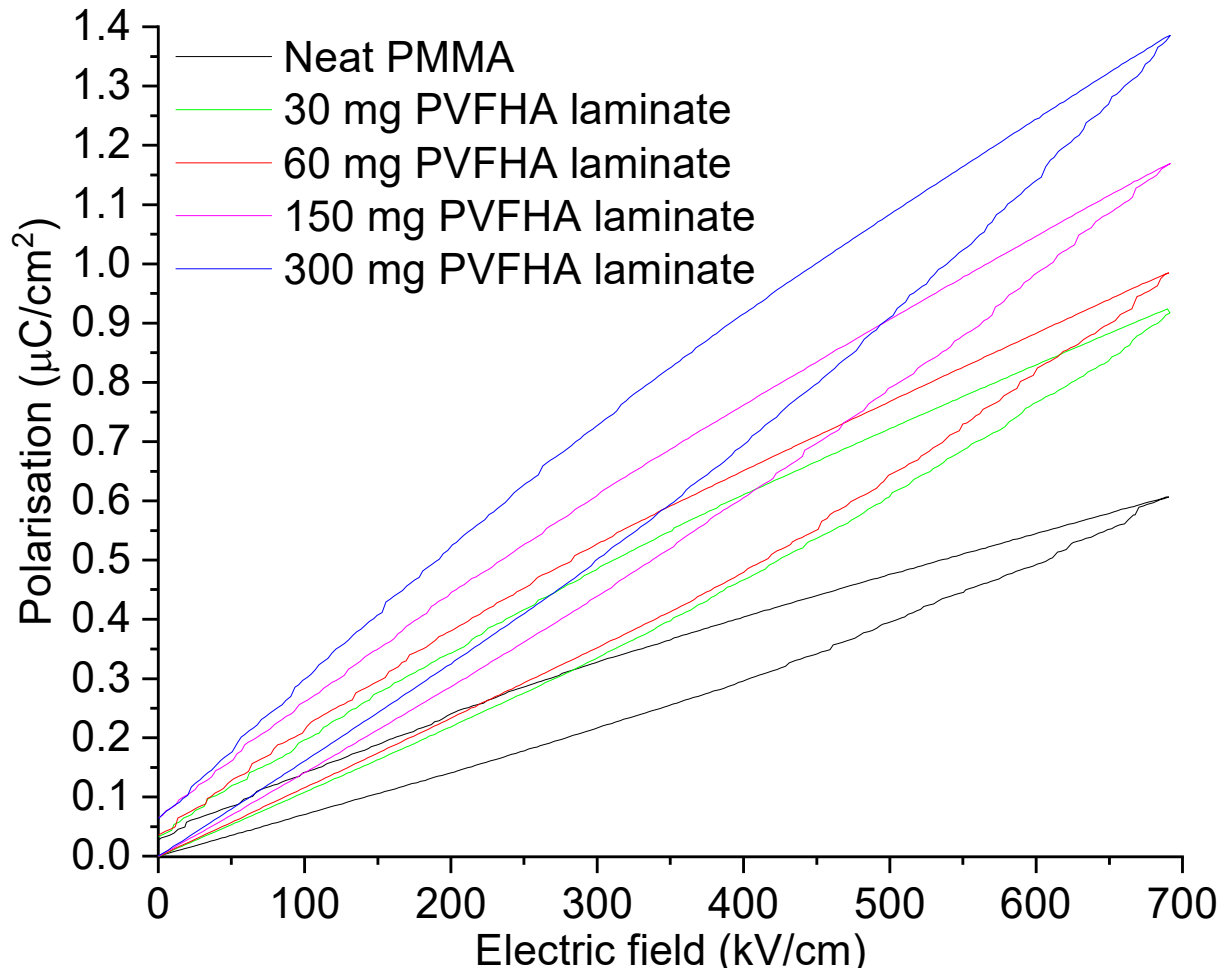


**Figure 0.24.** Comparison of various multilayer laminates with differing PVDF-HFP/AMIM nanofibre loadings. The discharged energy density at 900 kV/cm almost doubles to over 600 mJ/cm<sup>3</sup> at a 2:1 PMMA:PVFHA ratio compared to neat PMMA.

Ferroelectric tests were performed on a series of laminates, shown in **Figure 5.24**. Values for the curves have been derived and are given in **Table 5.3**. Unsurprisingly, the PVFHA nanofibre content of the laminates has a strong effect on the laminate polarisability, but with diminishing effect with progressively greater increases in nanofibre layer mass. In contrast, the discharged energy density  $U_e$  is seen to increase more or less linearly with PVFHA fibre loading. The relationship between these metrics are plotted in **Figure 5.25**, which confirm these conclusions,

as linear and quadratic curves are fitted to the data. Meanwhile, the discharge efficiency  $\eta$  doesn't seem to be substantially affected by the PVFHA nanofibre loading; if anything, it is improved with higher nanofibre content. Hence from this data, it seems obvious that increasing the PVFHA nanofibre loading as much as possible will improve laminate performance. However, there are three limiters on this. The first is that PVFHA nanofibres must be electrospun, which is a time intensive process, meaning in real applications it is difficult to produce a high throughput of laminates with a high PVFHA nanofibre content. Secondly, a higher PVFHA nanofibre loading leads to a thicker laminate, meaning a higher voltage is required to produce the same electric field in the laminate, increasing the amount of energy required to polarise the laminate. This may not be an issue in some applications – for example those that are utilising waste energy as the source of the voltage – but it is worth highlighting. Most importantly however, higher PVFHA nanofibre loadings will lead to lower electrical breakdown strengths. Due to the 10 kV limit of our voltage amplifier, we were unable to thoroughly test the breakdown limits of these laminates via models such as the Weibull model. Taking the 300 mg PVFHA nanofibre laminate as an example, the laminate is too thick to test above 770 kV/cm. In three of the four tests performed, this laminate reached 600, 620 and 550 kV/cm, at which point it underwent electrical breakdown. The data given in **Figure 5.24** is from the only test in which the sample reached the voltage amplifier limit of 10 kV, by which point the applied field was 770 kV/cm. Hence, when employing this sample in a real device, it is more likely undergo electrical breakdown under regular operating conditions than it's counterparts with lower PVFHA nanofibre loadings. Hence, a more moderate PVFHA nanofibre content is likely optimal. To support this, in the case of the 7 tests performed on the 150 mg PVFHA nanofibre loaded samples, apart from 1 outlier, this laminate was just as resistant to breakdown as the 60 mg and 30 mg PVFHA loaded laminates. This data implies the sweet spot is likely around a PMMA:PVFHA ratio of roughly 2:1.

**Table 0.3. Values derived from Figure 5.24**

Sample	$U_e$ (mJ/cm <sup>3</sup> )	$\eta$ (%)	$P_{max}$ (μC/cm <sup>2</sup> )
Neat PMMA	178.9	76.4	699.2
30 mg PVFHA	279.2	78.2	0.92
60 mg PVFHA	295.4	77.7	0.99
150 mg PVFHA	353.1	80.1	1.17
300 mg PVFHA	417.3	79.7	1.39

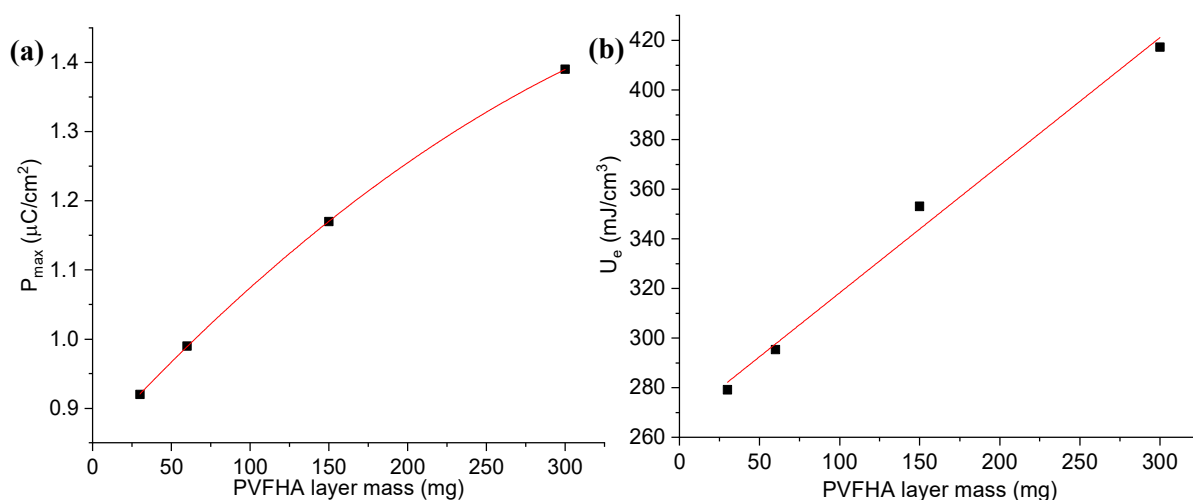


**Figure 0.25.** (a) Relationship of maximum polarisation against PVFHA nanofibre membrane mass content of laminates and (b) discharged energy density against the same mass variation

### 5.3.10. The effect of pre-pressing PVFHA nanofibres on energy storage properties

The advantage of utilising electrospun PVFHA nanofibres, as previously outlined, is that the resultant ferroelectric nanostructure in the as-spun fibres is highly polarisable due to their high crystallinity and  $\beta$ -phase composition. However, recalling the key target application for ferroelectric polymers – pulsed power applications – the aim is to utilise all-polymer dielectrics in long lifetime applications which act to enhance the energy efficiency of the system in which they are implemented. While our electrospinning methodology has proven to be effective at producing a nanostructure predominantly composed of ferroelectric domains, the response of this nanostructure during application and release of an applied field depends on the morphology of this crystalline structure. One aspect of this is the manifestation of so-called relaxor ferroelectric behaviour. This appears in crystalline structures which contain very small ferroelectric domains, referred to as nanodomains, which are more mobile than their larger counterparts. This results in smoother domain movement, and thus a higher propensity to both polarise along an applied field and to depolarise upon release of that field, generally producing a ferroelectric with an enhanced discharge efficiency,  $\eta$ .<sup>34,36</sup> However, there is another key aspect of ferroelectric domain morphology to consider which requires a broader consideration of the material properties.

The multilayer PMMA:PVFHA laminates constructed here are designed to have a thin film macro-morphology. It is designed such that an electric field is applied through-plane over a short distance to minimise not just the space and weight requirements of the device, but also the voltage required to run the device. A higher aspect ratio of the thin film morphology means a lower voltage is required to reach the same electric field, while said field is also applied over a large area, exposing as many domains as possible to the field, thus maximising the polarisation.

Under this geometry, the ferroelectric domains will produce the highest discharged energy density,  $U_e$ , when they begin oriented in-plane and rotate to align with the through-plane applied electric field. Thus, an optimised ferroelectric domain configuration in our laminates would also involve a preferred in-plane direction of crystallite orientation in the nanofibres.

Ren *et al.* developed a remarkable methodology to achieve these goals in their PVDF homopolymer samples, which has received wide attention due to its simplicity and what it reveals about the nature of highly efficient ferroelectric polymer capacitors.<sup>18,19,37</sup> In short, commercially available PVDF pellets are first hot-pressed into a PVDF thin film under the high pressure of 120 MPa, and at a temperature of 165 °C around the melting point of PVDF. The film is then folded and pressed again under the same conditions. This process was then iterated up to 6 times. As the process is repeated, a multitude of desirable crystallisation phenomena occur simultaneously. Not only is a high  $\beta$ -phase content acquired via this methodology (usually difficult to achieve via hot-pressing, as shown in chapter 3) but the size of the crystallites within the PVDF also gradually decreases with each ‘press and fold’ (P&F) iteration performed. The result is a highly polarisable thin film with low loss due to both the high  $\beta$ -phase fraction, and due to the high discharge efficiency associated with the ferroelectric nanodomains present within the structure. The total crystallinity of their hot-pressed PVDF does leave something to be desired however, reaching only 38%, while in chapter 3 it was shown that our electrospun PVFHA nanofibres reach over 50% crystallinity.<sup>18</sup> In a similar fashion to this P&F methodology, pre-pressing our PVFHA nanofibres was also an attempt to attain both lower ferroelectric losses due to a more mobile domain structure, and to produce a high in-plane alignment of crystallites to maximise polarisability.

After obtaining the pre-pressed nanofibres, the method for producing laminates was identical to that previously outlined for the neat nanofibres. Laminates were pressed at 160 °C to ensure samples were as thin as possible, meaning we could reach higher electric fields with the 10 kV voltage amplifier used for ferroelectric analysis, as well as providing high resilience to these high fields by elimination of as many voids and defects as possible. 160 °C should also be low enough to avoid the stark phase transitions seen in the FTIR data shown in **Figure 5.6**.

**Figure 5.26** provides P-E data of two laminates pressed at 160 °C, one incorporating pressed nanofibres and one incorporating unpressed fibres. The PVFHA nanofibre membrane weight was fixed at 150 mg in both cases, as this has been previously revealed to be an optimal loading. These two samples were found to have similar polarisability. This can be seen by the intersection of the discharge curves at around 400 kV/cm and their similar remnant polarisation. It should be noted that the sample containing the unpressed nanofibre does exhibit a slightly lower maximum polarisation, although this is likely within expected variance. In any case, pre-pressing the nanofibres does not seem to provide any noticeable advantages to sample performance. Tests on other laminates containing pressed nanofibres (at various temperatures

and weight ratios) also provided no evidence that pre-pressing the fibres made a substantial difference to performance, although these samples were less directly comparable due to varying processing conditions.

While the samples did not undergo breakdown the areas tested to acquire the data given in figure, they did undergo breakdown in other areas. The pre-pressed PVFHA fibre laminate was fairly resilient, undergoing breakdown in only 3 out of 8 tests at or below 800 kV/cm. In the other 5 tests, the sample reached between 650 and 1000 kV/cm before hitting the limits of the apparatus. In contrast, the unpressed PVFHA fibre laminate was able to reach 1000 kV/cm in 3 tests, not even undergoing breakdown in the best-case scenario of reaching 1250 kV/cm. In this test, the laminate was measured to have a discharged energy density  $U_e$  of 1.08 J/cm<sup>3</sup>, the highest obtained in any sample tested under any conditions in this project. This sample may have even obtained higher values for  $U_e$  at higher fields had a voltage amplifier with a larger maximum voltage been available. Otherwise however, this laminate showed similar breakdown characteristics to the pre-pressed fibre sample. Considering the lower thickness of the unpressed sample (simply due to natural variance in sample thicknesses arising from the pressing methodology), the breakdown characteristics of the two samples appear similar.

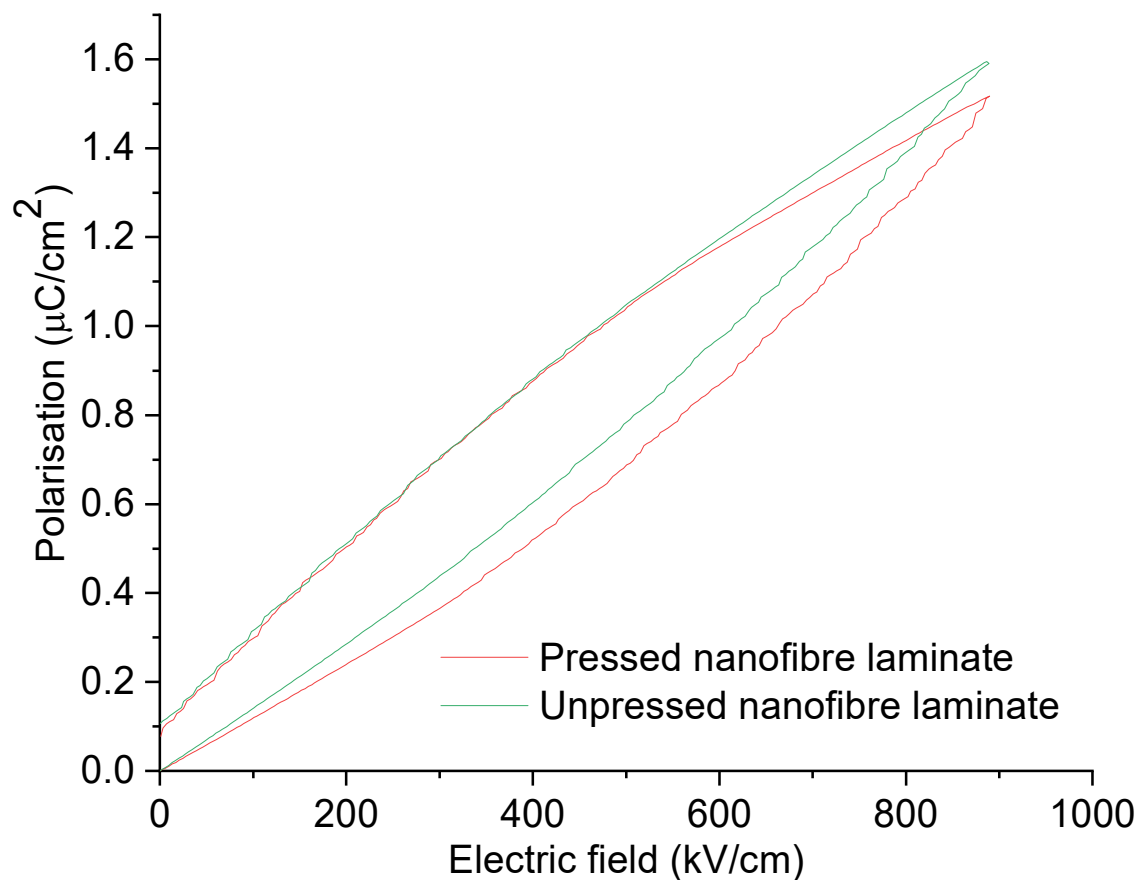


**Figure 0.26.** Comparison of ferroelectric performance of 3-layer laminates containing either of pre-pressed or neat (unpressed) PVFHA nanofibres, which seems to imply their performance is comparable.

### 5.3.11. The effect of PMMA layer thickness on energy storage performance

Finally, the effect of PMMA layer thickness was briefly investigated to ascertain how this may affect energy storage properties. While it has already been made clear that the PVFHA nanofibre content of the laminates has a significant impact on energy storage capacity, the PMMA layer weight has been kept fixed throughout these tests. 300 mg PMMA layers with a similar area to the PVFHA nanofibre membranes were not too difficult to produce with the doctor-blade/toluene solution approach, and since they seemed to do an excellent job of minimising remnant polarisation and associated ferroelectric losses, this layer weight was kept consistent. Producing thinner (and hence lighter) PMMA layers with a similar area without introducing inhomogeneities, voids and blemishes in the film was also not reliably possible, so in the interest of producing high quality laminates, this 300 mg weight was generally fixed. However, thicker PMMA layers were occasionally used. It is possible that a thicker insulating outer layer could lead to a higher resilience against electrical breakdown in the final laminate, but conversely it may result in a less polarisable laminate.

For example, a laminate containing 600 mg PMMA outer layers was created. This laminate included a 150 mg PVFHA nanofibre membrane pre-pressed at 140 °C, with the final laminate pressed at 160 °C. Ferroelectric tests comparing this laminate to an identical laminate with 300

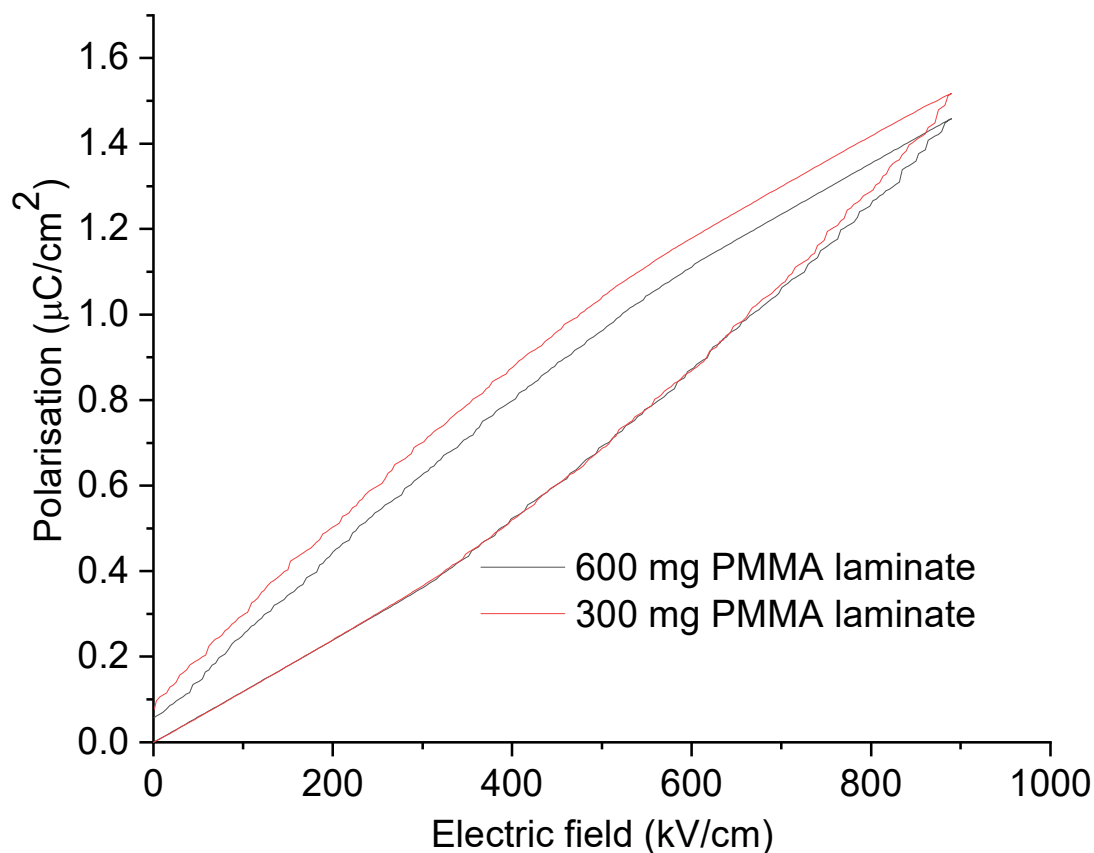


**Figure 0.27.** Comparison of polarisation-electric field loops of 3-layer PVFHA /PMMA laminates with 150 mg PVFHA fibre layers, but with different PMMA layer thicknesses of 300 and 600 mg. Both curves here are from tests at the 10 kV limit of our apparatus, reaching a field of 900  $\text{kV}/\text{cm}$ .



mg PMMA layers is shown in **Figure 5.27**, where it is clear the 300 mg PMMA sample has a slightly higher maximum polarisation. For a more thorough analysis of how the samples performed over multiple testing areas, data from each set of tests is provided in **Table 5.4**.

Surprisingly, despite the higher PMMA layer thickness, the final laminate had comparable thickness to that seen in other samples. The thickness varied between 100-175  $\mu\text{m}$  across the sample, with an average of 131  $\mu\text{m}$  over the areas in which the 6 ferroelectric tests were conducted. In contrast, the 300 mg PMMA sample varied between 100-150  $\mu\text{m}$ , with an average of 123  $\mu\text{m}$  over 8 testing areas. The 600 mg PMMA sample was very resilient to breakdown, only breaking down once – at the rather high field of 975 kV/cm – out of 6 tests, while exceeding 750 kV/cm 4 times. The 300mg PMMA sample instead broke down thrice in the 8 tests, at 450, 650 and 800 kV/cm, generally in thinner areas of the sample. Additionally, the discharge efficiency seen in the 600 mg PMMA sample was above 70% in all cases, with the best performing area – given in **Figure 5.27** – at 74.9%. The 300 mg PMMA sample was far less consistent, only hitting a discharge efficiency of around 70% in the best performing testing areas, such as the curve shown in **Figure 5.27**. The thicker PMMA layers do seem to help with decreasing the remnant polarisation of the laminate (much like adding outer PMMA layers in the first place), and in turn they improve the discharge efficiency. At the same field of 900 kV/cm, the two laminates have remarkably similar discharged energy densities,  $U_e$ , at 570 mJ/cm<sup>3</sup> for the 300 mg PMMA layer sample, and 575 mJ/cm<sup>3</sup> for the 600 mg PMMA layer sample.

**Table 0.4.** Data taken in multiple areas of two samples with different PMMA loadings, with the two tests given in **Figure 5.27** taken from the areas listed as the first tests of each sample in the table. All rows display data for the highest fields reached in each sample area. \*Sample underwent breakdown at this field – otherwise, electrical breakdown did not occur.

Sample	Thickness ( $\mu\text{m}$ )	Field (kV/cm)	$U_e$ (mJ/cm <sup>3</sup> )	Discharge efficiency (%)
300 mg PMMA	110	909	575	70.0
	125	800	489	70.1
	100	1000	478	67.7
	150	666	330	72.0
	140	714	238	59.7
	120	800*	439	70.0
	115	650*	359	54.7
	125	450*	108	83.7
600 mg PMMA	110	909	570	74.9
	130	769	507	72.0
	125	800	473	76.2
	150	666	335	74.4
	175	571	283	79.2
	100	975*	378	74.0

### 5.3.12. Optimised energy storage properties of 3-layer PMMA/PVFHA laminates

To gain further insight into the peak performance achieved by the processing methodology developed in this chapter so far, a plot of  $U_e$  vs applied field for the laminate with the highest  $U_e$  measured in any of our studies is given in **Figure 5.28(a)**. This sample, as outlined before, contains a neat nanofibre (not pressed before incorporation into the laminate), a 300 mg PMMA outer layer, a 150 mg PVFHA nanofibre central layer, and was pressed at 160 °C. Clearly this dataset follows a quadratic dependence, similar to the relationship between  $U_e$  and applied field seen for linear samples.<sup>38</sup> The sample hits a  $U_e$  of 1.08 J/cm<sup>3</sup> at a field of 1250 kV/cm, with a discharge efficiency of 71.9%. From the displacement-field curve of the tests on this area of this sample shown in **Figure 5.28(b)**, the sample clearly does not undergo polarisation saturation even at these high fields. This may be compared to the performance achieved in PVDF by Ren *et al.* with their press-and-fold technique, which – at an ultra-high 8800 kV/cm applied field – hits a very high 39.8 J/cm<sup>3</sup> at a discharge efficiency of 72.8%.<sup>19</sup> From the discharge curves of their sample, given in figure 7(e) of their paper, at a field of around 1250 kV/cm – the field at

which peak performance was attained in our samples – their samples have yet to undergo any polarisation saturation. Thus, their samples should similarly follow the quadratic dependence of  $U_e$  vs field seen in our sample. However, once a field around 2000 kV/cm is reached, ferroelectric polarisation saturation is clearly coming into effect in their sample. It also seems that their sample has a similar discharge efficiency as the applied field increases, with loops appearing similar in area and the remnant polarisation not increasing substantially. Due to the potential of polarisation saturation occurring in our own samples, it is difficult to extrapolate the quadratic data in **Figure 5.28(a)** to ultrahigh fields, especially considering such an endeavour also requires making the drastic assumption that the sample would not undergo breakdown at these ultrahigh fields. In fact, the maximum polarisation in the best performing PVDF sample presented Ren *et al.*'s paper only increases by around a factor of 2 when scaling up the field from 1250 kV/cm all the way to the 8800 kV/cm breakdown limit of their sample. Although, comparing the maximum polarisation seen in this sample at 1250 kV/cm – seemingly around 7  $\mu\text{C}/\text{cm}^2$  – is a fair amount higher than the 2.1  $\mu\text{C}/\text{cm}^2$  measured in our sample. Due to the 100% PVDF content of their samples, one would expect their sample to be more polarisable than our laminates at a given electric field, so this is not too surprising. Hence it may be that our sample would only undergo polarisation saturation at far higher fields than the press-and-fold samples. This is supported by the fact that polarisation saturation was never observed in any tests performed on any of our laminates. Additionally, the crystalline structure in the press-and-fold samples – as observed by XRD – is almost entirely restricted to the planar phases seen between  $2\theta = 18\text{--}21^\circ$ , which is in strong contrast to the varied crystallinity seen in our samples. Ren *et al.* also observed a broad peak in this region of their XRD spectra, implying the presence of smaller crystallites oriented perpendicular to the applied field – perfect for attaining a high maximum polarisations and low ferroelectric losses. Hence it is possible that the crystal structure

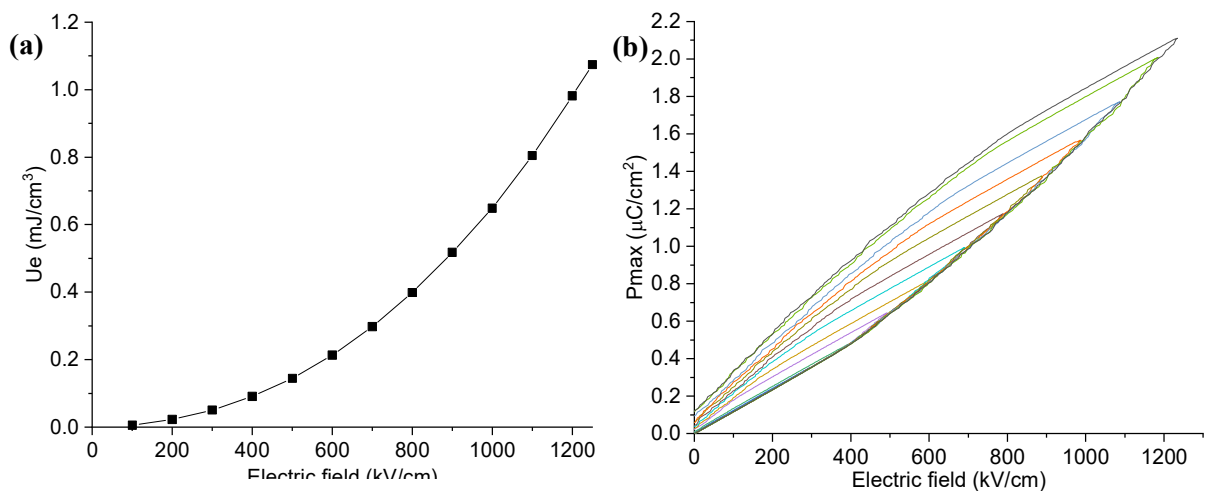


**Figure 0.28.** Data from tests of our highest  $U_e$  laminate; a 160 °C pressed sample with 300 mg PMMA outer layers and 150 mg PVFHA nanofibre inner layers. **(a)** Displays the dependence of discharge efficiency on the applied field, while **(b)** gives the P-E curves for each of these tests.

produced in our samples could be further optimised to attain the polarisation of this press-and-fold methodology.

### 5.3.13. Many layered PMMA/PVFHA nanofibre laminates

So far, the appeal of utilising a layered structure has been made apparent, as it has been shown that the pressing of PMMA layers around the PVFHA nanofibres can lead to significant reductions in electrical losses and concurrent enhancements in the discharged energy density  $U_e$ , allowing the polymer to act as a capacitor rather than a conductor. However, the nature of the physical mechanisms that lead to this enhancement are not clear. As previously explored however, there is a secondary advantage to the use of PMMA layers. These layers may block charge carriers at the polymer interface, so sheets of charge may build up at the junction between PVFHA and PMMA layers, producing an interfacial polarisation.<sup>39</sup> It stands to reason then that this interfacial polarisation would be enhanced with the addition of further PMMA and PVFHA layers. Hence, many-layered laminates were constructed to discern whether this would enhance energy storage and discharge capabilities.

Laminates were produced in a similar manor to that outlined previously. A doctor blade was employed to create a thin PMMA layer cast from a 20 wt% solution of PMMA in toluene. These layers were then cut to size and weighed before placing PVFHA nanofibre layers of a controlled weight in between, ensuring no nanofibre layer was overlapping the outside of the PMMA layers. The polymer multilayers were then hot-pressed for 5 minutes (2 minutes at 1 bar, then 3 minutes at 40 bar) at the high temperature of 160 °C. The high temperature was selected to ensure sample homogeneity above all else, as voids and defects were commonly observed in early attempts to make these many-layered laminates at lower temperatures. The samples were again allowed to cool to 30 °C under pressure to ensure the retention of the thermally stable  $\beta$ -phase as the sample recovers any lost crystallinity.

Firstly, the ability of the hot-pressing process to produce cohesive many-layered laminate structures was evaluated by scanning electron microscopy (SEM). **Figure 5.29** provides SEM images of the cross-sections of 5, 7 and 9-layer laminates, showing clear visual distinctions between the PMMA and PVFHA layers. From close-up images of the cross-sections, the layers seem well homogenised, with no voids or defects visible across the vast majority of the areas of cross-sections examined. An image of the cross-section of a neat PMMA thin film is provided for reference in **Figure 5.30**, where no layer structure is visible whatsoever. However as shown in **Figure 5.29 (d)**, there are very occasional points – usually where the fibre layer has fractured differently to the surrounding PMMA layers during sample preparation – where delamination has occurred. Although, this allows for inspection of the microstructure within the fibre layer itself. This reveals the retention of some of the fibrous nature of the laminates, again implying that some of the crystal structure of the nanofibres has likely been retained after pressing into

the laminate structure. In any case, there don't seem to be any fatal flaws in the produced microstructure overall, so the many layered approach appears viable. After this inspection, 15-layer structures were thus also made utilising very thin PMMA layers weighing 100 mg (compared to the usual 300 mg). Fibre layers of 4 mg and 30 mg weight were incorporated for comparison of structural and energy storage properties.

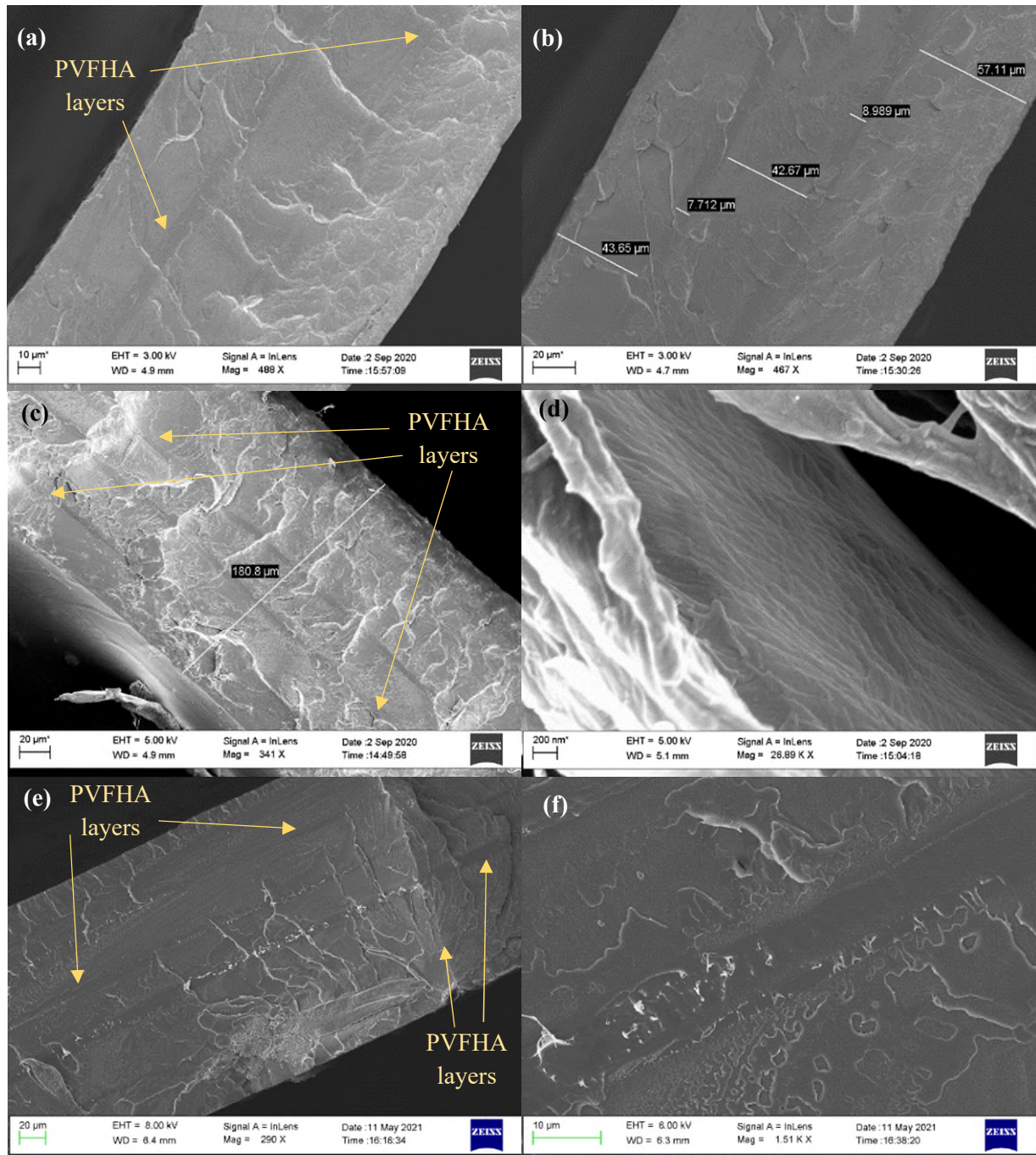


**Figure 0.29.** Cross-sections of (a, b) 5-layer (c, d) 7-layer and (e, f) 9-layer 10:1 PMMA:PVFHA nanofibre laminates pressed at 160 °C. Individual layers can be seen, with thicknesses given in (b), and typical laminate thickness provided in (c). (d) Shows a rare fracturing incident in one of the layers, exposing retention of some fibrous microstructure.



**Figure 5.31** provides some images of the cross-sections of these samples, again revealing clear visual distinctions between the layers, but an overall very cohesive layered structure. To once again confirm this, energy-dispersive X-ray spectroscopy (EDS) was performed. The EDS results for the 9-layer laminate structure is provided in **Figure 5.32**. The EDS imaging clearly identifies the position of the PVFHA nanofibre layers in between the PMMA layers, which is

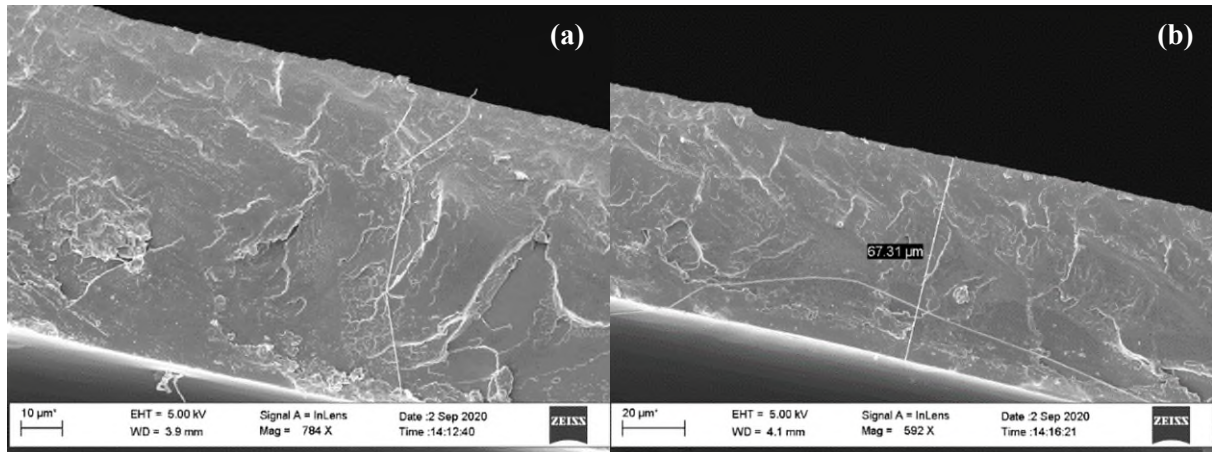


**Figure 0.30.** Cross-sectional images of a standalone PMMA layer, with the thickness given in (b)

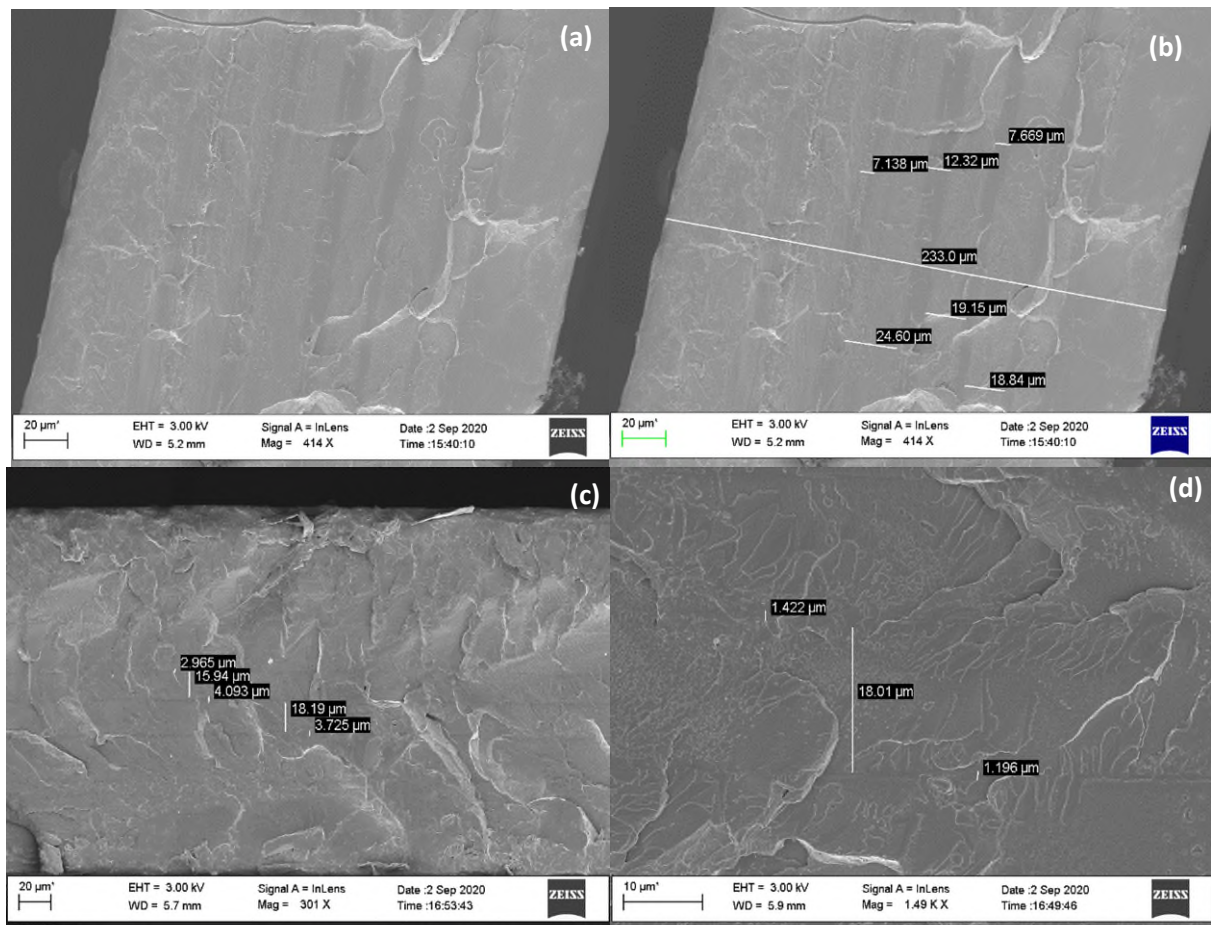


**Figure 0.31.** Cross-sections of 15-layer laminates containing (a, b) 100 mg PMMA and 4 mg PVFHA nanofibre layers and (c, d) 100 mg PMMA layers and 30 mg PVFHA nanofibre layers, pressed at 160 °C.

otherwise hard to identify in the plain SEM images. Worth noting is the clear discrepancy in thickness between the PVFHA nanofibre layers, implying that the pressing process may result in some degree of lateral inhomogeneity. This will of course mean that the polarisability of the laminate will also have lateral variance. The cause of this is largely attributed to the electrospinning process, which unavoidably produces nanofibre membranes with laterally inhomogeneous thickness; usually a general trend of decreasing thickness in the radial direction, with the highest thickness at the membrane centre. This is inevitable as during electrospinning, the fibres will become increasingly less likely to be deposited on the collector as distance from the spinneret increases. Although the use of thicker nanofibre membranes – those that were electrospun over a longer period of time – should produce higher homogeneity. Unfortunately though, due to time constraints, low thickness (/low weight) PVFHA layers also had to be used.

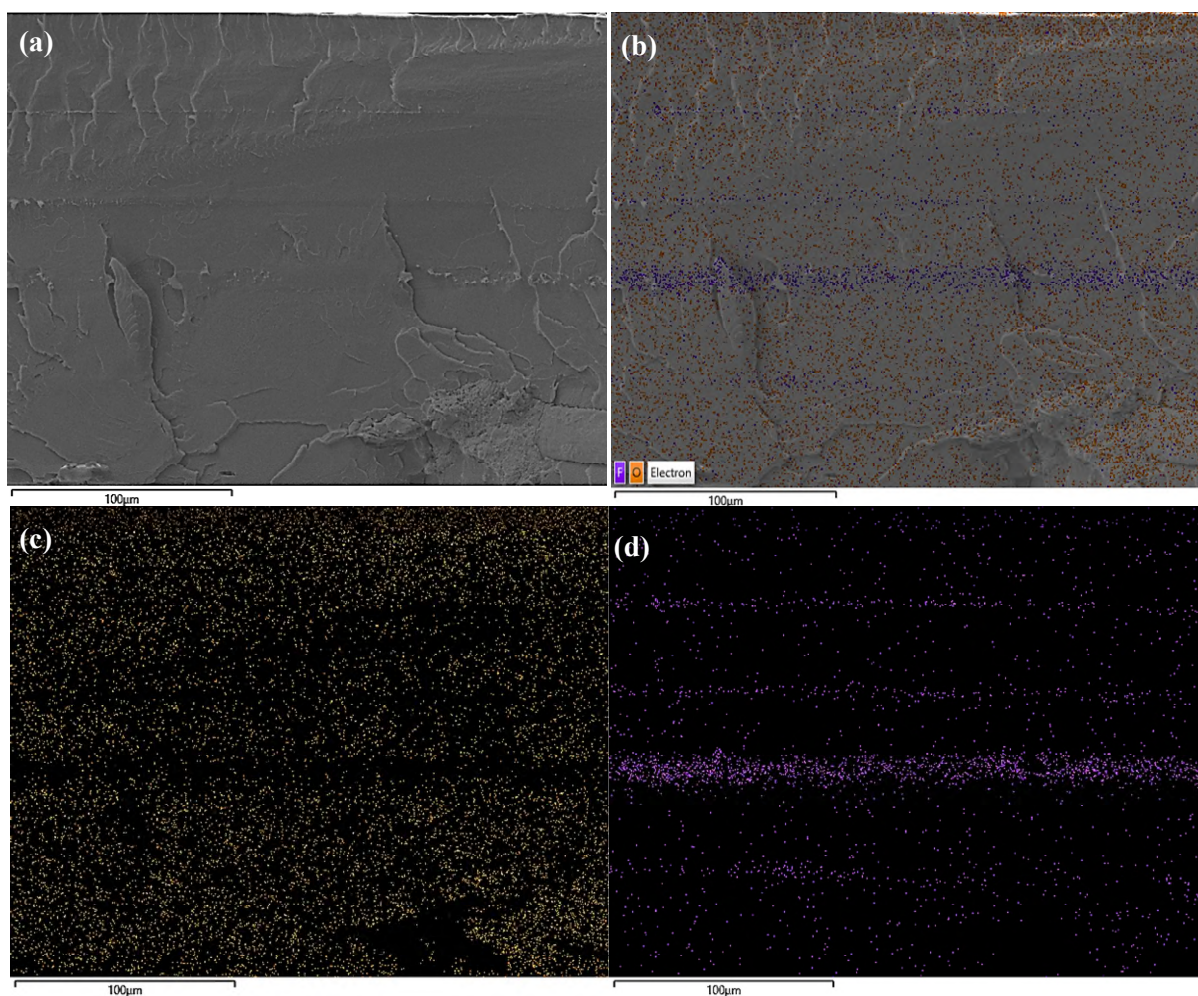


**Figure 0.32.** Cross-sectional image of a 10:1 PMMA:PVFHA 9-layer laminate pressed at 160 °C.

(a) Provides an SEM micrograph of the cross-section, with (b) providing the elemental map superimposed on top. (c) provides a raw map of the oxygen content, indicating the presence of PMMA, while (d) provides a map of the fluorine content, indicating the presence of PVDF-HFP.

#### 5.3.14. Energy storage in many layered PMMA/PVFHA nanofibre laminates

To discern the effects of utilising different numbers of layers in the laminate, many layered (5-9 layered) laminates containing 15 mg PVFHA nanofibre and 300 mg PMMA layers were characterised via P-E tests. The resultant curves at 400 kV/cm are shown in **Figure 5.33**. The data for these curves is also provided in **Table 5.5**, alongside data for the highest electric fields reached during testing. With increasing layer number, up to the 7-layer sample, the laminates show clear enhancements in polarisability and successively lower energy losses, which can be seen as an increase in discharge efficiency,  $\eta$ , in **Table 5.5**. One would expect an increase in maximum polarisation,  $P_{max}$ , with an increasing number of layers, even when not accounting for possible increases in interfacial polarisation, as the overall PHA:PMMA ratio will increase as the number of layers increases. However, at 9-layers,  $P_{max}$  was seen to decrease. Additionally, as can be seen in **Figure 5.33** and in **Table 5.5**, a higher number of layers tends to lead to a higher remnant polarisation,  $P_r$ . Hence although the ratio of the  $P_{max}$  to  $P_r$  is seen to increase up to the 7-layer sample, it decreases again in the 9-layer sample. Therefore, it is likely that in the 9-layer sample the structure is trapping some charge, preventing discharge, leading to the higher  $P_r$ . Repeat measurements in different areas of these laminates produced similar data, solidifying these observations. It also may be that sample polarisability becomes limited once too many layers are added due to the higher number of insulating layers shielding inner PVFHA layers from the applied field. Thus 9 layers may be the critical threshold in this sample composition of (300 mg PMMA and 15 mg PVFHA layers) for this effect to cause a net decrease in polarisability. Additionally, since good sample homogeneity becomes harder to produce with a high number of layers, this could lead to charge traps manifesting within the sample, which may contribute to the lower  $\eta$  observed.

From **Table 5.5**, it is evident that an increase in the number of layers leads to a vastly increased discharged energy density  $U_e$  at the same electric field, at least up to the 9-layer limit. **Figure 5.34** provides plots of the  $P_{max}$  observed in the samples as a function of electric field, with an additional extrapolation of the dataset up to high electric fields to provide an estimate of performance if higher voltages could be used. While this data doesn't account for energy losses, it clearly outlines the improvement in performance of the laminates when more layers are added. The increase in  $U_e$  is also clearly not linear, nor exponential, regardless of relating it to the number of layers or to the PMMA:PVFHA ratio in the samples. Indeed the 7-layer sample vastly outperforms both the 3-layer and 5-layer samples in any case. Regardless, the reasonably similar (and high)  $\eta$  of all the laminates as given in **Table 5.5** means there would not be a substantial difference even if losses *were* accounted for. Based on this data, the polarisation reached by the 7-layer sample is around 3-3.5 times higher than that seen in the 3-layer sample. Due to time constraints and this analysis suggesting that adding additional layers may limit sample performance, P-E tests on the 15-layer laminates were ultimately not performed.



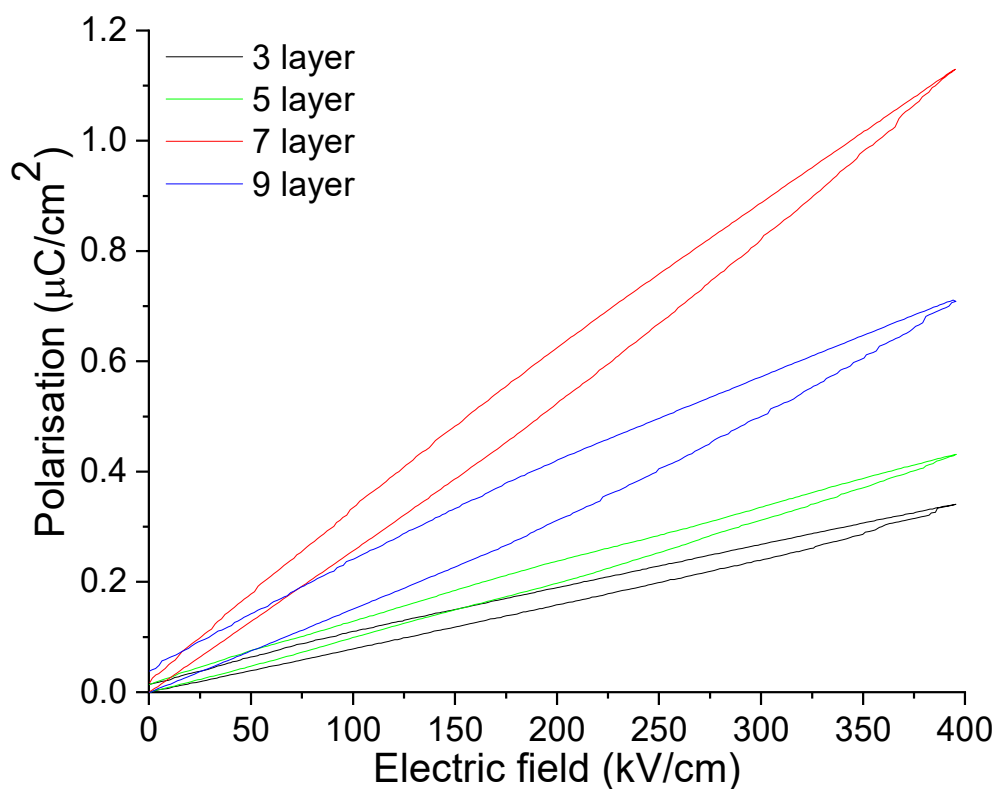


**Figure 0.33.** P-E loops for the multilayer laminates given in **Table 5.5**. The laminates clearly performed successively better with increasing the number of layers up to the 9-layer sample, when losses became more significant. This led to the lower observed discharge efficiency as well as a far lower maximum polarisation.

**Table 0.5.** Ferroelectric properties of various many layered laminates constructed with 300 mg PMMA layers and 15 mg PVFHA nanofibre layers (i.e. a 20:1 ratio), pressed at 160 °C. The first four rows give data at 10 kV, the limit of the apparatus, with the applied field  $E$  dependant on laminate thickness. There were no cases of electrical breakdown. The bottom 4 rows provide data at 400 kV/cm for comparison.

Sample	$U_e$ (J/cm <sup>3</sup> )	$\eta$ (%)	$E$ (kV/cm)	$P_r$ (µC/cm <sup>2</sup> )	$P_{max}$ (µC/cm <sup>2</sup> )	$P_{max}/P_r$
3 layers	456	70	1000	0.1396	1.1250	8.059
5 layers	129	84.5	500	0.0204	0.5725	28.06
7 layers	258	85	440	0.0688	1.2678	18.43
9 layers	202	63	500	0.1050	0.9381	8.934
3 layers	61	85	400	0.0141	0.3408	24.17
5 layers	80	87	400	0.0139	0.4309	31.00
7 layers	208	89	400	0.0176	1.1295	64.18
9 layers	123	80	400	0.0383	0.7091	18.51

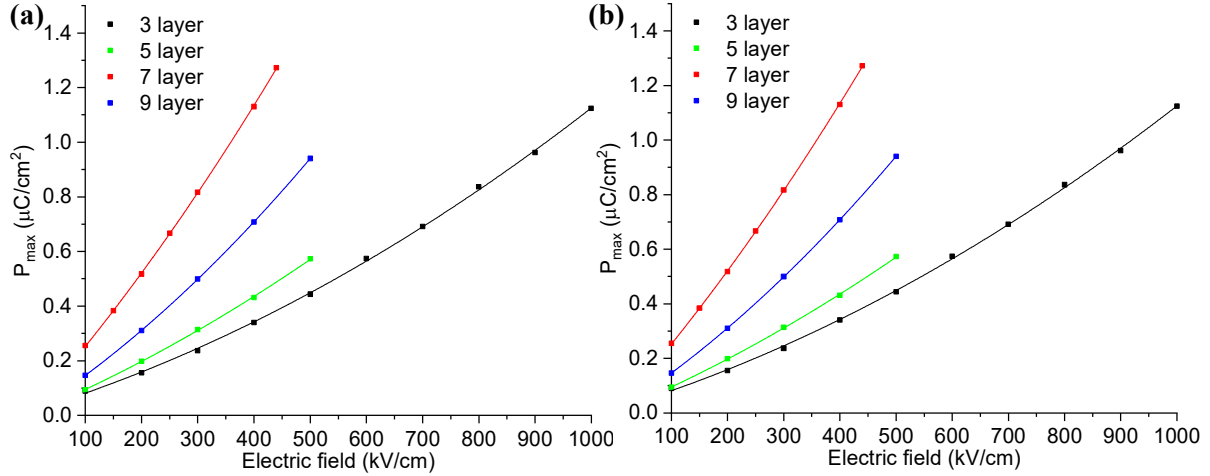


**Figure 0.34.** Maximum polarisation as a function of electric field for the samples given in **Table 5.5**. **(a)** Provides the data with polynomial fits applied to the data points. **(b)** Extrapolates the data points based on the fits produced to give an estimate of how the polarisation would increase if the voltage limit of the apparatus were higher. This extrapolation is an idealised estimate, as these samples may have undergone electrical breakdown before reaching these higher fields.

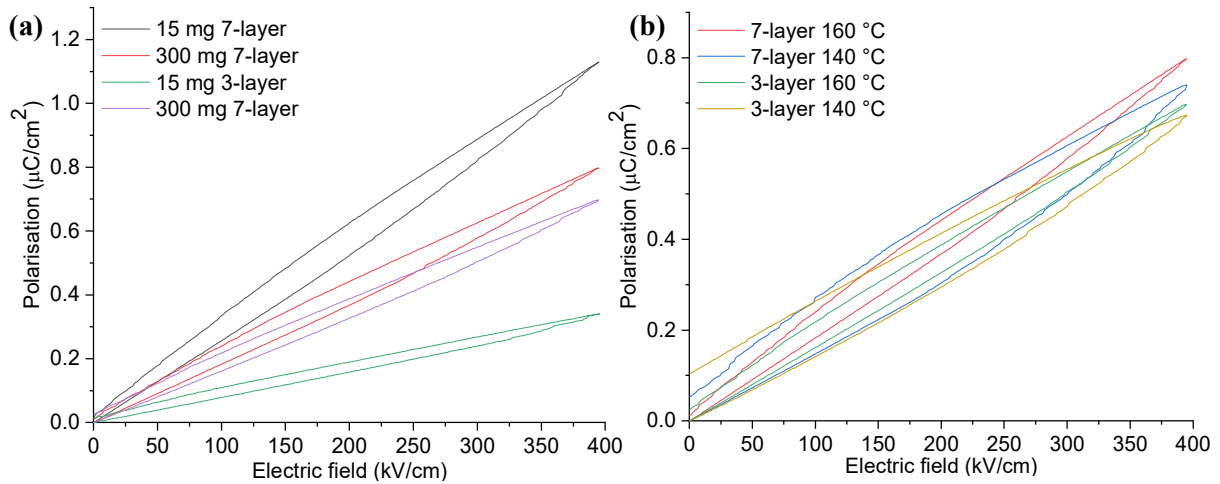


**Figure 0.35.** P-E loops of PMMA/PVFHA nanofibre laminates **(a)** pressed at 160 °C, with differing layer number and PVFHA nanofibre membrane weight and **(b)** pressed at both 160 °C and 140 °C, with differing layer numbers, containing 300 mg PVFHA nanofibre membranes.

**Table 0.6.** Key ferroelectric performance metrics measured from the curves in **Figure 5.35(b)**, at an electric field of 400  $\text{kV}/\text{cm}$ .

Sample	$U_e$ ( $\text{mJ}/\text{cm}^3$ )	$\eta$ (%)
7lyr, 160 °C	146.8	87.4
7lyr, 140 °C	122.4	73.7
3lyr, 160 °C	126.7	86.4
3lyr, 140 °C	106.6	72.8

To gain a more complete picture of the underlying physics, a selection of 7-layer samples were produced with higher PVFHA contents. **Figure 5.35(a)** provides P-E loops of 7-layer and 3-layer samples containing 300 mg PMMA layers alongside 15 mg and 300 mg PVFHA layers at an electric field of 400 kV/cm. Somewhat surprisingly there does not seem to be a strong correlation between the PVFHA nanofibre content and sample performance. In fact having a high number of layers seems to provide a greater enhancement to performance than increasing the PVFHA content in a sample containing a single layer of PVFHA nanofibres. This implies that interfacial polarisation effects in the laminates are dominating the contribution to the total polarisation. However the most revealing aspect of this data is that in the 3-layer case, the 300 mg PVFHA sample outperforms the 15 mg sample by a substantial margin, while in the 7-layer case the 15 mg PVFHA sample outperforms the 300 mg sample, also by a large margin. It's possible that the differing sample compositions being subjected to the same 160 °C pressing process has resulted in different phase transformations being induced, and that the 15 mg sample retained a more ideal crystal structure. In fact, comparing these 300 mg PVFHA samples to the 3-layer samples pressed at 160 and 140 °C (**Figure 5.35(b)**) reveals much lossier signatures for the samples pressed at 140 °C, regardless of the number of layers. The maximum polarisation is also marginally higher in the 7-layer and 160 °C pressed samples, with lower losses also apparent in these samples. A higher number of layers seems to enhance  $P_{max}$  more effectively than pressing at 160 °C, but a higher pressing temperature seems more conducive to reducing losses. **Table 5.6** gives the ferroelectric performance values deduced from these curves. Due to the similar performances across pressing temperatures and sample compositions, it seems unlikely that the performance differences seen in **Figure 5.35(a)** are due to differences in crystallinity.

To further investigate this, XRD and SAXS studies were also performed on 300 mg PVFHA 7-layer laminates pressed at 140 and 160 °C, which were compared to 3-layer laminates pressed at the same temperatures. From the XRD data in **Figure 5.36**, both the neat PVFHA nanofibre and the 7-layer 140 °C pressed laminate display quite similar signatures, with the exception of a visible PMMA hump in the laminate sample between 15-19°. In the case of the 160 °C laminate, this seems to be the only major signature visible, and also seems responsible for the very broad peak at ~30°, in a region where no PVDF-HFP peaks are expected, and there is a clear correlation with the XRD spectra of the neat PMMA film. Additionally, similar to the 3-layer case presented in the last chapter, the crystalline structure of the nanofibre imposed by electrospinning appears to have been lost at this higher pressing temperature; in this case there are no PVDF-HFP crystalline peaks visible whatsoever. Hence the loss of the fibrous structure observed in the SEM images in **Figure 5.26(c, d)** correlates with a loss of crystal structure. It seems that 140 °C is again the optimal pressing temperature in this 7-layer case.

In contrast to this, the WAXS data for the 7-layer laminates seem fairly different to the cases of the 3-layer laminates. Pressing at 140 °C, it seems that the 7-layer laminates indeed possess a higher degree of orientation in the  $\beta$ -phase crystallites than in the as-spun nanofibres. However, by 160 °C, as seen in the XRD spectra, the previously present crystallinity seems to have largely disappeared. Additionally, the data for the 7-layer laminates appears far noisier than those for the 3-layer laminates, as seen in the 1D WAXS spectra in **Figure 5.36(c, d)**, but all

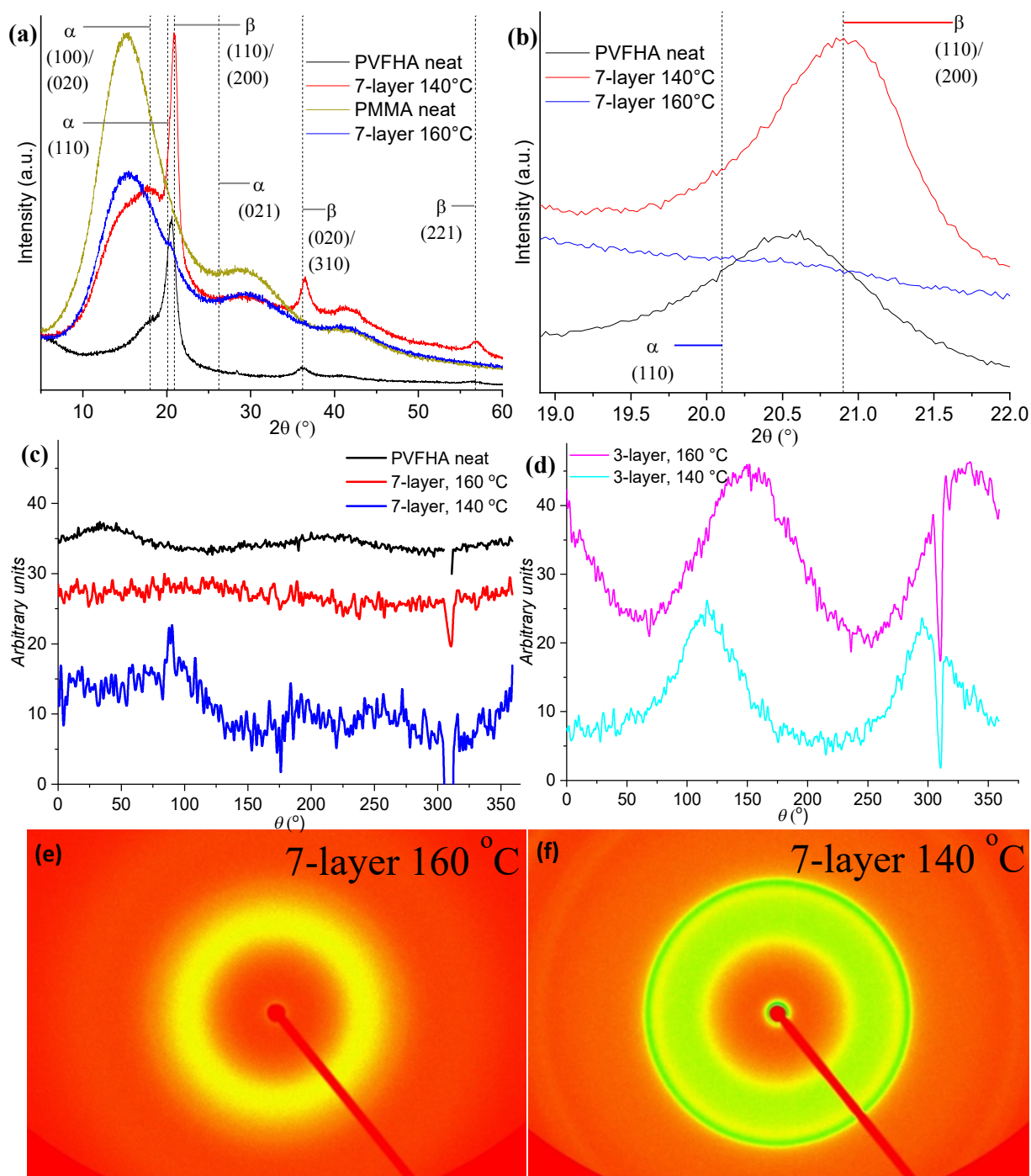


**Figure 0.36.** (a, b) XRD patterns for the 7-layer laminates pressed at 140 °C and 160 °C along with SAXS (c) intensity data and (e, f) diffraction patterns for these samples. (d) also provides SAXS intensity patterns of 3-layer samples for comparison, highlighting their far more substantial orientation.

samples still show some degree of orientation. Oddly enough, the previous WAXS study on the 3-layer laminates, given in **Figure 5.18**, shows clear – albeit minor – orientation in at 160 °C in comparison to the 7-layer case given in **Figure 5.36**, implying that a 3-layer structure was better at retaining the crystallinity imposed by the electrospinning process at this high pressing temperature. This was supported by the XRD spectra of this 3-layer laminate, which only exhibited the in-plane crystalline PVDF-HFP peak at 20-21°. It may be that the many layered structure resulted in a more uniform exertion of pressure across the whole film, resulting in a more thorough transfer of the heat to the inner PVFHA nanofibre layers, leading to almost total melting of the nanofibres. Finally, despite the familiar shift towards 21° in the XRD spectra of the 140 °C laminate compared to the as-spun nanofibre membrane, the WAXS data in **Figure 5.36(c)** is noisy compared to the 3-layer case in **Figure 5.36(d)** and doesn't display the regular pattern associated with the orientation we would expect. This is despite the even sharper WAXS diffraction pattern (**Figure 5.36(f)**) and the similarly well-defined XRD spectra for this sample in comparison to the 3-layer case in **Figure 5.17**. It may be that the induced orientation varies between the 3 PVFHA layers in this sample, leading to the far messier data, although there is no clear mechanism for why this might occur besides inhomogenous pressing. Regardless, it seems that at least some of the PVDF-HFP crystallites are oriented in-plane. Hence, the lack of orientation induced by pressing at 160 °C *or* by using many layers does not seem problematic. In fact, barring potential breakdown issues at ultrahigh fields, this may produce the multilayer architecture responsible for the impressive performances observed in **Figures 5.34** and **5.35**.

## 5.4. Conclusions

To conclude, it has been shown here that multilayer polymer laminates produced by hot-pressing PMMA layers around a near 100%  $\beta$ -phase content PVDF-HFP nanofibre membrane electrospun with the ionic liquid [AMIM] Cl can exhibit impressive ferroelectric properties at high electric fields. Notably, a consistently high discharge efficiency of 70-80% was retained, even into the ultrahigh field regime ( $>1000$  kV/cm) in some cases. This is attributed to the impressive insulating properties of PMMA, as well as its high miscibility with PVDF-HFP leading to highly cohesive laminates, resulting in low energy losses during both the charge and discharge procedures. PVFHA nanofibres have also been shown to outperform hot-pressed PVDF-HFP layers, with the critical pressing temperature of 160 °C seeming to be the maximum plausible pressing temperature at which the inner crystal structures begin to transform. XRD and SAXS studies also suggest that pressing at 140 °C could improve the crystal structure of the nanofibres for energy storage. Ferroelectric tests confirmed that laminates produced at this temperature likely have the highest polarisability of all laminates pressed between 120 and 180 °C; the range leading up to the total melting point of PVDF-HFP.

However there remain open questions about the ultrahigh field electrical breakdown resistance of these laminates, and whether pressing at 140 °C is truly optimal for producing homogenous laminates which are lacking in voids and defects, which may cause the onset of low field breakdown. Despite producing the highest polarisability, laminates produced at slightly higher pressing temperatures may in fact also produce laminates with higher breakdown resistance and similarly impressive energy storage properties, despite sacrificing some of the crystal structure imbued by the electrospinning process. The conclusion of 140 °C being an optimal pressing temperature is especially questionable in light of the later investigations into many layered laminates, where pressing at 160 °C was also observed to produce higher polarisability at relatively low fields than in samples pressed at 140 °C. Additionally, a PMMA:PVFHA nanofibre layer mass ratio of 2:1 was found to be roughly optimal based on the discharged energy density produced by studies at various mass ratios, with rudimentary investigations into the breakdown strength of these laminates revealing that mass ratios as high as 1:1 may begin to decrease the breakdown resistance of this laminate structure. For future work, further tests at ultrahigh fields with many samples should be performed to fully understand the breakdown properties of these laminates, and to gain a better understanding of the consistency of this processing method as well as the effect of temperature on ferroelectric performance.

Finally, it has been shown that hot-pressing using a stack of up to 7 alternating layers of PVFHA nanofibres and hot-pressed PMMA layers produces an even more polarisable structure which – at fields below the ultrahigh regime – have a remarkably high discharge efficiency. Substantial interfacial polarisation is speculated to be the source of this impressive behaviour, as when pressing at 160 °C and substantially altering the nanofibre crystal structure, their performance is surprisingly enhanced. Adding layers past this point however seems to begin to decrease the laminate polarisability and discharge efficiency, identifying 7 layers as a form of sweet spot. It also seems that in these many layer laminates, the PVFHA nanofibre layer mass has a far lower impact on polarisability than the number of layers, suggesting interfacial polarisation is the probable core source of the impressive performance of these laminate structures.

This structure holds particular promise, as only a small amount of PVFHA nanofibre membranes is needed for each layer to achieve the high levels of interfacial and orientational polarisation. Since the limiting factor with regards to scalability of the composites is the production rate of the PVFHA nanofibres, this low mass requirement to achieve the high polarisation makes this a particularly scalable all-polymer ferroelectric composite. A 7-layered PMMA/PVFHA composite may prove to be insulating enough for any ultrahigh field applications due to the high PMMA:PVFHA layer thickness and the high number of boundaries. The fantastic miscibility and processability of the two polymers with respect to the hot-pressing procedure – as well as their high compressibility and low melting point – may help to further

reduce the cost and difficulties of production, as well as keep the failure rate of the composites low due to a low likelihood of void and defect formation.

It should also be noted that while many SAXS and XRD studies were performed on the laminates and nanofibres to gain insight into the effect of electrospinning and hot-pressing on the orientation of crystallites in the PVFHA nanofibres, orientation was sparingly observed. Further to this, the observed orientation across many sets of samples did not correlate well with ferroelectric energy storage performance, often seeming to be unimportant in comparison to the high interfacial polarisation seemingly observed in the many layer samples. Whilst there is interplay between polarisation mechanisms – for example, highly oriented crystallites could induce higher polarisation at the interfaces – it seems as though other aspects of the material nanostructure and microstructure are more relevant to the energy storage performances ultimately realised.

## 5.5. References

1. Chen, J. *et al.* Multilayered ferroelectric polymer films incorporating low-dielectric-constant components for concurrent enhancement of energy density and charge-discharge efficiency. *Nano Energy* **54**, 288–296 (2018).
2. Zhou, Z. *et al.* Interphase/interface modification on the dielectric properties of polycarbonate/poly(vinylidene fluoride-co-hexafluoropropylene) multilayer films for high-energy density capacitors. *J. Polym. Sci. Part B Polym. Phys.* **51**, 978–991 (2013).
3. Yin, K. *et al.* Effects of Interphase Modification and Biaxial Orientation on Dielectric Properties of Poly(ethylene terephthalate)/Poly(vinylidene fluoride-co-hexafluoropropylene) Multilayer Films. *ACS Appl. Mater. Interfaces* **8**, 13555–13566 (2016).
4. Chen, X. *et al.* Enhanced dielectric properties due to space charge-induced interfacial polarization in multilayer polymer films. *J. Mater. Chem. C* **5**, 10417–10426 (2017).
5. Tseng, J. K. *et al.* Interfacial polarization and layer thickness effect on electrical insulation in multilayered polysulfone/poly(vinylidene fluoride) films. *Polymer (Guildf)*. **55**, 8–14 (2014).
6. Cai, X., Lei, T., Sun, D. & Lin, L. A critical analysis of the  $\alpha$ ,  $\beta$  and  $\gamma$  phases in poly(vinylidene fluoride) using FTIR. *RSC Adv.* **7**, 15382–15389 (2017).
7. Peng, G. *et al.* New crystal structure and discharge efficiency of poly(vinylidene fluoride-hexafluoropropylene)/poly(methyl methacrylate) blend films. *RSC Adv.* **4**, 16849–16854 (2014).
8. Song, J. *et al.* PVDF/PMMA/Basalt fiber composites: Morphology, melting and crystallization, structure, mechanical properties, and heat resistance. *J. Appl. Polym. Sci.* **131**, 1–8 (2014).



9. Ute, K., Miyatake, N. & Hatada, K. Glass transition temperature and melting temperature of uniform isotactic and syndiotactic poly(methyl methacrylate)s from 13mer to 50mer. *Polymer (Guildf)*. **36**, 1415–1419 (1995).
10. Notario, B., Pinto, J., Verdejo, R. & Rodríguez-Pérez, M. A. Dielectric behavior of porous PMMA: From the micrometer to the nanometer scale. *Polymer (Guildf)*. **107**, 302–305 (2016).
11. Teixeira, S. S., Dias, C. J., Dionisio, M. & Costa, L. C. New method to analyze dielectric relaxation processes: A study on polymethacrylate series. *Polym. Int.* **62**, 1744–1749 (2013).
12. Marshall, J. E. *et al.* On the solubility and stability of polyvinylidene fluoride. *Polymers (Basel)*. **13**, 1–31 (2021).
13. Evchuk, I. Y., Musii, R. I., Makitra, R. G. & Pristanskii, R. E. Solubility of polymethyl methacrylate in organic solvents. *Russ. J. Appl. Chem.* **78**, 1576–1580 (2005).
14. Wang, G., Yu, D., Kelkar, A. D. & Zhang, L. Electrospun nanofiber: Emerging reinforcing filler in polymer matrix composite materials. *Prog. Polym. Sci.* **75**, 73–107 (2017).
15. Li, M. *et al.* Ferroelectric phase diagram of PVDF:PMMA. *Macromolecules* **45**, 7477–7485 (2012).
16. Guan, F., Pan, J., Wang, J., Wang, Q. & Zhu, L. Crystal orientation effect on electric energy storage in Poly(vinylidene fluoride-co-hexafluoropropylene) copolymers. *Macromolecules* **43**, 384–392 (2010).
17. Guan, F., Wang, J., Pan, J., Wang, Q. & Zhu, L. Effects of polymorphism and crystallite size on dipole reorientation in poly(vinylidene fluoride) and its random copolymers. *Macromolecules* **43**, 6739–6748 (2010).
18. Meng, N. *et al.* Ultrahigh  $\beta$ -phase content poly(vinylidene fluoride) with relaxor-like ferroelectricity for high energy density capacitors. *Nat. Commun.* **10**, 1–9 (2019).
19. Ren, X. *et al.* Giant energy storage density in PVDF with internal stress engineered polar nanostructures. *Nano Energy* **72**, 104662 (2020).
20. Wang, J., Adami, D., Lu, B., Liu, C. & Maazouz, A. Multiscale Structural Evolution and Its Relationship. *Polymers (Basel)*. **12**, (2020).
21. Mishra, S. *et al.* Effect of multi-step processing on the structural, morphological and dielectric behaviour of PVDF films. *Ionics (Kiel)*. **26**, 6069–6081 (2020).
22. Kang, S. J. *et al.* Localized pressure-induced ferroelectric pattern arrays of semicrystalline poly(vinylidene fluoride) by microimprinting. *Adv. Mater.* **19**, 581–586 (2007).
23. Gregorio, R. Determination of the  $\alpha$ ,  $\beta$ , and  $\gamma$  crystalline phases of poly(vinylidene fluoride) films prepared at different conditions. *J. Appl. Polym. Sci.* **100**, 3272–3279 (2006).
24. Gomes, J., Nunes, J. S., Sencadas, V. & Lanceros-Mendez, S. Influence of the  $\beta$ -phase content and degree of crystallinity on the piezo-and ferroelectric properties of poly(vinylidene fluoride). *Smart Mater. Struct.* **19**, (2010).
25. Li, W., Liu, Y. Y., Bai, Y., Wang, J. & Pang, H. Anchoring ZIF-67 particles on

- amidoximerized polyacrylonitrile fibers for radionuclide sequestration in wastewater and seawater. *J. Hazard. Mater.* **395**, 122692 (2020).
26. Jurczuk, K., Galeski, A., Mackey, M., Hiltner, A. & Baer, E. Orientation of PVDF  $\alpha$  and  $\gamma$  crystals in nanolayered films. *Colloid Polym. Sci.* **293**, 1289–1297 (2015).
  27. Laihonon, S. J., Gustafsson, A., Gäfvert, U., Schütte, T. & Gedde, U. W. Area dependence of breakdown strength of polymer films: Automatic measurement method. *IEEE Trans. Dielectr. Electr. Insul.* **14**, 263–274 (2007).
  28. Han, K. *et al.* A Hybrid Material Approach Toward Solution-Processable Dielectrics Exhibiting Enhanced Breakdown Strength and High Energy Density. *Adv. Funct. Mater.* **25**, 3505–3513 (2015).
  29. Diaham, S. *et al.* Dielectric breakdown of polyimide films: Area, thickness and temperature dependence. *IEEE Trans. Dielectr. Electr. Insul.* **17**, 18–27 (2010).
  30. Lalia, B. S., Guillen-Burrieza, E., Arafat, H. A. & Hashaikh, R. Fabrication and characterization of polyvinylidene fluoride-co-hexafluoropropylene (PVDF-HFP) electrospun membranes for direct contact membrane distillation. *J. Memb. Sci.* **428**, 104–115 (2013).
  31. Hartono, A. *et al.* Effect of Mechanical Treatment Temperature on Electrical Properties and Crystallite Size of PVDF Film. *Adv. Mater. Phys. Chem.* **03**, 71–76 (2013).
  32. Lin, B. *et al.* Enhanced dielectric permittivity in surface-modified graphene/PVDF composites prepared by an electrospinning-hot pressing method. *Compos. Sci. Technol.* **172**, 58–65 (2019).
  33. Wang, Y. *et al.* Ultrahigh energy density and greatly enhanced discharged efficiency of sandwich-structured polymer nanocomposites with optimized spatial organization. *Nano Energy* **44**, 364–370 (2018).
  34. Zhang, H. *et al.* A review on the development of lead-free ferroelectric energy-storage ceramics and multilayer capacitors. *J. Mater. Chem. C* **8**, 16648–16667 (2020).
  35. Shima, M., Sato, M., Atsumi, M. & Hatada, K. Dipole moments of isotactic and syndiotactic poly(methyl methacrylate) and their temperature dependence. *Polym. J.* **26**, 579–585 (1994).
  36. Chen, Q., Shen, Y., Zhang, S. & Zhang, Q. M. Polymer-Based Dielectrics with High Energy Storage Density. *Annu. Rev. Mater. Res.* **45**, 433–458 (2015).
  37. Ren, X., Meng, N., Yan, H., Bilotti, E. & Reece, M. J. Remarkably enhanced polarisability and breakdown strength in PVDF-based interactive polymer blends for advanced energy storage applications. *Polymer (Guildf)*. **168**, 246–254 (2019).
  38. Palneedi, H., Peddigari, M., Hwang, G. T., Jeong, D. Y. & Ryu, J. High-Performance Dielectric Ceramic Films for Energy Storage Capacitors: Progress and Outlook. *Adv. Funct. Mater.* **28**, 1–33 (2018).
  39. Wei, J. & Zhu, L. Intrinsic polymer dielectrics for high energy density and low loss electric energy storage. *Prog. Polym. Sci.* **106**, 101254 (2020).

## Chapter 6

### Conclusions and prospects for future work

#### 6.1. Conclusions

This thesis predominantly focussed on the production of polyvinylidene difluoride (PVDF) and PVDF-HFP (PVDF-co-hexafluoropropylene) with a high ferroelectric  $\beta$ -phase crystalline content by using the ionic liquid 1-allyl-3-methylimidazolium chloride (AMIM). The effect this had on the crystallography of the produced polymers was characterised, as well as their ferroelectric performance, with the end goal of producing a material that could be implemented in a pulsed power device capable of achieving a high energy discharge density,  $U_e$ , at high efficiency. Electrospun nanofibres proved the most adept material archetype for this aim, so this method was focussed on. Although, due to their physical and electrical properties – most importantly their fragility – they are not suitable for use as a dielectric in isolation, so a layered structure integrating more physically robust and electrically insulating polymers was pursued.

In chapter 3, the electrospinning process of PVDF was optimised, which involved maximising a few aspects concurrently. Initial endeavours into creating highly ferroelectric PVDF investigated the viability of a few polymer processing methods – solution casting, hot-pressing, and of course electrospinning. Spectroscopic characterisation experiments confirmed that electrospinning PVDF was producing the highest proportion of  $\beta$ -phase PVDF of the three methods, and thermal characterisation showed that the nanofibres also possessed a high total crystallinity. Hence the process of electrospinning PVDF nanofibre membranes was further investigated. As a homogenous nanofibre membrane with a high polymer crystallinity was desired while also containing as much of the ferroelectric  $\beta$ -phase as possible, the ionic liquid AMIM was added to the electrospinning solution to increase its conductivity. This was conceptualised to increase the alignment of PVDF molecular dipole alignment, resulting in the production of polar crystal phases. The electrospinning process was not only stabilised, but also achieved the desired aim of producing an even higher  $\beta$ -phase content. The AMIM electrospun nanofibres initially reached a 68%  $\beta$ -phase crystallinity – much higher than the highest proportion reached via hot-pressing or solution casting, where PVDF hot-pressed with AMIM reached a 45%  $\beta$ -phase crystalline fraction. The PVDF copolymer PVDF-HFP was also employed to enhance the ferroelectricity of the nanofibres due to its higher innate permittivity compared to the PVDF homopolymer. However, this has the undesirable side-effect of further decreasing the already slow electrospinning production throughput. Hence, efforts were made to offset this slow production rate as much as possible while retaining the high observed  $\beta$ -phase crystallinity. Ultimately, this led to an optimised electrospinning solution containing 20 wt% PVDF-HFP, 0.5 wt% AMIM and 79.5 wt% DMF.

In chapter 4, initial attempts at incorporating these nanofibres into a multilayer architecture were made. The aim here was to utilise the highly ferroelectric crystal structure of the PVDF-HFP/AMIM (PVFHA) nanofibres, which in insulation are not viable for electrical energy storage. Additionally, the unique morphology of electrospun polymers was exploited, as metal organic framework (MOF) nanoparticles were grown on their surface in an attempt to further increase the polarisability of the multilayer laminates produced. However, after attempts to grow several forms of zeolitic imidazole framework (ZIF, a class of MOFs) nanoparticles onto the surface of the PVFHA nanofibres, it was determined that these nanofibres possessed diameters too low for such coatings to adhere to their surfaces effectively. Hence the polymer polyacrylonitrile (PAN), a polymer also commonly used in electrospinning but that typically produces much larger nanofibres, was selected for coating instead. ZIF nanoparticles were successfully coated onto the nanofibres, and 5-layer laminates were fabricated incorporating the PVFHA nanofibres was created with a hot-pressing methodology, utilising solution cast PVDF layers on the outside to protect the PVFHA nanofibres. Unfortunately, this composite structure fell short of its goals in terms of both its structural cohesiveness and energy storage capabilities. The poor miscibility of the PVFHA nanofibre layer with the PAN/ZIF nanofibre layer resulted in voids in the laminate between these layers. While this did not usually lead to complete structural collapse, it occasionally caused delamination issues in small areas of the films. This likely caused the second issue, that being that the ferroelectric performance of the laminates involved high dielectric losses and often early electrical breakdown. Voids and defects in polymer laminates are well known for producing high dielectric losses, and notably for being nucleation sites for breakdown events. Thus, after the findings of this chapter, the integration of MOF nanoparticles and PAN nanofibres into the laminate structure was dropped so that focus could be shifted onto how to capitalise on the crystal structure of the PVFHA nanofibres for ferroelectric energy storage.

Considering these results, in chapter 5, the multilayer architecture was investigated further, but this time with an emphasis on the structural cohesiveness to ensure low dielectric losses and high electrical breakdown strengths. Eliminating voids and defects in the structure was the issue primarily limiting the performance of the materials in these respects, so a polymer highly miscible with the electrospun PVFHA nanofibre membranes was first selected. Polymethyl methacrylate (PMMA) quickly proved itself to be a viable partner to the nanofibres due to its highly insulating electrical properties and high miscibility and processability with the PVFHA nanofibres. When processing the PVFHA nanofibres with the PMMA, emphasis was placed on retaining the crystalline nanostructure of the PVFHA nanofibres imbued by electrospinning, meaning methodologies utilising high temperatures were not considered viable. While a few attempts were made to solution cast PMMA over the nanofibres to avoid high temperatures altogether, this was quickly found to be unviable due to the high density of voids and defects

produced. So, hot-pressing was instead pursued, which was largely viable due to the melting point of PMMA being a fair amount lower than that of the PVFHA nanofibres. The high pressures and temperatures involved with hot-pressing avoids defects and voids appearing in the produced laminates, so the main hurdle for this methodology was whether the crystal nanostructure and material architecture could produce a high discharged energy density  $U_e$ . Further to this, the potential for hot-pressing to enhance the crystal nanostructure of the nanofibres was investigated, as the high pressures they are subjected to were postulated to potentially reduce their crystallite size – increasing their mobility and hence polarisability – or increase the crystallite alignment, increasing their polarisability. After substantial investigation into how different aspects of the processing methodology affected the nanostructure, microstructure, and energy storage performance, the largest enhancement to polarisability that was identified was bestowed by the use of many layers in the laminate structure. This implied that the most significant form of polarisation present was interfacial polarisation between the highly insulating PMMA layers and the highly polarisable PVFHA nanofibre layers. The high thickness ratio of the PMMA to PVFHA nanofibres helped to prevent electrical breakdown, even when the mass ratio of PMMA:PVFHA was near 1:1, while the many layered architecture and highly polarisable PVFHA nanofibre layers lead to impressive. This is a unique advantage provided by nanofibre layers compared to those produced by hot-pressing or solution casting, as the nanofibre membranes are highly porous and compressible before pressing, leading to the high thickness ratio and simultaneous low mass ratio. However, the performance limits of the best of these laminates are unknown, as the limits of voltage amplifier used for ferroelectric testing were regularly hit before electrical breakdown of these laminates, particularly in the cases with a high number of layers. Thus, further, more exhaustive testing of this architecture is required to analyse the potential of these straightforward, all-polymer dielectric laminates.

## 6.2. Prospects for future work

The use of PVDF nanofibres in multilayer dielectric polymer laminates has been investigated for the first time in this work. Key advantages of the processing approach have been evaluated, notably the capability of the devised hot-pressing methodology to retain a highly polar PVDF crystalline nanostructure whilst also producing a cohesive multilayer laminate which is resistant to electrical breakdown. However, some aspects of this methodology should be further explored to discern the true potential of these laminate structures, most notably:

- Temperature: the effect of pressing temperature on the laminates was explored extensively in this project, although a single optimal pressing temperature was difficult to discern, with different experiments suggesting differing affects of the temperature on the laminate structures produced. *In-situ* spectroscopy or X-ray diffraction experiments

during hot-pressing could uncover the underlying mechanisms of phase change in the multilayer laminates, enabling more directed processing approaches.

- Number of layers: with interfacial polarisation being a key contributor to the performance of the laminates, the limits of composites containing a high number of layers could be further investigated. Ultrahigh field breakdown analysis should be performed, particularly in the case of laminates with a high number of layers, as the insulating limit of the laminates is likely to be the main limiter on the performance of these materials.
- Quenching: one unexplored technique that could be applied to the multilayer laminates to further idealise their crystal structure is quenching the laminates in an ice bath upon removal from the press. This could avoid undesirable crystal-phase relaxation processes when the laminates are cooling, rather locking in the nanostructure present during pressing, potentially improving the polarisability of the laminates.

Additionally, alternative electrospinning methodologies – such as those utilising a rotating drum collector with multiple spinnerets – should also be investigated, as one of the key limiters on this methodology reaching industrial applicability is the production throughput. If PVFHA nanofibre membranes can be manufactured with a scalable form of the process outlined in chapter 3, pulsed power devices utilising these nanofibres may become commercially viable, particularly noting the low cost of the materials required to produce the laminates.

It's also possible that utilising more complex multilayer architectures could lead to more impressive performances. 3 component polymer multilayer laminates may produce multilayer laminates with even higher resilience to electrical breakdown, and could take further advantage of the high interfacial polarisation observed in the laminates towards the end of chapter 5. Producing cohesive laminates with many polymer components is a complicated endeavour, as processability and miscibility of the polymers must be considered, but has been achieved in some works with a single hot-pressing step. Adapting these methodologies with the context of retaining the nanostructure of the PVFHA nanofibres could prove difficult, however.

Finally, there are also other subtleties that could be investigated regarding the processing methodology. For example, an electric field could be applied during the hot-pressing procedure in order to align the ferroelectric crystallites in PVDF-HFP in-plane, potentially increasing the polarisability of the laminate when applying a through plane electric field. When combined with a high pressure and pressing near the melting point of the PVFHA nanofibres, this could be the key to producing relaxor-like ferroelectric behaviour in the laminates, as this combination of processing conditions brings together the advantages of hot-pressing and electrospinning, likely producing small, aligned  $\beta$ -phase PVDF crystallites.